Aus dem Institut für Robotik und Kognitive Systeme

Direktor:
Prof. Dr.-Ing. Achim Schweikard

A robotic assistance system for transcranial magnetic stimulation and its application to motor cortex mapping

Inauguraldissertation
zur
Erlangung der Doktorwürde
der Universität zu Lübeck
- Aus der Technisch-Naturwissenschaftlichen Fakultät -

Vorgelegt von Lars Matthäus
geboren in Berlin

Lübeck, im Oktober 2008

Lars Matthäus
Research Assistant
Institute for Robotics
and Cognitive Systems
Universität zu Lübeck
Ratzeburger Allee 160
23538 Lübeck, Germany

1. Berichterstatter	Prof. Dr.-Ing. A. Schweikard
2. Berichterstatter	Prof. Dr. rer. nat. U. Hofmann
Tag der mündlichen Prüfung:	19.01.2009
Zum Druck genehmigt. Lübeck, den	19.01.2009

gez. Prof. Dr. rer. nat. Jürgen Prestin
- Dekan der Technisch-Naturwissenschaftlichen Fakultät -

Contents

List of Figures

Zusammenfassung

Die vorliegende Arbeit beschreibt ein robotisches Assistenzsystem für die transkranielle Magnetstimulation (TMS) und dessen speziellen Einsatz zur Darstellung funktioneller Areale im Gehirn. Das System beruht auf einem seriellen 6-Gelenk-Roboter zur Positionierung einer TMS-Spule und einem optischen Lageverfolgungssystem zur Bestimmung der Position des Kopfes des Patienten. Es zeichnet sich dadurch aus, dass es eine Nachführung der Spule bei Bewegungen des Kopfes ermöglicht und somit auf eine Fixierung des Patienten ohne Genauigkeitseinbußen verzichtet werden kann. Der vorgestellte Algorithmus zur Darstellung funktioneller Areale verwendet die Muskelantworten des Patienten für Stimulationen an verschiedenen Positionen am Kopf, die Orte der Stimulation und ein Modell des elektrischen Feldes der Spule, um mit Hilfe statistischer Verfahren den Punkt der höchsten Wahrscheinlichkeit für die kortikale Repräsentation des Muskels zu berechnen.

In heutigen TMS-Behandlungen wird die Spule nach wie vor vom Arzt per Hand am Kopf positioniert und möglichst genau über dem Stimulationsgebiet gehalten. Alternativ wird der Kopf des Patienten fixiert und die Spule in einen Spulenhalter geklemmt. Mit Hilfe von Neuronavigationsmethoden gelingt es recht gut, die Spule so über einem vorbestimmten Zielgebiet zu positionieren. Wird die Spule von Hand gehalten, besteht jedoch die Schwierigkeit, die Genauigkeit über einen langen Zeitraum, zum Beispiel 30 Minuten für eine Tinnitus-Behandlung, aufrecht zu halten. Wird eine Genauigkeit von wenigen Millimetern in der Position und wenigen Grad in der Orientierung der Spule gefordert, so ist eine rigide Fixierung des Patienten bisher unvermeidbar. Dies führt zu einem erheblichen Komfortverlust für den Patienten und durch die damit verbundene Anspannung und Erregung zu einer veränderten Wirkung der TMS.

Das in dieser Arbeit vorgestellte roboterbasierte System löst dieses Problem. Durch permanente Lageverfolgung des Kopfes ist die Zielposition zu jedem Zeitpunkt bekannt. In einem zweistufigen Verfahren wird zunächst die Spule durch den Roboter an den gewünschten Zielpunkt gebracht. Sobald dieser erreicht ist, wird ein Modul zur Bewegungskompensation aktiviert, welches Änderungen in der Lage des Stimulationspunktes durch geeignete Roboteransteuerung ausgleicht.

Die hohe Positioniergenauigkeit von einem Millimeter und der schnelle Bewegungsausgleich mit einer Latenz von 100 Millisekunden sind jedoch nicht die einzigen Vorzüge des TMS-Robotersystems: Das System erlaubt es außerdem, Stimulationspunkte gezielt wieder anzufahren und somit TMS-Behandlungen zu wiederholen. Weiterhin ist es möglich, Stimulationspunkte im Voraus zu definieren und automatisiert anzufahren. Dies trennt die Behandlungsplanung, welche hohes medizinisches Wissen verlangt, von der Durchführung der Behandlung und kann somit auf längere Sicht zu mehr Personaleffizienz und Kosteneinsparungen führen.

Aus theoretischer Sicht treten bei der Umsetzung des Systems zwei Probleme auf. Zum einen kann eine Zielstellung der Spule durch verschiedene Gelenkstellungen des Roboters realisiert werden, so dass eine Auswahl zwischen diesen so genannten Konfigurationsmodi nötig ist. Zum anderen muss zur Positionierung eine sichere und realisierbare Trajektorie gefunden werden, die die Spule von der aktuellen Position in die Zielposition überführt.

Das erste Problem, die Wahl des Konfigurationsmodus des Roboters für eine gegebene Stellung der Spule, wird mit Hilfe einer Metrik im sechsdimensionalen Gelenkraum des Roboters gelöst. Mittels Rückwärtsrechnung werden alle möglichen Gelenkstellungen des Roboters berechnet und diejenige ausgewählt, welche bezüglich der Metrik am dichtesten an der Momentanstellung des Roboters liegt.

Das zweite Problem der Bahnplanung kann auf Grund seiner theoretischen Komplexität nur heuristisch gelöst werden. Der in dieser Arbeit vorgestellte Ansatz kombiniert eine einfache Bahn für den Spulenmittelpunkt mit einer optimierten Rotation der Spule entlang dieser Bahn. Die einfache Trajektorie des Spulenmittelpunktes stellt sicher, dass es niemals zu einer Kollision zwischen Spule und Kopf kommen kann. Die optimierte Orientierungsänderung der Spule ermöglicht es, für eine Vielzahl von Start- und Zielpunkten am Kopf eine für den Roboter realisierbare Trajektorie zu finden und dabei die Spule schnell und ohne große Schwenkbewegungen zum Zielpunkt zu führen. Die Optimierung bezieht sich hierbei auf eine diskrete Anzahl von Kippwinkeln der Spule entlang der Bahn sowie die verschiedenen Robotermodi zur Realisierung der Stellungen der Spule. Das Optimierungskriterium ist die maximale Orientierungsänderung der Spule von einer Stützstelle der Trajektorie zur nächsten.

Das vorgestellte Robotersystem vereinfacht und präzisiert die Erhebung von Stimulationsdaten zur Darstellung funktioneller kortikaler Areale. Durch den Ausgleich der Kopfbewegungen des Patienten können die evozierten Muskelpotentiale für die Stimulation an einem Punkt sinnvoll gemittelt und dem Stimulationspunkt zugeordnet werden. Ziel ist es nun, aus einer Anzahl von 10 bis 40 solcher Paare aus Stimulationsort und Muskelantwort den kortikalen Repräsentationspunkt des gemessenen Muskels zu berechnen.

Die bisher in der Fachliteratur publizierten Methoden ermitteln die kortikale Repräsentation meist durch Berechnung des mit der Stimulationsantwort gewichteten Mittels der Stimulationspunkte und anschließender Projektion des Schwerpunktes auf den Kortex. Dies ignoriert jedoch vollständig die Geometrie des von der Spule erzeugten elektrischen Feldes und kann daher nur für eine Teilklasse von TMS-Spulen, so genannte Achtspulen, angewendet werden. Die erzielten Genauigkeiten in der Lokalisation der kortikalen Repräsentation liegen im Bereich von einem Zentimeter. Einzig eine Publikation von Thielscher und Kammer beschreibt einen Algorithmus, der die individuelle Spulen- und Feldform in die Berechnung einbezieht. Jedoch erfordert das Verfahren ein spezielles und zeitaufwändiges Protokoll und ist in seiner Genauigkeit bisher nicht evaluiert.

In dieser Arbeit wird ein neuer Algorithmus zur Berechnung der kortikalen Repräsentation vorgestellt. Der Algorithmus beruht auf einem vereinfachten biophysikalischen Modell der Stimulation, welches eine monoton wachsende funktionelle Abhängigkeit der Muskelantworten von der elektrischen Feldstärke am Repräsentationspunkt beinhaltet. Daher wird für die zur Stimulation verwendete Spule die Feldverteilung berechnet oder gemessen und mit

den Stimulationspunkten kombiniert, um so für jeden Punkt des Kortex und jeden Stimulationsort eine angenäherte Feldstärke zu ermitteln. Für jeden Punkt des Kortex wird dann mittels eines statistischen Tests die Wahrscheinlichkeit eines funktionellen oder monotonen Zusammenhangs zwischen diesen Feldstärken und den Muskelantworten bestimmt.

Anhand von insgesamt 52 Stimulationsdatensätzen von sieben Probanden wurden verschiedene statistische Tests zur Evaluation des in den Wertepaaren von Feldstärken und Muskelantworten repräsentierten funktionellen oder monotonen Zusammenhangs getestet. Es zeigte sich, dass der Kendallsche Rankkoeffizient τ eine geeignete Statistik für das vorliegende Problem ist. Die Auswertung der Daten mit dieser Statistik ergibt ein klares Wahrscheinlichkeitsmaximum, welches für die Stimulation mit Achtspulen mit alternativen Lokalisierungen mittels funktioneller Magnetresonanztomografie und direkter elektrischer Stimulation während eines operativen Eingriffs übereinstimmt.

Weiterhin ermöglicht der hier vorgestellte Algorithmus das erste Mal die funktionelle Lokalisierung auch für andere Spulentypen als Achtspulen. Die Arbeit demonstriert dies am Beispiel einer Rundspule, welche im Gegensatz zur Achtspule keine fokussierte Feldverteilung aufweist. Die berechneten Repräsentationspunkte für die Stimulation mit der Rundspule erreichen zwar im Vergleich mit funktioneller Magnetresonanztomografie nicht die Genauigkeit der Lokalisation mit Achtspulen, liegen aber mit einer Differenz von einem Zentimeter im Bereich der in der Literatur berichteten Genauigkeit der konventionellen Verfahren für Achtspulen.

Das vorgestellte Verfahren hat im Vergleich zu bestehenden Algorithmen aus der Literatur den Vorteil, dass mehrere Muskelrepräsentationen parallel mit hoher Genauigkeit in kurzer Zeit lokalisiert werden können. Dies ermöglicht insbesondere den Einsatz für die präoperative Planung von Tumorresektionen im Bereich des motorischen Kortex. So konnte durch den Einsatz des Robotersystems und des beschriebenen Lokalisationsalgorithmus für zwei Patienten eine klare Abgrenzung des funktionellen Handareals gegenüber Tumorgewebe gezeigt werden. Dieser Befund wurde in der darauf folgenden Operation zur Resektion des Tumors durch elektrische Stimulation am Hirn bestätigt. Die postoperative vollständige Beweglichkeit der Hand zeigte dann direkt die Korrektheit der Vorhersage der TMS-Handlokalisierung außerhalb des Tumorgewebes.

Abstract

To overcome the problems of conventional image guided transcranial magnetic stimulation (TMS), we developed a robotic system to place the coil at a target position and to keep it in place even if the head of the patient moves. The system is able to position the coil tangentially at any point on the head with any predefined rotation about the coil's vertical axis. Motions of the head are detected using a tracking system and compensated by steering the robot to the updated target position.

The introduction of a robot for TMS coil positioning does not only solve the problems of exact targeting and motion compensation, it also enables a number of novel features: Firstly, it allows for precise continuation of the stimulation in consecutive sessions. Secondly, it makes it simple to stimulate in a predefined grid pattern. Thirdly, it separates treatment planning from treatment execution as it is known from radiotherapy and radiosurgery. Finally, it might offer new possibilities of treatment, e.g. by controlled coil movement over the scalp during repetitive stimulation.

The system's main components are a serial robot arm with six joints and a marker-based optical tracking system. Both devices are linked by a control computer, which converts the target coordinates from the medical image data into real world coordinates and commands robot joint settings to place the TMS coil there. Hereby, real-time tracking data from the camera system is used to determine the current position of the head.

Two major challenges had to be overcome for robot aided TMS. Firstly, we developed a new way to deal with robot redundancy, i.e. an algorithm how to chose a configuration from the set of possible joint settings encoding the same pose of the TMS coil. When we command the robot to a new position, we first calculate all possible target joint settings and choose the one closest to the actual joint setting according to the Euclidean metric in joint space.

The second challenge was to define a safe, robust, and fast heuristic for the trajectory from the actual position to the target position for the coil. Our solution is to combine a foolproof trajectory for the centre of the coil – namely a circular motion with some distance from the head from the start to the target spot – with an optimised orientation change along the way. The resulting heuristic is safe, because of the simple trajectory of the coil's centre. It is also robust, because the freedom in orientation allows to find a realisable coil path for most of the start and target points around the head. The heuristic can be implemented in a fast way; it usually needs about 100 ms to compute a trajectory.

Evaluation of the system yielded a mean accuracy of the system of about 1 mm. The motion compensation module was evaluated to work with a latency of about 100 ms, i.e. it takes about 0.1 seconds before the robot starts to compensate for a head movement. Our

experiments with 20 subjects show that these data allow for successful stimulation in the areas of tinnitus treatment, treatment of chronic pain, and motor cortex mapping.

One major application of our robot aided TMS system has been the precise localisation of cortical representations of muscles. The use of the robot for the procedure has two advantages compared to manual (image guided) TMS: it makes it easy to define and approach target points, e.g. along a grid-like pattern, and it keeps the TMS coil at the target position, even if the head moves, so that several MEPs can be averaged. The second point is of special importance as TMS evoked MEPs have been shown to possess great variability. Thus, averaging strongly improves the mapping results.

We approach the problem of motor cortex mapping from a biophysical point of view. Our model assumes a monotonic functional relationship between the electric field strength at a cortical representation of a muscle and its MEP. Thus, we find the cortical representation by identifying the point on the cortex where such a relationship is most likely given the experimental data. In detail, for a point p on the cortex we approximate the electric field strength E_p for each stimulation point (coil position) i. We then estimate the likelihood of a monotonic functional relationship by looking at the list of pairs $(E_p(i), MEP(i))$.

We show in this thesis that if we use Kendall's τ as an estimator for the monotonic relationship, we get a clear maximum site for the cortical representation. Furthermore, applied to a mapping with a figure-of-eight coil the predicted representation agrees with data from fMRI within the resolution of the fMRI data (4 mm). For the first time, our method allows mapping with non-focal coils like circular coils. Even though the data obtained with a circular coil yield a mapping with a noticeable distance from the fMRI maximum (about 1 cm), we still match the accuracy results for figure-of-eight coils from the literature here.

Our technique for motor cortex mapping was used in a trial study on six patients with tumors in the central region. For such a lesion, mapping with metabolic based technologies like fMRI or PET often fails to identify the cortical representation of muscles, because the high metabolism of the tumor covers the signal from the motor area. As the neuronal excitation by TMS is not influenced by the vicinity of tumor tissue, TMS allows a mapping also in these cases. In the pilot study, we were able to clearly map the cortical representation of up to four hand muscles for the left and the right hand for all patients. All maps gave localisations which were in accordance with anatomical data. For two patients, a comparison with direct electrical stimulation during surgery was possible and confirmed the TMS mapping results.

1. Introduction

Transcranial magnetic stimulation (TMS) is a method for stimulating the brain non-invasively and painlessly. Developed by Barker, Jalinous, and Freeston [8], it is based on the principle of electromagnetic induction. A strong current is driven through a coil in a short period of time. The rapid change of current creates a changing magnetic field around the coil. The field penetrates the skull nearly without loss and induces a current in the brain, exciting neurons there [123]. Thus, parts of the brain close to the coil can be stimulated, resulting for example in an excitation of the motor cortex and subsequent muscle twitching in related limps [12]. A schematic view of the principles of TMS is given in Figure 1.1.

1.1. Purpose of this work

To date, TMS has only limited clinical relevance. Although it has been shown beneficial in the treatment of neurological and neurophysiological disorders such as depression, stroke, tinnitus or epilepsy, big inter-individual treatment outcomes hindered the routinely use of TMS so far. Furthermore, the positive effects of TMS do not yet exceed the results of conventional therapies (medication, behaviour therapy, physical training).

A main reason for the unsatisfactory treatment results so far seems to be the limited understanding of the neuronal and cognitive effects of TMS. Therefore, much research effort is directed towards better models of the effects of TMS on the brain.

Key elements in the derivation of new and better models of TMS effects on the brain are reliable experimental data. Conventionally, TMS is applied manually to the head (Figure 1.2.A). The investigator holds the coil to a position she / he deems suitable for stimulation and releases the pulse. If the motor area is stimulated, the investigator gets an immediate feedback in form of muscle twitches of the patient. The response is often used to refine the coil position until the target muscle responds strongest. For other areas of the brain, there is no such direct feedback. Therefore, the coil is often placed according to a standardised atlas, e.g. using the 10-20 EEG system [55].

The state-of-the-art for exact targeting with TMS is to use image guidance technology known from neurosurgery [48], Figure 1.2.B. Hereby, the TMS coil and the head are tracked using a set of artificial markers attached to the head and to the coil. Registering the head to medical image data (MRI, fMRI, CT, PET, etc.) allows to visualise the coil's position with respect to the anatomical or functional data and so to target the desired region.[1]

[1] MRI stands for magnetic resonance imaging, CT for computed tomography.

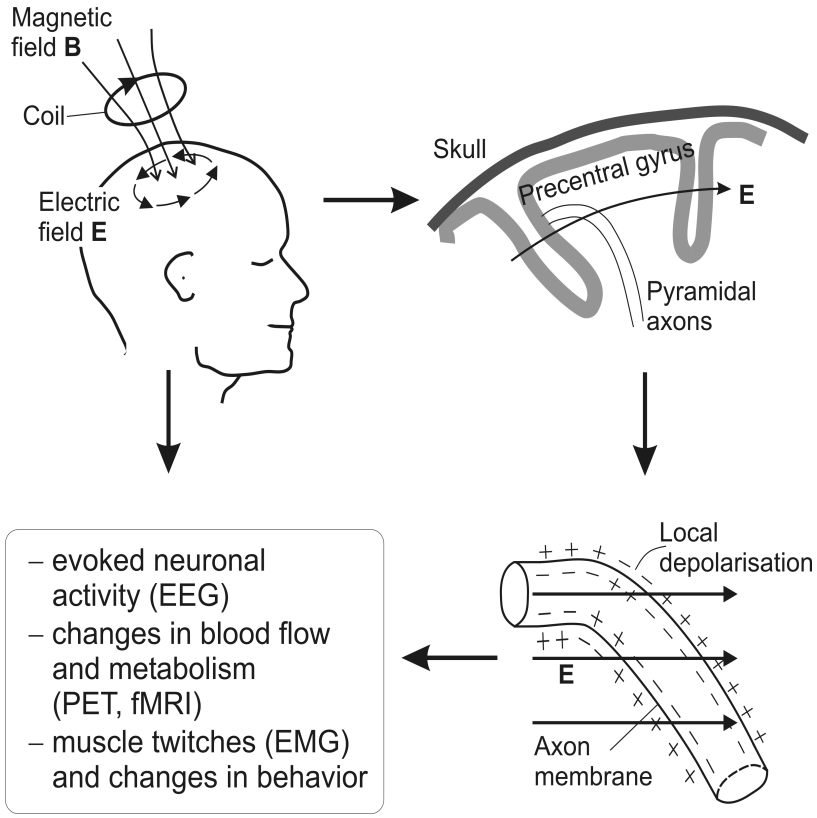

Figure 1.1.: Principles of transcranial magnetic stimulation. The changing currents in the coil create a changing magnetic field (upper left). The field passes through the skull and induces an electric field in the brain (upper right). The electric field leads to a local depolarisation of axons (lower right). If the field strength is above the excitation threshold, the neuron becomes activated. The activation of larger groups of neurons results in a macroscopic response (lower left). Figure from [153], with friendly permission of the author.

Still, the quality of the stimulation depends on the experimenter's skills. She / he is responsible for bringing the coil to its target position and to hold it there for the duration of the stimulation, both using image guidance. This task is not as easy as it seems. An exact tangential placement of the coil is hard to establish: often the coil is tilted, shifting the locus of activation away from the target region. Furthermore, protocols for repetitive stimulation (rTMS) require the coil to be held in place for up to an hour. Achieving this without the loss of accuracy over time is clearly impossible for a human operator. The alternative, a rigid fixation of the head and the employment of a mechanical coil holder, is inconvenient for the patient. This is a major problem, because the response to TMS has been shown to change severely with the state of alert of the patient and his muscle tonus [71], so tension or even pain have to be avoided to ensure a reliable stimulation outcome.

The robot system for aiding transcranial magnetic stimulation presented in this thesis is aimed for precise and repeatable stimulation. Furthermore, it should make the experiments independent of the examiner's skills to place the coil correctly and hold it in position for the duration of the stimulation session by active motion compensation. Finally, by making head

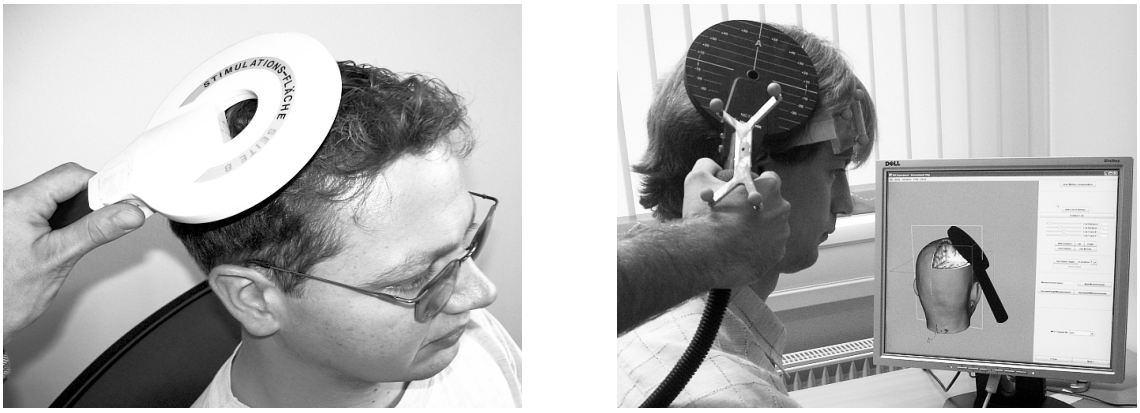

A B

C

Figure 1.2.: Evolution of coil placement in TMS. A: Manual coil placement without guidance. B: Manual coil placement with support from image guidance. C: Coil placement by a robot, compensating for head movements e.g. during a TMS-EEG experiment.

fixation obsolete it should allow more comfortable experiments for the participant. This would reduce the influences of muscle tension or pain from fixation on the experimental outcome.

The second objective of this thesis is to improve the quality of TMS motor cortex mapping algorithms to make it applicable to pre-surgical planning for the resection of tumors in the central region. The main question in this context is whether the tumor has infiltrated the motor cortex or not. In the first case, a full resection of the tumor is possible. In the second case, a partial resection or an alternative therapy must be chosen, because a full resection would paralyse the patient.

Due to the strong and erratic metabolic activity of tumor tissue, conventional mapping of the motor cortex with fMRI or PET fails if the tumor is close to it.[2] On the contrary, the effects of TMS are not influences by the presence of tumor tissue. This makes TMS to

[2]fMRI stands for functional magnetic resonance imaging, PET for positron emission tomography.

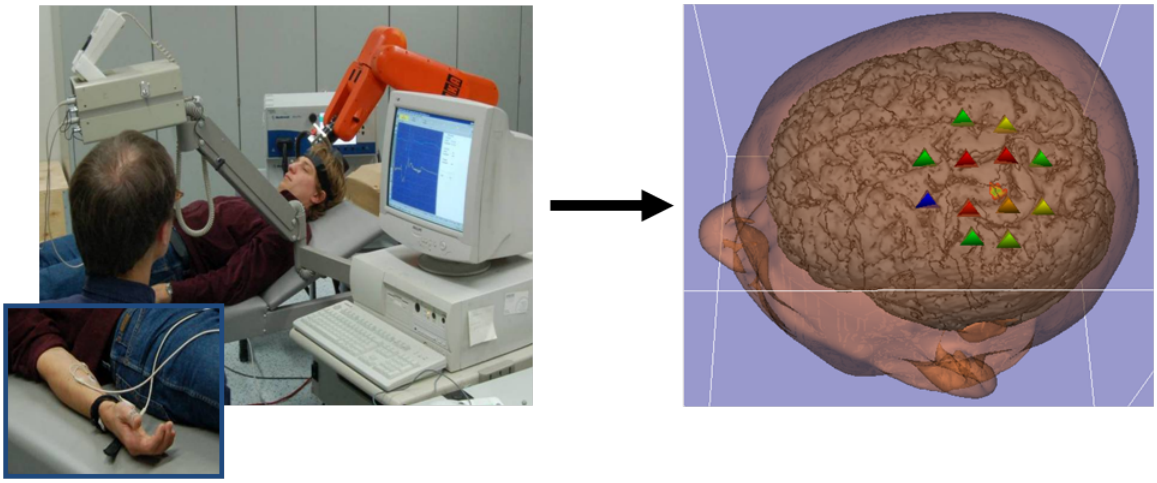

Figure 1.3.: Principles of motor cortex mapping with TMS. Right: The coil is placed at different positions around the head, the cortex is stimulated, and the muscle response (MEP) measured. Left: From the data pairs of coil position and corresponding MEPs (position and colour of the trihedrons in the picture) we calculate the most likely cortical representation of the mapped muscle (coloured area on the brain).

a potentially useful tool to identify the region of the brain where the motor functions are represented. The usefulness hereby depends crucially on the accuracy of the mapping.

The basic principle of mapping with TMS is to stimulate at several positions on the head and to record the muscle response for each stimulation, the so-called motor evoked potential (MEP). From the emerging pattern of stimulation points and corresponding MEPs one then calculates the cortical representation site of the muscle. An overview of the motor cortex experiment is given in Figure 1.3.

Transcranial magnetic stimulation has been used to determine the localisation of muscle representations as early as 1990 [36]. But apart from one publication by Thielscher and Kammer in 2002 [175], the influence of the coil on the mapping results has been ignored so far. Thus, it comes with no surprise that TMS mapping has been found to agree only within centimetre range with mapping using other modalities such as fMRI [92], PET [26], or direct electrical stimulation [77]. Furthermore, the algorithms are based more on abstract geometric reasoning than on neurophysiological modelling, making their results at least questionable.

Therefore, we derive in this thesis a new algorithm from a model of excitory effects of TMS on the motor neurons.

1.2. Organisation of this work

This thesis is structured as follows. In Chapter 2 we start with a brief overview over the medical and neuroscientific applications of TMS (Section 2.1). We then turn to the biophysical principles behind TMS. We explain how TMS is thought to excite neuronal

tissue (Section 2.2.1), first for the well understood case of a long distal axon and then for the case of the brain. As the principal quantity behind the stimulation is the electric field in the vicinity of the neurons, we introduce the governing equations for the electric field and derive formulae which allow the computation of the electric field of a TMS coil in air and in tissue (Section 2.2.2). In the final part of the chapter, Section 2.3, we explain the basic technology of a TMS stimulator and present the different coil designs in use for TMS.

Chapter 3 deals with the robot solution for TMS. The chapter starts with an overview over the state-of-the-art in image guided and robot aided TMS (Section 3.1). Next, we describe our system set-up, placing special emphasis on the modularity of the system and the exchangeability of the single components such as the tracking system or the robot (Section 3.2). We then turn to our algorithmic solutions for solving the ambiguity in robot configuration modes and for calculating a valid trajectory from one stimulation point to the next (Section 3.4). The chapter concludes with technical and algorithmic solutions to ensure the safety of the system (Section 3.5).

In Chapter 4 we present our solution to the motor cortex mapping problem. Again, we first describe the state-of-the-art in the field (Section 4.1). Next, we introduce possible statistics for evaluating the degree of monotonic or functional correspondence between the lists of the electric field strength and the muscle responses (Section 4.3). In Section 4.4 we describe how we obtained the electric field values for the TMS coils we used in our experiments. We present two methods here, namely measuring the field and simulating it. Finally, in Section 4.5 we present data from the mapping experiments conducted so far. The data are used to test the mapping statistics for their suitability in our motor cortex mapping algorithm. Furthermore, we compare the mapping results with alternative mappings from fMRI and direct electrical stimulation during surgery.

Chapter 5 presents medical and neuroscientific applications in which the robot system has been used. We briefly describe the medical or neuroscientific background of each application, point to the advantages of using a robotic TMS system for them, and highlight necessary adaptations of the system.

Chapter 6 first discusses the robot system's performance. This is done in two ways: by quantifying the static and dynamic errors in positioning the TMS coil on a phantom head (Section 6.1) and by analysing the system's performance in real-world applications in a qualitative way (Section 6.2). We then discuss the performance of our motor cortex mapping algorithm and analyse possible shortcomings in our biophysical assumptions and in our approximations to make the algorithm work (Section 6.3). We end the chapter with a thorough discussion of possible improvements to the robot system and the motor cortex mapping algorithm in the future (Section 6.4).

The work closes with an appendix, deriving a discrete formula for the Correlation Ratio statistic which gives stable values even if very few sample pairs are present. The formula is required for the motor cortex mapping statistic in Chapter 4.

2. Transcranial Magnetic Stimulation

The contribution of this work is technical. This chapter briefly outlines the main aspects of the medical and physics background of TMS. We describe the basic principles of how the TMS coil produces the electric field and how this field is thought to stimulate the neurons in the brain. Afterwards, we introduce the basic equipment for TMS and have a closer look at the different stimulation coil geometries in use.

2.1. Medical applications of TMS

The applications for TMS are manifold today. In clinical routine, single pulse stimulation is by far the most common form of TMS. With single TMS pulses, no lasting effects (longer than one second) have been observed, so this modality is purely used for diagnostic means. On the other hand, repetitive stimulation (rTMS) has been shown to elicit changes in cognition that can last for several weeks. This makes rTMS a promising therapeutic tool. Unfortunately, so far such cognitive changes could not be produced in a reliable manner for a diverse range of patients. Therefore, rTMS is still mainly a tool for research and not for the clinical practice.

2.1.1. Single pulse TMS

Single pulse TMS is mainly used as a diagnostic tool to study the excitability of the motor cortex, the functional integrity of intracortical neuronal structures, the conduction along corticospinal, corticonuclear and callosal fibres, as well as the function of nerve roots and peripheral motor pathway to the muscles [74]. The main parameters in the examinations are the conduction time (time between stimulus and recorded motor response), the stimulation intensity required for a response (possibly in relation to the intensity required at a secondary stimulation site), the "hotspot" (point of maximum response; only for figure-of-eight coils), and the silent period (time span in which no response to a second stimulus – TMS, auditory, visual – can be obtained). In detail, single pulse TMS has been used in the diagnosis of spinal cord injury [35], multiple sclerosis [21], Huntington's disease [105], Parkinson's disease [110], writer's cramp [113], and many more. For a first overview see [123].

Furthermore, single pulse TMS is used for mapping the motor cortex in brain research [20, 38, 54, 119] and before neurosurgical interventions [80, 107, 189]. The basic idea is to use the different motor responses obtained from different coil placements to calculate the localisation of the muscle representation in the cortex. Chapter 4 is solemnly devoted to

the problem of motor cortex mapping; please refer to Section 4.1 for an overview of the state-of-the-art.

2.1.2. Repetitive TMS

Repetitive transcranial magnetic stimulation, i.e. stimulation applied with a repetition frequency of 1 to 20 Hz, can inhibit or facilitate brain functionality in the stimulated area [121], depending on the frequency. Therefore, rTMS has been applied to a wide range of therapeutic and research areas. Most prominent, perhaps, is the treatment of depression [49, 122]. But very active research is also undertaken in the areas of tinnitus [34, 73, 128], chronic pain [86, 131, 139], and stroke rehabilitation [43, 70], to name but a few.

Further TMS research deals with the study of the visual cortex [5] and central nervous information processing [52]. Increasingly, TMS is combined with other neuroimaging methods like functional magnetic resonance imaging (fMRI) [16], positron emission tomography (PET) [44] and electroencephalography (EEG) [177].

2.2. Biophysical Principles

TMS is based on the principle of induction. By discharging a capacitor, a strong current is driven through a coil which is held close to the head. The rising and falling current produces a time-varying magnetic field. This field passes through the skull nearly undisturbed. The change of the magnetic field induces an electric field which excites the brain tissue underneath the coil. Section 2.2.1 summarises how an electromagnetic field causes the activation of a neuron and creates thus a physiological response. Section 2.2.2 explains the physics of TMS, i.e. how the field is produced by the coil and how it interacts with conducting material like brain tissue.

2.2.1. The biology

Despite the name transcranial *magnetic* stimulation, it is the electrical component of the electromagnetic field that is responsible for the neuronal excitation in TMS. Neurons are activated by a super-threshold depolarisation of a part of the axon compared to the resting state, i.e. when the resting membrane potential of about -70 mV is sufficiently increased. The electric field of the TMS pulse affects the membrane potential of the axon and can thus activate the neuron.

The exact mechanism of activation of neurons in the brain by electric fields is quite complicated and not yet completely understood. Before we introduce the influencing factors for TMS excitation in the brain, we have a look at the simpler and better understood activation of long distal axons.

2.2.1.1. Excitation of long distal axons

The transmembrane potential V along the axon's direction x is well approximated by the cable equation [104, 137, 146, 170]:

$$\lambda^2 \frac{\partial^2 V}{\partial x^2} - V - \tau \frac{\partial V}{\partial t} = f(x,t). \tag{2.1}$$

Hereby, λ and τ are the space and time constants of the axon with typical values of $0.1\,\text{mm} \leq \lambda \leq 1\,\text{mm}$ and $100\,\mu\text{s} \leq \tau \leq 500\,\mu\text{s}$ [123]. The function f, the so-called activation function, describes the external excitation of the axon [136]. According to Ruohonen [151, 152], the activation function for TMS takes the form

$$f(x,t) = \lambda^2 \frac{\partial E_x}{\partial x} - 2RE_T, \tag{2.2}$$

where E_x is the electric field strength in direction of the axon, E_T is the electric field strength transverse to the axon, and R is the diameter of the axon.

From Equations (2.1) and (2.2) we see that a high transmembrane voltage, and thus an activation of the neuron, can occur for

1. a strong electric field transversal to the axon,
2. a strong electric field gradient along the axon,
3. a strong electric field at a bend of the axon.

Activations 1 and 2 are immediately clear from Equation (2.2). Activation 3 can be thought of a special case of 2: a bend in the axon leads to change in electric field strength along the axon, E_x, even if the electric field itself is spatially constant. For example, consider an electric field of constant strength E_0 and constant direction and an axon which first runs parallel to the field vectors and then bends away in a 90° angle. The electric field strength along the axon is thus $E_x = E_0$ before the bend and $E_x = 0$ after the bend. If the curvature of the axon is sufficiently large, i.e. the radius of the bend is small, this change happens within a very small distance along the axon and can thus elicit an action potential.

The cable model (2.2) is only valid for long axons in rest, i.e. without activation. As soon as the stimulation is above the threshold, non-linear dynamics set in, requiring a much more complicated mathematical treatment. Modelling, on the basis of the Hodgkin-Huxley-Model [56], is still possible for single neurons [9, 10, 146]. But in the brain, a too large number of neurons in all states of excitation are present as that a quantitative description of the excitation is possible [123, 153]. Therefore, a mainly qualitative treatment of the stimulation phenomenon is given in the literature.

2.2.1.2. Excitation of the brain

The principle of neuronal activation in the brain by TMS is the same as for peripheral nerves: The electric field leads to a local super-threshold hyper- or depolarisation of the neuron. Neurons in the brain often have a specific orientation. The axons of corticospinal

neurons[1] run normal to the surface of the cortex. Usually, these axons are organised in so-called cortical columns. The perpendicular arrangement of the columns led Fox et al. to suggest that TMS excitation is achieved by a strong electric field perpendicular to the cortical surface [44].

Other scientists have argued that the activation pattern from stimulating the motor cortex prompts towards interneurons as the source of excitation in TMS [32, 33, 83]. Interneurons connect neighbouring afferent and efferent neurons and are generally of short length (about 1 mm). In contrast to corticospinal neurons, their axons show no directional preference.

To make matters more complicated, the locus of activation seems to depend also on the stimulation strength. Comparison with direct electrical stimulation revealed that low intensity TMS elicits indirect neuronal responses (so-called I-waves), whereas high intensity stimulation elicits also direct corticospinal responses (D-waves) [32, 33, 59, 83, 123]. There is no consensus yet over the exact origin of the I-waves; it is hypothesised that interneurons and axon collaterals of deeper neurons (layers III and IV of the cortex) are responsible for activating the corticospinal neurons [2, 3, 123]. The direct activation of corticospinal neurons (D-wave) is generally thought to take place at the axon.

The type of activation is most probable either Activation 1, a strong electric field transverse to the axon, or Activation 3, a bend of the axon. Therefore, most scientists locate the area of stimulation at the site of the strongest electric field strength [77, 92, 123], a view that is also taken in this thesis.

We remark that this model – activation at the site of highest electric field strength – does not explain the observation that the motor response to TMS depends on the orientation of the TMS coil. Brasil-Neto et al. [20] and Mills et al. [106] demonstrated that the response to a stimulus is strongest when the figure-of-eight coil is oriented perpendicular to the central sulcus and weakest if its oriented parallel to it. So far, only Fox et al. offered a controversial explanation, namely that TMS affects mainly the cortical columns [44].

2.2.2. The physics

In this section we analyse TMS from a purely non-biological point of view, i.e. we ignore any effects from neuronal excitation. This simplification allows us to derive equations for the electric field induced by TMS in the brain on a macroscopic scale. As we have seen in the last section, the locus of TMS activation is thought to be the point of strongest electric field.

[1] Corticospinal neurons connect the brain with the spinal cord.

In general, all non-biological effects of TMS are fully described by Maxwell's Equations [103]

$$\nabla \cdot \mathbf{D} = \rho, \tag{2.3}$$
$$\nabla \cdot \mathbf{B} = 0, \tag{2.4}$$
$$\nabla \times \mathbf{E} = -\frac{\partial \mathbf{B}}{\partial t}, \tag{2.5}$$
$$\nabla \times \mathbf{H} = \mathbf{J} + \frac{\partial \mathbf{D}}{\partial t} \tag{2.6}$$

and the material equations

$$\mathbf{D} = \epsilon \mathbf{E}, \tag{2.7}$$
$$\mathbf{B} = \mu \mathbf{H}, \tag{2.8}$$
$$\mathbf{J} = \sigma \mathbf{E}. \tag{2.9}$$

Hereby, the vector fields $\mathbf{D}, \mathbf{E}, \mathbf{H}, \mathbf{B}, \mathbf{J}$ denote the electric flux density, the electric field, the magnetic field intensity, the magnetic field, and the current density, respectively. The scalar field ρ denotes the charge density. The material constants $\epsilon = \epsilon_0 \epsilon_r, \mu = \mu_0 \mu_r, \sigma$ denote the permittivity, the permeability, and the conductivity, respectively.

This set of equations is rather difficult to solve in the presence of a non-homogeneous, geometrically complicated conductor like the head. Fortunately, the full power of Maxwell's Equations is not necessary for understanding the effects of TMS.

2.2.2.1. Quasi-static approximation

A typical TMS pulse lasts about 100 µs, corresponding to a frequency of 10 kHz. As shown theoretically in [51, 94, 129, 179] and demonstrated numerically in [19, 184], Maxwell's Equations can be simplified in three aspects for TMS:

1. The wavelength of the TMS pulse is about $\mathrm{c}/10^{-4}\,\mathrm{s} = 3 \times 10^4\,\mathrm{m}$, c being the speed of light. This wavelength is much larger than the diameter of the head. Further, the capacitive effects of the head tissue are negligible at TMS frequency. Thus, we can assume the magnetic field to follow the same time course $f(t)$ at every point r in space: $\mathbf{B}(r,t) = \mathbf{B}(r)f(t)$.

2. The ratio of the change of the displacement current $\frac{\partial \mathbf{D}}{\partial t}$ to the conduction current $\mathbf{J}$ is given by $\frac{\omega\epsilon}{\sigma}$, ω being the angular frequency. For TMS frequencies and head tissue it is in the range of 10^{-2} to 10^{-3}. This simplifies equation (2.6) to $\nabla \times \mathbf{H} = \mathbf{J}$ and implies

$$\nabla \cdot \mathbf{J} = 0. \tag{2.10}$$

3. The square of the magnetic skin depth[2] $\delta^2 \approx \frac{2}{\mu\sigma\omega}$ of the biological material is about 10 times bigger than the diameter of the head. The ratio of the original magnetic field

[2] This is an electromagnetic property of the tissue material and has nothing to do with the thickness of the skin covering the bone. Nevertheless, it is also measured in metre.

(produced by the TMS coil) to the secondary magnetic field (produced by the currents induced in the brain) is proportional to the square of the ratio of the magnetic skin depth to head diameter. So for TMS applied to the head, we need only to consider the magnetic field produced by the coil.

The simplifications enable a quasi-static solution, i.e. a solution which safely excludes capacitive, inductive and wave propagation effects. In the following, we summarise the governing electromagnetic equations for TMS, using the quasi-static approximation.

2.2.2.2. The equations

In TMS, the electric field $\mathbf{E}$ can be thought of as composed of two sources. Source 1 is the change in the magnetic field $\mathbf{B}$ produced by the coil. It holds, by Faraday's law,

$$\nabla \times \mathbf{E_1} = -\frac{\partial \mathbf{B}}{\partial t}. \tag{2.11}$$

This primary electric field causes free charges to shift and accumulate at a boundaries where the conductivity jumps in value. Those charges produce a counter-field or secondary electric field. This field is defined by the potential ϕ of the charges:

$$\mathbf{E_2} = -\nabla\phi. \tag{2.12}$$

By Equation (2.4), $\mathbf{B}$ can be represented by a vector potential $\mathbf{A}$:

$$\mathbf{B} = \nabla \times \mathbf{A}. \tag{2.13}$$

So the electric field is given by

$$\mathbf{E} = \mathbf{E_1} + \mathbf{E_2} \tag{2.14}$$

$$= -\frac{\partial \mathbf{A}}{\partial t} - \nabla\phi. \tag{2.15}$$

Together with Equations (2.9) and (2.10) this implies

$$\nabla \cdot (\sigma \nabla\phi) = -\nabla \cdot \left(\sigma \frac{\partial \mathbf{A}}{\partial t}\right). \tag{2.16}$$

By the quasi-static approximation, $\mathbf{B}$ and thus $\mathbf{A}$ do only depend on the current flow at time t in the coil c. For a point r, the magnetic vector potential is given by the Biot-Savart Law:

$$\mathbf{A}(r) = \frac{\mu_0}{4\pi} \int_{\mathbb{R}^3} \frac{\mathbf{J}(\mathbf{r}')}{|\mathbf{r} - \mathbf{r}\prime|} \mathrm{d}V \tag{2.17}$$

$$= \frac{\mu_0}{4\pi} \int_c \frac{I(\mathbf{r}')}{|\mathbf{r} - \mathbf{r}\prime|} \mathrm{d}\dot{\mathbf{c}} \tag{2.18}$$

In both equations, r' denotes the integration variable. The second equation follows from the first by restricting the integration to the wire of the coil c. Integrating the current density

$\mathbf{J}$ over the cross section of the wire gives the traditional current I that flows through the coil. The expression $\mathrm{d}\dot{\mathbf{c}}$ in second equation expresses that the integral is taken along curve of the wire.

The magnetic potential $\mathbf{A}$ alone does not define ϕ uniquely; Equation (2.16) has an infinite number of solutions. The necessary restriction comes from the boundary condition for the current flow. For two neighbouring volumes V_1 with conductivity σ_1 and V_2 with conductivity σ_2 let $\mathbf{n}$ denote the normal vector to the boundary. The current flow that flows out of V_1 must equal the current that flows into V_2 (Neumann boundary condition):

$$\mathbf{n} \cdot \mathbf{J_1} = \mathbf{n} \cdot \mathbf{J_2}. \tag{2.19}$$

Summarising, the stimulating electric field can be computed in the quasi-static limit by first computing the magnetic vector potential $\mathbf{A}$ produced by the coil and solving the partial differential equation (2.16) under the Neumann boundary condition (2.19) for ϕ. The resulting electric field is obtained by combining the change of the magnetic vector potential $\mathbf{A}$ and the gradient of the electric potential ϕ, Equation (2.15).

2.2.2.3. Properties

We derive briefly two important properties of TMS: no normal electric field at surfaces and no in-depth focusing possible.

No normal electric field at surfaces Inserting Ohm's law (2.9) in the Neumann boundary condition (2.19) we arrive at

$$(\sigma_1 - \sigma_2)\mathbf{n} \cdot \mathbf{E} = 0. \tag{2.20}$$

This implies that at boundaries of materials with different conductivities the electric field is always aligned tangentially to the boundary. The continuity of $\mathbf{E}$ ensures that this approximately holds also in the close neighbourhood of the boundary. This makes the suggestion of Fox et al. [44] to consider the electric field normal to the surface as activating quantity in TMS at least questionable and favours the explanation that macroscopic TMS excitation is due to the activation of interneurons which run tangentially to the cortex surface and bend to connect to deeper layers, see Section 2.2.1.2.

No in-depth focusing We follow the argumentation of [51]. Let us assume a region of constant conductivity, permittivity, and permeability. Taking the curl of (2.5) and substituting (2.6) and the material equations, we obtain

$$\nabla \times (\nabla \times \mathbf{E}) = -\mu\sigma\frac{\partial \mathbf{E}}{\partial t} - \mu\epsilon\frac{\partial^2 \mathbf{E}}{\partial t^2}. \tag{2.21}$$

We know from calculus that $\nabla \times (\nabla \times \mathbf{f}) = \nabla(\nabla \cdot \mathbf{f}) - \triangle \mathbf{f}$ for any differentiable vector field $\mathbf{f}$[3], so together with the quasi-static approximation (2.10) Equation (2.21) evaluates to

$$\triangle \mathbf{E} = \mu\sigma \frac{\partial \mathbf{E}}{\partial t} + \mu\epsilon \frac{\partial^2 \mathbf{E}}{\partial t^2}. \tag{2.22}$$

Using a Fourier expansion of E in t and comparing both sides of (2.22), we see that

$$\triangle \mathbf{E} = 0 \tag{2.23}$$

to first order in frequency for all points in the region. This converts (2.22) to a homogeneous wave equation. By the maximum principle, any solution[4] of (2.23) attains its maximum on the boundary of the region. Therefore, an in-depth focusing of TMS pulses, i.e. a coil geometry or an arrangement of coils that produce a 3D maximum of the electric field strength or of a component of the electric field, is impossible.

2.2.2.4. Reciprocity Theorem

TMS can be thought of as the "inverse" technology to Magnetoencephalography (MEG). In MEG, the magnetic field produced by electric currents in the brain is analysed by measuring the current induced in coils close to the head. In TMS, current is driven through coils close to the head, producing a magnetic field, which induces a current flow in the head. So it comes to no surprise that also the physical description of the effects is inversely related.

Let c be a coil outside the head V. Let $\mathbf{E}$ be the electric field inside the head, $\mathbf{J}$ the current flow in the head, I the current flow in the coil, and $\mathbf{B}$ the magnetic field passing through the coil. Then the following reciprocity theorem holds [51, 94, 153]:

$$\int_V \mathbf{E}(\mathbf{r}) \cdot \mathbf{J}(\mathbf{r}) d\mathbf{r} = -\frac{dI(t)}{d(t)} \int_c \mathbf{B} \cdot da. \tag{2.24}$$

Hereby, the electric field $\mathbf{E}$ is thought to be due to a changing current $\frac{dI(t)}{d(t)}$ running through the coil and the magnetic flux $\Phi = \int_c \mathbf{B} \cdot da$ through the coil to be due to a current density $\mathbf{J}$ in the head. It holds

$$\Phi = \int_V \mathbf{L} \cdot \mathbf{J} dV \tag{2.25}$$

with a function $\mathbf{L}$, the so-called lead field[5], depending on the shape and placement of the coil and the electromagnetic properties of the head. Taking $\mathbf{J}$ to be a point source at $\mathbf{r}$, i.e. $\mathbf{J}(\mathbf{r}') = 0$ for $\mathbf{r}' \neq \mathbf{r}$, we get

$$\mathbf{E}(\mathbf{r}) = -\frac{dI(t)}{d(t)} \mathbf{L}(\mathbf{r}). \tag{2.26}$$

[3] The laplace operator is understood to be applied component-wise, i.e. $\triangle \mathbf{f} = \begin{pmatrix} \partial_x^2 f_x + \partial_y^2 f_x + \partial_z^2 f_x \\ \partial_x^2 f_y + \partial_y^2 f_y + \partial_z^2 f_y \\ \partial_x^2 f_z + \partial_y^2 f_z + \partial_z^2 f_z \end{pmatrix}$.

[4] The solutions to the wave equation are the so-called harmonic functions. Besides the maximum principle, it holds the superposition principle: Any linear combination of a solution is itself a solution. So the result is unaltered if not one, but several TMS coils are used.

[5] The lead field is a theoretical concept which assigns to every point a vector $\mathbf{c}$ such that for a current point source $\mathbf{p}$ at that point the measured potential in the coil is given by $\Phi = \mathbf{c} \cdot \mathbf{p}$, see [94]. The name "lead field" comes from EEG terminology in which the recording coils for the potential are called leads.

The important observation is that Equation (2.26) can be read in both directions: If the electric field is known, it determines the change in current flow in the coil (MEG). If the change in current flow through the coil is given, it yields the electric field at $\mathbf{r}$ (TMS). The mediator in both cases is the lead field $\mathbf{L}$. The calculation of $\mathbf{L}$ is standard in MEG and has been a fundamental task in solving the forward problem in MEG.

As a consequence, many calculations from MEG can be recycled in the analysis of TMS problems. Further, some important theoretical results translate readily to TMS. For example, it has been shown that it is impossible to measure radial electric sources in the brain with MEG [94, 129]. Translated to TMS this implies that it is not possible to generate at any point an electric field in direction inside or outside the head; at least not if the head is approximated as a radially symmetric conductor.

2.3. TMS devices

At the moment, there are two major companies manufacturing TMS devices: The MagStim Company, Whitland, Dyfed, UK and MagVenture, Farum, Denmark[6]. Besides these two major manufactures, there are a number of smaller competitors on the market. The most important of them being probably Nexstim, Helsinki, Finland and, for Germany, the MAG & More GmbH, Munich, Germany.

In this section we give a short overview over the stimulators used in TMS and provide a description of the different coil types used for stimulation. The description does not cover differences between the products of different manufacturers as they were not assessed in the scope of this work. For more about stimulator design see e.g. [65, 126, 130].

2.3.1. Stimulators

The three main components of each stimulator are a capacitor, a thyristor, and a stimulation coil. Before the stimulation, the capacitor is loaded to store between 100 and 3000 Joule. For stimulation, the thyristor allows a quick short-circuit so that the capacitor discharges via the coil within 100 µs. The rising and falling current in the coil produces a changing magnetic field which leads to a stimulation of the neuronal tissue, see Section 2.2. Figure 2.1 displays the Medtronic MagPro TMS device and presents some technical data.

Mono- and biphasic stimulation First stimulators operated just as described above. After opening the thyristor, the capacitor was allowed to discharge completely. This operation mode is known as monophasic stimulation, because the current in the coil and the magnetic field have the same orientation during the whole pulse. Nevertheless, as the current first

[6] Until March 2008, MagVenture products were distributed by Medtronic Inc., Minneapolis, MN, USA. As most of our experiments were performed before that date, we use the term "Medtronic" to denote systems from MagVenture throughout the thesis. Now, MagVenture products are distributed by Alpine Biomed Corp., Fountain Valley, CA, USA. Older systems from the company are also known under the name "Dantec".

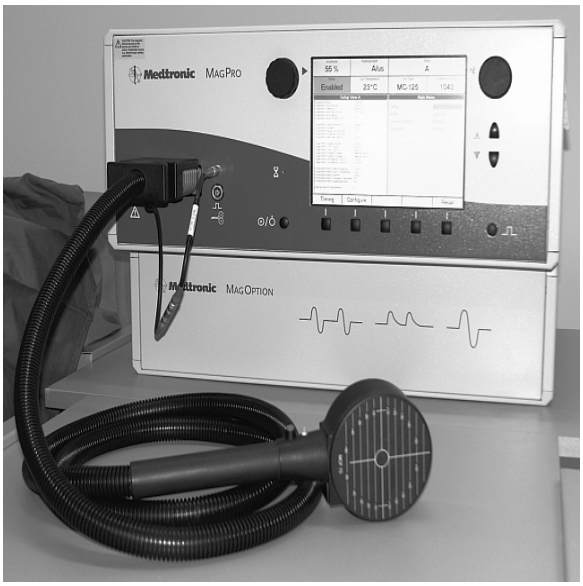

Figure 2.1.: Medtronic MagPro TMS stimulator with circular coil. The box houses strong capacitors for storing energies between 100 and 3000 Joule. For stimulation, a thyristor short-circuits the capacitor via the stimulation coil (in the foreground). Within 100 µs the capacitor discharges, yielding a maximum current change of up to 200 A/ µs and producing a magnetic field of up to 2 tesla close to the coil. The device depicted here is able to repeat the stimulation up to 100 times a second, although repetition frequencies of more than 20 Hz are hardly used in TMS.

rises and then falls, the induced electric field in the neuronal tissue changes its direction after the peak current in the stimulator has been reached, see Equation (2.26).

Nowadays, most common are biphasic stimulators, which recover some of the energy of the first pulse. This recycled energy is discharged after the first pulse to yield a second current pulse in opposite direction. Thus, the overall current flow through the coil resembles a full period of a sinusoidal wave.

Repetitive stimulation and paired pulse stimulation Many applications of TMS, especially those treating neuronal disorders, require the stimulation to be repeated every 50 ms to 2 s (rTMS). Such repetitive stimulation requires a fast recharging of the capacitors and special cooling of the electrical system. In fact, overheating of the TMS coil is the biggest problem in rTMS. The manufacturers try to overcome this problem with passively cooled coils (the windings are immersed in a special liquid with high heat capacity) or actively cooled coils (a hose is connected to the coil and special cooling liquid is passed through it).

In paired pulse stimulation, a second pulse of the same or different intensity is given 0.5 to 250 ms after the initial pulse. This interstimulus interval is too short to recharge the capacitor for the first pulse, so this technique requires a second charged capacitor when the paired pulse is released. This adds to the size, weight, and price of devices capable of paired pulse stimulation.

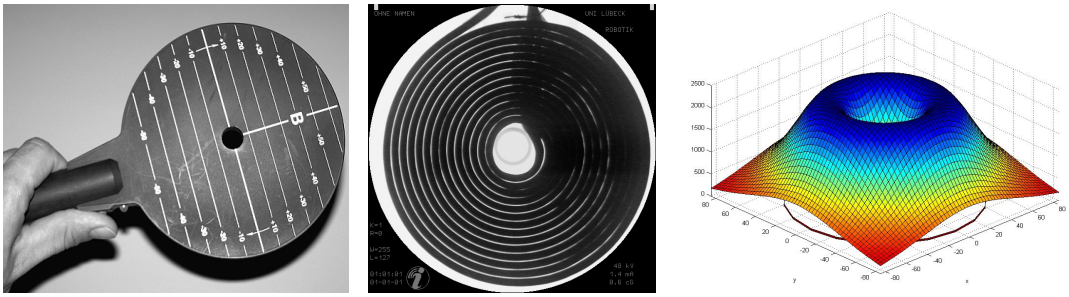

A *B* *C*

Figure 2.2.: Circular coil used for TMS. A: Medtronic MC125 coil. B: X-ray image of the same coil. C: Electric field strength produced by the coil in a plane parallel to the coil and in 1 cm distance from it. The red band below the graph indicates the outer dimensions of the coil.

2.3.2. Coils

The piece of equipment which influences the stimulation most is the TMS coil. Its shape and size determine the shape of the magnetic field produced and thus the electric field distribution in the brain. We cover here the main geometric properties of the electric field produced by the coils, for a detailed description of how to measure and simulate the fields see Section 4.4.

2.3.2.1. Circular coils

The first coil designs for TMS were circular coils [8], Figure 2.2.A. The winding of the coil forms an Archimedean spiral, which could either start close to the centre of the coil (as depicted in Figure 2.2.B) or at about half the radius of the coil (see the pictures in [8, 130]).

The magnetic field produced by circular coils has a very simple shape. It is strongest over the centre of the coil and falls off radially. But the induced electric field, which is the important quantity for stimulation, has a very different shape. We will see in Section 4.4.1 that the electric field of a planar coil is always parallel to the coil's plane. Together with the (near) rotational symmetry of the circular coils this implies that the electric field over the centre of the coil must always vanish. So there will be no stimulation effects under the centre of a circular coil. From Equation (2.18) and the rotational symmetry of the coil we further conclude that the electric field at a point (x, y, z)[7] runs in direction $(-y, x, 0)$, i.e. the electric field vector is tangential to a cylinder with radius $\sqrt{x^2 + y^2}$.

Figure 2.2.C depicts the electric field strength of a circular coil in a distance of 1 cm from the coil. We see that the electric field is strongest at about half the radius of the coil and decays to about a third of its maximum value over the rim.

[7] Coil origin at $(0, 0, 0)$, z denoting the vertical distance from the coil.

2.3.2.2. Figure-of-eight coils

Figure-of-eight coils can be thought of as composed of two circular coils where one of the coils is turned upside down and shifted until the rims of both coils overlap. If one follows the winding geometry, the wire first spirals outwards of one circular part of the "8" and then inwards into the other circular part, see Figure 2.3.B. This has the effect that the wires of both circular parts run nearly parallel in the overlapping section. More importantly, the current flow vectors in all wire sections in the overlaying part are parallel (and not antiparallel).

Figure-of-eight coils are the most commonly used coils in TMS nowadays. The main reason for it lies in their centred electric field, see Figure 2.3.C. The maximum of the electric field is produced where the left and the right loop overlap. The electric field under the centre is oriented parallel to the tangential line dividing both circles, i.e. parallel to the coil's handle. The relatively constant field strength and orientation underneath the centre makes it simple to use the coil for stimulation as both the stimulation point and the electric field direction are easily controlled.

Although the strongest electric field is created below the centre of the coil, the side maxima below the outer parts of the "8" should not be ignored. By the superposition principle, the side maxima have about half of the field strength of the centre maximum. In cases where the figure-of-eight coil is placed such that the outer parts are also close to the head, substantial activation can occur below these areas. For example, if the auditory cortex (close to the ears) is stimulated with the coil pointing upwards, one wing of the coil gets close to the face, exciting the nervus facialis and causing twitches of the ipsilateral facial muscles.

Non-planar figure-of-eight coils The planar arrangement of the two wings of the figure-of-eight coil restricts the addition of the effects of the outer parts of the wings to a minimum. By bending the wings towards each other, the magnetic fields of the wings overlap stronger. It is hoped that this affects also the induced electric field, leading to a more focal stimulation or a more pronounced stimulation in depth.

Some evidence supports these ideas: Thielscher et al. report that a slightly bend figure-of-eight coil (wing angles 16° and 18.5°) has a 1.2 fold higher efficiency than a similar planar figure-of-eight coil [176]. Efficiency hereby means that for the same stimulator output (i.e. same $\dot{I}(t)$) the bend coil achieved a higher electric field strength at the cortex for a spherical head model. The authors also demonstrated that this corresponds to a better excitation of cortical areas beneath the coil centre in reality [68].

Our simplified simulations could not confirm their findings. We modelled the electric field of three figure-of-eight coils with different wing angles in air[8], but saw no differences in the absolute electric field strength along a vertical line below the coil's centre for the first three centimetres. For distances between 3 and 10 cm, the electric field of the planar coil was even stronger than the field of the bend coils.

[8] For more on modelling see Section 4.4.2.

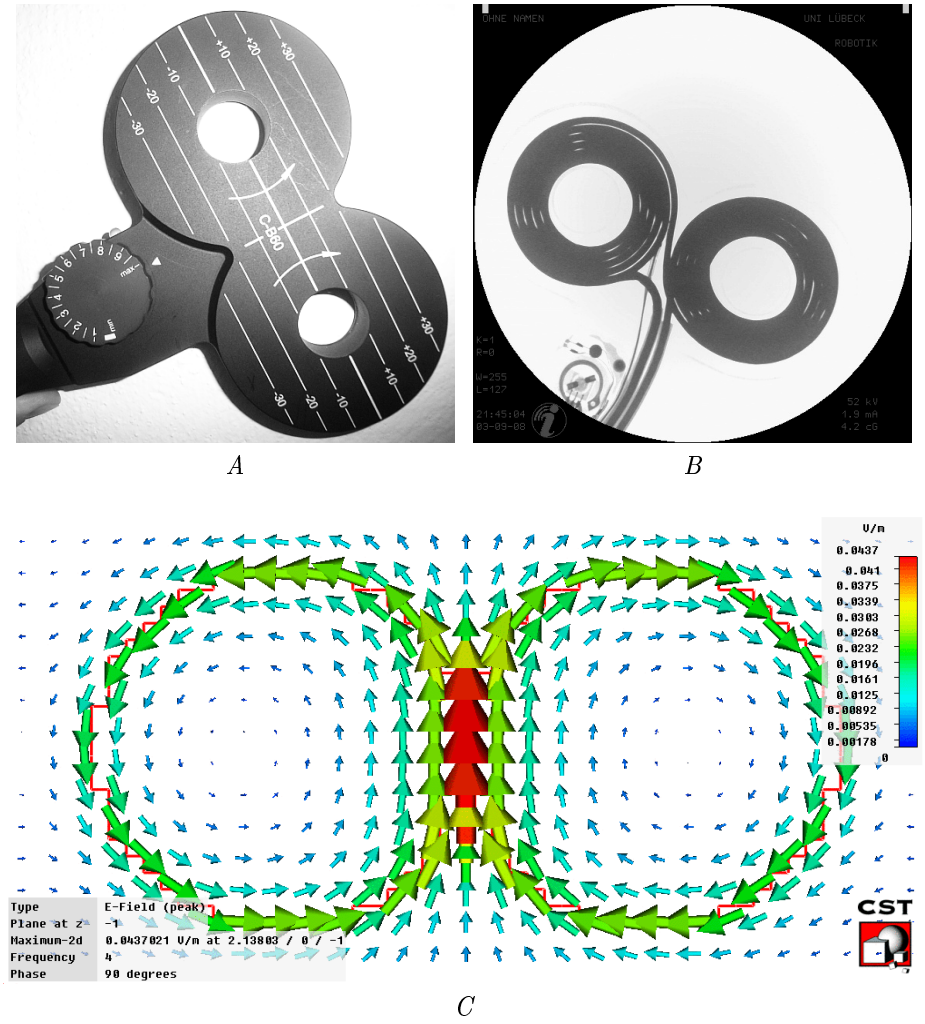

Figure 2.3.: Figure-of-eight coil used for TMS. A: Medtronic CB-60 figure-of-eight coil. The dial at the coil controls the pulse strength. B: X-ray image of the same coil. C: Simulated electric field produced by a simple geometric model of a figure-of-eight coil in a plane parallel to the coil and in 1 cm distance from it. The red curve indicates the wire of the coil, the size and colour of the arrows indicate the electric field strength, the direction of the arrows indicate the direction of the field. Simulation performed using CST Studio Suite (CST AG, Darmstadt, Germany).

In detail, all coils were simulated as single loop coils with wing circle radius of 5 cm. The wings had an angle of 0°, ±17°, and ±45° to the horizontal plane, respectively. The resulting absolute electric field strength for a current change of $100\frac{\mathrm{A}}{\mu\mathrm{s}}$ is displayed in Figure 2.4.

We think the discrepancy between Thielscher's findings and our simulations can be explained by the induced currents in the head model of Thielscher as compared to simulating the field in air in our model. This result should be taken as an example that the secondary current term $\nabla\phi$ in Equation (2.18) should not be easily disregarded.

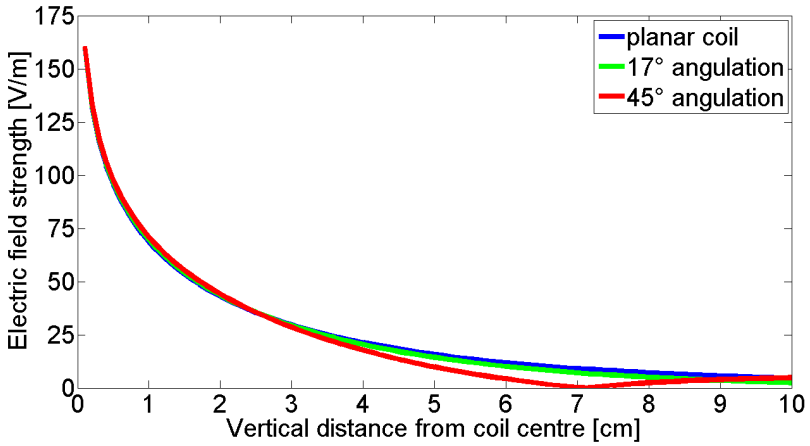

Figure 2.4.: Comparison of electric field decay for bend figure-of-eight coils. The coils were simulated as two circular loops of 5 cm radius with a single wire. The current change in the coils was taken to be 100$\frac{\mathrm{A}}{\mu\mathrm{s}}$. The figure shows that at least in air there is little difference in the electric field decay if the wings of the figure-of-eight coil bend towards each other.

2.3.2.3. New coil designs

The TMS community is constantly seeking ways to improve the stimulation further. Besides changes in the stimulation protocol, Section 2.3.1, new coil geometries offer a chance of enabling

- a more focused stimulation,
- a more efficient stimulation,
- a stimulation of deeper brain regions.

In the following, we briefly introduce two of the recent ideas from literature.

H-Coil The H-coil design of Roth and Zangen, Figure 2.5.A, was developed to stimulate deep brain regions more effectively [148, 149, 195]. From theory we know that it is impossible to achieve a higher electric field strength in depth than on the surface of the brain, see Section 2.2.2.3. But it might be possible to obtain a better ratio of in-depth field strength to surface field strength. We note that the absolute field strength has little relevance in this context as the governing equations are linear in $\dot{I}(t)$, so apart from the regions with zero electric field strength one could produce any field strength by using a strong-enough stimulator.

The developers of the H-coil claim that their new coil design indeed accomplishes better in-depth to surface ratios than other coils. We tested this claim using again a simulation of the electric field in air. For comparison we chose a figure-of-eight coil with wing diameter of 7 cm and two circular coils with radii of 4 cm and 8 cm, respectively. The size of the figure-of-eight coil and the small circular coil are conventional in TMS. The size of the large circular coil is to match the size of the H-coil (length: 16 cm, width: 8 cm).

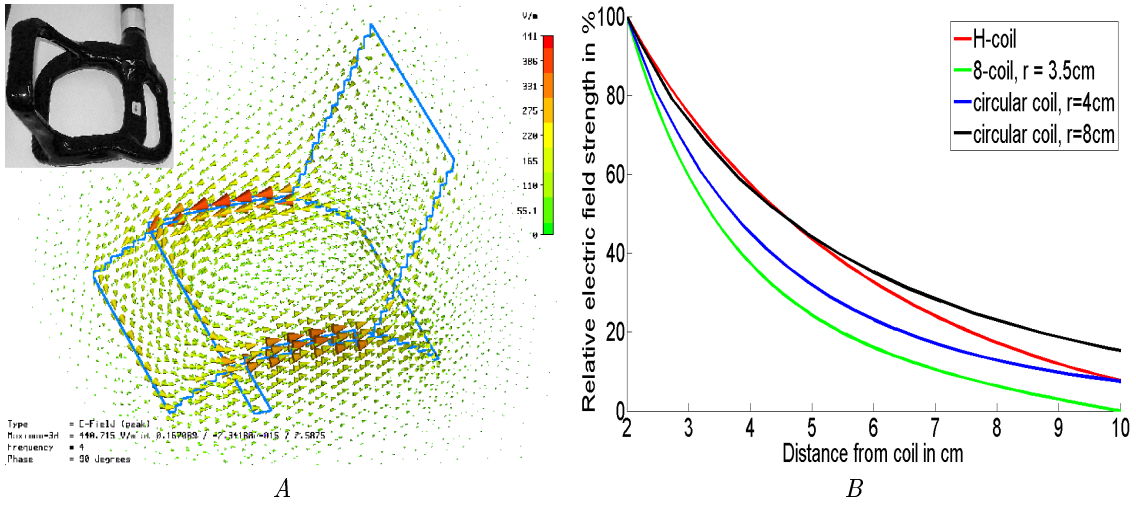

Figure 2.5.: H-coil design of Roth and Zangen. A: Schematic view with induced electric field in air. B: Comparison of the electric field decay in air for the H-coil, a figure-of-eight coil, and two circular coils. The fields are normalised to the respective field strength at 2 cm distance from the coils. The figure shows that the effect of slower electric field decay for the H-coil (red curve) compared to conventional coils (blue and green curves) is probably due its enlarged size and not to its special shape. Comparison with a circular coil of similar size (black curve) reveals only little difference for distances up to five centimetres from the coil. The simulation was performed using CST Studio Suite.

We calculated the electric field strength along a line running perpendicularly away from the midpoint of the middle bar of the H-coil, vertically away from the centre of the figure-of-eight coil, and vertically away from the rim of the circular coils, respectively. The results are referenced to the electric field strength at 2 cm from the respective coil, which is about the distance of the brain surface from the coil. Figure 2.5.B displays the results. We see that the H-coil's field () indeed decays slower than the fields of the conventional TMS coils. But when comparing the field's decay with the oversized circular coil's field decay, the H-coil has no advantage any more, the field of the circular coil decays even slower at distance of more than 3 cm from the brain surface.

Partially shielded coils As a last design, we would like to discuss the idea of Kim et al. here, who suggested to place a conductive plate with a hole in the middle between coil and head [72]. This has the effect that the primary current in the coil and the secondary current in the plate form a new current path, Figure 2.6.A, changing the characteristics of the coil significantly, Figure 2.6.B. The result is an amplification of the electric field below the coil's centre and a shielding of the side maxima under the wings of the coil. In a more abstract sense, a smaller figure-of-eight coil is created this way.

We think the idea is remarkable, because by having a second conductor besides the head, one could attempt to model the electric field much easier than by designing new coils. Nevertheless, as the conducting shield or plate behaves approximately like a second coil, the

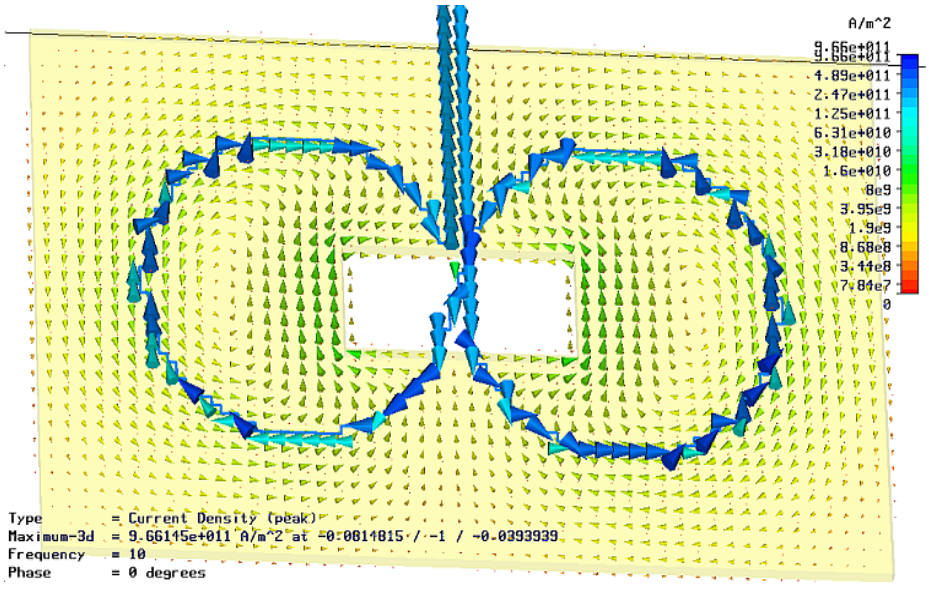

A

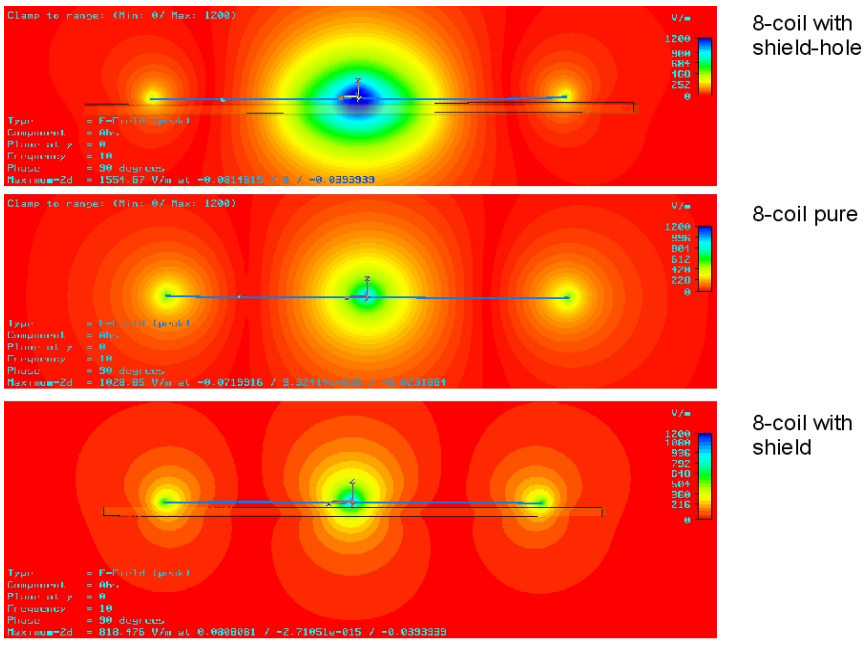

B

Figure 2.6.: Partially shielded coil suggested by Kim et al. . A: Primary current in the coil and secondary current induced in the shield plate. B: Comparison of the electric field produced by the same figure-of-eight coil with partial shield (shield with hole, top), with no shield (middle), and with a full shield (shield without hole, bottom). The electric field strength below the coil's centre is increased for the coil with a shield with a hole (top) compared to the unshielded figure-of-eight coil (middle) as the larger area of blue and green colours (high field strength) shows. The simulation was performed using CST Studio Suite.

fundamental restrictions of TMS (surface field always tangential, no in-depth maximum) from Section 2.2.2.3 remain unchanged.

Finally, we remark that the quasi-static approximations from Section 2.2.2.1 are not valid when metals are brought into the field. Specifically, Condition 3 is not met for metal: For example, the skin depth δ of copper is about $5 \cdot 10^{-4}\,\mathrm{m}$, so $\left(\frac{size\ plate}{\delta}\right)^2 \gg 1$, indicating that the magnetic field produced by the current in the plate is not negligible compared to the magnetic field from the coil. Thus, the equations from Section 2.2.2.2 cannot be used here; a more general version of Maxwell's Equations must be applied. Computing the field distributions for such conditions is possible using e.g. the CST Studio Suite software.

3. The robotic assistance system for TMS[1]

This chapter describes the robotic system to aid transcranial magnetic stimulation. Firstly, we review existing approaches for delivering precise stimulation. We then turn to three problems which cannot be solved with existing technology, namely exact coil orientation, motion compensation, and repeated stimulation. In Section 3.2 we describe the set-up of our robotic system and discuss some peculiarities in connection with the robot we use. Section 3.3 turns to the prerequisites of robot aided TMS, namely our tracking solution to determine the position of the head and the registration of it to 3D medical images like magnetic resonance imaging (MRI) or computed tomography (CT). Section 3.4 constitutes the main part of the chapter. Here we present our algorithms for planning a stimulation in virtual reality, moving the coil to the right position, and keeping the coil at the spot when the head moves. In particular, we solve the problem of how to choose an optimal trajectory in robot joint space in the presence of redundant robot states. The chapter closes with a discussion of the safety requirements of the system and our solutions to meet them.

3.1. State-of-the-art

3.1.1. Stereotactic TMS

Some of the applications presented in Section 2.1 require only a coarse positioning of the TMS coil with respect to the head. Examples include most single pulse diagnostic TMS uses. However, many applications like motor cortex mapping, visual cortex stimulation, and some rTMS treatments benefit from stereotactic navigation support, i.e. technology that enables exact positioning and repositioning of the coil with respect to the skull. The reason is that the field produced by most modern TMS coils has a sharp spatial gradient, leading to changes in the stimulation response even if the coil is moved only by a few millimetres [123, 147], Section 4.4.

3.1.1.1. Coil tracking

Stereotactic TMS requires devices to track the position and orientation of the coil. Mainly three different technologies are utilised for this purpose.

[1] Parts of this chapter have been published in [98, 101, 102].

A B C

Figure 3.1.: Tracking devices for stereotactic TMS. A: Mechanical arm solution employed by Krings et al. , [78]. The arm is used to record the position of landmarks on the head and the coil. With friendly permission of the author and the publisher. B: Electromagnetic tracking solution used by Noirhomme et al. . The coil is digitised using the pen, the head is tracked using the sensor taped to the forehead. Picture from [115], ©2005 IEEE, with friendly permission of the author and the publisher. C: Optical tracking device "Zeiss" used by Herwig et al. , [53]. Head and coil are tracked using LED markers attached to them. With friendly permission of the author and the publisher.

- The first group relies on flexible mechanical arms to hold the coil [24, 77], Figure 3.1.A. The coil is positioned adjusting the joints of the mechanical arm. Position and orientation of the coil are obtained measuring the joint angles and calculating the direct kinematics of the arm.

- The second group uses electromagnetic tracking for the coil [112, 115], Figure 3.1.B. Hereby, a small sensor, containing three orthogonal wire loops, is attached to the coil. An electromagnetic sender is placed near the stimulation setup and a software calculates the position of the sensor with respect to the sender from the induced currents in the wire loops.

- The last and largest group utilises marker based infrared stereo-optical tracking systems [40, 50, 53, 160], Figure 3.1.C. The method is adapted from stereotactical navigation in neurosurgery [48]. Several active, i.e. light emitting, or passive, i.e. reflective, markers are attached directly to the coil. For tracking, each marker is identified in a pair of stereo images and its localisation is calculated by triangulation.[2] A computer uses predefined templates to identify different markers so that several devices can be tracked at once.

All three methods have in common that not the position of the coil is recorded, but the position of attached handles or markers. Hence a transformation of the recordings is necessary. This is established either by accurately measuring the distances and angles from the tracked handles or markers to the inherent coil coordinate system, sometimes using special calibration boards, Figure 3.2, or by pivoting the coil centre around a fixed point.

[2]Some devices like the FashPoint (Image Guided Surgery Technology Inc., Boulder, CO, USA) or the accuTrack (Atracsys LLC, Bottens, Switzerland) use three line cameras (1D) instead of two 2D cameras to track the markers. The basic principle of triangulation is nevertheless the same.

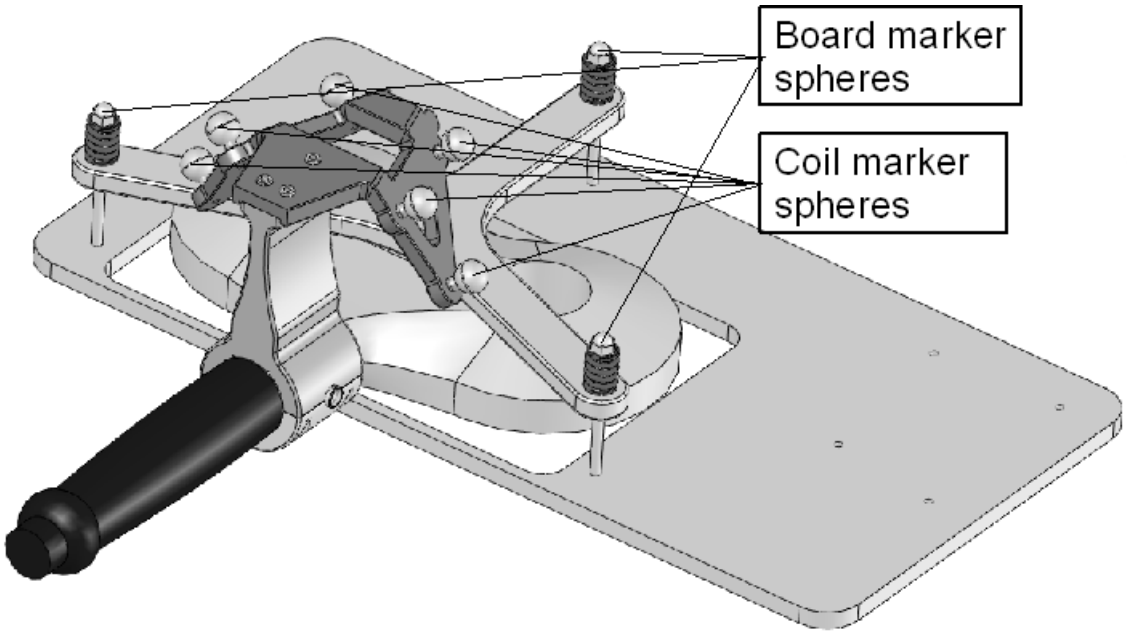

Figure 3.2.: Schematic image of a calibration board used for calibrating the MagStim figure-of-eight coil. The coil is tracked using the reflective spheres marker attached to the handle. The relation between coil geometry and handle marker is established by placing the coil in a defined position in the calibration board. The transform between marker coordinate system and coil coordinate system is determined by measuring the board's coordinates and the handle marker's coordinates and using the know transform between calibration board and coil. With friendly permission of Advanced Neuro Technology, Enschede, Netherlands.

3.1.1.2. Head tracking and navigation

Tracking of the coil is useless unless its position can be related to the position of the head of the patient. The simplest approach is to fix the head with a headrest and assume it to be in the same position during the stimulation session and for each new stimulation session [24]. This does not allow for navigated TMS in the strict sense, but only for controlled repeated stimulation at the same spot over several sessions.

A more advanced concept uses a pointing device, mostly tracked by the same means as the coil, to determine the position of several anatomical or artificial landmarks at the beginning of each session. During the session, the head is still kept in place by a headrest or thermoplastic mask and assumed not to move [44, 154]. By registering the landmarks from one session to another session, changes in head fixation can be corrected. If a virtual head model is available, the head can be registered to it using the landmarks, allowing for image guided TMS.

Most systems allow for a moving head during the session. Here, the head must be constantly tracked. For this purpose, the patient either wears a headband with attached passive markers [40, 53, 79] or active markers are directly glued onto the skin [38, 115]. Head and coil position are constantly recorded and related to each other in real time. In this simple form, changes

in coil position relative to the head can be detected and corrected by the operator. But nearly always, the head is registered to a virtual model in a previous step for image guided TMS.

All systems presented suffer from one important peculiarity: Neither the coil, nor the head are tracked directly. Instead attached markers are used. If the markers move with respect to the coil (head), this cannot be detected by the system and leads to false tracking information. Thus, several systems offer the possibility to check if the tracking environment has changed, e.g. by holding an additional pointer to a pre-defined position on the coil (head) and checking whether the recorded position agrees with the predicted position from tracking the coil (head).

3.1.1.3. Image guided TMS

The registration of the patient's real head to a three dimensional (3D) data set is another important feature of most stereotactic TMS systems. The main image modality used is MRI, possibly further combined with functional magnetic resonance imaging (fMRI) or positron emission tomography (PET). It enables the relation of the coil position (and hence the external stimulation site) to the anatomical or functional brain region underneath the coil.

It is clear that every brain mapping system must reference the stimulation points to the underlying brain anatomy to predict the brain representation site of the stimulated muscle [18, 38, 40, 54, 79, 115, 119]. But image guided TMS is also indispensable for therapeutic applications in non-motor areas of the brain. The target area is first identified using functional imaging like fMRI or PET and then precisely stimulated with TMS [73, 139]. For more examples see Chapter 5.

There are currently two main methods in use to register the individual patient's head to its MRI data set. The first method relies on a set of landmarks which must be detected in MRI data set and on the real head [53, 79]. First, the correspondence between each representation of a landmark on the real head and in the MRI data set is established manually. Then the transform from MRI image space to real head coordinates is calculated as the rigid motion minimising the sum of squared distance between the real landmarks and the corresponding transformed image landmarks [58].

The second registration method tries to find the transform minimising the distance between the real head surface and the image (or virtual) head surface. Hereby, the real head surface is represented as a number of surface points sampled using either a pointer device [115] or a laser range scanner [38]. The virtual head surface is segmented from MRI data using different image processing algorithms. The transform is often calculated using iterative methods like the Iterative Closest Point algorithm (ICP, [13]).

Both methods have been shown to perform well in practice. The landmark algorithm is generally more robust, but less accurate. Its performance can be improved by introducing artificial landmarks. The surface matching method often suffers from the optimising algorithm being trapped in a local optimum. Hence a good start value is important. For a more

detailed discussion see the literature about stereotactical navigation in neurosurgery, e.g. [48].

3.1.2. Robotised TMS

As described in the previous section, image guidance is an established technique in TMS. However, the coil still has to be placed by a human operator. This leaves three problems unsolved, despite the guidance by the navigation system:

- Coil tilt – The standard procedure in TMS is to place the coil exactly tangential to the head. Even a tilt by a few degrees changes the electric field pattern induced in the brain considerably and hence influences the stimulation result ([147], Section 4.4). Whereas human operators can position the coil quite exactly with the help of image guidance, exact tilt is very hard to establish. Most researchers try by supporting the coil with one hand at the head. While this may help to keep the coil at its place, it does not guarantee exact tilt.
- Motion compensation – In many rTMS applications the coil must be held at the same position for more than 15 minutes. For a human operator this is a difficult task without compromising accuracy. An alternative would be to fix the head and use a coil holder. The problem hereby is the growing discomfort for the patient over time and a possibility that increasing muscle tonus influences the stimulation results. Furthermore, non-invasive frames to fix the patient such that even small movements are suppressed are expensive and include often custom made parts adapted to the patient's anatomy. This increases the costs of the treatment and the preparation times.
- Repeated stimulation – With the increasing use of TMS for therapy, the number of applications requiring the coil to be positioned at a previously defined point, e.g. when the patient is to be treated again, rises. Manual positioning of the coil at a previous position is difficult, even under navigation support. The alternative solution, fixating the head and employing mechanical coil holders with dials at the joints, suffers from the problems described in the previous point.

Using a robot to position the coil solves all three problems. It enables precise placement and orientation of the coil, motion compensation, and easy storage and retrieval of coil positions with respect to the head. The general idea is not new, the employment of a robot for such tasks was successfully demonstrated in radiosurgery with the Cyberknife system [142, 157, 162–165].

Until now no robotic system for motion compensated TMS is known, although three robotic systems for automated positioning of a TMS coil where presented in the past. The first system was developed by Bohning and colleagues [17], Figure 3.3.A. The robot consists of two translational and four rotational joints and possesses six degrees of freedom. It is hence able to position the coil at an arbitrary point with any given orientation within its workspace. The system was produced for exclusive use in an MRI scanner and is thus build compact and can only reach points at the back of the head. Furthermore, the hydraulic

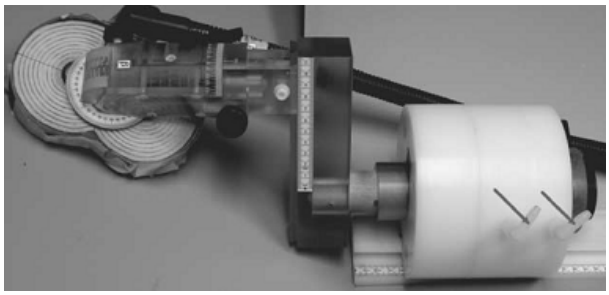

A

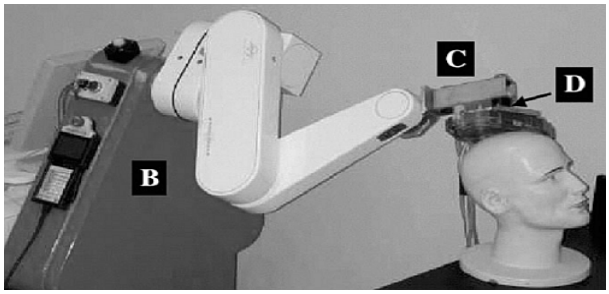

B

C

Figure 3.3.: Existing robot devices for TMS. A: Hydraulic device by Bohning et al. for positioning a TMS coil in a MRI scanner. Figure from [17] with friendly permission of the publisher. B: System by Lancaster et al. , based on a NeuroMate neurosurgical robot. Picture from [82] with friendly permission of the author and the publisher, ©Human Brain Mapping, 2004. Reprinted with permission of Wiley-Liss, Inc. a subsidiary of John Wiley & Sons, Inc. C: System at the BioMag Laboratories (Finland), based on a gentry design. Picture from [62], with friendly permission of the author.

joints of the system have to be adjusted manually to their desired settings by opening and closing pressure valves.

The second system was presented by Lancaster and colleagues [82], Figure 3.3.B. It utilises a NeuroMate robot originally constructed for robotised neurosurgery. The robot has six rotational joints leading to six degrees of freedom in coil positioning. To our knowledge this robotic system has only been used for studies interleaving TMS with PET [44, 45], where the patient's head was fixed with a thermoplastic mask.

A third system has existed in the BioMag laboratories in Finland. Details about it seem to have never been published, but a short remark about a motorised coil holder can be found in [153]. Apart from this very brief description and the photograph in Figure 3.3.C from [62], we only know that the system has possessed three degrees of freedom and is not used any more on a regular basis [Risto J. Ilmoniemi, personal communication].

Another robotic system, mechanically more adapted to place the coil on the spherical head than the serial robots discussed above, was discussed recently [85, 138]. However, this system has not been implemented yet and as of 2007 it is still in planning phase.

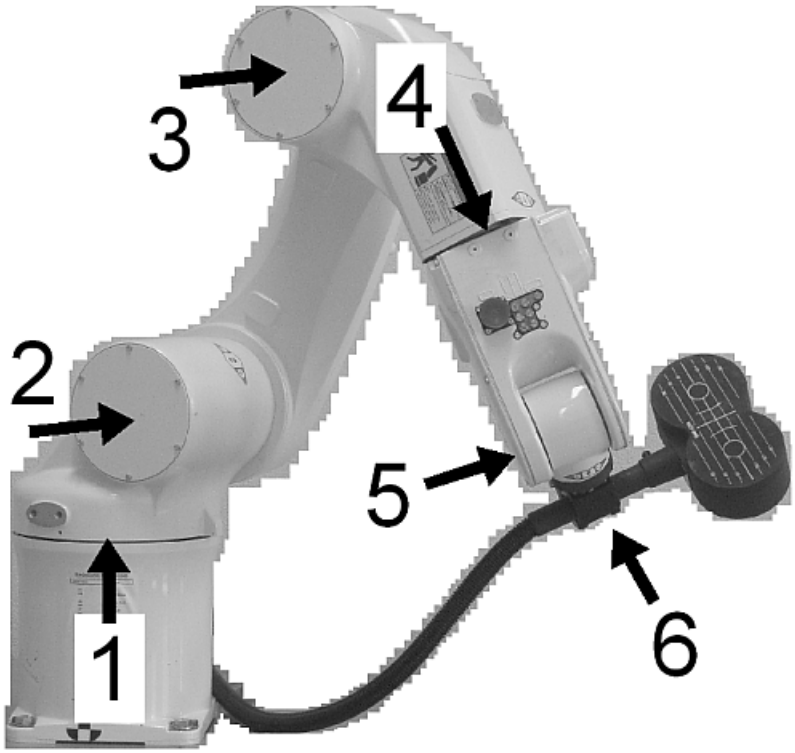

Figure 3.4.: Adept Viper s850 robot used in our TMS experiments. The labels give the joint numbers. The arrows are roughly aligned with the axis of rotation for the respective joint.

3.2. System set-up

Based on the success of image guided TMS and driven by the limitations discussed in Section 3.1.2, we started devising a robotised TMS system for general use.

The system is based on the serial six joint robot Kuka KR3 (Kuka Roboter GmbH, Augsburg, Germany, [81]) with an accuracy of 0.05 mm or the mechanically similar Adept Viper s850 (Adept Technology, Inc., Livermore, CA, USA, [1]). For tracking we use the Polaris infrared stereo-optical tracking system (Northern Digital Inc., Waterloo, Ontario, Canada, [116]) with an RMS accuracy of 0.25 mm. Also the MicronTracker 2 video optical stereo tracking device (Claron Technology Inc., Toronto, Ontario, Canada, [25]) has been tested for tracking.

Stimulation can be performed using any TMS device as long as the TMS coil can be clamped to the robot end-effector. In our experiments we used the MagPro X100 stimulator (Medtronic, Inc., Minneapolis, MN, USA) with the circular coils MC-125, MCF-75 and MCF-125 and the figure-of-eight coil MCF-B65 and the MagStim 200^2 stimulator (The MagStim Company Ltd, Spring Gardens, Whitland, UK) with the standard MagStim figure-of-eight coil. The basis for image guidance was given by T1-weighted 3D MRI data with a voxel resolution between 1 and 2 millimetres. Finally, the user interface for displaying the image data and planning of the robotised stimulation was programmed in JAVA utilising algorithms from the Visualization Toolkit (VTK) [161].

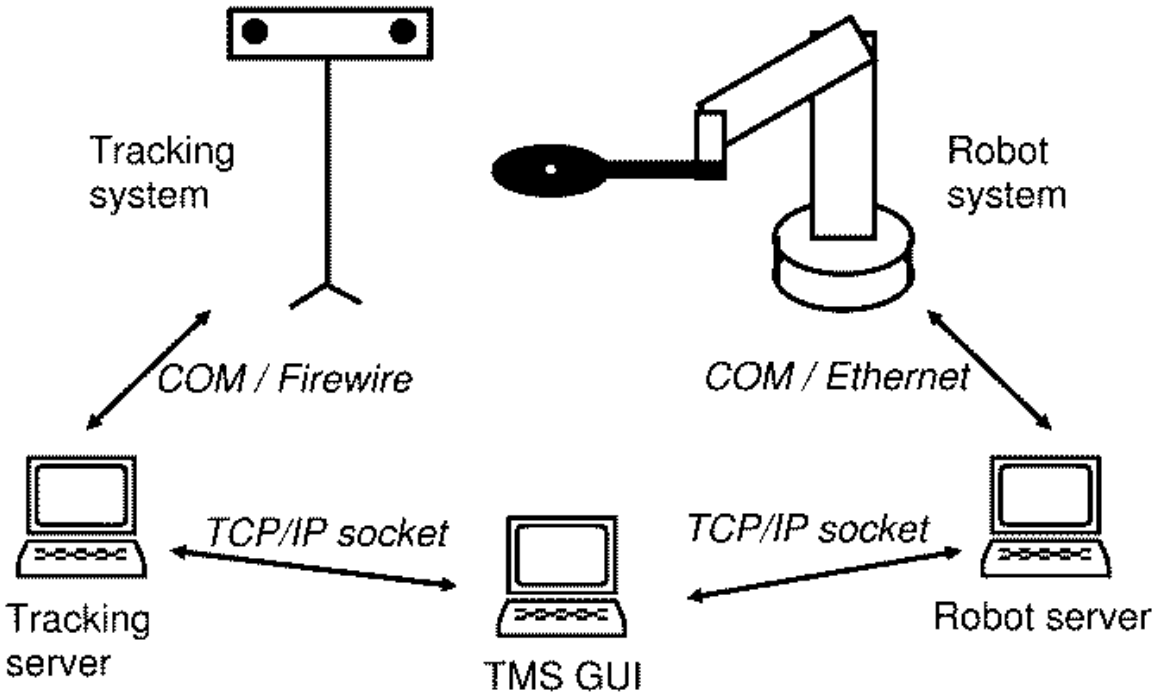

Figure 3.5.: Communication scheme for robot and tracking system. Using an additional program to communicate with the robot and tracking hardware gives biggest flexibility in the choice of hardware. Note that the server can run on the same computer as the TMS graphical user interface (GUI). But it is also possible to run them on extra computers and connect to them via ethernet.

3.2.1. Device Independence

Our aim was to keep the hardware architecture of the system as open as possible. That means that the system can be easily adapted to another robot or another tracking system. The reason for that is the ongoing technical development in the fields of medical navigation and robotics. So we want to be able to test and include other robot or tracking solutions into the system, further improving it. As mentioned in the previous section, we tested the system with two robots and two tracking systems so far. Our experiences are reported in Section 6.2.

Our solution is to run the tracking software and the robot software as independent programs from the graphical user interface controlling the TMS session. We use a client-server-architecture based on sockets to communicate between TMS program on the one side and robot and tracking program on the other side [96]. The robot and tracking programs hereby act as servers, the TMS program being the client, see Figure 3.5. The communication protocol is based on ASCII-Strings, enabling easy testing and debugging.

So to include another robot into the system, all that is needed is an adaptation of the robot server program, translating the ASCII commands from the TMS program into commands specific for that robot. Furthermore, basic forward and inverse kinematics must be implemented in the server. Similarly, for a new tracking system only the request for data and the formatting of the coordinates must be adapted in the tracking server program.

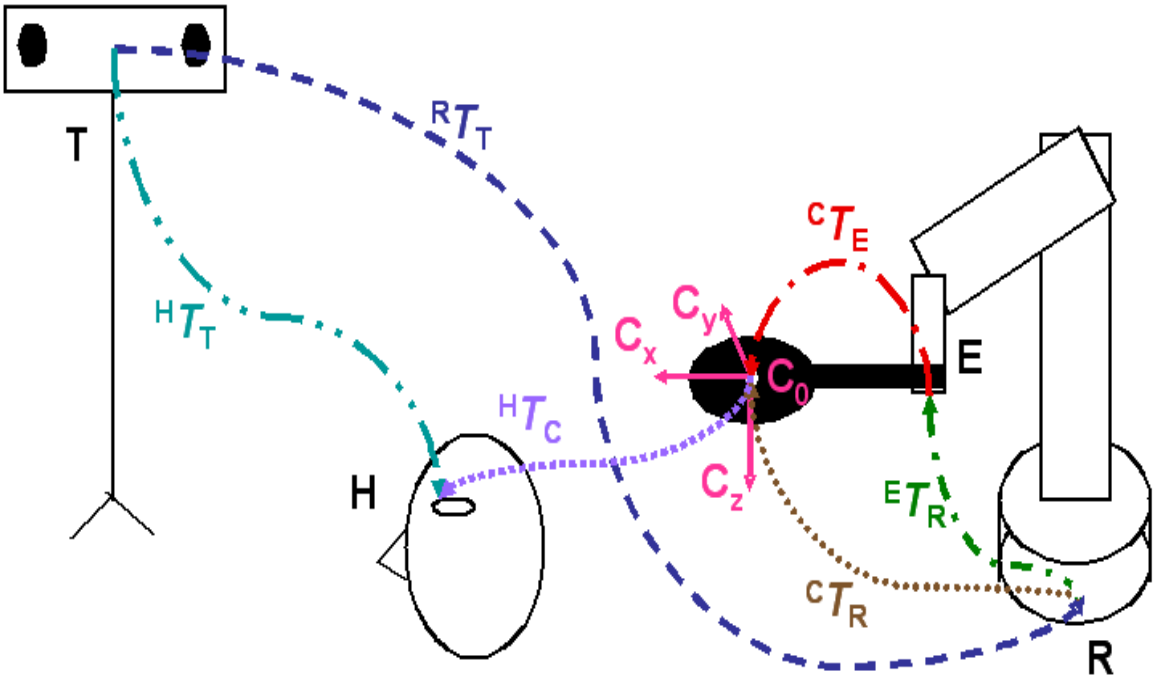

Figure 3.6.: Some of the transforms used in navigated robotised TMS. The letters denote T – tracking system, R – robot base, E – robot end-effector, H – head marker, C – coil centre. Also given is the coil coordinate system C_x, C_y, C_z. Not shown is the image coordinate system I.

As mentioned, the system is also independent of the TMS system used. The only requirement is that the coil can be attached to the robot end-effector. Therefore it is enough that it has a 5 cm long handle. For visualisation purposes, a model of the coil should be included in the TMS program. This requires accurate measurement of the coil dimensions and representation of the shape in terms of simple geometric objects like cylinders and cuboids. Most coil designs are versions of circular or figure-of-eight shaped coils. For those coils we have included templates in our program. As we will see in Section 3.2.2, no additional hardware like markers or calibration boards are necessary to track and register new coils, they can be used straight away.

3.2.2. Hardware Registration

As a prerequisite for using a navigated, robot controlled coil we need to determine the transform[3] ${}^{\mathrm{R}}T_{\mathrm{T}}$ from the tracking system T to the robot base R and the transform ${}^{\mathrm{C}}T_{\mathrm{E}}$ from the robot end-effector E to the coil centre C, see Figure 3.6. Note that unless the tracking system or the robot are moved or the coil montage is changed, these two transforms are constant.

[3] Throughout the Chapter we denote transforms from a coordinate system A to a coordinate system B by ${}^{\mathrm{B}}T_{\mathrm{A}}$. Note that ${}^{\mathrm{B}}T_{\mathrm{A}}({}^{\mathrm{A}}\mathbf{e_1}, {}^{\mathrm{A}}\mathbf{e_2}, {}^{\mathrm{A}}\mathbf{e_3}, {}^{\mathrm{A}}\mathbf{0})$, i.e. the transformation of the unit base in A to B, gives the pose (= position and orientation) of A with respect to B. Hence we also use ${}^{\mathrm{B}}T_{\mathrm{A}}$ to denote poses.

3.2.2.1. Calibration robot – tracking system

We start by determining ${}^{\mathrm{R}}T_{\mathrm{T}}$. Firstly, we attach a tracking marker to the robot end-effector, see Figure 3.7.A. Secondly, we move the robot to $n \geq 3$ positions and record the pose of both, the end-effector E in robot coordinates R ($^{\mathrm{R}}T^i_{\mathrm{E}}$) and the marker M in tracking coordinates T ($^{\mathrm{T}}T^i_{\mathrm{M}}$), $i \in \{1, \ldots, n\}$. This converts the problem to the well-known "hand-eye-calibration" problem (see [169] for an overview). For every pose i we have[4]

$$ {}^{\mathrm{R}}T_{\mathrm{T}}\,{}^{\mathrm{T}}T^i_{\mathrm{M}} = {}^{\mathrm{R}}T^i_{\mathrm{E}}\,{}^{\mathrm{E}}T_{\mathrm{M}}, \tag{3.1} $$

where the transforms ${}^{\mathrm{R}}T_{\mathrm{T}}$ and ${}^{\mathrm{E}}T_{\mathrm{M}}$ are unknown, but constant. Representing the transformations as homogeneous matrices, Equation (3.1) yields 12 non-trivial scalar equations for 24 unknown scalars (the entries of ${}^{\mathrm{R}}T_{\mathrm{T}}$ and ${}^{\mathrm{E}}T_{\mathrm{M}}$). When we move the robot to n different pose, the known transforms ${}^{\mathrm{T}}T^i_{\mathrm{M}}$ and ${}^{\mathrm{R}}T^i_{\mathrm{E}}$ change n times, whereas the unknown parameters are constant. Hence, the number of equations raises to $12n$, the number of unknowns is always 24. Note that for $n = 2$ the system has no unique solution, because for a given solution ${}^{\mathrm{R}}T_{\mathrm{T}}$, ${}^{\mathrm{E}}T_{\mathrm{M}}$ also ${}^{\mathrm{R}}\tilde{T}_{\mathrm{T}} = {}^{\mathrm{R}}T_{\mathrm{T}}\,{}^{\mathrm{T}}T^1_{\mathrm{M}}\left({}^{\mathrm{T}}T^0_{\mathrm{M}}\right)^{-1}$, ${}^{\mathrm{E}}\tilde{T}_{\mathrm{M}} = {}^{\mathrm{E}}T_{\mathrm{M}}\left({}^{\mathrm{T}}T^0_{\mathrm{M}}\right)^{-1}{}^{\mathrm{T}}T^1_{\mathrm{M}}$ is a solution (see also [180]). Thus we need at least $n = 3$ poses. It is also not hard to show that three poses in general position are sufficient to determine ${}^{\mathrm{R}}T_{\mathrm{T}}$ and ${}^{\mathrm{E}}T_{\mathrm{M}}$ uniquely [23, 180]. As there is always jitter in the measurements, we normally record more than these three poses. We determine the transform parameters of ${}^{\mathrm{R}}T_{\mathrm{T}}$ and ${}^{\mathrm{E}}T_{\mathrm{M}}$ by finding minimal error solution x of the over-determined system $Ax = b$, where $x \in \mathbb{R}^{24}$ is formed by the unknown parameters and $A \in \mathbb{R}^{12n\times 24}$, $b \in \mathbb{R}^{12n}$ are given by the (known) measurements. This results in x being the solution to the linear system $A^tAx = 0$. We remark that the resulting matrix for ${}^{\mathrm{R}}T_{\mathrm{T}}$ is not necessarily a rigid transform (i.e. $\left({}^{\mathrm{R}}T_{\mathrm{T}}\right)_{3\times 3} \notin SO(3)$[5]), because of jitter effects, but our experience shows that for $n > 10$ such effects are negligible.

3.2.2.2. Calibration robot end-effector – TMS coil

Having established a common reference system for the robot and the tracking system, we now attach the coil to the robot end-effector using a specially designed steel and aluminium clamp, see Figure 3.7.B. We use a tracked pointer to record the coordinates of the coil centre point c_0, a point c_1 on the line from the coil centre to the coil front, and a point c_2 on the line from the coil centre to the right coil rim, respectively. We define the coil coordinate system C with respect to the tracking system as

$$ C_{\mathrm{origin}} = c_0, \tag{3.2} $$

$$ C_X = \frac{c_1 - c_0}{\|c_1 - c_0\|} \tag{3.3} $$

$$ C_Y = \frac{(c_2 - c_0) - C_X < c_2 - c_0, C_X >}{\|(c_2 - c_0) - C_X < c_2 - c_0, C_X >\|}, \tag{3.4} $$

$$ C_Z = C_X \times C_Y. \tag{3.5} $$

[4] The concatenation of transforms is represented by a left-multiplication of the corresponding coordinate change matrices. We follow this notation and write ${}^{\mathrm{C}}T_{\mathrm{A}} = {}^{\mathrm{C}}T_{\mathrm{B}}\,{}^{\mathrm{B}}T_{\mathrm{A}}$ instead of ${}^{\mathrm{C}}T_{\mathrm{A}}(\cdot) = {}^{\mathrm{C}}T_{\mathrm{B}}({}^{\mathrm{B}}T_{\mathrm{A}}(\cdot))$

[5] $SO(3)$ is the Special Orthogonal Group of $3x3$ matrices, which represents rotations in $\mathbb{R}^3$. For $A = (a_1a_2a_3) \in SO(3)$ holds $a_i^t a_j = \delta_{ij}$ and $\det A = 1$.

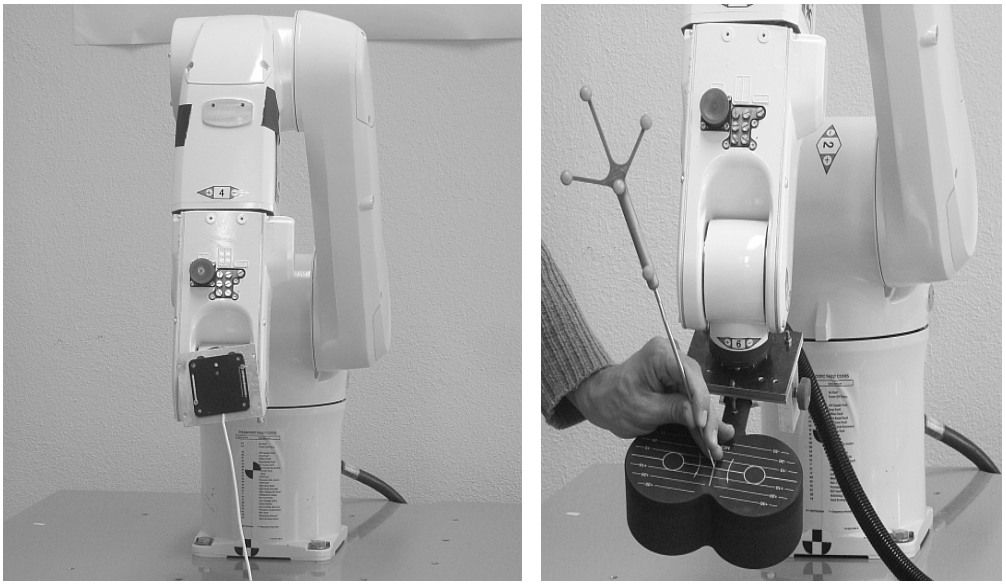

A *B*

Figure 3.7.: A: Robot-camera-calibration, ${}^{\mathrm{R}}T_{\mathrm{T}}$. The Robot is moved to random positions at which the end-effector pose in robot coordinates and the marker pose in tracking coordinates are recorded. The calibration between robot and tracking system is determined as the transform which explains the measured data best. B: Robot-coil-calibration, ${}^{\mathrm{C}}T_{\mathrm{E}}$. The coordinates of the pointer tip are recorded and transferred into robot coordinates using ${}^{\mathrm{R}}T_{\mathrm{T}}$. We record the position of the coil's centre (shown), a point along the coil's x-axis (line running to the front), and a point in the y+-half-plain (the side where the operator stands). The so-defined coordinate system is offset by the coil's thickness to the coil's underside. The transform ${}^{\mathrm{C}}T_{\mathrm{E}}$ is then simply calculated using this coil coordinate system and a recording from the robot's end-effector pose.

C with respect to the robot base R is then given by ${}^{\mathrm{R}}T_{\mathrm{C}} = {}^{\mathrm{R}}T_{\mathrm{T}}{}^{\mathrm{T}}T_{\mathrm{C}}$. From the robot kinematics and the current robot joint angles we know ${}^{\mathrm{E}}T_{\mathrm{R}}$, so finally ${}^{\mathrm{C}}T_{\mathrm{E}} = {}^{\mathrm{C}}T_{\mathrm{R}}{}^{\mathrm{E}}T_{\mathrm{R}}^{-1}$, see Figure 3.6. For convenience, we also allow to define c_0, c_1, c_2 on the upside of the coil and translate the coordinate system C along C_Z by the user defined coil thickness. This works of course only for planar coils, i.e. coils with flat upside and underside parallel to each other. It is especially useful for Medtronic coils which have a line pattern, featuring the centre, X-, and Y-direction, printed on the upside, see Figure 3.7.B.

3.2.3. A robot-specific problem: Configuration modes

Before we describe our approach to robotised TMS, we would like to elaborate on one specific problem of serial robots, namely how to choose between the several joint settings for one end-effector pose. It is well known that a serial six-arm robot like the Kuka KR3 or the Adept Viper s850 has eight joint settings to implement a given position and orientation of the end-effector [168]. In short, the configuration mode for arm (*lefty*/*righty*) determines if the robot operates towards its front or back, the configuration mode elbow (*up*/*down*) determines if Joint 3 is above or below the shoulder-hand-line (the line connecting Joint 2

with Joint 5), and the configuration mode hand (*flip*/*noflip*) determines if Joint 5 is smaller or greater than 0°, see Figure 3.8. Taken together, the three configuration modes (or states) result in 2^3 possible joint settings for a given pose.

If the end-effector is commanded to a specific pose, a configuration mode must also be supplied. Conventionally, the user specifies it either directly with the move command or the configuration mode of the start pose is implicitly assumed also for the target pose.

The first option (direct command mode input) is problematic, because it requires constant user input and much experience from the user which mode is best (in a sense to be specified) for a given target pose.

The second option (end command mode equals start command mode) is problematic in at least two ways. Firstly, joint limitations restrict the workspace for each configuration mode, so that it might not be possible to reach a pose with the start configuration mode whereas it would be possible to reach it with a different configuration. For example, for the Adept Viper s850, Joint 2 cannot be moved more than 20° in downwards direction. Imagine a target position at floor level, close to the robot base. Such a position can only be reached in elbow-*up* mode, because the equivalent elbow-down mode would require a Joint 2 setting of more than 20° in downward direction.

Secondly, small changes in pose can result in big changes in joint setting, causing a large movement of the robot. For example, imagine a robot in *lefty-up-flip* mode (Joint 5<0°), pointing away from the robot base. Now fix this configuration mode and increase the height (z-value) of the end-effector without changing its orientation. As a result, Joint 5 straightens until it reaches 0°. If z is increased further, Joint 4 needs to turn by 180° such that Joint 5 remains at negative value to avoid a change in hand-state. In the extreme case, an infinitesimal change in end-effector position can lead to a 180° change in joint setting. Note that this singular behaviour can be avoided by changing the configuration mode appropriately (in this example from *flip* to *noflip*).

Our solution to avoid the need for constant educated user input or big joint value changes when crossing singularities is the introduction of a simple metric in joint space. For two joint settings $J^1 = (j_1^1, \ldots, j_6^1)$ and $J^2 = (j_1^2, \ldots, j_6^2)$ we define

$$\mathrm{d}(J^1, J^2) := \max_{i=1}^{6} \alpha_i |j_i^1 - j_i^2|, \qquad \alpha_i > 0. \tag{3.6}$$

The metric d measures the maximum change of a single joint when moving from J^1 to J^2. The factors α_i allow to punish or to favour movements of specific joints. For example, in our application we chose $\alpha_1 = 4$, $\alpha_2, \ldots, \alpha_6 = 1$ to punish large movements of Joint 1.

To choose the best configuration mode to reach a commanded target pose T, we calculate all eight joint settings $J^{T,s}$, $s \in \{\mathit{lefty}, \mathit{righty}\} \times \{\mathit{up}, \mathit{down}\} \times \{\mathit{flip}, \mathit{noflip}\}$. For all possible configurations we calculate the distance $\mathrm{d}(J^{start}, J^{T,s})$ to the start joint setting J^{start} in accordance with Equation (3.6). The configuration mode with the minimal distance $\mathrm{d}(J^{start}, J^{T,s})$ is selected to reach the target pose.

In a similar way we deal with joints with a rotation range of 360° or more, like Joints 4 and 6 of the Adept Viper s850 robot (±190° and ±360°, respectively). For such a joint we

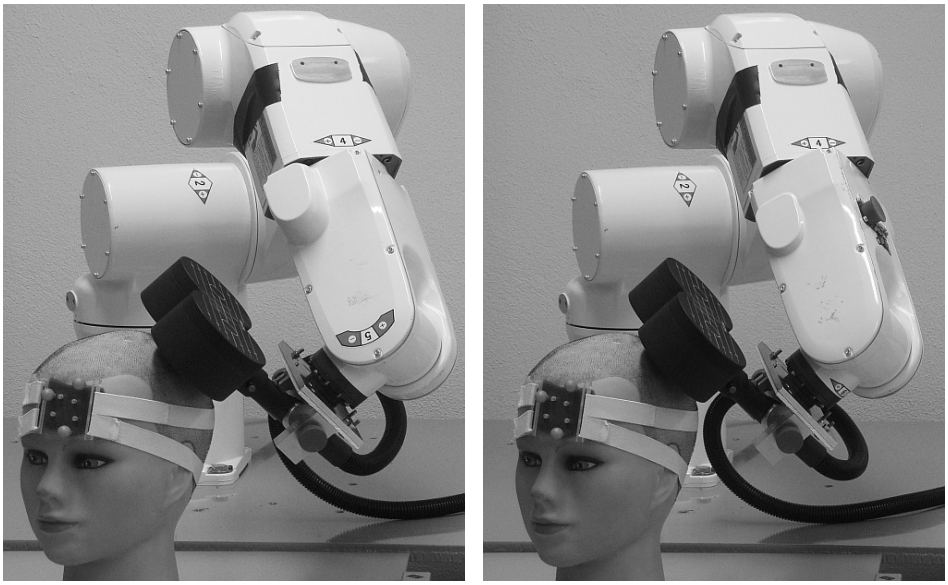

A *B*

Figure 3.8.: The two commonly used hand configuration modes for TMS: flip *(A) and* noflip *(B). In both images, the arm is in* lefty *configuration and the elbow in* up *configuration.*

replace the expression $|j_i^1 - j_i^2|$ in Equation (3.6) by $|j_i^1 - \tilde{j}_i^2|$ where $\tilde{j}_i^2 = j_i^2 + k * 360°$, $k \in \mathbb{Z}$, is the closest feasible joint value to j_i^1. For example, imagine Joint 4 to be at $j_4^{start} = 175°$ and a target pose with $j_4^{target} = 185°$. Suppose Joint 4 is restricted to $\pm 179°$. In order to reach the target pose in the same configuration, a turn of $-350°$ in Joint 4 is necessary. Alternatively, the hand configuration can be changed: $j_4^{target} = 5°$, $j_5^{target} = -j_5^{start}$, $j_6^{target} = j_6^{start} \pm 180°$. This would be the choice of our minimal joint change strategy, because $\mathrm{d}(J^{start}, J^{target,\text{change hand status}}) = 180° < 350° = \mathrm{d}(J^{start}, J^{target,\text{keep hand status}})$. But if Joint 4 has a range $\pm 190°$, we choose $\tilde{j}_4 = 185°$. This would be optimal, because then $\mathrm{d}(J^{start}, \tilde{J}^{target}) = 10°$.

3.3. Navigation and Image Guidance

We describe in the following our solution to display the TMS stimulation point with respect to 3D anatomical data, which is known as image guided TMS. The procedure consists of two main steps: We need to determine the position of the coil with respect to the head ${}^{\mathrm{H}}T_{\mathrm{C}}$ and we need to calculate the transform ${}^{\mathrm{H}}T_{\mathrm{I}}$ between real head coordinates H and image data coordinates I (registration).

For the first step we only need to determine the position of the head; the position of the coil is known from the robot joint readings and the end-effector to coil transform ${}^{\mathrm{E}}T_{\mathrm{C}}$. Section 3.3.1 thus only explains our solution to track the head.

In Section 3.3.3 we explain how we relate the real head to the 3D anatomical image, a

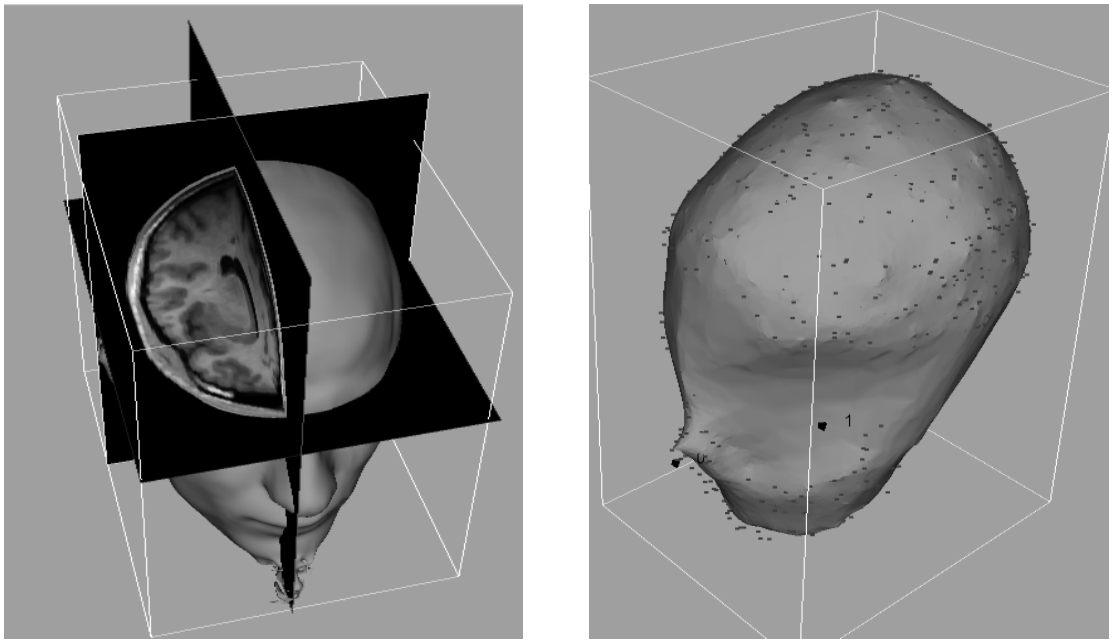

Figure 3.9.: Reconstruction of the virtual head outline from MRI data (left) and from 813 real outline points (right, using the power crust algorithm [4]). Note that for the right picture outline points were sampled mainly on the scalp, where the coil is to be positioned.

process known as registration. Our approach to calculate the registration transform ${}^{\mathrm{H}}T_{\mathrm{I}}$ requires a preprocessing step, where a virtual head outline is reconstructed from MRI data. This procedure is therefore previously explained in Section 3.3.2.

3.3.1. Tracking

Tracking of the head poses no problem, at least in theory. We follow the approach of [40, 53, 79] and equip the patient with a headband with a passive marker for the Polaris tracking system. It must be ensured that the headband is not moved on the scalp during the treatment. This proved to be problematic when the patient was treated in a lying position. Therefore, we also experimented with the MicronTracker tracking system with paper markers which can be glued to the patient's forehead. With both systems, the head coordinate system H is defined by the inherent coordinate system of the marker.

Determining the position of the coil requires the transforms between tracking system, robot and coil to be established, see Section 3.2.2. The coil position with respect to the tracking system is then given by ${}^{\mathrm{T}}T_{\mathrm{C}} = {}^{\mathrm{T}}T_{\mathrm{R}}{}^{\mathrm{R}}T_{\mathrm{E}}{}^{\mathrm{E}}T_{\mathrm{C}}$. Note that the only variable term on the right hand side is ${}^{\mathrm{R}}T_{\mathrm{E}}$. This transform is constantly updated from the robot joint readings every time the robot moves. In this sense, our coil tracking scheme extends the mechanical arm solution discussed in 3.1.1.1.

3.3.2. Virtual Head Reconstruction

Once we know the head marker position and the coil position in a common coordinate system, we can reference the coil to the head marker (${}^{\mathrm{H}}T_{\mathrm{C}}$). The remaining step is to transform this to the image data. Therefore, we reconstruct the virtual head outline from MRI image data. This can be done using relatively simple means. First, we apply a median filter to reduce noise. Then we use a threshold filter to obtain a binary image: All voxels with low grey value, which is normally air, are mapped to black; all voxels with a grey value above the threshold, normally tissue, are mapped to white. Next, we obtain the surface of the white volume with a contour filter, employing e.g. the marching cubes algorithm [91]. Finally, we select the surface with the biggest volume, because the low grey values of the throat, the auditory canal, and the cerebrospinal fluid (CSF) lead to some isolated surfaces in the reconstruction, which can be removed this way. Figure 3.9 gives an example for a reconstruction from MRI data with voxel spacing of 1 mm. Note that the reconstruction can be done prior to TMS treatment and does not require the presence of the patient.

A special situation arises from the fact that for many TMS sessions, even in research, no MRI data of the patient is available. Nevertheless, robot support in positioning, repositioning and motion compensation is desired also in these cases. As discussed in Section 3.4, our robot application relies on the virtual head outline for positioning. Our solution is to sample a dense cloud of outline points, i.e. in the range of 1000 points, especially in the stimulation area. We then use the surface reconstruction algorithms power crust [4], Hoppe's algorithm [57], or Delaunay triangulation [30] to yield an interpolating surface. After smoothing [172] we are able to use the resulting surface as base for robotised treatment (Figure 3.9).

3.3.3. Registration Step

To register the head to its virtual outline, we acquire several hundred outline points ${}^{\mathrm{T}}p_{\mathrm{i}}$ of the real head by moving a tracked pointer over the scalp. Hereby, we follow the scheme of [115], i.e. we sample the points over a large area of the scalp producing a hat-like pattern, see Figure 3.10. We also record the coordinates of at least three landmarks, e.g. the outer orbital rim of the left and right eye and the tip of the nose. The whole procedure takes about three to five minutes. We reference all points to the head marker,

$$ {}^{\mathrm{H}}p_{\mathrm{i}} = {}^{\mathrm{T}}T_{\mathrm{H}}^{-1}({}^{\mathrm{T}}p_{\mathrm{i}}), \tag{3.7} $$

so there is no need to fix the patient for the procedure.

For the registration we mark the points on the virtual head corresponding to the landmark points and calculate the best landmark transform using the optimal solution of Horn [58]. Because of difficulties identifying exactly the same points as landmarks on the real and virtual head, the calculated transform is too erroneous to be used. We therefore take it only as the start value for an Iterative Closest Point scheme [13], which optimises the transform to minimise the quadratic distance between the transformed real surface points ${}^{\mathrm{I}}T_{\mathrm{H}}({}^{\mathrm{H}}p_{\mathrm{i}})$ and the virtual outline.

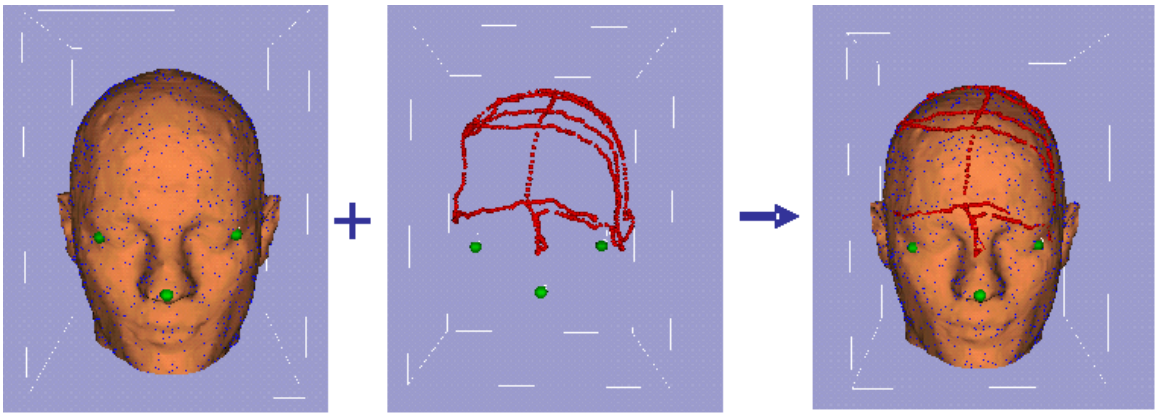

Figure 3.10.: Registering the virtual head to the real head using landmarks and surface points. Left: Surface points (red) and landmarks (green) from the real head. Middle: Virtual head model. Right: Virtual head model registered to the real head.

To stabilise the resulting transform against outliers from sampling the head surface, we delete all sampled outline points with a distance of more than three times the RMS distance of all outline points to the virtual surface and re-run the ICP. This procedure is repeated until no more outliers are detected.

In case of a reconstruction of the virtual head surface from outline points, the whole registration procedure is of course obsolete. In this case, the transform ${}^{\mathrm{H}}T_{\mathrm{I}}$ is set to the identity transform and the registration step is omitted.

We note at this point that all subsequent stimulation data are stored with respect to the virtual coordinate system I. This allows the identification of points in repeated sessions without the (impossible) requirement of placing the head marker every time the same way. For example, a stimulation point ${}^{\mathrm{H}}p_1$ on the real head in Session 1 is represented internally as ${}^{\mathrm{I}}p = {}^{\mathrm{I}}T_{\mathrm{H}}^{1\,\mathrm{H}}p_1$. The point can be re-approached by the robot in Session 2 by its head marker coordinates ${}^{\mathrm{H}}p_2 = {}^{\mathrm{H}}T_{\mathrm{I}}^{2\,\mathrm{I}}p$, see also the following sections.

3.4. Robotised Treatment

So far, our solution realises a stereotactic TMS system with a mechanical arm for coil localisation and a passive tracking system for head localisation as described in Section 3.1.1. Also the image guidance of the coil is a standard feature by now, even though our two step registration solution has not been presented before and leads to higher registration accuracy than landmark or ICP registration alone.

The novel feature of our system is control of the TMS coil by the robot. The main problem to be solved when including an autonomous positioning device is the trajectory planning. That means, we need to develop an algorithm which allows the coil to be moved to a user defined point without colliding with the patient. Our approach is a two step method. Firstly, we define a preliminary trajectory using a heuristic, Section 3.4.2. The heuristic is independent of the robot device and calculated using only the virtual head outline, the

actual coil position with respect to the head, and the user defined target position. Secondly, we relax the trajectory and optimise it for the specific robot we use, taking into account the position of the head relative to the robot, the robot movement characteristics, and the robot workspace limitations, Section 3.4.3.

The robotised treatment itself consists of three steps:

1. Planning the stimulation by defining target points for the coil, Section 3.4.1.
2. Moving the robot to position the coil at a target point, adjusting for head movements during the transition, Sections 3.4.2, 3.4.3.
3. Compensate movements of the head after reaching the target position, Section 3.4.4.

Here, a graphical user interface allows for easy and convenient definition of new target points, storage and retrieval of treatment sessions for repeated stimulation, and display and analysis of stimulation responses. Figure 5.3 shows a screenshot of the user interface.

3.4.1. Planning the treatment

To define a target point $\mathbf{p}$, the physician marks a point on the virtual head surface by simply clicking on it. Alternatively, a point on the underlying 3D anatomical (or superimposed functional) data can be marked. p is then taken to be the closest surface point to the marked point, because for successful stimulation the coil should be positioned as close as possible to the target.

The target point can also be defined on the real head. Therefore the user holds a tracked pointer device M to the target point. Using the tracking information of the headband, ${}^{\mathrm{T}}T_{\mathrm{H}}$, and the transform ${}^{\mathrm{I}}T_{\mathrm{H}}$, ${}^{\mathrm{T}}T_{\mathrm{M}}$ is translated into image coordinates, yielding the virtual target point p.

A coil model C is then positioned above $\mathbf{p}$, oriented tangentially to the surface. That means that the coil's $\mathbf{C_Z}$-vector is aligned anti-parallel with surface normal $\mathbf{n}$ at the stimulation point. The vector $\mathbf{n}$ is calculated using the discrete neighbourhood of $\mathbf{p}$ on the virtual head surface.

The user is given the option to change the distance d_C of the coil to the skin. This is necessary, because some obstacles like EEG electrodes might hinder the direct placement of the coil on the scalp. Mathematically, a change in distance is a simple translation of the coil along the head's normal vector at the stimulation point.

Setting $\mathbf{p}$, d_C, and $\mathbf{C_Z}$ leaves only the yaw angle of the coil, i.e. its rotation around its z-axis undefined. In TMS, a rotation angle of 0° normally means that the coil handle points backwards. But there is no definition of what an angle of e.g. 45° means. After discussing the matter with the neurologists in the project, we agreed on the following definition: Let N be the normal to the coronal plane[6] and T_pS be the tangent plane to the head surface S in p. Define $N_{\parallel}$ to be the orthogonal projection of N on T_pS. Now the yaw angle γ of the coil is set such that for $\gamma = 0°$ the coil's x-axis C_X aligns with $N_{\parallel}$.

[6] This is the plane which divides the body in a front and a back part. So N points to the front of the body.

In our user interface a slider and a text field allow precise adjustments of γ, e.g. to the standard 45° for motor cortex stimulations. Furthermore, we allow a translation along the coil's x- and y-axis. This is not necessary for clinical application, but offers some new possibilities in TMS research. For example, the stimulation focus of a circular coil is not below its centre, but distributed ring-like under its rim. Shifting the coil allows to position the rim as close to the target structure as possible.

This way the physician defines the treatment completely in virtual reality. The whole procedure requires less than a minute and can be done during the TMS session, in order to define new stimulation points, as well as prior to the session if the stimulation target is already known. This is comparable to the situation in radiotherapy or radiosurgery, where the treatment can be planned well in advance and is then implemented by a robot [162].

3.4.2. Trajectory planning I: Heuristics

After the virtual coil target pose ${}^{\mathrm{I}}T_{\mathrm{C^e}}$ is set, a trajectory to move the coil from its actual position to ${}^{\mathrm{I}}T_{\mathrm{C^e}}$ is calculated. Therefore, the actual position of the real coil with respect to the head is determined, see Section 3.3, and transformed to image coordinates, yielding ${}^{\mathrm{I}}T_{\mathrm{C^s}}$.

A virtual trajectory[7] ${}^{\mathrm{C}}\Gamma_{\mathrm{I}}$ for the coil from its current position ${}^{\mathrm{I}}T_{\mathrm{C^s}}$ to its target position ${}^{\mathrm{I}}T_{\mathrm{C^e}}$ is calculated as follows:

The coil is first taken away from the head by a distance d along the current surface normal by a translational movement. The direction of the move is taken as the vector from the centre of the virtual head m to the start coil position ${}^{\mathrm{I}}p_{\mathrm{C^s}}$. The step is omitted if the coil is already more than 100 mm away from the head, e.g. at the beginning of the treatment session.

After the translational movement away from the head, the coil is moved along a circular arc to a distance d over the target region. The centre of the arc is hereby taken to be the centre of the virtual head, m.

During the arc movement the orientation of the coil is gradually changed such that the coil's z-axis is always aligned anti-parallel to the normal vector of the arc. The yaw angle is set such that it performs a linear change from γ^s to γ^e, both given by the start and target position of the coil:

Let $c : [0,1] \to I,\ t \mapsto c(t)$ be the arc length parameterised curve representing the arc. Clearly, c is differentiable. So let $F = F(t)$ be the Frenet frame[8] for c with $F_x(t) = \dot{c}(t)$, $F_y(t) = \frac{m-c(t)}{\|m-c(t)\|}$. Note that the coil's z-axis at any point $c(t)$ on the arc is given by $F_y(t)$. Define the vector v^s as the orthogonal projection of the coil's x-vector at ${}^{\mathrm{I}}T_{\mathrm{C^s}}$, C_x^s, on

[7] We denote a trajectory, i.e. the path of an object O given in coordinates A, by ${}^{\mathrm{A}}\Gamma_{\mathrm{O}}$. Note that ${}^{\mathrm{A}}\Gamma_{\mathrm{O}}$ maps a time parameter t to a position and orientation of O. We define ${}^{\mathrm{A}}T_{\mathrm{O^s}} := {}^{\mathrm{A}}\Gamma_{\mathrm{O}}(0)$, ${}^{\mathrm{A}}T_{\mathrm{O^e}} := {}^{\mathrm{A}}\Gamma_{\mathrm{O}}(1)$.

[8] In differential geometry, a frame F for a differentiable curve c is a coordinate system moving along the curve. The origin of F at time t is at $c(t)$. The x-axis of F at t is parallel to $\dot{c}(t) = \frac{dc}{dt}$. The Frenet frame for a curve in $\mathbb{R}^3$ is the Gram-Schmidt orthonormalisation of $(\dot{c}, \ddot{c}, \dot{c} \times \ddot{c})$. For more details see any introductory textbook on differential geometry, e.g. [31].

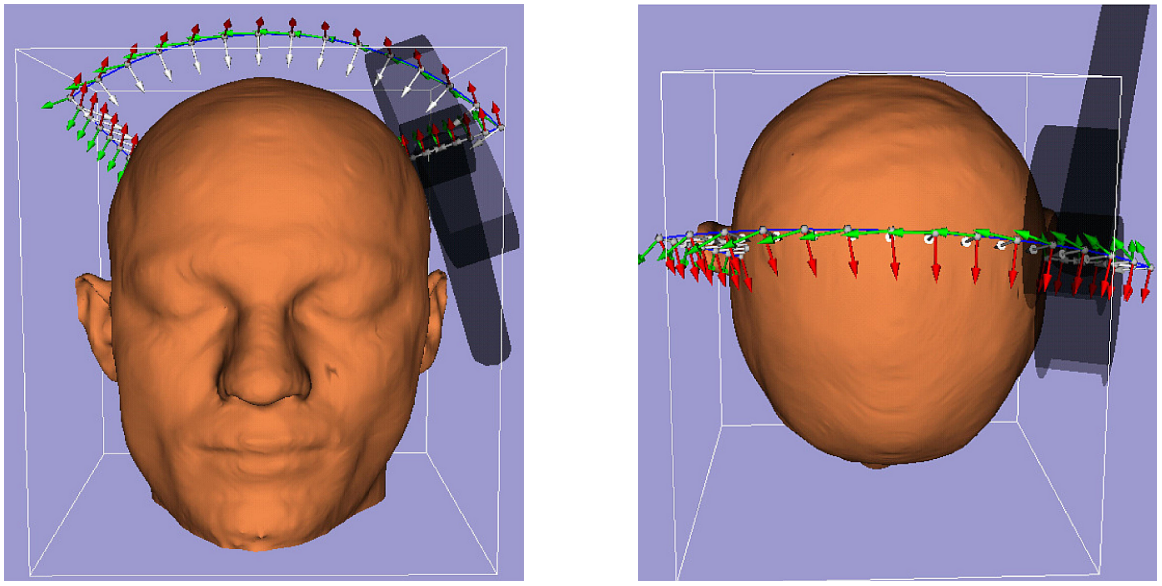

Figure 3.11.: Front view (left) and top view (right) of a coil trajectory. The coil is first taken away from the head with a translational movement, then rotated over the target region and finally lowered to the next stimulation point. Note that the coil's z-axis (white arrows) always points towards the head centre when on the arc movement. The coil's x- and y-axes (red and green arrows) are gradually rotated to match orientation at target point.

the plane spanned by $(F_x(0), F_z(0))$. To be exact, C_x^s is parallel translated to $F(0)$ before projection. Let γ^s be the angle between $F_x(0)$ and v^s. Similarly, define v^e as the orthogonal projection of the coil's x-vector at ${}^{\mathrm{I}}T_{\mathrm{C^e}}$ on the plane spanned by $(F_x(1), F_z(1))$ and γ^e as the angle between $F_x(1)$ and v^e. Then the yaw angle of the coil at a point $c(t)$ on the arc is given as $\gamma(t) = (1-t)\gamma^s + t\gamma^e$. It is the angle between the coil's x-axis and $F_x(t)$.

Because a continuous complex movement like an arc trajectory with change in orientation is hard to establish with current robot controllers, we simplify the setting by defining only a number n_a of interpolation poses along the arc. This will be superfluous as soon as robot programming languages allow easy commanding of parameterised movements, but for the Kuka and Adept robots we use, this is unavoidable. One of the problems associated with such a continuous movement is the control of the redundant joint settings for a pose by the state parameters for hand, elbow, and arm. We will present an algorithm that solves this ambiguity in Section 3.4.3, using the discretisation n_a.

For the last part of the trajectory, the coil is lowered to the head by another translational movement. The direction of the move is taken as the z-vector of the coil at the target point. This movement is divided into n_t equidistant interpolation poses to allow better robot control. To ease notation, we include the target pose ${}^{\mathrm{I}}T_{\mathrm{C^e}}$ in the set of interpolation poses.

The parameters d, n_a, and n_t are set in dependence of the arc angle ϕ. They increase linearly with ϕ up to a maximum value. For an example of a trajectory see Figure 3.11.

In total, the discrete trajectory has $1+n_a+n_t$ poses. The first one, ${}^{\mathrm{I}}T_{\mathrm{C}}^{0} = {}^{\mathrm{I}}T_{\mathrm{C^s}}$, has already an associated robot joint configuration. For the remaining $n = n_a + n_t$ poses ${}^{\mathrm{I}}T_{\mathrm{C}}^{i}$, the so-called interpolation poses, a joint setting needs be determined. This is covered in Section 3.4.3.

The calculated trajectory is displayed in the virtual scenario for approval by the user. Thereafter, the coil trajectory is transformed to real world coordinates using the actual position of the head ${}^{\mathrm{R}}T_{\mathrm{H}}$ in robot coordinates and the registration of the head to the image data ${}^{\mathrm{I}}T_{\mathrm{H}}$. Thus, we get the coil trajectory ${}^{\mathrm{C}}\Gamma_{\mathrm{R}}$ in robot coordinates as

$$ {}^{\mathrm{R}}\Gamma_{\mathrm{C}} = {}^{\mathrm{R}}T_{\mathrm{H}}{}^{\mathrm{I}}T_{\mathrm{H}}^{-1}{}^{\mathrm{I}}\Gamma_{\mathrm{C}}. \tag{3.8} $$

The final step is to translate ${}^{\mathrm{R}}\Gamma_{\mathrm{C}}$ into a trajectory for the robot end-effector ${}^{\mathrm{R}}\Gamma_{\mathrm{E}}$. But that is just a multiplication with the inverse of the end-effector to coil transform

$$ {}^{\mathrm{R}}\Gamma_{\mathrm{E}} = {}^{\mathrm{R}}\Gamma_{\mathrm{C}}{}^{\mathrm{E}}T_{\mathrm{C}}^{-1}. \tag{3.9} $$

3.4.3. Trajectory planning II: Optimisation

So far, the trajectory was planned without reference to the robot used. This follows our general concept of device independence, Section 3.2.1. The advantage of the concept is that a new robot type can be incorporated into the set-up with very little effort. For example, the robot development of Renaud et al. might prove superior to the serial six joint robots now used, since it is solely designed for robot aided TMS [138].

But our approach of planning the trajectory independently of the robot has also a disadvantage: Robot workspace limitations and robot move characteristics are not taken into account. Thus, we incorporated an optimisation step into our system, adapting the trajectory to overcome the limitations of the specific six joint serial robot we use. Clearly, this optimisation step must be robot specific. Nevertheless, we think that the general concept presented here can be utilised for many robot types and situations.

As explained in Section 3.2.3, there are up to eight possible joint settings for the Kuka KR3 or the Adept Viper s850 to reach a given pose; one for each set of configuration states. We have already described an algorithm to choose the target configuration mode given start joint values and target pose. This algorithm, based on a metric in joint space, performs optimally in the sense that for a given start position J^{start} and target pose ${}^{\mathrm{R}}T_{\mathrm{T}}$ there is no configuration setting which allows to reach ${}^{\mathrm{R}}T_{\mathrm{T}}$ with less joint movement.

For a trajectory ${}^{\mathrm{R}}\Gamma_{\mathrm{E}}$ with n interpolation points we have 8^n possible configuration settings along the trajectory. Let $\mathfrak{C} = \prod_{i=1}^{n} \left(\{\mathit{lefty}, \mathit{righty}\} \times \{\mathit{up}, \mathit{down}\} \times \{\mathit{flip}, \mathit{noflip}\}\right)$ denote the set of possible configuration settings along the trajectory. This section explains how to choose an element $c \in \mathfrak{C}$ for the realisation of the trajectory, i.e. a configuration mode for each interpolation point.

3.4.3.1. Optimal paths

First of all, we need a way to compare two paths $c_1, c_2 \in \mathfrak{C}$. Therefore we assign a positive value $value(c)$ to each path. This enables us to speak of an optimal path c_{opt} in the sense that $value(c_{opt}) \leq value(c)$ for all $c \in \mathfrak{C}$. The main idea is to move the coil as smoothly as possible between the interpolation points, i.e. to avoid unnecessary movements of the coil.

Minimal robot joint movement We extend the idea of assessing a robot move by a metric in joint space. We define

$$\mathrm{rjm}(c) := \max_{i=0}^{n-1} \mathrm{d}(J^i, J^{i+1}), \tag{3.10}$$

where J^i is the joint configuration to reach pose i of the trajectory with the configuration state c_i and $\mathrm{d}(J^i, J^{i+1})$ is the metric in joint space defined in Equation (3.6). $\mathrm{rjm}(c)$ measures the maximum joint change along the trajectory from one interpolation point to the next.

The advantage of this objective function is the evaluation speed. Furthermore, rjm is conservative in the sense that small joint movements result only in small coil movements. Thus, an optimal path according to Equation (3.10) is guaranteed to lead the coil from one trajectory point to the next avoiding large changes in coil position or orientation along the way. For an example see the end of this section.

Minimal coil orientation change Our second approach is to look directly at the change in orientation when the robot moves from one pose to the next. Let

$$M(J) := \big(\mathbf{M_x}(J), \mathbf{M_y}(J), \mathbf{M_z}(J), \mathbf{M_p}(J)\big) := {}^{\mathrm{R}}T_{\mathrm{E}}(J)\,{}^{\mathrm{E}}T_{\mathrm{C}}$$

denote the homogeneous matrix describing the coil's pose for a robot with joint values $J = (j_1, \ldots, j_6)^t$. The vectors $\mathbf{M_x}$, $\mathbf{M_y}$, $\mathbf{M_z}$ encode the x-, y-, and z-part of the coil orientation, $\mathbf{M_p}$ encodes the coil position. To assess the different possible realisations of the trajectory ${}^{\mathrm{R}}\Gamma_{\mathrm{E}}$ by elements of $\mathfrak{C}$, we evaluate how much the coil orientation changes from the joint setting for one interpolation point, J^i, to the next, J^{i+1}. Therefore we parameterise M as

$$M^i(t) := M(tJ^i + (1-t)J^{i+1}), \qquad t \in [0,1]. \tag{3.11}$$

Note that this implicitly assumes a joint interpolated robot trajectory, i.e. a synchronous movement of all robot joints from J^i to J^{i+1}, which is indeed the case for the robots we use. We determine the path length of the curve the orientation vectors $\mathbf{M_o}(t)$, $o \in \{x, y, z\}$, describe in S^2 to measure how much $\mathbf{M_o}(t)$ change when the robot moves from J^i to J^{i+1}:

$$s_o(J^i, J^{i+1}) = \int_0^1 \|\dot{\mathbf{M}}_o^i(t)\| dt. \tag{3.12}$$

We describe briefly how to calculate $\dot{\mathbf{M}}_o(t)$: Denote the Jacobian of ${}^{\mathrm{R}}T_{\mathrm{C}}(\mathrm{J})$ by $\mathbf{J}$, i.e. $\mathbf{J}_{a,b} = \frac{\partial {}^{\mathrm{R}}T_{\mathrm{E}}^{\lfloor (a-1)/4 \rfloor + 1, (a-1)\%4+1}}{\partial j_b}$, $a \in \{1, \ldots, 12\}$, $b \in \{1, \ldots, 6\}$.[9] Then

$$\dot{M}_{k,l}(t) = \mathbf{J}_{(4(k-1)+l,\cdot)}\big|_{J=J(t)}(J^{i+1} - J^i), \tag{3.13}$$

and

$$\dot{\mathbf{M}}_x(t) = (\dot{M}_{1,1}(t), \dot{M}_{2,1}(t), \dot{M}_{3,1}(t)), \tag{3.14}$$
$$\dot{\mathbf{M}}_y(t) = (\dot{M}_{1,2}(t), \dot{M}_{2,2}(t), \dot{M}_{3,2}(t)), \tag{3.15}$$
$$\dot{\mathbf{M}}_z(t) = (\dot{M}_{1,3}(t), \dot{M}_{2,3}(t), \dot{M}_{3,3}(t)). \tag{3.16}$$

To assess the change in coil orientation from J^i to J^{i+1}, we define

$$S(J^i, J^{i+1}) := \sqrt{\frac{s_x^2(J^i, J^{i+1}) + s_y^2(J^i, J^{i+1}) + s_z^2(J^i, J^{i+1})}{2}}. \tag{3.17}$$

Note that if $M^i(t)$ describes a simple rotation around an arbitrary vector in S^2 by an angle ϕ, S_i is exactly ϕ.

Finally, we can assign the following scalar value to an element $c \in \mathfrak{C}$ to evaluate the maximum coil orientation changes along the trajectory:

$$\mathrm{coc}(c) := \max_{i=0}^{n-1} S(J^i, J^{i+1}). \tag{3.18}$$

3.4.3.2. Calculating an optimal path - greedy algorithm

We have so far defined two preorders on $\mathfrak{C}$, rjm and coc, allowing us to talk about minimal elements in $\mathfrak{C}$. Such elements have the property that they describe either a trajectory realisation with minimal maximum joint change between two interpolation points, Equation (3.10), or a trajectory realisation with minimal coil orientation change between two interpolation points, Equation (3.18).

The first idea to realise the trajectory ${}^{\mathrm{R}}\Gamma_{\mathrm{E}}$ is to use a greedy algorithm. Suppose the coil is at trajectory pose i with robot joint values J^i. We choose the joint setting for pose $i+1$ as

$$J^{i+1} = \min_{c_{i+1}} \mathrm{d}(J^i, J^{i+1,c_{i+1}}) \tag{3.19}$$

or

$$J^{i+1} = \min_{c_{i+1}} S(J^i, J^{i+1,c_{i+1}}), \tag{3.20}$$

[9] ${}^{\mathrm{R}}T_{\mathrm{E}}^{\lfloor (a-1)/4 \rfloor + 1, (a-1)\%4+1}$ refers to the element $(\lfloor (a-1)/4 \rfloor + 1, (a-1)\%4+1)$ of the homogeneous matrix describing the pose of the coil in robot coordinates. $\lfloor a/4 \rfloor$ is the biggest integer that is less or equal to $a/4$ and $a\%4$ the remainder of the (integer) division of a by 4. The calculation of the Jacobian of a parameterised serial chain, e.g. the robot with a rigidly attached coil, is standard in robotics [168].

depending on the objective function we use.

It is immediately clear that this algorithm is theoretically not optimal, i.e. there are start and end points such that for the trajectory holds $value(c_{greedy}) > value(c_{opt})$, because minimal steps at the beginning of the trajectory might lead the robot in a joint position J^i where all next joint possibilities (the different configuration states for pose $i+1$) have a large distance to J^i. This is not just a theoretical scenario; for an example see the end of the section.

3.4.3.3. Calculating an optimal path - graph algorithm

As we have seen, the greedy strategy can fail, so we have to investigate full paths and not just movements from one trajectory point to the next to find an optimal path. Clearly, the brute-force-approach of calculating the value for each $c \in \mathfrak{C}$ and sorting the c fails, because $\mathfrak{C}$ consists of 8^n elements (n being the number of interpolation points) and large trajectories have often more than 20 interpolation points.

The problem simplifies if we express it in the language of graph theory. Let

$$V = \{v_{i,k} | i \in \{0, \ldots, n\},\ k \in \{1, \ldots, K(i)\}\} \tag{3.21}$$

be the set of vertices of the graph G, where $K(0) = 1$ and $K(i > 0)$ is the number of possible configuration states for ${}^{\mathrm{R}}\Gamma^i_{\mathrm{E}}$, and

$$v_{0,0} = J^{start} = J^0, \tag{3.22}$$

$$v_{i,k} = J^{i,state_k}. \tag{3.23}$$

Here, $state_k$ denotes the k^{th} element in the set of possible configuration states for pose i. We define the set of directed edges E of G as

$$E = \{e^i_{a,b} | i \in \{0, \ldots, n-1\},\ a \in \{1, \ldots, K(i)\},\ b \in \{1, \ldots, K(i+1)\}\}, \tag{3.24}$$

where

$$e^i_{a,b} = (v_{i,a}, v_{i+1,b}). \tag{3.25}$$

The notation $e = (v_1, v_2)$ means that edge e runs from v_1 to v_2. According to the structure of the problem, we define the i^{th} layer of G as $L_i = \{v_{i,k} | k \in \{1, \ldots, K(i)\}\}$. Note that all $v \in L_i$ represent the same pose of the robot (and thus the TMS coil), but the pose is realised with differing robot joint settings. An element $c \in \mathfrak{C}$ can be represented as a path in $G(V, E)$ from $v_{0,0}$ to a vertex $v \in L_n$: $p^c := (v_{0,0}, v_{1,c_1}, \ldots, v_{n,c_n})$ with $v_{i,c_i} = J^{i,c_i}$. We define $e^i_c := (v_{i,c_i}, v_{i+1,c_{i+1}})$, $\mathrm{d}(e^i_c) := \mathrm{d}(J^{i,c_i}, J^{i+1,c_{i+1}})$, see Equation (3.10), and $S(e^i_c) := S(J^{i,c_i}, J^{i+1,c_{i+1}})$, see Equation (3.18).

Before we continue, we note the following properties of $G(V, E)$:

- If $v_1 \in L_i$ and $v_2 \in L_{i+1}$ then $(v_1, v_2) \in E$, i.e. all vertices in neighbouring layers are connected by an edge.
- The trajectory can be realised by the robot if and only if $K(i) > 0$ for all $i \in \{0, \ldots, n\}$.

- $\mathrm{rjm}(c) = \max_{i=0}^{n-1} \mathrm{d}(e_c^i)$
- $\mathrm{coc}(c) = \max_{i=0}^{n-1} S(e_c^i)$

We are now ready to give the algorithm for determining an optimal path in $\mathfrak{C}$. We first initialise $G(V, E)$ layer-wise, i.e.

```
1 Graph.init{
2   List V, E, L, Lprev
3   int[n] EdgeLayer
4   Vertex startVertex = new Vertex(J^start)
5   Lprev.add(startVertex)
6   V.add(startVertex)
7   for(i=1 to n){
8     if(K(i)==0){
9         throw new Exception("Trajectory not possible.")
10    }
11    for(k=1 to K(i)){
12        Vertex v = new Vertex(J^(RΓ^i_E, state_k))
13        V.add(v)
14        L.add(v)
15        for(w in Lprev){
16            Edge e = new Edge(w,v)
17            E.add(e)
18            EdgeLayer[i]++
19        }
20    }
21    Lprev = L
22    L.clear
23  }
24 }
```

In the code snippet, `List` stands for an arbitrary list class with the canonical operations `add(Element)` and `clear` (delete all elements). The lists `V` and `E` store the vertices and edges, respectively, of the graph $G(V, E)$. An element of the class `Vertex` stores the joint values for this vertex and a list for all incoming and outgoing edges. An element of the class `Edge` stores the start and end vertex of the edge and an edge value $f(e)$. $f(e)$ is either $\mathrm{d}(e)$ (rjm) or $S(e)$ (coc), depending on which definition we use for an optimal path. Finally, the array `EdgeLayer` stores the number of edges with start vertex in a given layer.

After `V` and `E` are initialised, we determine an optimal path in $G(V, E)$ as follows:

```
1 Graph.findOptPath{
2   E.sortDescending //edge with biggest value comes first
3   i = 0
4   max = 0 //will store biggest value on minimal path
5   while (i < E.size) {
6     Edge e = E.get(i)
```

```
7       if (e.isDeletable) { //check if last edge in this layer
8           e.delete //removes e from E, also deletes orphan and
                widow vertices
9           continue //continues while loop, i is not incremented
10      }
11      if (i == 0){// first non-delete-able edge has max value
12           max = e.value
13      }
14      i++ //a non-deletable element has been found, increment in
            E to find next
15    }
16  }
```

The method `Edge.isDeletable` returns `true` if there is at least one more edge in the same layer. The method `Edge.delete` is implemented recursively:

```
1  Edge.delete {
2      E.remove(this)
3      EdgeLayer[this.layer]--
4      if (this.startNode != null) {
5          this.startNode.out.remove(this)
6          if (this.startNode.getNumOutEdges == 0)
7              this.startNode.deleteBackward;
8      }
9      if (this.endNode != null) {
10         this.endNode.in.remove(this)
11         if (this.endNode.getNumInEdges == 0)
12             this.endNode.deleteForward
13         }
14     }
15     this.startNode = null;
16     this.endNode = null;
17 }
```

```
1  Vertex.deleteBackward {
2      V.remove(this)
3      while (this.in.size > 0) {
4          Edge e = this.in.get(0);
5          this.in.remove(e);
6          e.endNode = null;
7          e.delete;
8      }
9  }
```

```
1  Vertex.deleteForward {
2      V.remove(this)
3      while (this.out.size > 0) {
```

```
4           Edge e = _out.get(0)
5           this.out.remove(e)
6           e.startNode = null
7           e.delete
8       }
9   }
```

Let us remark a few things on the algorithm for finding the minimal path in $G(V, E)$. As the value of a path in G is set by its maximum edge, we try to remove all edges with high values as long as there is a path from $v_{0,0}$ to L_n. We make use of the following invariants:

1. For each v$\in$V$-\{L_n\}$ there is an outgoing edge connecting it to the following layer.

2. For each v$\in$V$-\{v_{0,0}\}$ there is an incoming edge connecting it to the previous layer.

3. There is at least one edge between neighbouring layers, i.e. `EdgeLayer[i]`>0 for all i$\in \{0, \ldots, n-1\}$.

At the beginning, Properties 1, 2 are ensured by the initialisation. Property 3 is tested during the initialisation and the algorithm is aborted if there is an empty layer in the beginning. If an edge `e` is deleted, we check if its start vertex `s` has any outgoing edges left. If yes, 1 holds trivially. If no, we recursively delete `s` and all incoming edges, ensuring 1. Similarly, we check if `e`'s end vertex `t` has any incoming edges left. If yes, 2 holds trivially. If no, we recursively delete `t` and all outgoing edges, ensuring 2. We have to prove that this does not violate 3: First, we delete the initial edge `e` only if `EdgeLayer[e.layer]`>0, so for this deletion 3 is ensured. Secondly, if we delete `e` there is another edge `e'` in the same layer. Let `s'` be its start vertex. If `s` $=$ `s'`, `s` is not deleted, because it has more outgoing edges than just `e`. If `s` $\neq$ `s'`, the incoming edges for `s` are not the only edges in `EdgeLayer[e.layer-1]`, because by 2 there exists also an incoming edge for `s'`, so all incoming edges of `s` can be deleted. By induction, the recursive backwards deletion process does not violate 1 – 3. A similar argument shows the correctness of the forward deletion process.

After termination of the `Graph.findOptPath` method we are left with a graph `G(V,E)` with `EdgeLayer[i]`$=1$ for all `i`. Hence, our path p in $G(V, E)$ is given by traversing `G(V,E)` from `startVertex`, i.e. $v_{0,0}$, to the remaining vertex in L_n. As there is only one outgoing edge left for each vertex on the path, this is straight forward.

The proof that p is optimal is not hard: Let q be a second path and suppose $value(q) < value(p)$. Let `e_p` be a maximum edge of p, i.e. `e_p.value` $\geq$ `e'_p.value` for all `e'_p`$\in p$. Let $i =$ `e_p.layer` and `e_q` the i^{th} edge of q. At one point in time the method `Graph.findOptPath` calls `e_p.isDeletable` and gets `false` as return. (Otherwise it would delete `e_p`). Thus, `e_q` $\notin$ `E` at this time and hence it has been deleted before. Because `e_p.value` $>$ `e_q.value`, it can't have been deleted directly, i.e. in Line 8 of `Graph.findOptPath`. But this implies that another edge `e_q'` of q has been deleted directly before. (Otherwise `e_q` would not be part in an orphan or widow-chain and thus not be deleted indirectly.) Hence, `e_q'.value` $\geq$ `e_p.value`, which contradicts our initial assumption $value(q) < value(p)$.

3.4.3.4. Trajectory relaxation

We have now established a method to find the optimal way to implement the trajectory. Still, there are two problems remaining:

1. What if the trajectory cannot be realised by the robot because there is a pose i which cannot be reached in any robot configuration mode?
2. What if the optimal realisation of the trajectory still contains a large move of either the robot joints (rjm) or the coil (coc)? Such a big move could bring the coil close to the patient's head during the transition from one controlled pose to the next.

Our solution to both problems is to relax the coil pose. We define

$$ {}^{\mathrm{I}}\Gamma_{\mathrm{C}}^{i,\alpha} := {}^{\mathrm{I}}\Gamma_{\mathrm{C}}^{i} Rot_y(\alpha), \tag{3.26} $$

where $Rot_y(\alpha)$ denotes a rotation around the y-axis by α. We use equidistant steps of e.g. 10° to compute about 10 poses for each trajectory step i, e.g. from $\alpha = -60°$ to $\alpha = 30°$. These poses are then transformed into end-effector poses using Equations (3.8) and (3.9), resulting in poses ${}^{\mathrm{R}}\Gamma_{\mathrm{E}}^{i,\alpha_k}$. In the same way as in the previous section, we have different configuration modes s_l to realise ${}^{\mathrm{R}}\Gamma_{\mathrm{E}}^{i,\alpha_k}$, so we define again a graph $G(V, E)$ with

$$ v_{0,0,0} = J^{start} = J^0, \tag{3.27} $$

$$ v_{i,k,l} = J^{i,\alpha_k,s_l}. \tag{3.28} $$

Again, all vertices with the same first index i are in the same layer, and neighbouring layers are fully connected. So we can use the same algorithm as above to find the optimal path through ${}^{\mathrm{R}}\Gamma_{\mathrm{E}}^{i,\alpha_k}$. Because $\alpha = 0$ is included in every pose relaxation, it holds $value(p_{opt,relax}) \leq value(p_{opt,no-relax})$.

3.4.3.5. Example

We exemplify the different objective functions for trajectory realisations and the effects of trajectory relaxation. We chose a point on the left side of the head as a start point and a point on the right side of the head as the end point of the trajectory, see Figure 3.12. The robot's joint setting in the start pose were (26.9°, −28.0°, 165.8°, −45.9°, 75.2°, 120.4°), i.e. the robot was in *noflip* mode, see Figure 3.12.B. We restricted the arm and elbow mode to *lefty* and *up*, respectively, and calculated the trajectory implementations for the following metrics and algorithms

- minimal robot joint movement rjm, greedy algorithm,
- minimal robot joint movement rjm, graph algorithm, tangential interpolation poses,
- minimal robot joint movement rjm, graph algorithm, relaxed interpolation poses,
- minimal coil orientation change coc, graph algorithm, tangential interpolation poses,
- minimal coil orientation change coc, graph algorithm, relaxed interpolation poses.

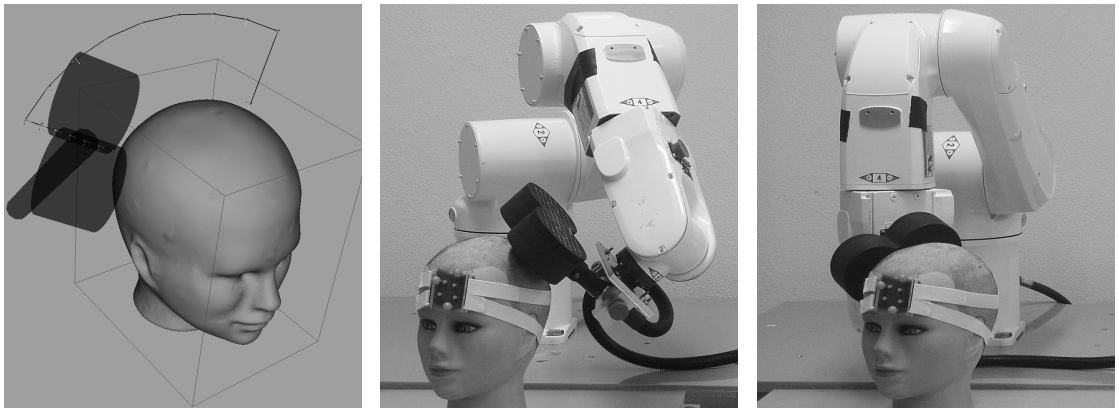

A B C

Figure 3.12.: Trajectory for exemplifying the results for different trajectory implementation algorithms. The coil is to be moved from the left side of the head (start of the trajectory curve in Figure A, Figure B) to the right side of the head (displayed coil position in Figure A, Figure C). For each interpolation poses a number of different robot joint settings exist to reach this pose. In between the interpolation poses, the robot moves in joint interpolated mode, see Section 3.4.3.1. The task is to choose a joint setting for each interpolation pose such that the overall coil movement is minimal.

The resulting movements of the robot (Joints 4 – 6) and the coil are displayed in Figure 3.13. For all algorithms, the robot reached the target pose in *flip* configuration, see Figure 3.12.C. Thus, the final joint settings for all algorithms were the same: ($-0.7°$, $-36.7°$, $216.3°$, $-33.9°$, $-79.0°$, $23.4°$). But there were big differences in how this hand configuration change was realised.

The greedy algorithm first turned Joint 4 in negative direction until the joint limit of $-190°$ was reached (Interpolation point 7). This realised the minimal joint change from one interpolation pose to the next. But the eighth interpolation point could not be reached by decreasing the value of Joint 4 further. Thus, Joint 4 had to change by nearly $180°$, Joint 5 had to change from $+60°$ to $-60°$ and Joint 6 had to change by about $180°$ to get to Interpolation point 8 (see also the discussion in Section 3.2.3). This resulted in a huge move of the coil with a cumulated coil orientation change of over $120°$, Figure 3.13 top. The configuration change brought the coil's front dangerously close to the head, changing the coil's orientation from tangential ($0°$ pitch angle) to about $-60°$ pitch angle.[10]

If we persist on the tangential orientation at each interpolation pose, the optimal solutions for a minimal coil orientation change (coc) and a minimal joint movement (rjm) agree. We see that the big move from the greedy algorithm is avoided by implementing the configuration change earlier in the trajectory, in Trajectory segment 6. When we compare the graphs for the greedy and the optimal tangential algorithm for Joint 5, we see that the configuration change was chosen at the trajectory segment in which Joint 5 could not get closer to $0°$ by a greedy move. Note that the orientation change of the coil for a move of Joint 4 increases with the angulation of Joint 5. Thus, it comes to no surprise that by choosing the configuration

[10] The pitch angle measures the rotation about the y axis. For the coil, this axis runs perpendicular to the handle direction and the coil's surface.

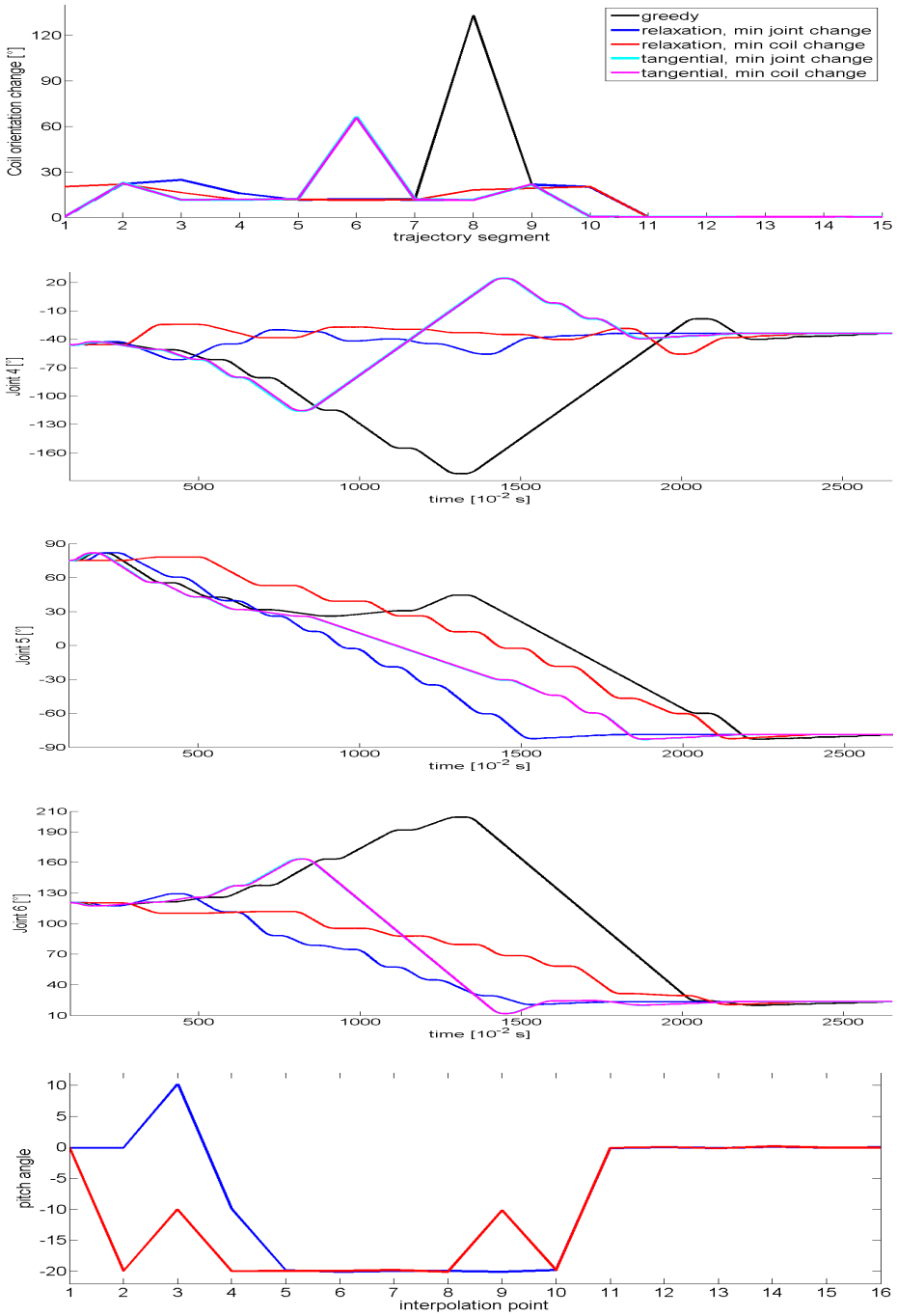

Figure 3.13.: Robot trajectories using different configuration algorithms. The graphs show the cumulated coil orientation change during the transition from one interpolation point to the next (top), the angular changes of Joints 4 – 6 (middle) and the pitch relaxation used in the two relaxation algorithms (bottom). Note that the joint graphs are not aligned with the coil change and the pitch relaxation graph, but rather show the true time course for the different algorithms. This allows a comparison of the computation times for the trajectory (horizontal parts of the joint graphs).

mode change at half the angular value of Joint 5, the resulting cumulated coil orientation change is only about half as big. We remark that the changes in Joints 4 and 6 for the configuration change were similar for the greedy and the trajectory optimal algorithms, so the important difference between the greedy and the tangential solution lies in the value of Joint 5 for the configuration change.

The relaxation of the trajectory allows to decrease the value of Joint 5 further at the interpolation points. For both objective functions (coc and rjm) this results in trajectories with smooth coil transitions between the interpolation points. The maximum coil orientation change for the minimal joint movement algorithm was about 25°, the maximum coil orientation change for the optimal algorithm was 22°. Both algorithms yielded a trajectory which changed the joint angles nearly monotonously from start to target values. Therefore, the resulting trajectories did not differ much. The coc trajectory realised the major change in Joint 4 right at the beginning in one big step whereas the rjm algorithm used several smaller steps for it. Further, the coc algorithm used Joint 4 at the end to counterbalance a bigger move of Joint 6. This resulted in a slightly smaller cumulated coil orientation change in Trajectory segment 9. The biggest difference between the algorithms is the relaxation angle (or pitch angle) chosen at the beginning. The coc algorithm turns the coil towards the head in the first trajectory segment by $-20°$ and keeps this tipping towards the head during the whole trajectory. The rjm algorithm first turns the coil away from the head by 10° (Interpolation point 3), but reverts this turn in the next two moves to $-20°$. This results in slightly less smooth coil transitions during the first phase of the trajectory.

3.4.3.6. Run-time analysis and implementation issues

The relaxation of the trajectory poses creates a much bigger computational task than finding an optimal path for a non-relaxed trajectory: Let A be the number of discretisation steps for α and M the number of configuration modes[11]. Assuming n interpolation points for the trajectory, the resulting graph has n layers with $A * M$ vertices and one layer with one vertex (namely the start vertex). The number of edges is thus given by $|E| = (n-1) * (A * M)^2 + A * M$.

In the initialisation phase, each edge must be initialised, its value be computed, and the edge be added to the edge list `E`. This results in a runtime of $\mathbf{O}(nA^2M^2)$. It is worth noting that computing the coil orientation change (coc, Equation (3.17)) takes much longer than evaluating the maximum joint change (rjm, Equation (3.6)), because the former needs to compute the Jacobian of the robot direct kinematics and to integrate numerically, whereas the latter just computes the difference of two six-tuples and takes the maximum value. So the constant hidden in the **O**-notation is rather large for coc and small for rjm.

To obtain an optimal path in the graph, we sort the edges by their value, requiring asymptotically $\mathbf{O}((nA^2M^2)\log(nA^2M^2))$ operations, and test for each edge exactly once if it can

[11] M is at most $2^3 = 8$, but for our application we mostly restrict the arm configuration to *lefty*, reducing M to 4. If we work with a sitting subject, we can further set elbow to *up*, so that only 2 configuration modes for the hand remain.

be deleted or not[12],$\mathbf{O}(nA^2M^2)$. The process of deleting an edge itself is relatively fast, so that the asymptotic constant is small. This is also true for the sorting step, so we expect the initialisation to be non-negligible for the overall run time, even if it is of lower asymptotic order.

In our experiments we found that for $A = 10$, $M = 2$, and $n = 25$ the coc initialisation took about $t_{\text{coc}}^{init} = 65\,\text{ms}$, the rjm initialisation took about $t_{\text{rjm}}^{init} = 12\,\text{ms}$, and the `Graph.findOptPath` method took about $t^{opt} = 5\,\text{ms}$. If we consider all 8 possible configuration modes, i.e. $M = 8$, these figures increase to $t_{\text{coc}}^{init} = 860\,\text{ms}$, $t_{\text{rjm}}^{init} = 190\,\text{ms}$, and $t^{opt} = 90\,\text{ms}$. We see that for numbers of our concern, not the asymptotically governing sorting process of the edges is important for the run time, but the initialisation phase. Tests show that the process of filling the lists for the vertices and edges consumes most of time of the `Graph.init` method. To conclude, the running time for finding an optimal path in ${}^{\text{R}}\Gamma_{\text{E}}$ grows about quadratically in A and M and linearly in n for the small ranges of n, A, M we deal with.

The total run time of about one second for $A = 10$, $M = 8$, and $n = 25$ for the coc method shows the computational limits of the algorithm. For an initial trajectory calculation in joint space, such a computation time (and hence delay in treatment) might be bearable. But we need to keep in mind that the poses of the trajectory ${}^{\text{R}}\Gamma_{\text{E}}$ change constantly, because the head position ${}^{\text{R}}T_{\text{H}}$ changes, see Equation (3.8). Thus, we need to re-compute an optimal path in joint space to implement ${}^{\text{I}}\Gamma_{\text{C}}$ after reaching each pose. This means that for a trajectory with $n = 25$ interpolation points we have to expect a total computation time of about 12 seconds. (The computation time for each pose decreases, because n is getting smaller.)

To save time, we implemented the following two step process: First, we compute an optimal path for the non-relaxed trajectory. Only if there is no such path (because a pose cannot be realised) or if the path value is too big, we compute an optimal path for the relaxed trajectory. If also the relaxed trajectory cannot be realised or if the value of it is still too big, the user has to choose either another target, reposition the patient or move the robot by hand such that the coil is closer to the target region.

Finally, a relaxation of the tangential pose ${}^{\text{I}}\Gamma_{\text{C}}^{i}$ by α brings the coil rim ($\alpha < 0$) or coil handle ($\alpha > 0$) closer to the head. To avoid the coil touching the head, we therefore restrict the range of α in dependence of the distance of ${}^{\text{I}}\Gamma_{\text{C}}^{i}$ from the head surface: From $\alpha \equiv 0$ at the head surface to $\alpha \in \{-90°, 30°\}$ at sufficiently distant points along the trajectory.

3.4.4. Motion compensation

Motion compensation aims to keep the coil at its designated position if the head moves. We distinguish two areas of motion compensation: during the trajectory move and after reaching the target pose.

[12] This holds true also for the recursive process of deleting widow or orphan vertices and edges, because each edge considered in this process is directly deleted and will thus not appear in the main loop of the `Graph.findOptPath` method.

3.4.4.1. Trajectory adaptation

As briefly explained in the previous section, we compensate for head movements during the transition from one stimulation point to the next by adjusting the trajectory after reaching an interpolation point. Therefore we determine the head position ${}^{\mathrm{R}}T_{\mathrm{H}}$ and update ${}^{\mathrm{R}}\Gamma_{\mathrm{E}}$ using Equations (3.8) and (3.9). As neither the Kuka robot nor the Adept robot allow a safe adaptation of a once started move command[13], we have no possibility to correct head movements during the transition from one interpolation point to the next. Hence we plan the trajectory such that the distances between the interpolation points are small and the autonomous movements of the robot are short.

3.4.4.2. Keeping the target pose

After reaching the target pose, the second motion compensation feature sets in to compensate for head movements during the stimulation. Mathematically, we need to keep the transform from the coil centre to the head marker ${}^{\mathrm{H}}T_{\mathrm{C}}$ constant if the head position ${}^{\mathrm{T}}T_{\mathrm{H}}$ changes. This amounts to moving the robot end-effector to

$$ {}^{\mathrm{R}}T_{\mathrm{E}} = {}^{\mathrm{R}}T_{\mathrm{T}}\,{}^{\mathrm{T}}T_{\mathrm{H}}\,{}^{\mathrm{H}}T_{\mathrm{C}}\,{}^{\mathrm{C}}T_{\mathrm{E}}. \tag{3.29} $$

To avoid sudden big changes in robot joint values, we use the metric defined in 3.2.3 to calculate the best configuration mode for the target position ${}^{\mathrm{R}}T_{\mathrm{E}}$.

We remark that this second motion compensation feature makes no reference to the virtual head model. Both, the motion compensation equation (3.29) and the online adaptation of coil pose require only the knowledge of the headband position, ${}^{\mathrm{T}}T_{\mathrm{H}}$, and the desired position of the coil with respect to the headband, ${}^{\mathrm{H}}T_{\mathrm{C}}$. Note that ${}^{\mathrm{H}}T_{\mathrm{C}}$ can be defined by the initial pose ${}^{\mathrm{H}}T_{\mathrm{C}}$ when starting the motion compensation module. Even though we haven't used this fact yet, one can imagine a quick set-up procedure, where the coil is pre-positioned manually near the head, steered to its target position by online pose adaption using visual guidance, and kept there for the time of a rTMS treatment. For example, this might be sufficient for the rTMS treatment of depression, where the left prefrontal cortex is stimulated for about 20 minutes using short trains of high frequency rTMS [49].

As an extension to the motion compensation feature, we allow an online change of the coil position with respect to the head (${}^{\mathrm{H}}T_{\mathrm{C}}$). The user can adapt ${}^{\mathrm{H}}T_{\mathrm{C}}$ by changing the distance of the coil from the head or rotating the coil around its z-axis. Mathematically, this corresponds to a concatenation of ${}^{\mathrm{H}}T_{\mathrm{C}}$ with ${}^{\mathrm{C}}T_{\mathrm{A}}$, where A is either a z-translation by d_z: $\begin{pmatrix} 1 & 0 & 0 & 0 \\ 0 & 1 & 0 & 0 \\ 0 & 0 & 1 & d_z \\ 0 & 0 & 0 & 1 \end{pmatrix}$, or a rotation around z by α_z: $\begin{pmatrix} \cos(\alpha_z) & -\sin(\alpha_z) & 0 & 0 \\ \sin(\alpha_z) & \cos(\alpha_z) & 0 & 0 \\ 0 & 0 & 1 & 0 \\ 0 & 0 & 0 & 1 \end{pmatrix}$. The advantage of

[13] The Adept robots allow to change the position of the move target, but in a rather uncontrolled manner: The target position is concatenated with a correction matrix, yielding the new target pose. This pose is then approached without further user control. Especially, there is no control over the configuration mode to reach the new pose or over the speed in which the trajectory is adapted. This disqualifies this functionality for our purposes. For example, imagine a miss-reading of the head position by the tracking system, causing a shift in the trajectory of the robot by 10 cm. This shift will be realised by the Adept trajectory adaptation within the next time step, i.e. 12 ms, bringing the robot to a very high speed.

this feature is twofold. Firstly, we can adapt to errors in the head reconstruction (Section 3.3.2) or head registration (Section 3.3.3) by moving the coil first to a position 1 cm above the stimulation point (using the method presented in Section 3.4.1) and then reducing this distance online until the coil touches the head slightly. Secondly, the coil rotation angle α_z is often set by visual inspection, especially if no MRI information is available and the virtual head is reconstructed using sampled outline points (Section 3.3.2). Here, the feature of online coil pose change speeds up the process of defining the stimulation point.

3.4.4.3. Implementation issues

For safety reasons, we restrict the allowed change in joint values for each joint, see Section 3.5. This is necessary, because joint limits might prevent the adaptation to small pose changes with small joint changes. In our experiments this was sometimes the case for Joint 4. When the stimulation pose was reached with e.g. $j_4 = 185°$ (the range of Adept's fourth joint is from $-190°$ to $190°$), a changed head position would have required a j'_4 angle of e.g. $195°$. Since this is cannot be realised with the Adept, the closest feasible joint setting would be $j'_4 = 5°$, $j'_5 = -j_5$, and $j'_6 = j_6 \pm 180°$. (Note that this position, which means a configuration change of the hand, is closer in joint space than $j'_4 = -175°$, $j'_5 = j_5$, $j'_6 = j_6$.) The transition from J to J' would induce a large coil movement, which might press the coil against the patient's head. This is clearly not acceptable. So there is no other way than to avoid such a move altogether, even for the price that some head motions cannot be compensated.

In our implementation of the motion compensation at the target point (Section 3.4.4.2), we first determine the actual head position ${}^{\mathrm{T}}T_{\mathrm{H}}$ and command the robot to the target pose ${}^{\mathrm{R}}T_{\mathrm{E}}$ according to Equation (3.29). Then we repeat this sequence. As neither the Kuka KR3 nor the Adept Viper s850 allow a safe modification of a commanded move, the two steps (head tracking – robot move) have to be performed in strict order. Nevertheless, as head movements are normally small, we still reach a pose update frequency in the range of the maximum tracking frequency, i.e. 30 – 60 Hz for the Polaris system.

Jitter in measurements, i.e. the variational error in determining the head marker's pose, is a serious problem for the motion compensation feature. Especially the passive Polaris system proved to be vulnerable for miss-readings in the orientation of the head marker. Due to a leaver of about 10 cm, an error of $0.1°$ in orientation reading of the head marker ${}^{\mathrm{T}}T_{\mathrm{H}}$ results in a shift of the stimulation point by 0.17 mm. On the contrary, errors in the readings of the translational part of the head marker translate directly to errors in position of the stimulation point, e.g. a miss-reading of 0.1 mm in position of the head marker causes the stimulation point to be shifted by the same value.

Tests in our laboratory have shown that the readings of the normal vector for the head marker we use in our application (passive Polaris tool with 3 reflective spheres) have a mean deviation of $0.15°$ to $0.2°$ from the averaged normal.[14] This results in an average shift of

[14] Value over 20,000 measurements; value independent of orientation towards the camera and independent of translational movements.

the stimulation point of 0.34 mm. This value should be compared to the mean translational error of about 0.25 mm.

Unfortunately, these values could not always be reproduced in practice. Error sources like inhomogeneous reflectance of the passive spheres (damaged coating, dirt, hair partly covering them) or increased infrared background light (sun) decreased the quality of the tracking data drastically. Sometimes, changes in stimulation position by up to 10 mm could be observed under sub-optimal conditions.

Our solution to stabilise the tracking data is to average the last n readings of the tracking system. For the translational part, we use the simple mean formula for averaging. For averaging the orientation, we use a method based on a tensor representation of the rotation in $\mathbb{R}^{16}$ [22]. Note that averaging orientations is always problematic, especially when the transformations between the single readings get large, because one needs to ensure that the result is a valid representation of an orientation again. Furthermore, there is no agreed set of conditions for the averaging formula. The method of [22] was found to yield stable and agreeable results, together with fulfilling some basic requirements such as rotation invariance. Figure 3.14 shows the orientation error of the moving marker for different values of n. We see that the error is reduced by a third when averaging just three values and by one half for $n = 7$, but that further reductions require far bigger averaging values n.

The disadvantage of averaging is of course the additional latency before a movement is followed. We are using a running average, implemented in the form of a ring buffer, so a movement of the head is detected by an n^{th} of its value with the tracking frequency f and compensated after time $\frac{n}{f}$. Based on the results from Figure 3.14, we use an running average size n of 3 to 10, depending on the quality of the tracking data in the TMS session, to reduce jitter in the measurements. This relatively small number also ensures that the influence of averaging on compensation time for head motion is small, see Section 6.1.2.

3.5. Safety

An inherent problem of all robot operations in the vicinity of humans is safety. For TMS this is especially crucial, since the distance between the robot controlled coil and the patient's head is required to be zero. A false move of the robot could hit the patient with the coil and harm him / her. We met the safety demands by introducing a number of security features. Firstly, all robots we use have an emergency stop switch, which immediately shuts down the robot power and applies the brakes. Secondly, the robot speed is reduced to 3% of its maximum speed, resulting in a maximum joint speed of 7.2°/s (Joints 1, 3), 6.3°/s (Joint 2), 11.25°/s (Joints 4,6), and 9°/s (Joint 5), respectively [81]. Thirdly, large movements like positioning the coil at a different point at the head are separated into several smaller moves. After each one a small pause reduces the position speed again. Fourthly, changes in robot joint angles can be limited, preventing large moves changing from one configuration space to another. Finally, we avoid fixing the patient's head, enabling the patient to move away from the robot if the coil is pressed too strongly against the head.

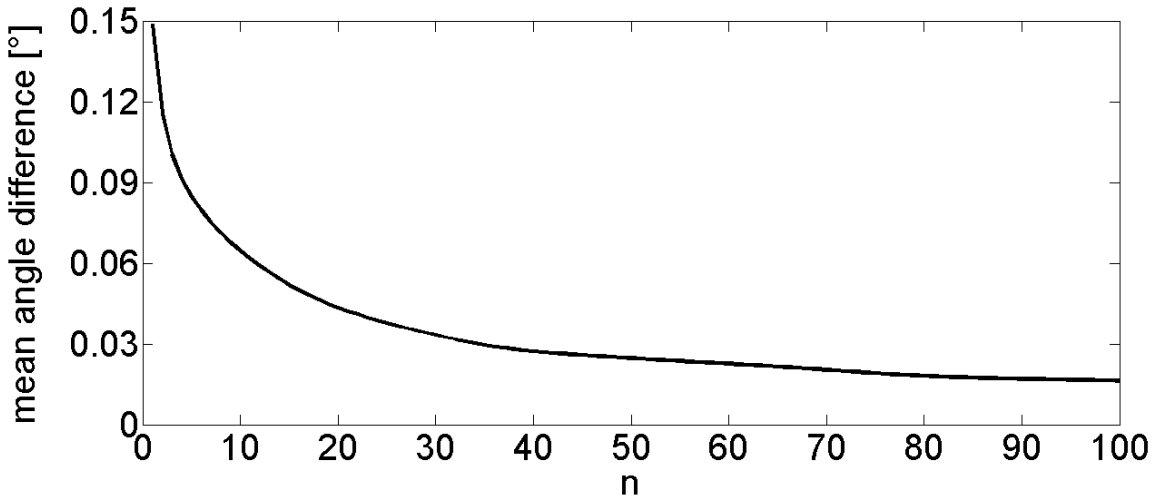

Figure 3.14.: Smoothing of the orientation part of the tracking data. Mean deviation of the head marker's normal vector from the overall average for different running average size n. Sample size: 50064, marker geometry: 3 passive reflective spheres. The marker was moved by the Adept robot in a pure translational fashion with an amplitude of 5 mm and a frequency of about 1 Hz.

As discussed in 3.4, the robot position is calculated using the registration of the real head to its virtual image. Hence we need to make sure that this registration is as exact as possible. To test this, we move a tracked pointer over the real head, keeping its tip in contact with the surface. Using ${}^{\mathrm{H}}T_{\mathrm{T}}$ and ${}^{\mathrm{I}}T_{\mathrm{H}}$, the tip coordinates are transformed into virtual coordinates and displayed as a sphere with radius 2 mm. If the registration is correct, the sphere should be half submerged into the virtual head outline, its centre lying directly on it. Furthermore, we point on landmarks on the real head, checking if the transformed tip lies on their counterparts on the virtual head. If one of the criteria is not met, registration and / or virtual surface reconstruction must be re-performed.

A similar procedure can be used to check the registrations ${}^{\mathrm{R}}T_{\mathrm{T}}$ and ${}^{\mathrm{E}}T_{\mathrm{C}}$. For all coils used, exact virtual representations are used in the software. We use the tracked pointer device and hold it on the surface of the robot attached coil. After transforming the pointer coordinates to the virtual space I, its visualisation must lie exactly on the surface of the virtual coil. We can also check the correct correspondence of coil centre and coil rim. If there is a noticeable discrepancy between real pointer position and virtual pointer position, registration of tracking system to robot and / or registration of coil to robot end-effector must be re-performed.

3.5.1. Force sensor

As a direct means to check the if the coil is touching the head, we use a force control unit [41]. This device is placed between the robot end-effector and the coil handle and replaces the conventional coil holder. The device is made of two plastic plates, connected by a spring, and contains three force sensors which are placed between the two plates. The force sensors

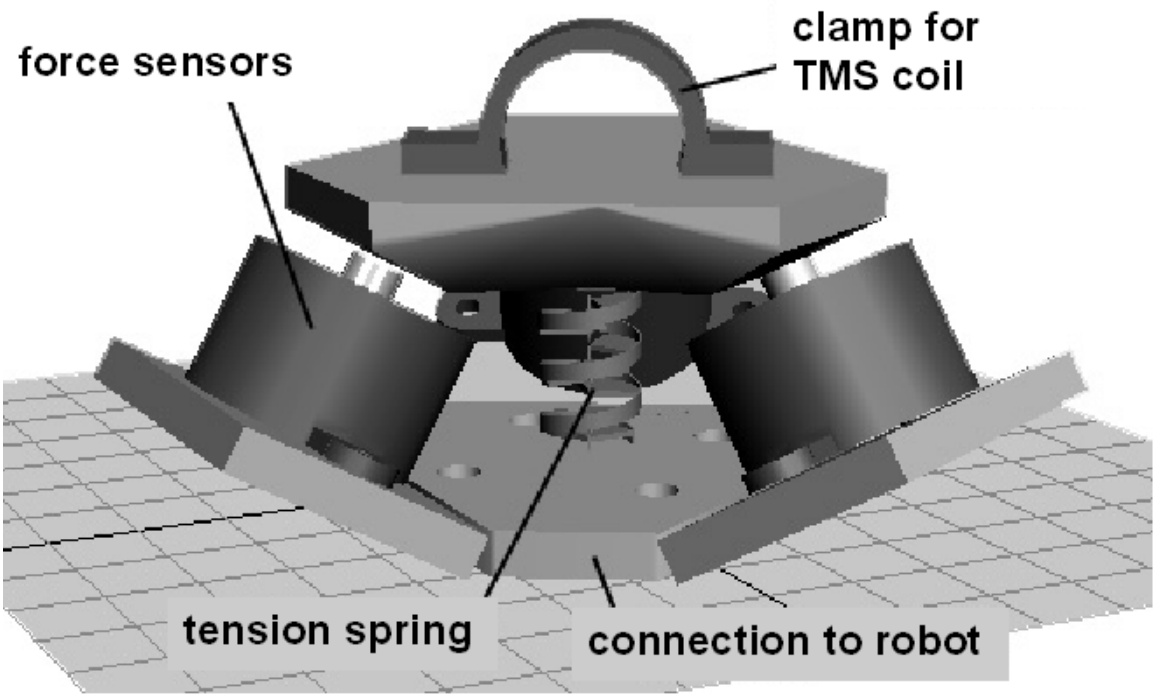

Figure 3.15.: Force sensor for detecting collisions of the coil. The underside of the unit is attached to the robot, the coil is clamped in the arc on the upper side. The spring between the plates ensures that positive and negative forces can be detected, i.e. forces in direction towards and away from each sensor.

are connected to the TMS control computer via a RS232 interface. The unit is attached to the robot with Plate 1, the coil is clamped at the outside of Plate 2, see Figure 3.15.

The spring which connects the two plates ensures that there is always a certain pressure on the force sensors. If the coil touches the head, it will create a momentum. This leads to a changed pattern of force at the sensors, e.g. more pressure on the sensors towards the coil's head, less pressure on the sensor on the far side of the device. The change in force is evaluated and the robot is controlled accordingly: If a strong force is measured, we must assume a collision and halt the robot immediately issuing an emergency stop. If a weak force is measured during the final approach to the head, we stop the robot's movement towards the head using the normal deceleration mode, move 1 mm backwards, and start motion compensation module from Section 3.4.4.2, which keeps the coil at its place relative to the head.

There is also momentum and force from the weight of the coil's head (especially for passively cooled coils, which weight up to 1.5 kg). The weight-related forces on the sensors change with the orientation of the coil, making it difficult to detect weak forces on the coil. Thus, we compare the forces during the approach to the head with the forces at the start of this linear movement. Then the weight-related forces will not change, because the orientation of the coil does not change.

3.5.2. Redundant robot control with tracking systems

We have explained already that the avoidance of a fixed head by introducing motion compensation has the advantage that even in the unlikely case of a robot collision the impact on the head will be minimal. This holds of course only if the robot speed is not too high. Therefore, one possibility to improve safety further is to introduce a control of the robot speed by the tracking system. In this section we discuss two algorithms to calculate the robot speed via a marker and present formulae for the maximum distance before the too high robot speed can be detected.

We will see that this distance depends on two parameters: The tracking frequency and the tracking accuracy. Unfortunately, for the tracking systems available no one enables to track enough robot parts, i.e. providing enough markers, while having a tracking frequency and tracking accuracy that the robot could be stopped within one centimetre. So to-date the following calculations have only academic value. But if there will be a tracking system which allows e.g. 10 markers to be tracked with a speed of 4000 Hz and an accuracy of 0.1 mm, a module controlling the robot speed via this tracking system should be included in our system for robot aided TMS.

3.5.2.1. Simple Algorithm

Before we begin some general calculations: Let s_j be the accuracy of the tracking system, i.e. the measured jitter for a static probe. Let f be the tracking frequency. Then the jitter speed ν_j, i.e. the erroneously measured speed of the probe is given by $\nu_j = f\|s_j\|$.

The distance the robot travels while the speed ν is measured is given by $d = \frac{\nu}{f}$, i.e. the distance the robot moves between two tracking measurements. Let ν_{max} be the maximum possible speed of the robot end-effector as determined by its specification.

Let ν_{crit} be the critical speed which must not be exceeded for safety reasons. If we request the jitter speed to be less than 10% of it to avoid false alarms, i.e. $\nu_j \leq 0.1\nu_{crit}$, and if the accuracy of the tracking system is given by s_j, the maximum allowed tracking frequency is given by $f = 0.1\frac{\nu_{crit}}{s_j}$.

If the robot changes its speed "instantaneously" to ν_{max}, it thus travels $d_{max} = 10s_j\frac{\nu_{max}}{\nu_{crit}}$ until the maximum speed can be detected.

Thus, given the maximal robot speed ν_{max}, a critical speed ν_{crit}, and a required stop distance of d_{max}, we get the formulae

$$s_j = \frac{d_{max}\nu_{crit}}{10\nu_{max}}, \tag{3.30}$$

$$f = \frac{\nu_{max}}{d_{max}}. \tag{3.31}$$

Example Let us assume we require the robot to stop within $d_{max} = 20\,\text{mm}$ and let the safe speed be restricted to $\nu_{crit} = 400\frac{mm}{s}$. If we are working with the Adept Viper s850, the maximum composite speed is about $\nu_{max} = 8000\frac{mm}{s}$. Thus the required accuracy is $s_j = 0.1\,\text{mm}$ for a tracking frequency of $f = 400\,\text{Hz}$.

Alternatively, given tracking frequency f, tracking accuracy s_j, and robot parameters ν_{max} and ν_{crit}, we have

$$d_{max} \geq \max\{\frac{\nu_{max}}{f}, \frac{10\nu_{max}s_j}{\nu_{crit}}\}. \tag{3.32}$$

The important observation is that no further improvement of d_{max} is possible by just increasing tracking frequency; the accuracy is just as critical.

Thus, even if a tracking system works with 4000 Hz, if the accuracy is 0.1 mm, we will not be able to stop the robot in less than 20 mm, given the robot specifications $\nu_{crit} = 400\frac{mm}{s}$, $\nu_{max} = 8\frac{m}{s}$. Further, the tracking frequency has to be reduced to 400 Hz to avoid false alarms of too high robot speed caused by the tracking jitter.

3.5.2.2. Moving average

The situation improves if we consider several measurements and average the successive velocity vectors. We assume a gaussian jitter for the tracking system with mean $\mu = 0$ and standard deviation σ. So the velocity calculated in measurement i is $v_i = f(p_i + x_i - p_{i-1} - x_{i-1})$, where p_i denotes the correct position of the probe at measurement i and $x_i \in \mathcal{N}(0, \sigma)$ denotes the jitter in measurement i. Note that the sum of two independent Gaussian random variables is Gaussian again with mean $\mu_1 + \mu_2$ and standard deviation $\sqrt{\sigma_1^2 + \sigma_2^2}$. Hence the velocity error is Gaussian with mean 0 and standard deviation $\sqrt{2}f\sigma$. If we average the velocity calculated from the last n measurements, i.e.

$$v_i^{av} = \frac{1}{n}\sum_{k=0}^{n-1} v_{i-k} = \frac{f}{n}(p_n + x_n - p_0 - x_0), \tag{3.33}$$

the distribution of the error of v_i^{av} is $\mathcal{N}(0, \sigma\frac{\sqrt{2}f}{n})$. Thus, the error vector length when averaging over n velocity vectors decreases linearly with n. The number n of velocities we need to average to reach an accuracy of $\frac{\nu_{crit}}{10}$ with more than 99% probability is hence $n = 3\sqrt{2}f\sigma\frac{10}{\nu_{crit}}$.

Again, we ask how far the robot can maximally travel before we detect it. For every reading of the tracking system we average the last n velocities and compare the norm of the result to ν_{crit}. Assume that $\|v_{i<0}\| \leq \nu_{crit}$, $\|v_0\| > \nu_{crit}$, $\|v_{t<T}^{av}\| = \|\frac{1}{n}\sum_{k=0}^{n-1} v_{t-k}\| \leq \nu_{crit}$, and $\|v_T^{av}\| > \nu_{crit}$, $T \in \{0, \ldots, n-1\}$, i.e. at time $t = 0$ we first exceed the critical speed and at time $t = T$ we notice it. Then the distance the robot moves after first exceeding ν_{crit} is

$$\begin{aligned} d_{max} &= \frac{1}{f}\|\sum_{k=0}^{T} v_{T-k}\| \leq \frac{1}{f}\|(\sum_{k=1}^{n-1} v_{T-k}) + v_{T-n} - v_{T-n} + v_T\| \leq \frac{1}{f}(n\nu_{crit} + 2\nu_{max}) \\ &\leq \frac{\frac{30\sqrt{2}f\sigma}{\nu_{crit}}\nu_{crit}}{f} + \frac{2\nu_{max}}{f} < 30\sqrt{2}\sigma + \frac{2\nu_{max}}{f}. \end{aligned} \tag{3.34}$$

Note that for $n = 1$ the stronger estimate $d_{max} \leq \frac{\nu_{max}}{f}$ holds trivially.

As for the simple algorithm, increase in frequency does not necessarily lead to a better performance in terms of d_{max} as this limits only the second summand in (3.34). Again, improvements in accuracy are as important for lowering d_{max} as higher tracking frequencies.

Example Let us assume again $\nu_{crit} = 400\frac{\text{mm}}{\text{s}}$, $\nu_{max} = 8\frac{\text{m}}{\text{s}}$. Then Equation (3.34) yields for the following tracking systems

1. accuTrack (Atracsys) , one LED: $f = 4000\,\text{Hz}$, $\sigma = 0.1\,\text{mm}$. Then n = 43 and $d_{max} < 5\,\text{mm} + 4\,\text{mm} = 9\,\text{mm}$.
2. accuTrack (Atracsys) , four LEDs: $f = 1000\,\text{Hz}$, $\sigma = 0.1\,\text{mm}$. Then n = 11 and $d_{max} < 5\,\text{mm} + 16\,\text{mm} = 21\,\text{mm}$.
3. Polaris (NDI), one marker: $f = 60\,\text{Hz}$, $\sigma = 0.20\,\text{mm}$. Then n = 1 and $d_{max} < 133\,\text{mm}$.

In general, if we require a stop within a distance d, σ depends linearly on d and f inverse linearly, resulting in $n = 2\frac{\nu_{max}}{\nu_{crit}}$. Conversely, the optimal trade-off between tracking frequency and tracking accuracy depends on the maximum speed of the robot:

$$\sigma f = \frac{\nu_{max}}{15\sqrt{2}}. \tag{3.35}$$

4. Motor cortex mapping with TMS[1]

The aim in motor cortex mapping with TMS is to deduce the region in the brain where a muscle is represented from a number of stimulations at different sites around the head, the obtained muscle responses, and the electromagnetic characteristics of the coil. In this chapter, we derive a new algorithm for calculating the cortical representation of a muscle. The algorithm uses the calculated electric field strength at a point on the brain surface and the motor response from several stimulations to infer a likelihood for the cortical representation to be at this point, see Section 4.2.

We present a number of statistics to compute this likelihood, Section 4.3, and explain how to obtain the electric field produced by various TMS coils, Section 4.4. The final part of the chapter gives experimental results and answers the question which statistic is best for our purpose, Section 4.5.

4.1. State-of-the-art

So far, motor cortex mapping with TMS is only possible for a prominent subclass of coils, namely figure-of-eight shaped coils. For those coils, several flavours of the Centre of Gravity (CoG) method (see Section 4.3.5) exist to predict from a number of stimulations with known coil position and known muscle response the cortical representation of this muscle [11, 20, 26, 38, 54, 77, 92, 119, 144, 167, 174, 185]. All methods have in common that they imply the strongest stimulation to be directly under the centre of the coil.

For figure-of-eight shaped coils this is indeed the case, but for also widely used circular coils this is far from true. Here, the maximum stimulation is not localised directly under the coil centre, but rather has the form of a torus underneath the coil rim [123]. Some new coil designs like the H-coil [148] also have no unique focus point, so the established TMS motor cortex mapping methods fail in these cases, because they do not directly consider the electric field produced by the coil.

The accuracy of the CoG map has been found to be about 1 cm: Wassermann et al. reported the CoG to agree within 5 to 22 mm with the localisation from PET in four healthy subjects [185]. Classen et al. found a mean difference between PET and CoG of 4.7 mm in Talairach coordinates (a normalised coordinate system for the brain) for 14 subjects [26]. Lotze et al. compared the CoG with localisation from fMRI and saw a mean difference of 13.9 mm in five subjects [92]. Terao et al. found an agreement of projected CoG and fMRI of 2 to 4 mm over five subjects [174]. Herwig et al. reported a mean deviation of 10 mm between CoG

[1] Parts of this chapter have been published in [42, 100].

and fMRI maximum [54]. Finally, Krings et al. found the CoG projection to the cortex to agree within 1 cm with the mapping results from direct electrical stimulation during brain surgery for two subjects [77].

The only alternative to the CoG methods presented to-date comes from Thielscher and Kammer [175]. Their method includes the calculation of the electric field of the figure-of-eight coil and could thus in principle be extended to other coil geometries. In detail, they moved a figure-of-eight coil in steps of 1 cm along a line perpendicular to the central sulcus and stimulated at each position i with stimulator output ranging from 20% to 100%. For each stimulation point, this yielded a data set of stimulator output versus MEP. A sigmoidal curve was fitted to the data and the stimulator strength x at which a half-maximal MEP would be elicited was interpolated. For each coil position i the electric field distribution over the cortex for a stimulation with strength x_i was then calculated using a magnetic dipole model of the coil and a spherical head model. Finally, the authors calculated the variance of the electric field strength values for every point on the cortex and claimed that the cortical representation is to be found at the point of minimal variance. This seems reasonable if one assumes that the same electric field strength at the cortical representation point leads to the same MEP and that different electric field strengths lead to different MEPs.

The authors did not validate their method against alternative functional imaging, but claimed that for all four subjects of the study the cortical representation of the right APB muscle (a thumb muscle) was identified at the lateral part of the hand knob. The images presented in the publication further show a narrow stripe of low variance values perpendicular to the stimulation line, so that some ambiguity in localisation along this direction can be assumed.

Apart from the unclear validation state for the method, the biggest disadvantage is the time consuming and rather unconventional protocol. The authors used between 9 and 13 stimulation points with four stimulations at each stimulator output level and a minimum of 5 seconds interstimulus interval, so a mapping time of 1 hour must be expected. Further, the method has only been tested for one stimulation line, so it is unclear whether the results of the mapping along two different lines agree and whether an extension to a grid-like pattern reduces the localisation ambiguity along the direction perpendicular to the stimulation line.

4.2. Motor cortex mapping - the general principle

Although the underlying biophysical processes leading to a macroscopic response to TMS are still not completely clarified, it seems to be established that the effects of the stimulation on the central nervous system are related to the strength of the electric field delivered to the representation site by the pulse [44, 123, 175]. The exact muscle response Y to a stimulation depends on the placement of the coil with respect to the head, the electromagnetic characteristics of the coil, which are governed mainly by its shape, and the stimulator output.

As motivated in Section 2.2.1, we assume the relation between electric field strength $E(\mathbf{p}^\mathbf{r})$ at the muscle representation point $\mathbf{p}^\mathbf{r}$ on the cortex and the measured evoked muscle response

Y to be a monotonous function, i.e. $Y = f(E(\mathbf{p^r}))$. Note that f will not be linear and may have a discontinuity at the motor threshold.

For our mapping, we consider each point $\mathbf{p}$ on the brain surface separately. We calculate the electric field strengths e_i at $\mathbf{p}$ when firing the TMS coil at the stimulation sites $i = 1, \ldots, n$. This is done with the help of the coil field map obtained as described in 4.4 and yields a list $\{e_1(\mathbf{p}), \ldots, e_n(\mathbf{p})\}$. This list is different for each point $\mathbf{p}$, because the electric field produced by the coil is highly inhomogeneous, see Figure 4.3.

Let $\{y_1, \ldots, y_n\}$ be the list of measured motor responses, obtained as explained in Section 4.5.1.3. Note that this list is independent of $\mathbf{p}$. We now seek a statistic $S : \mathbb{R}^{2n} \to \mathbb{R}$, i.e. a map $((e_1(\mathbf{p}), y_1), \ldots, (e_n(\mathbf{p}), y_n)) \mapsto S((e_1(\mathbf{p}), y_1), \ldots, (e_n(\mathbf{p}), y_n))$, with the property

$$S((e_1(\mathbf{p^r}), y_1), \ldots, (e_n(\mathbf{p^r}), y_n)) > S((e_1(\mathbf{p}), y_1), \ldots, (e_n(\mathbf{p}), y_n)), \qquad \forall \mathbf{p} \neq \mathbf{p^r}. \tag{4.1}$$

That means that we require the statistical value at the representation point $\mathbf{p^r}$ to be bigger than at all other points on the cortex.

For the final map we repeat the S-calculation for every point on the brain surface. We evaluate $S(\mathbf{p}) := S((e_1(\mathbf{p}), y_1), \ldots, (e_n(\mathbf{p}), y_n))$ for each point $\mathbf{p}$ separately and colour the point by its $S(\mathbf{p})$ value. The point with the highest S-value is then the most probable point for the representation of the muscle mapped.

Unfortunately, the true electric field strength at points in the brain is unknown, because the scalp, skull, cerebrospinal fluid, and brain weaken and distort the electric field produced by the coil. There have been many attempts to simulate those effects [94, 175]. But so far, most models used only crude approximations of the true individual head and brain geometry (mainly using spherical head models). Furthermore, electromagnetic properties of the head tissues are not well established and have been shown to possess great inter-individual differences [117]. As described, we require the knowledge of the electric field at all points at the brain surface for all stimulation points, creating a big computational task if modelling was used.

Instead, we ignored the influence of the head on the electric field and used the measured electric field of the coils in air, from hereon denoted by X. Hence we replace the term $S((e_1(\mathbf{p}), y_1), \ldots, (e_n(\mathbf{p}), y_n))$ by $S((x_1(\mathbf{p}), y_1), \ldots, (x_n(\mathbf{p}), y_n))$ in the discussion above. We will see from the results in Section 4.5.3 that our approach is able to handle the inaccuracy induced by this approximation.

A justification for our model is given in Figure 4.1. The red curve displays the (approximated) electric field strength at the representation point $X(\mathbf{p^r})$ versus the motor response Y, i.e. the pairs $((x_1(\mathbf{p^r}), y_1), \ldots, (x_n(\mathbf{p^r}), y_n))$. The green and blue curves give an example how this relation changes if we do not consider the representation point $\mathbf{p^r}$, but a point $\mathbf{p^1}$ in 7 millimetres distance (green curve) and a point $\mathbf{p^2}$ in 14 millimetres distance (blue curve), respectively. We see that at the hotspot $\mathbf{p^r}$ the graph electric field versus muscle response is only slightly oscillating, showing nearly a monotonic increase of the muscle response with the electric field strength at that brain surface point.

The map in Figure 4.1 is calculated using the rank coefficient τ statistic, see Section 4.3.1. There is a clear distinction between the curves for high, intermediate, and low mapping

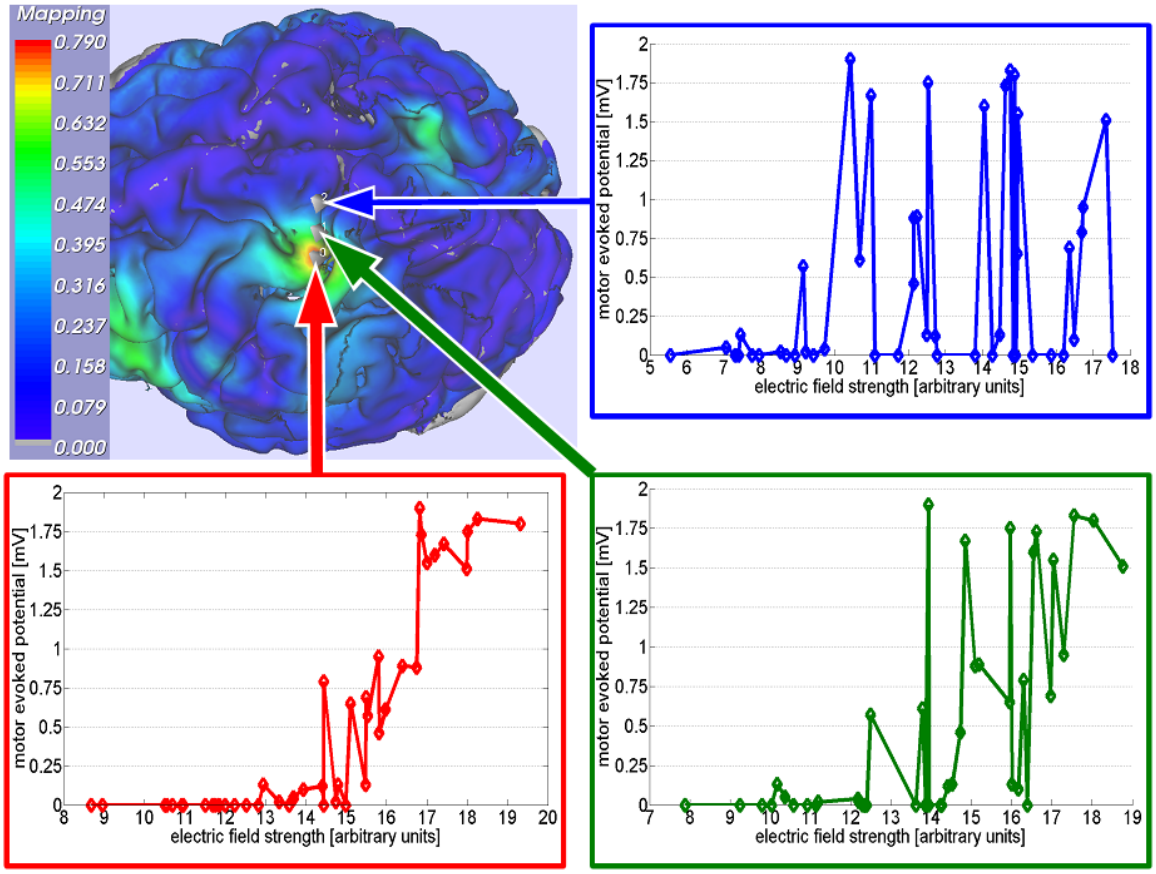

Figure 4.1.: Calculated electric field strength $X(\mathbf{p})$ (arbitrary units) and elicited MEP responses Y (peak to peak, in mV*) at the APB muscle for three different points on the brain surface. The points are chosen such that $\mathbf{p_0}$ is at the mapping maximum point (red), $\mathbf{p_1}$ has intermediate mapping value (green), and $\mathbf{p_2}$ has low mapping value (blue). Note that the Y-values are the same in all three graphs, only the respective X-values differ. The brain colour in the upper left picture is according to the rank coefficient τ value, see Sections 4.3 and 4.5.2. Stimulation was performed with a bend figure-of-eight coil at 46 stimulation sites with a fixed stimulator output, see Experiment 3.*

values. The lower the mapping value, the more oscillating the curve becomes, showing less monotonic and less functional dependence of the motor response values Y on the electric field values $E(\mathbf{p})$. Stimulation was performed with a figure-of-eight coil and the abductor pollicis brevis muscle (thumb muscle) responses were measured for 46 stimulation sites.

4.3. Mapping Functions

In this section we describe a number of statistics which are good candidates to fulfill Equation (4.1). As we assume the correspondence between the electric field strength at the representation point and the motor responses to be a monotonous function, the statistics we consider here yield high values for such data. Each statistic focuses on another aspect of the functional monotonic dependence, e.g. the monotonicity or a functional dependence.

4.3.1. Kendall's rank coefficient τ

Kendall's rank coefficient τ measures the degree of correspondence between two rankings. In other words, it gives a measure of monotonicity of the relation between two variables. If $\{(x_1, y_1), \ldots, (x_N, y_N)\}$ are n realisations of (X, Y), we define

$$C_{ij} = \begin{cases} 1 & \text{if } (x_i - x_j) \cdot (y_i - y_j) > 0 \\ 0 & \text{else} \end{cases}, \qquad D_{ij} = \begin{cases} 1 & \text{if } (x_i - x_j) \cdot (y_i - y_j) < 0 \\ 0 & \text{else} \end{cases}. \tag{4.2}$$

Hence, $C := \sum_{i<j} C_{ij}$ is the number of concordant pairs, $D := \sum_{i<j} D_{ij}$ is the number of discordant pairs and the rank coefficient

$$\tau(X, Y) := \frac{C - D}{\frac{1}{2}n(n-1)} \tag{4.3}$$

is a normalised measure of monotony of the relation of X and Y. If the relation is monotonously increasing, $\tau = 1$, if the relation is monotonously decreasing, $\tau = -1$. We note that τ is a symmetric measure, i.e. $\tau(X, Y) = \tau(Y, X)$.

A particularity requiring special attention is the case of equal sample values $x_i = x_j$ or $y_i = y_j$, because they lead to neither concordant nor discordant pairs, but are counted in the denominator. We chose to handle this using Kendall's τ b - formula, i.e. we replaced $\frac{1}{2}n(n-1)$ by $\sqrt{C + D + n_y}\sqrt{C + D + n_x}$ with n_y denoting the number of pairs with $i < j$, $x_i \neq x_j$, $y_i = y_j$ and n_x denoting the number of pairs with $i < j$, $x_i = x_j$, $y_i \neq y_j$. For the implementation we used the algorithm suggested in [130].

4.3.2. Correlation Coefficient

Pearson's Correlation Coefficient ρ measures the degree of linear correspondence between two random variables X, Y. It is defined as

$$\rho(X, Y) = \frac{cov(X, Y)}{\sqrt{Var(X)}\sqrt{Var(Y)}}. \tag{4.4}$$

So, if $Y = aX + b$ for $a, b \in \mathbb{R}$, $\rho(X, Y) = \text{sign}(a)$. Clearly, the Correlation Coefficient is a symmetric measure, i.e. $\rho(X, Y) = \rho(Y, X)$. Further, it holds $-1 \leq \rho(X, Y) \leq 1$. Finally, if $\rho(X, Y) = \pm 1$ then $\tau(X, Y) = \pm 1$.

4.3.3. Normalised Mutual Information

Mutual Information is a very general measure of a relation between two variables. It is defined as

$$I(X, Y) = H(X) + H(Y) - H(X, Y), \tag{4.5}$$

where $H(X)$ and $H(Y)$ denote the entropy of X and Y, respectively, and $H(X,Y)$ denotes the joint entropy of (X,Y). It holds $0 \leq I(X,Y) \leq \min(H(x), H(Y))$, so if we normalise $I(X,Y)$ as

$$\tilde{I}(X,Y) := \frac{I(X,Y)}{\min(H(x), H(Y))}, \tag{4.6}$$

we ensure $0 \leq \tilde{I}(X,Y) \leq 1$ [66, 75]. Hereby, we define $\frac{0}{0} := 0$, so that zero mutual information always corresponds to zero normalised mutual information.

For discrete variables $X \in \{X_1, \ldots, X_n\}$, $Y \in \{Y_1, \ldots, Y_m\}$, H is defined as

$$H(X) = -\sum_{i=1}^{n} p(X = X_i) \log(p(X = X_i)), \tag{4.7}$$

$$H(X,Y) = -\sum_{i=1}^{n}\sum_{j=1}^{m} p(X = X_i, Y = Y_j) \log(p(X = X_i, Y = Y_j)), \tag{4.8}$$

where $p(\omega)$ denotes the probability of an event ω. Given a sample $x_1, \ldots, x_n$, we use the sample probability $p(X = X_i) := \frac{\#\{x_k | x_k = X_i\}}{n}$.

If, as in our case, X and Y are continuous, we define intervals $[X_i, X_{i+1})$, $[Y_j, Y_{j+1})$ and replace $X = X_i$ by $X \in [X_i, X_{i+1})$ and $Y = Y_j$ by $Y \in [Y_j, Y_{j+1})$ in Equations (4.7) and (4.8).[2] Note that the result depends on the intervals defined.

Some important properties of $\tilde{I}$ include:

- $\tilde{I}$ is a symmetric measure, i.e. $\tilde{I}(X,Y) = \tilde{I}(Y,X)$.
- $\tilde{I}(X,Y) = 0$ if X and Y are independent.
- $\tilde{I}(X,Y) = 1$ if and only if there is a functional dependence between X and Y, [66].
- If the relation between X and Y is approximately monotonic, then $\tilde{I}(X,Y)$ and $\tau(X,Y)$ are of the same magnitude, otherwise $\tilde{I}(X,Y)$ is larger than $\tau(X,Y)$, [66].

4.3.4. Correlation Ratio

Correlation Ratio, historically denoted as η, can be used to measure the functional dependence of two random variables $X, Y : \Omega \to \mathbb{R}$. It was introduced by K. Pearson in 1905 [125]. Its main application lies in ordinal statistics, but it has also been applied recently in multimodal image registration as a measure of correspondence [140]. The Correlation Ratio of Y given X is defined as

$$\eta(Y|X) := \frac{Var[E(Y|X)]}{Var[Y]}, \tag{4.9}$$

where $E(Y|X)$ denotes the conditional expectation of Y given X. Note that η is an asymmetric measure, i.e. in general $\eta(Y|X) \neq \eta(X|Y)$.

[2] This method to make discrete formulae applicable for continuous entities is called binning.

It is easy to show that $E(Y|X)$ is the best functional approximation of Y in L^2, the vector space of square integrable random variables [120]. Thus, Correlation Ratio relates the total variance of Y to the Variance of the part of Y which is explained by X. See [140] for a geometric derivation of $\eta(Y|X)$ in L^2.

By the total variance theorem [156]

$$Var[Y] = Var[E(Y|X)] + E(Var[Y|X]), \tag{4.10}$$

where $Var[Y|X]$ denotes the conditional variance of Y given X. Hence

$$1 - \eta(Y|X) = \frac{E(Var[Y|X])}{Var[Y]} \tag{4.11}$$

measures the part of Y unexplained by X.

Note that if the joint density $p(x, y)$ of (X, Y) exists, $E(Y|X)$ and $Var[Y|X]$ are given by

$$E(Y|X = x) = \int yp(y|x)dy = \int y\frac{p(x,y)}{p(x)}dy = \frac{1}{p(x)}\int yp(x,y)dy, \tag{4.12}$$

$$Var[Y|X = x] = \int (y - E(Y|X = x))^2 p(y|x)dy. \tag{4.13}$$

Some simple consequences follow directly from the definition of η:

- It holds $\eta(Y|X) \in [0, 1]$, since $0 \leq Var[E(Y|X)]$ and $0 \leq E(Var[Y|X])$.
- If $Y = \phi(X)$ for a measurable function ϕ then $E(Y|X) = \phi(X) = Y$ and hence $\eta(Y|X) = 1$.
- If X and Y are independent then $p(x, y) = p(x)p(y)$ and $E(Y|X) \equiv E(Y)$. Hence $Var[E(Y|X)] = 0$ and $\eta(Y|X) = 0$.

Correlation Ratio is related to the Correlation Coefficient as follows: $\eta(Y|X)$ measures the *functional dependence* of Y on X, whereas $\rho(X, Y)$ measures only the *linear dependence* of X and Y. Since functional dependence includes linear dependence, $\eta(Y|X) \geq |\rho(X, Y)|$ and if $\rho(X, Y) = \pm 1$ then $\eta(Y|X) = 1$. Further, any monotonic relation implies a functional relation, thus if $\tau(X, Y) = \pm 1$ then $\eta(Y|X) = 1$.

The estimation of η from only a few (20 to 40) samples with continuous range is difficult, because binning does not yield stable results. Thus, we devised a new algorithm to estimate η. In short, we approximate the joint density of (X, Y) by Parzen Windowing with a product kernel. This leads to a version of Equation (4.13) that can be solved analytically, resulting in the formula

$$1 - \eta(Y|X) = \frac{\sum_{j=1}^{N} y_j^2 - \sum_{i=1}^{N} \left(\frac{\sum_{j=1}^{N} y_j g_j(x_i)}{\sum_{j=1}^{N} g_j(x_i)} \right)^2}{\sum_{j=1}^{N} y_j^2 - \frac{1}{N} \left(\sum_{j=1}^{N} y_j \right)^2}. \tag{4.14}$$

Here, $g_j(x)$ is a windowing function centred at x_j, i.e. a positive function in L^1 with $\int_{\mathbb{R}} g(x)dx = 1$ and $\int_{\mathbb{R}} g(x)xdx = x_j$. A detailed derivation of Formula (4.14) can be found in Appendix A.

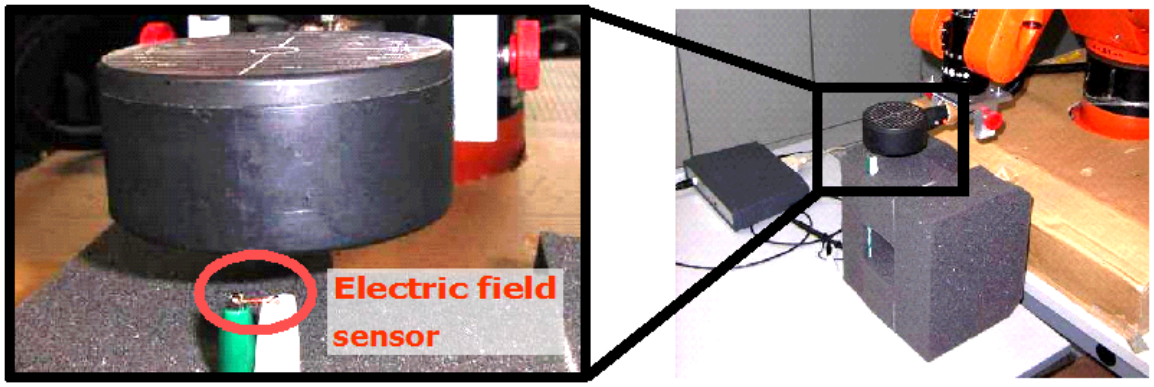

Figure 4.2.: Measurement setup for obtaining the electric field produced by the MCF-75 circular coil. The E-field is purely horizontal, thus inducing only a voltage in the horizontal wire probe.

4.3.5. Centre of Gravity (CoG)

The projection of the centre of gravity of the measurements onto the cortex has been shown to give reasonable mapping results for figure-of-eight coils, see Section 4.1. Conventionally, the coil coordinates are weighted by the MEP response provoked when stimulating at this site and averaged. The resulting spot, which in general lies neither on the scalp nor on the cortex, is then projected onto the cortex. Hereby, several projection methods exist, [119].

The standard formula for the Centre of Gravity reads

$$\mathbf{p}_{CoG}^{\text{variable MEP}} := \frac{\sum_{i=1}^{n} y_i \mathbf{p}_i}{\sum_{i=1}^{n} y_i}, \tag{4.15}$$

where $\mathbf{p}_i$ is the coil centre point for the i^{th} stimulation and y_i is the corresponding MEP amplitude.

To unify this concept with our form of mapping, we need to define a mapping value for each point $\mathbf{p}$ on the cortex. In our implementation, it is given as the normalised distance to $\mathbf{p}_{CoG}$. The normalisation is linear and such that the nearest cortex point has value 0, the farthest has value 1. This gives similar results as the convex hull algorithm suggested by [119].

4.4. Coil Data

Several different coil forms are in use for TMS. Most common are figure-of-eight coils, shaped like a double torus, and circular coils. Each coil stimulates the brain differently, because the electromagnetic field produced differs for each coil type. So to analyse the stimulation data, the characteristics of the coil must be known. Therefore we measured or simulated the electric field produced by the coil in a separate experiment.

4.4.1. Measuring the coil's electric field

In the absence of free charges and for low frequencies[3], the electric field $\mathbf{E}$ produced by changing currents $I = I(t)$ in the coil with geometry c is given by

$$\mathbf{E}(r,t) = -\frac{\mu_0 \dot{I}(t)}{4\pi} \int_c \frac{\mathrm{d}\dot{\mathbf{c}}}{|\mathbf{r}-\mathbf{c}|}, \tag{4.16}$$

see [94, 111] and Equations (2.15), (2.18). Hereby, μ_0 denotes the permeability of free space, $\dot{I}$ the change of the current flow in the coil, and $\dot{\mathbf{c}}$ the tangential vector along the coil curve c. As a direct consequence of (4.16), the electric field of a planar coil, i.e. $\mathbf{c}_z \equiv 0$, has no vertical component. So by placing a small straight copper wire with geometry w horizontally beneath the coil and connect it via vertical running cables to an oscilloscope [36, 150], Figure 4.2, the measured voltage at time t equals

$$V = \oint \mathbf{E} \cdot \mathrm{d}\dot{\mathbf{S}} = \int_w \mathbf{E}(\mathbf{w}) \cdot \mathrm{d}\dot{\mathbf{w}} \approx |w| \mathbf{E}(\mathbf{w},t) \cos\phi, \tag{4.17}$$

where ϕ denotes the angle between wire direction and E-field direction. In (4.17) we assumed the wire length $|w|$ to be small, so that $\mathbf{E}$ is constant along it.

By (4.16), the electric field of a circular coil is rotationally symmetric and for $\mathbf{w}_y = 0$ holds $\mathbf{E}_x = 0$. So it is enough to measure the E-field in the $x-z$-plane having the straight wire segment aligned with the y-axis, $\dot{\mathbf{w}}_x = \dot{\mathbf{w}}_z = 0$.

For the figure-of-eight coil, we measured $\mathbf{E}_x$ and $\mathbf{E}_y$ in two separate experiments with different probe orientation and combined the measures using Pythagoras' Theorem.

To obtain the full electromagnetic characteristics, we placed the coil at regularly spaced grid positions and invoked a stimulation pulse with 70% stimulator output. By measuring the induced voltage in the sensor (4.17) at each position, we obtained a grid of electric field strengths for the coil [155], Figure 4.3. The measurement series were completely automated, using a Kuka KR3 robot (Kuka GmbH, Augsburg, Germany) and a PCS100 8 bit digital oscilloscope (Velleman Components N.V., Gavere, Belgium) with a sampling frequency of 800 kHz.

4.4.2. Simulating the coil's electric field

As an alternative to measuring the electric field produced by a TMS coil, we describe in this section a method to simulate it. In Sections 2.2.2 and 4.4.1 we have already given the fundamental equations governing the electric field distribution for a TMS coil. In case of simple coil geometries, e.g. circles, and simple coil surroundings, e.g. air, these equations can be solved analytically. But even the so-called circular coils have a non-trivial winding geometry, namely in form of a spiral. So Equation (4.16) has to be solved numerically.

[3] A TMS pulse lasts about 100 µs, yielding a frequency of 10 kHz. This is considered low, because the corresponding wavelength of $3 \cdot 10^4$ m is several orders of magnitude bigger than the head and the electric field sensor. For more about the quasi-static approximation see Section 2.2.2.1.

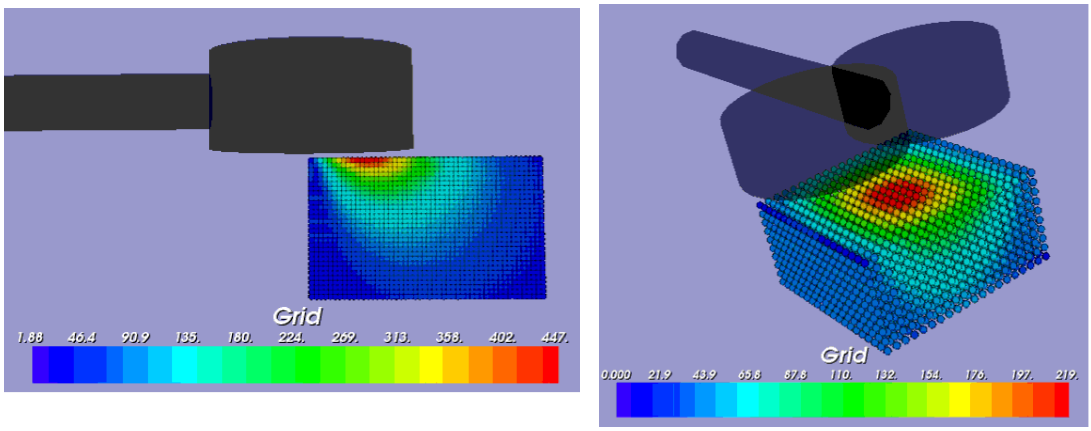

Figure 4.3.: Electric field produced by the Medtronic MCF-75 circular coil (left) and the MagStim figure-of-eight coil (right). The field of the circular coil is rotationally symmetric, therefore only one radial slice is shown. The measures are given in mV induced in the sensor. The grid comprises of 20 x 50 points, spaced at 2 mm, for the circular coil, and 20 x 20 x 10 points, spaced at 0.5 mm, for the figure-of-eight coil. Note that for technical reasons the E-field map of the circular coil starts closer to the coil, hence the stronger maximum reading compared to the figure-of-eight coil.

We implemented a solution to Equation (4.16) in MATLAB (The MathWorks, Inc, Natick, MA, USA), using recursive adaptive Simpson quadrature to evaluate the integral. As a test, we simulated the electric field in air of a Medtronic MCF-75 circular coil and the conventional MagStim figure-of-eight coil.

4.4.2.1. Circular coil MCF-75

The parameters for the simulation, i.e. the coil's wire winding curve, were taken from the data sheets of the manufacturer: Medtronic specifies three times seven windings with inner diameter of 5 mm, outer diameter of 32.5 mm and winding height of 12 mm. In our implementation we modelled this as three layers of seven concentric circles with equally spaced radial distance between the circles and layers at $z = 0\,\text{mm}$, $z = -6\,\text{mm}$, and $z = -12\,\text{mm}$.

Figure 4.4 shows a comparison between the measured and the simulated field. Note that the surface plot depicts the electric field strength in the x-z-plane, i.e. along a radial slice of the coil. The two line plots depict the decay of the electric field along the lines $0\,\text{mm} \leq x \leq 98\,\text{mm}$, $y = 0\,\text{mm}$, $z = 5\,\text{mm}$ and $x = 24\,\text{mm}$, $y = 0\,\text{mm}$, $5\,\text{mm} \leq z \leq 63\,\text{mm}$. The first line runs parallel to the coil's surface and is placed 5 mm away from it, which is the smallest distance we mapped with the robotised procedure from Section 4.4.1. The second line runs perpendicular to the coil's surface and starts at the radial distance $x = 24\,\text{mm}$; exactly where the electric field attains its maximum value along the first line.

The comparison shows that

- the simulated and the measured field attain their maximum at the same radial distance $x = 24\,\text{mm}$,

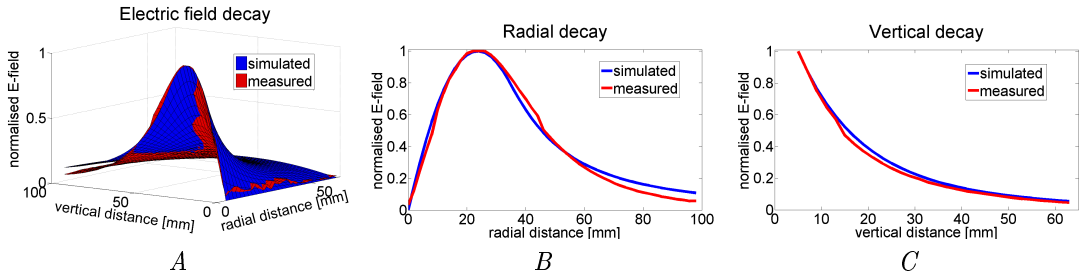

Figure 4.4.: Comparison of the measured electric field strength (red) and the simulated electric field strength (blue) of the Medtronic MCF-75 circular coil. The electric field strength is normalised for each plot. Figure A shows the electric field strength on the radial slice $y = 0$, $0\,\text{mm} \leq x \leq 98\,\text{mm}$, $5\,\text{mm} \leq z \leq 63\,\text{mm}$. Figure B shows the fields along the radial line $y = 0$, $z = 5\,\text{mm}$. Figure C shows the fields along the vertical line $x = 24\,\text{mm}$, $y = 0$.

- the increase in field strength along the radial line up to the maximum at $x = 24\,\text{mm}$ is about the same for the simulated and the measured field,
- the simulated field has a stronger decay along the radial line than the measured field from the maximum point $x = 24\,\text{mm}$ up to about $x = 45\,\text{mm}$,
- after $x = 45\,\text{mm}$ the decay of the measured field is stronger than the decay of the simulated field, leading to a higher value of the simulated field from $x = 60\,\text{mm}$ onwards,
- the vertical decay along the line $x = 24\,\text{mm}$ is very similar for the simulated and the measured field.

The good agreement between measured and simulated data supports both, the correctness of the simulation and the accuracy of the measurements. The slight discrepancies in horizontal decay are thought to stem from inaccuracy in calibrating the coil and electric field sensor to the robot, implying that a radial movement of the coil by the robot is not truly parallel to the coil's winding plane.

4.4.2.2. Planar figure-of-eight coils

We also simulated the field of the fluid cooled figure-of-eight coil MCF-B65 from Medtronic and the standard 70 mm figure-of-eight coil from MagStim. Note that this time the field is not rotationally symmetric any more, so we need a full 3D grid to record the electromagnetic properties of the coil.

The MCF-B65 coil was simulated with 2 times 10 concentric circles, one set of 10 for the left wing and one set for the right wing. The smallest circle had a radius of 17.5 mm, the biggest one had a radius of 37.5 mm. The centres of the sets of concentric circles were 65 mm apart.

Figure 4.5.A shows the absolute electric field strength for the MCF-B65 coil in a plane parallel to the windings and 5 mm away. We see that the effects of the two adjacent circular windings add at the coil's centre, producing a field approximately twice as strong as below the single circular windings.

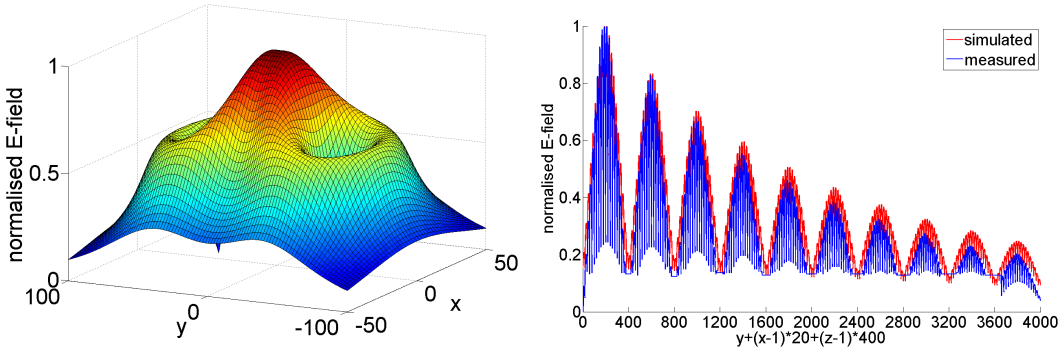

Figure 4.5.: Electric fields of several planar figure-of-eight coils. A: Simulated absolute electric field strength of the Medtronic MCF-B65 coil. B: Comparison of the x-component of the measured electric field strength (blue) and the simulated electric field strength (red) of the standard 70 mm MagStim figure-of-eight coil. The electric field strength is normalised for each plot. The field is evaluated at the vertices of a regular 5 mm spaced grid of size 20 × 20 × 10. The grid points are enumerated in order y-x-z and displayed on the ordinate. For example, the value at $t = 972 = 12 + (9-1) * 20 + (3-1) * 400$ is the normalised electric field strength at grid point $(9, 12, 3)$, which has coil coordinates (-2.5,7.5,45). The next point, $t = 973$, is just right of it, having coil coordinates (-2.5,12.5,45).

The standard 70 mm figure-of-eight coil from MagStim was simulated with 2 times 9 concentric circles. The smallest circle had a radius of 26 mm, the biggest one had a radius of 44 mm. The centres of the sets of concentric circles were 90 mm apart.

Figure 4.5.B shows a comparison between the measured and the simulated electric field strength along the x-axis for the MagStim coil. As the effective area for stimulation for figure-of-eight coils does not extend to the wings[4], we restricted the measurements to a volume below the centre. We measured and simulated the electric field strength at the vertices of a 20 × 20 × 10 grid with vertex distance of 5 mm. The origin of the grid was at position $(-47.5, -47.5, 30)$ in coil coordinates, i.e. the grid was placed symmetrically below the coil with a vertical distance of 3 cm. For visualisation purposes, we enumerated the points in the grid in the order y-x-z and displayed the electric field values for each point. So the values in each set $\{i * 400, \ldots, (i+1) * 400 - 1\}$ represent the data for one z-layer of the grid, the values in each set $\{j * 20, \ldots, (j+1) * 20 - 1\}$ represent the data for one line perpendicular to the coil.

We see again that the simulation generally agrees well with the measured data. The discrepancies between the two curves in Figure 4.5.B are probably due to problems with the measurement range from the oscilloscope. To record high voltages as well as low voltages, we had to switch the measurement range, which resulted in some inconsistencies in the recordings. Therefore, the small measured values are probably higher in reality.

[4]This is not only because the field is about twice as strong below the centre as below the outer wing windings, but also because the coil is placed tangentially at the head with the centre touching it. This implies a bigger distance of 1 to 2 cm of the outer wing windings to the brain, so that the electric field produced there is negligible.

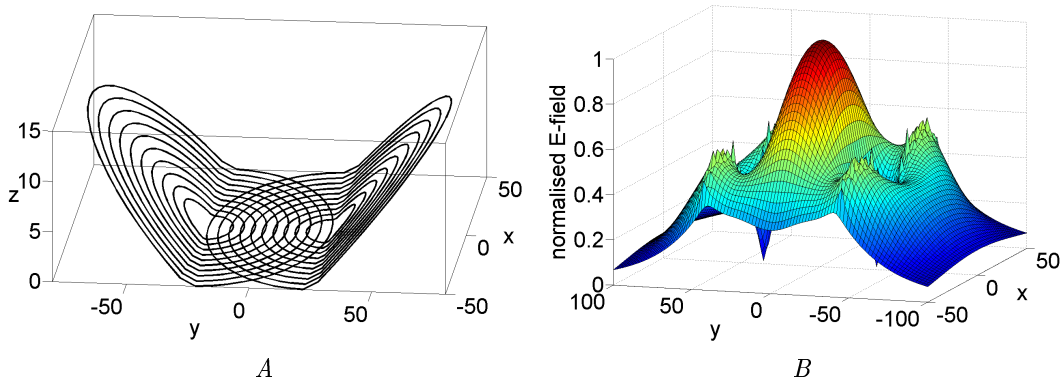

Figure 4.6.: Electric field of the angled figure-of-eight coil Medtronic MC-70. A: Idealised geometry of the windings used for simulation. Note the different axes' scalings B: Simulated absolute electric field strength in a horizontal plane 5 mm above (in the view of A) the coil. Note that the plane intersects the windings, hence the spikes in the electric field strength at $y = \pm 46\,\mathrm{mm}$.

4.4.2.3. Angled figure-of-eight coils

The last simulation was performed for the Medtronic MC-B70 figure-of-eight coil. This coil was used in mapping 7 patients with brain tumors and is thought to be able to elicit motor responses even for less responsive subjects [176]. This is achieved by slight angular design of the coil. As no complete manufacturer's specification of the coil is available, we took idealised data from the Medtronic coil data sheet and [176]: We simulated 10 concentric windings for each wing with inner diameter of 10 mm and outer diameter of 50 mm. The wings centres are separated by 50 mm, the inclination of the outer wing parts is 14.5° and starts at the wing's centre, see Figure 4.6A.

For this coil, our electric field measurement experiment, Section 4.4.1, gives distorted results, because the coil windings are non-planar and thus there will always be a current induced in the cables connecting the probe with the oscilloscope. Hence, we did not compare this simulation against a measurement, but took the conforming results for the two planar coil types as indication for the correctness of our simulation. Figure 4.6B shows exemplarily the absolute electric field strength in a plane 5 mm below the angular edge. Note that the plane crosses the windings of the wings, hence the increase in field strength (spikes) at $y = \pm 46\,\mathrm{mm}$.

4.5. Experimental Data

After the theoretical foundation has been laid, we are now ready to describe our approach to motor cortex mapping using statistical measures. We describe briefly in Section 4.5.1 how the experimental data is obtained before we explain in Section 4.5.2 how the statistics from Section 4.3 are used to calculate a likelihood map for the representation of a muscle in the brain. Section 4.5.3 finally presents results of our approach.

4.5.1. Experimental Setup

A first set of mapping procedures was performed on a 27 years old, right handed, healthy male. Data was obtained in two separate sessions, denoted Experiment 1 and Experiment 2, with differing coil geometries (circular and figure-of-eight) and differing mapping procedures. Details are given in the consecutive sections.

A second set of mapping procedures was performed on six patients suffering form tumors (WHO grade I-IV) in or neighbouring the central region of one hemisphere. We stimulated both hemispheres in five of the patients in consecutive sessions and only the tumor hemisphere in the sixth patient. Two of the patients underwent brain surgery and were stimulated before and after surgery on both hemispheres. In total, data was obtained in one to five sessions per patient, using a protocol denoted in the following as Experiment 3. For optimal stimulation response, we used the angular Medtronic MC-B70 figure-of-eight coil. Further details are given in the consecutive sections.

The medical part of the experiments was supervised by the Institute for Neurology, University of Lübeck (Experiment 1) and the Department of Clinical Neurophysiology, University of Göttingen (Experiments 2 and 3). Informed consent for all procedures was given by all probands.

4.5.1.1. TMS

TMS was applied as single biphasic pulse with interstimulus intervals of more than 2 seconds. TMS was delivered with a Medtronic MagPro X100 stimulator (Medtronic Inc., Minneapolis, MN, USA) and the circular MCF-75 coil (Experiment 1), with a MagStim "Rapid^2" stimulator (The MagStim Company, Whitland, Dyfed, UK) with the standard figure-of-eight coil (Experiment 2), and with a Medtronic MagPro X100 stimulator and the angular MC-B70 figure-of-eight coil (Experiment 3). In all experiments the coils were placed tangentially to the scalp with the coil centre touching the head slightly. Most accurate positioning was ensured using a robot and MRI based navigation. In Experiments 2 and 3, the figure-of-eight coil was oriented with an angle of 45° (with the handle of the coil pointing to the back of the subject, namely the coil tip was pointing the nose of the subject) with respect to the medial line of the head. The circular coil in Experiment 1 was placed such as to enable easy positioning with the robot; this is unproblematic since the rotationally symmetric electric field of the coil does not change with coil orientation.

4.5.1.2. Coil Navigation

We used the robotised system presented in Chapter 3 with active motion compensation to command the robot to specified stimulation points and keep it in place during the stimulation. Motion compensation was especially important since all mapping algorithms we used require several stimulations with the coil exactly at the same site.

4.5.1.3. Motor Response

The second ingredient for each TMS motor mapping algorithm is the strength of response of a muscle to TMS delivered at a certain position. We have used two different protocols.

Motor responses were recorded using Ag/AgCl electrodes and a Toennies-Multiniler IV (Jaeger-Toennies, Würzburg, Germany) hardware (Experiment 1) / CED 1401 (Cambridge Electronic Design, Cambridge, UK) hardware (Experiments 2, 3). In all experiments, recording electrodes were placed on the thenar (APB) and on the hypothenar (ADM). For Experiment 3 we additionally mapped the ADD muscle and in one case also the extensor digitorum muscle (a muscle at the underarm lifting the hand and spreading the fingers). The signal was band-pass filtered between 1.6 Hz and 1 kHz and sampled at 5 kHz rate. The amplitude of the MEP was calculated from negative to positive peak. The subject was lying on a couch (Experiment 1) / sitting on an armchair with his arms supported (Experiments 2, 3), in a relaxed state. Relaxation has been checked by mean of EMG recordings.

In the first protocol (Experiments 1, 3), we used a fixed strength of the stimulator for the stimulation. For Experiment 1, this was set to 100% of the maximum stimulator output. For Experiment 3, up to five spots have been stimulated with different intensities for a first survey to initially choose the stimulation intensity in order to avoid using a too strong pulse with the risk of overstressing the patients during the mapping procedure. The intensity chosen was the one which was able to deliver activations for the recorded muscles without provoking discomfort in the patients. For the mapping procedure we took the 3 stimuli averaged (Experiment 1) / 10 stimuli averaged (Experiment 3) peak-to-peak measures of the EMG muscle response (in mV) at the different stimulation sites as Y-values (see Section 4.5.2). Note that this enabled us to measure the APB , the ADM, and the ADD muscle responses at the same time using multi-channel MEP recording.[5]

In the second protocol (Experiment 2), we recorded the stimulator output needed to elicit a MEP of 1 mV peak-to-peak amplitude in 5 out of 10 stimuli. The recordings were expressed in form of percentage of the maximum output delivered by the device. So the measure indicating the response strength, the Y-values in our algorithm below, are the required stimulator strengths. Clearly, this protocol requires the mapping of ADM and APB muscle in two independent stimulation series.

We should remark that Protocol 2 gives more accurate and reproducible Y-values [175], but suffers from the fact that for coil positions far from the "Hotspot" no stimulations with responses of 1 mV can be obtained due to the limited strength of the simulator. Furthermore, this procedure is much more time consuming, reducing the number of stimulation sites, and is thus hardly applicable if more than two muscles are to be mapped in one TMS session.

[5] The abbreviations stand for: APB – abductor pollicis brevis muscle, a thumb muscle for spreading the thumb away from the hand, ADM – abductor digiti minimi muscle, the muscle that spreads the little finger away from the hand, ADD – a thumb muscle that moves the thumb towards the hand.

4.5.2. Mapping Algorithm

4.5.2.1. Statistical maps

We calculate the statistic value $S((x_1(\mathbf{p}), y_1), \ldots, (x_n(\mathbf{p}), y_n))$ for each brain surface point $\mathbf{p}$ and one of the statistics S (rank coefficient τ, correlation coefficient ρ, mutual information $\tilde{I}$, correlation ratio η) presented in Section 4.3.[6] Note that the values of S change with $\mathbf{p}$ because X changes with it. For the final map we colour each point $\mathbf{p}$ by its $S(\mathbf{p})$ value.

If $\mathbf{p}$ is the cortical representation point of the muscle, we expect S to be 1. For all other points we expect it to be less than 1. For example, consider a remote point $\mathbf{p}'$, where the electric field strength of the coil is zero for all stimulation sites, $x_i(\mathbf{p}') = 0$, $i = 1, \ldots, n$. This implies $E(Y|X(\mathbf{p}')) \equiv E(Y)$, hence $Var[E(Y|X(\mathbf{p}'))] = 0$ and $\eta(Y|X(\mathbf{p}')) = 0$. Also, $C = D = 0$ in Equation (4.3), so $\tau(X(\mathbf{p}'), Y) = 0$. Similarly, $\rho(X(\mathbf{p}'), Y) = 0$ and $\tilde{I}(X(\mathbf{p}'), Y) = 0$.

Alternatively, if no segmented brain surface is available, we calculate the statistical value for every point on a three dimensional regular grid. This results in a voxel representation of the map, which can be analysed and displayed in much the same way as MRI and fMRI maps. An example of such a map is displayed at the end of Section 4.5.3 in Figure 4.14. The disadvantage of this method is that it could produce high mapping values at unphysiological points such as white matter, cerebrospinal fluid, and even the skull.

4.5.2.2. Centre of Gravity

For Experiments 1 and 3 we employed the standard formula, Equation (4.15). For Experiment 2 we adapted the Centre of Gravity method as follows: Let y_{max} be the maximum stimulator intensity for which we could evoke an MEP of 1 mV. Define the centre of gravity point as

$$\mathbf{p}_{CoG}^{\text{variable stim output}} := \frac{\sum_{i=1}^{\tilde{n}} (y_{max} - y_i)\mathbf{p}_i}{\sum_{i=1}^{\tilde{n}} (y_{max} - y_i)}, \tag{4.18}$$

where y_i are the stimulator outputs in percent and $\mathbf{p_i}$ are the stimulation sites. The sum runs only over the $\tilde{n}$ stimulation sites for which we could evoke an MEP of 1 mV.

4.5.2.3. fMRI

For comparison, functional magnetic resonance images (fMRI) of the brain were acquired for two finger movement tasks for the subject of Experiments 1 and 2. Task one was to tip all fingertips of the right hand with the right thumb, yielding the brain activation area of the right APB. Task two consisted of spreading the right little finger sideways, activating mainly the area of the right ADM.

The paradigm used for each mapping was a block design with six volume data sets of activation and rest, respectively. Data were recorded on a 1.5T Siemens scanner with anatomical

[6] $x_i(\mathbf{p})$ is the approximated electric field strength at $\mathbf{p}$ when the coil is fired at the i^{th} stimulation site and y_i is the motor response measured for firing the coil at this stimulation site, see Section 4.2.

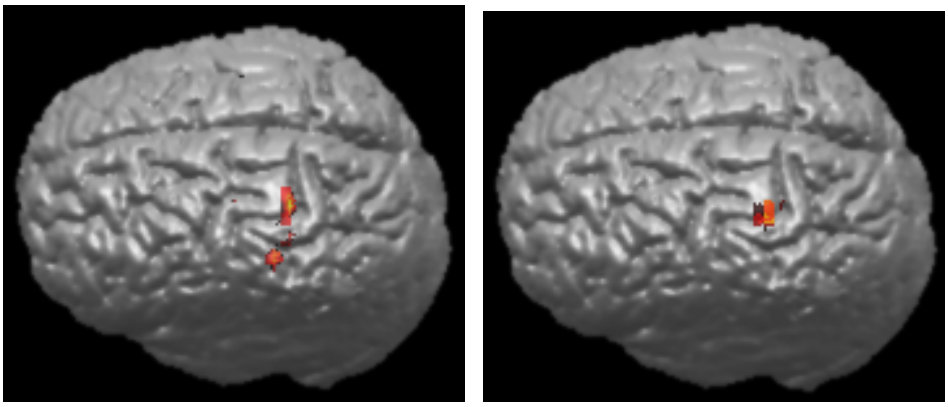

A: ADM *B:* APB

Figure 4.7.: A: fMRI activation for spreading the right little finger sideways, which mainly activates the abductor digiti minimi muscle (ADM). B: fMRI activation for tapping all other fingers of the right hand with the right thumb, which mainly activates the abductor pollicis brevis muscle (APB).

MRI resolution of 1 mm and functional MRI resolution of 4 mm. Data were analysed using SPM2 software [46] and visualised using MRIcro software [143].

Figure 4.7 displays the fMRI maps with thresholds of 12 for the APB task (range -8.4 – 17.9) and 6 for the ADM task (range -6.5 – 10.0). The coordinates[7] of the maximum activation were $(64, 106, 199)$ for the ADM muscle and $(62, 111, 199)$ for the APB muscle, i.e. the APB-maximum was about 5 mm anterior to the ADM-maximum.

4.5.3. Results

Three mapping experiments were performed as described in Section 4.5.1.3. In the experiments, statistical values at 247,239 points (Experiments 1, 2) and 252,333 – 345,198 points (Experiment 3) $\mathbf{p}$ on the segmented brain surface were estimated using the statistics presented in Section 4.3. Further, the CoG algorithm (Experiments 1, 3) and the inverse CoG algorithm (Experiment 2) were employed for comparison, see Section 4.5.2.2.

For the correlation ratio η evaluation, the windowing functions g_i were taken to be Gaussians with standard deviation $\sigma = 10\frac{x_{max}-x_{min}}{n}$, i.e. 10 times the average distance between two adjacent electric field strengths. Note that for every point $\mathbf{p}$ the list of electric field strengths $x_i(\mathbf{p})$ differs and hence also σ changes.

Table 4.1 gives the evaluation times for the mapping functions presented in Section 4.3 for a brain surface with 247,239 points and 34 coil positions. The calculation was performed on a standard PC with 2.8 GHz and 2GB RAM.

[7] All coordinate values in the chapter are given in millimetres in MRI image coordinates; x-axis runs left to right, y-axis back to front, and z-axis upwards. The origin is in the bottom-left-back corner of the bounding box of the head.

Statistic	τ	η	$\tilde{I}$	ρ	CoG
Calculation time [s]	20	75	15	20	5

Table 4.1.: Evaluation times for the mapping functions presented in Section 4.3 for the brain outline of Experiments 1 with 247,239 points and for 34 measurements (coil positions).

4.5.3.1. Experiment 1

MEP measurements at 34 coil positions were obtained for mapping with the circular MCF-75 coil. Coil positions were irregularly arranged roughly frontal to the central sulcus. Due to the lying position of the proband, more posterior positions could not be reached by the robot. The stimulation was given with a fixed intensity of 100% stimulator output at all positions. The reason for the unusual high choice of stimulator output was that this way we obtained muscle responses for as many stimulation sites as possible. Figure 4.8 shows exemplarily the results for the τ map of the ADM stimulation. The stimulation sites and resulting muscle responses are displayed as colour-coded spheres. The mapping value is encoded in the colour of the brain surface points.

We evaluated all statistics and the Centre of Gravity algorithm for the 34 data pairs $(x_i(\mathbf{p}), y_i)$ for each point $\mathbf{p}$ on the brain surface. The resulting maps are displayed in the left columns in Figure 4.9 for the ADM muscle and Figure 4.10 for the APB muscle, respectively. In the statistical graphs, we set the maximum colour value to the maximum mapping value and the minimum colour value 15% below the maximum mapping value. In the Centre of Gravity graphs, we first linearly scaled the brain surface point mapping values such that the closest point to the CoG has value 0 and the farthest has value 1. We then only coloured the points in the range 0 to 0.02.

As a test if it is possible to compensate for the lacking postcentral measurements, we added a ring of 17 artificial stimulation sites in big distance to the hotspot to the data and assigned a motor response of zero to them. This increases the number of sample data points for the statistics. We repeated the mapping calculations for now 51 data pairs $(x_i(\mathbf{p}), y_i)$ for each point $\mathbf{p}$ on the brain surface. The resulting maps are displayed in the right columns in Figure 4.9 for the ADM muscle and Figure 4.10 for the APB muscle, respectively. The colouring of the maps is as for the raw data.

The maps for both muscles and the τ, ρ, artificial η, and CoG algorithms show a single, spatially sharply bounded maximum each. The $\tilde{I}$ algorithm shows no clear maximum site. The coordinates of the maximum value point and the distances to the fMRI hotspot are given in Table 4.2. The distance of the τ, η, and ρ maxima to the fMRI hotspot is between 7 and 13 millimetres and thus within the range of the established accuracy for TMS mapping, Section 4.1. On the other hand, we clearly see that the conventional CoG algorithm fails for the circular coil: The distance of the CoG maximum to the fMRI hotspot is 23 millimetres (APB) and 29 millimetres (ADM), respectively.

All TMS mapping maxima, apart from the $\tilde{I}$ mapping, are located lateral and anterior to the corresponding fMRI hotspots. For the artificial data, also points near the fMRI hotspot have a high $\tilde{I}$ value. For the τ, ρ, and η algorithms, the ADM maximum is posterior to the APB

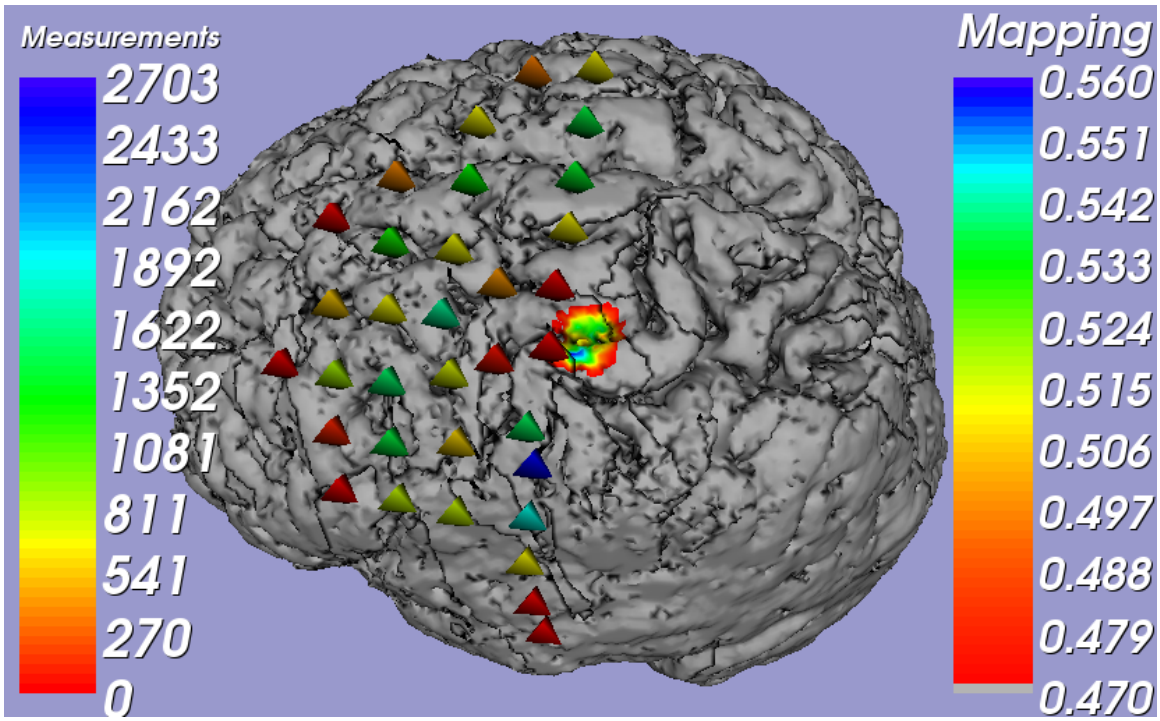

Figure 4.8.: Results of the mapping calculations for the right ADM muscle for Experiment 1 (Medtronic MCF-75 circular coil) and the τ statistic.

maximum, i.e. it has a smaller y-value. On the contrary, for the Centre of Gravity maps, the ADM maximum points are located anterior to the APB maximum points. Anatomically, all areas of high mapping value, apart from the ρ ADM map, are located on the posterior gyrus. The ρ ADM map has its maximum on the anterior gyrus.

Comparing the results using the raw data with the results using the added artificial data points, we see only little change in the τ and ρ maps and no change in the CoG maps[8]. The mapping quality of the Correlation Ratio η map improves using artificial measurements: The artificial data reduce the side maxima in the ADM map and enhance the maximum in the APB map. The results for the Mutual Information $\tilde{I}$ map change when including the artificial data, but with no clear improvement of the map quality itself.

4.5.3.2. Experiment 2

As explained in Section 4.5.1.3, the maps obtained with the MagStim figure-of-eight coil according to Protocol 2 differed from the previously described maps. We did not record the muscle response, but the TMS-stimulator output to obtain a muscle response of 1 mV peak-to-peak. This measure can be thought of inverse to the MEP measure, because the stronger the muscle response to a fixed intensity stimulus the less intensity is needed to

[8]For the CoG maps this is immediately clear from the definition, Equation (4.15)

	τ	η	ρ	$\tilde{I}$	CoG
ADM raw max	(54,114,197)	(58,107,196)	(58,110,198)	(67,97,200)	(55,133,195)
dist to fMRI	13.0	6.8	7.3	9.5	28.7
ADM art max	(55,112,197)	(58,107,196)	(58,110,198)	(87,124,155)	(55,133,195)
dist to fMRI	11.0	6.8	7.3	52.8	28.7
APB raw max	(53,117,196)	(112,178,169)	(51,116,195)	(84,159,199)	(55,133,195)
dist to fMRI	11.2	88.8	12.7	52.8	23.4
APB art max	(53,114,196)	(55,119,197)	(55,116,197)	(92,117,158)	(55,133,195)
dist to fMRI	9.9	10.8	8.8	51.2	23.4

Table 4.2.: Coordinates of the maxima for mapping the ADM and APB muscle using the Medtronic MCF-75 circular coil. The distance to the corresponding fMRI maximum (ADM coordinates: (64,106, 199), APB coordinates: (62, 111, 199)) is given below the coordinates of the maximum point.

obtain a fixed muscle response. Nevertheless, we still assume

$$S(X^r, Y) = S(X(\mathbf{p}^r), Y) = 1 \tag{4.19}$$

to hold for the representation point $\mathbf{p}^r$, S being one of the statistics from Section 4.3 and Y now being the stimulator output to elicit the 1 mV motor response.[9] For the rank coefficient τ we expect now negative values, because of the monotonously decreasing relationship between coil normalised field strength $X(\mathbf{p}^r)$ and the necessary stimulator output Y to elicit a muscle response of 1 mV. To unify this scenario with the procedure from Experiment 1, we take $|\tau|$ as the mapping function.

In the experiment, 12 coil positions were used for mapping. This rather low number of points is the price we had to pay for using this more stable recording method, because for each coil position we had to find the stimulator output evoking a 1 mV muscle response. Therefore about 5 – 10 trials per muscle were necessary. So we evaluated all statistics and the Centre of Gravity algorithm for the 12 data pairs $(x_i(\mathbf{p}), y_i)$ for each point $\mathbf{p}$ on the brain surface. The resulting maps are displayed in the left columns in Figure 4.11 for the ADM muscle and Figure 4.12 for the APB muscle, respectively.

Because the calculation of the statistics S from only 12 points can be unstable, we tested if the mapping quality improves if we increase the sample size for the statistics. Therefore, we added 19 artificial measurement points far away from the hotspot region to the data. As discussed in Section 4.5.1.3, there are no meaningful values to assign to non-responding points. We arbitrarily chose the Y-value of 111 for them. Thus, in total we re-calculated the statistics and the Centre of Gravity algorithm for now 31 data pairs. The resulting maps are displayed in the right columns in Figure 4.11 for the ADM muscle and Figure 4.12 for the APB muscle, respectively.

The maps for both muscles and the τ, ρ, and CoG inverse algorithms show a single, spatially sharply bounded maximum each. The η and $\tilde{I}$ algorithm show no clear maximum site for the raw data. For the ADM data including the artificial points, the $\tilde{I}$ and η algorithms produce

[9] Clearly, $X(\mathbf{p})$ still stands for the normalised electric field strength at $\mathbf{p}$, i.e. the electric field strength for a fixed stimulator output.

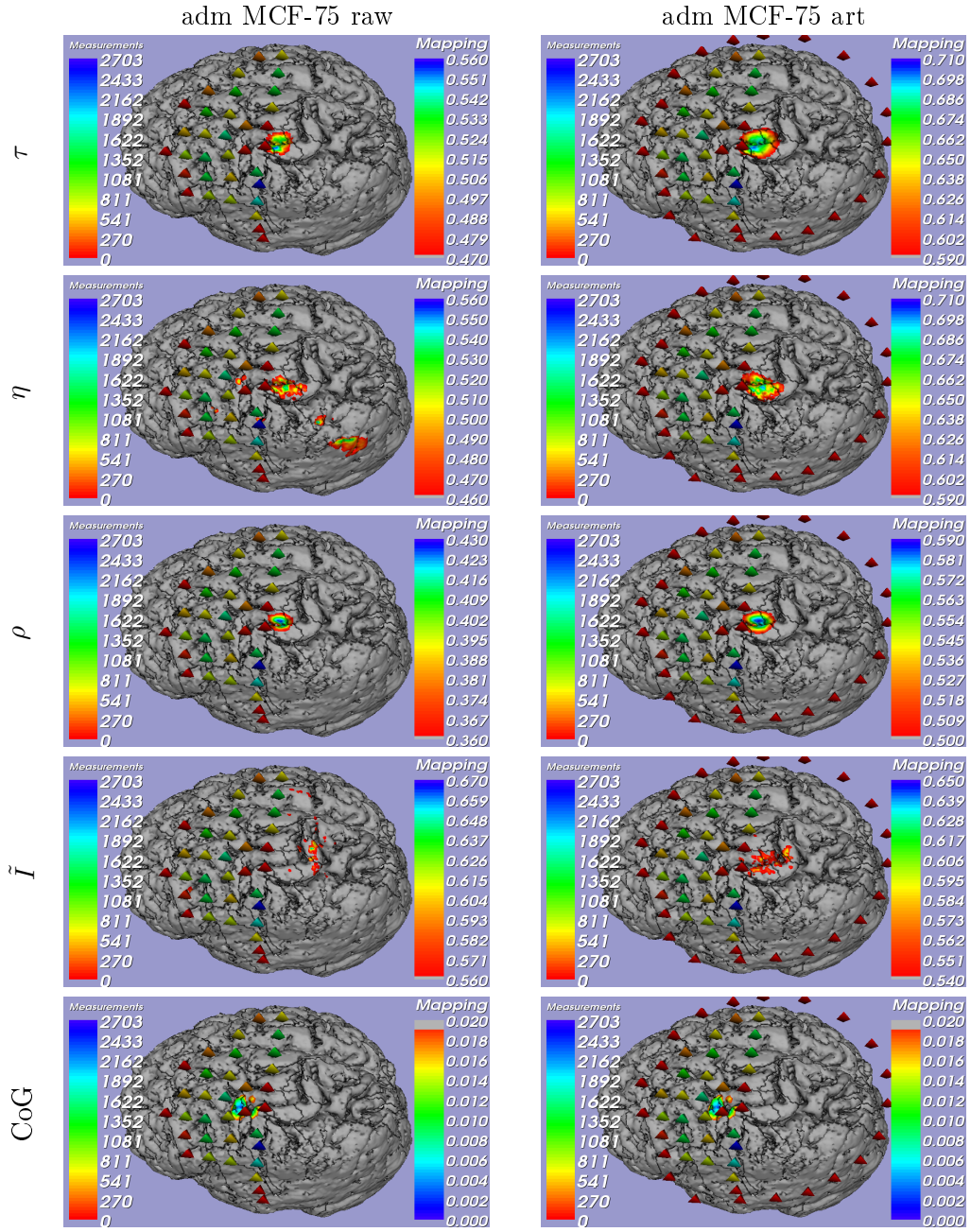

Figure 4.9.: Results of the mapping calculations for the right ADM muscle for Experiment 1 (Medtronic MCF-75 circular coil). The left column shows the results using only the recorded data from the experiment. The right column shows the results using additional artificial "zero-measurements". The tetrahedra in the pictures indicate the stimulation positions. The colour of the tetrahedra encodes the obtained MEP signal. The colour of a brain region depicts the value of the statistical mapping algorithm for the point. Mapping colours range from grey and red (unlikely representation of the ADM muscle) to blue (very likely representation).

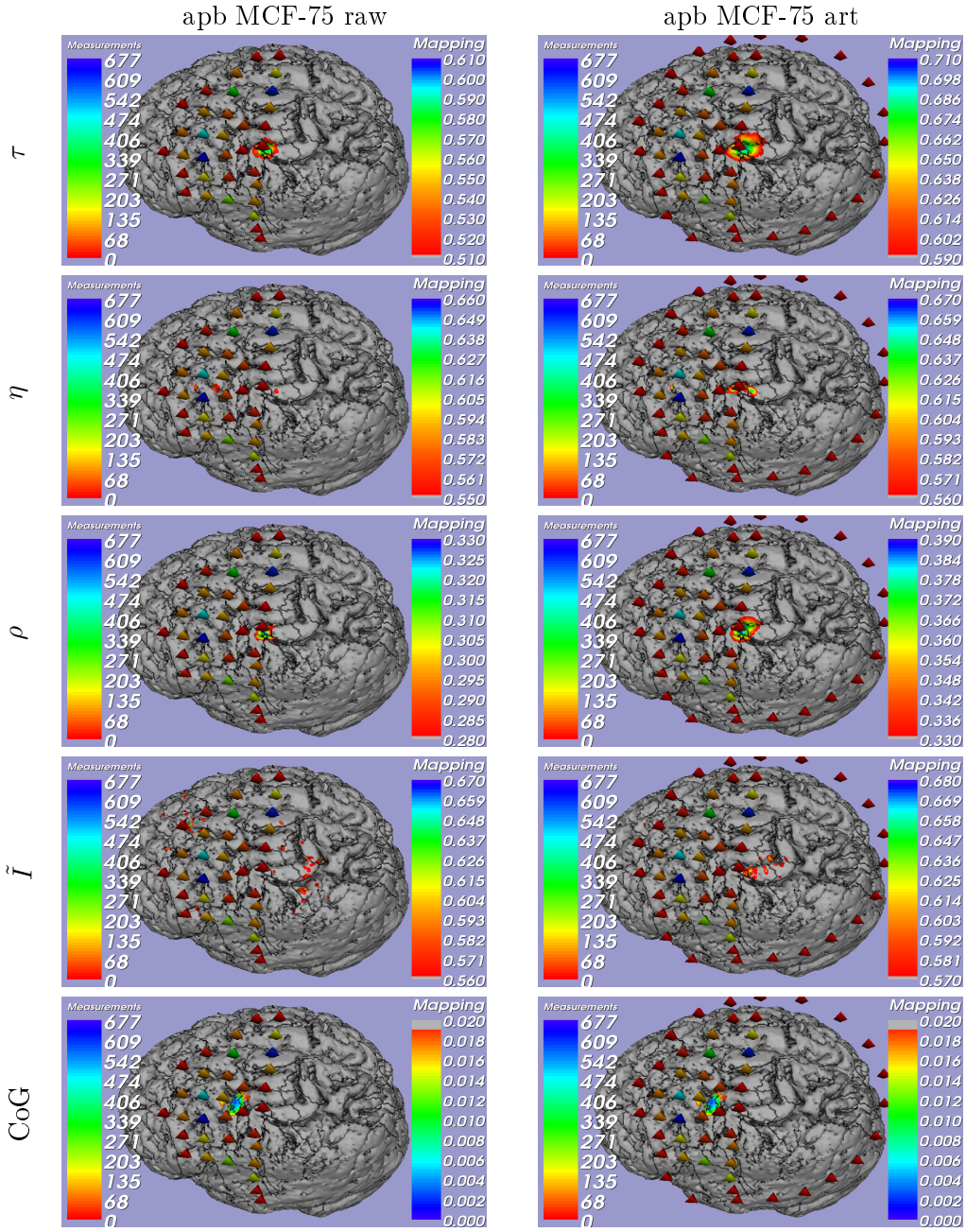

Figure 4.10.: Results of the mapping calculations for the right APB muscle for Experiment 1 (Medtronic MCF-75 circular coil). The left column shows the results using only the recorded data from the experiment. The right column shows the results using additional artificial "zero-measurements". The tetrahedra in the pictures indicate the stimulation positions. The colour of the tetrahedra encodes the obtained MEP signal. The colour of a brain region depicts the value of the statistical mapping algorithm for the point. Mapping colours range from grey and red (unlikely representation of the APB muscle) to blue (very likely representation).

	τ	η	ρ	$\tilde{I}$	CoG inv
ADM raw max	(61,109,200)*	(59,114,199)†	(61,108,200)*	(60,121,198)†	(61,112,200)
dist to fMRI	4.4	9.4	3.7	15.6	6.8
ADM art max	(62,108,200)	(61,114,198)*	(62,111,201)*	(62,115,200)*	(61,112,201)
dist to fMRI	3.0	8.6	5.7	9.3	7.0
APB raw max	(58,111,198)*	(58,111,197)†	(58,111,196)*	(59,110,196)†	(59,113,200)
dist to fMRI	4.1	4.5	5.0	4.4	3.7
APB art max	(58,111,198)	(62,110,200)†	(60,113,200)*	(64,114,200)*	(61,113,201)
dist to fMRI	4.1	1.4	3.0	3.7	3.0

*Table 4.3.: Coordinates of the maxima for mapping the ADM and APB muscle using the standard MagStim figure-of-eight coil. The distance to the corresponding fMRI maximum (ADM coordinates: (64,106, 199), APB coordinates: (62, 111, 199)) is given below the coordinates of the maximum point. For points marked with a star (*), the maximum value was at an internal point in the brain, which was falsely segmented as brain surface. The * point is the maximum point on the brain surface. For points marked with a dagger (†), the statistic had no clear maximum point, so the point closest to the fMRI maximum was taken.*

a small area, about 3 mm in diameter, containing several maximum points. The same holds true for the artificial APB data and the $\tilde{I}$ algorithm. The results for the η mapping of the APB improve using the artificial data, but still no clear maximum area is discernable.

The coordinates of the maximum value point and the distances to the fMRI hotspot are given in Table 4.3. All algorithms calculate the cortical representation for the APB muscle to be within a distance of 5 mm to the fMRI hotspot. This is about the resolution of the fMRI image and thus an optimal result. For the ADM muscle, only the τ and the ρ algorithm achieve this optimum in localising the muscle's representation. The adapted CoG algorithm's maximum has about 7 mm distance to the fMRI hotspot and the η and the $\tilde{I}$ algorithms have about 9 mm distance to the fMRI hotspot.

All single ADM mapping maximum spots are located slightly lateral and anterior to the corresponding fMRI hotspot. Anatomically, they are all on the anterior gyrus in an area known as the hand knob. The APB mapping maxima are also located on the hand knob, slightly posterior to the corresponding fMRI hotspot.

For the τ, ρ, and CoG inverse maps, the APB-maximum is located anterior-lateral to the ADM-maximum, complying with the fMRI mapping. The same is true for the centre of mass of high mapping value points for the η algorithm using the artificial data. The $\tilde{I}$ shows a reversed result: The APB is located slightly posterior-medial to the ADM.

Comparing the results using the raw data with the results using the added artificial data points, we see only little change in the τ, ρ, and CoG inverse maps. The mapping quality of the η and $\tilde{I}$ maps improve using artificial measurements.

Figure 4.13 shows exemplarily the $(X(\mathbf{p}), Y)$ pairs for three different brain surface points $\mathbf{p}$ and the ADM muscle. The points are chosen such that $\mathbf{p_0}$ is close to the η mapping maximum, $\mathbf{p_1}$ is close to the fMRI hotspot, and $\mathbf{p_2}$ is a point with low mapping value in some distance to the fMRI maximum. The figure shows how the relation between the electric field strength E at a brain point $\mathbf{p}$ and the stimulator output Y necessary to evoke a motor

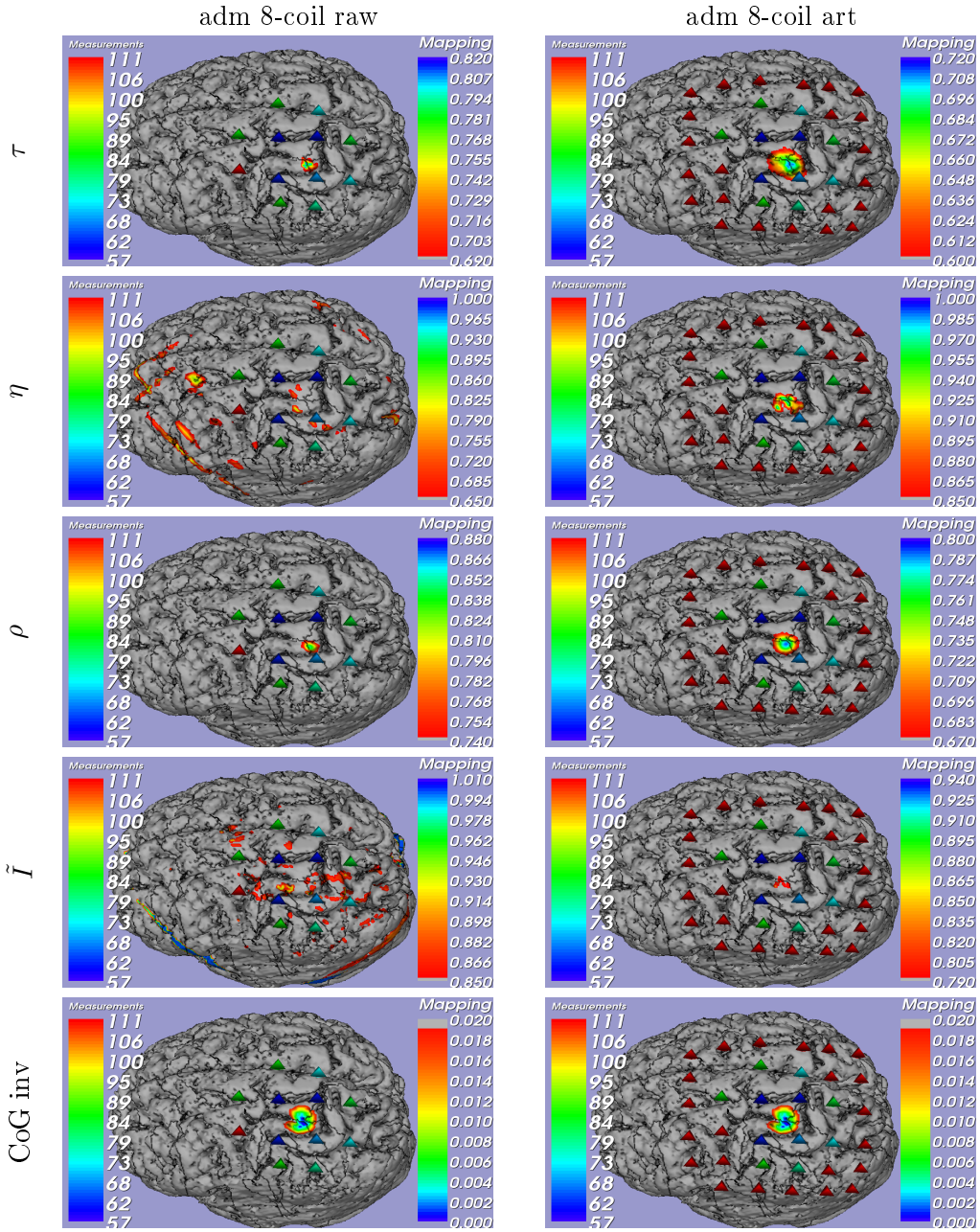

Figure 4.11.: Results of the mapping calculations for the right ADM muscle for Experiment 2 (standard MagStim figure-of-eight coil). The left column shows the results using only the recorded data from the experiment. The right column shows the results using additional artificial "zero-measurements". The tetrahedra in the pictures indicate the stimulation positions. The colour of the tetrahedra encodes the stimulator output needed to obtain a muscle response of 1 mV. The colour of a brain region depicts the value of the statistical mapping algorithm for the point. Mapping colours range from grey and red (unlikely representation of the ADM muscle) to blue (very likely representation).

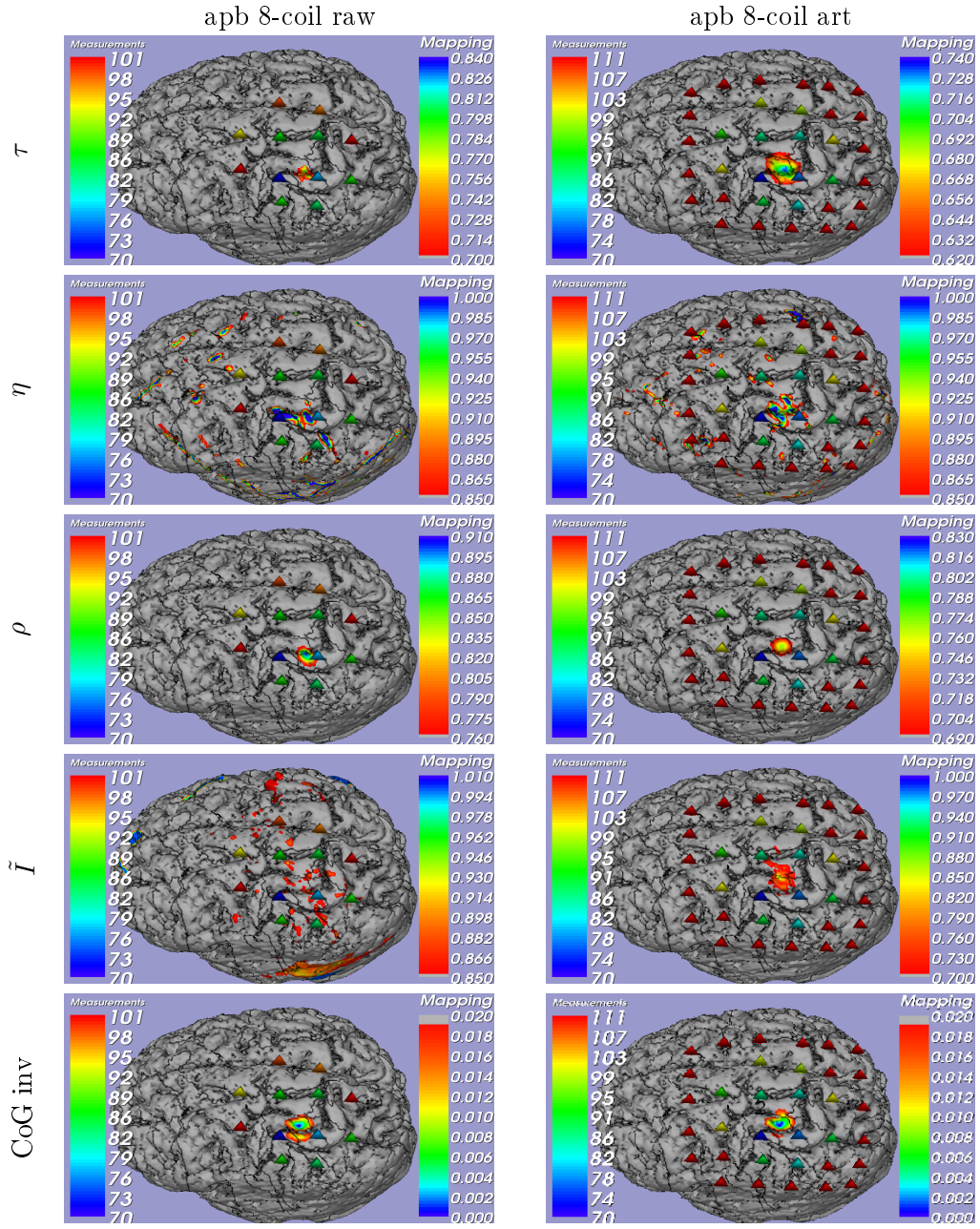

Figure 4.12.: Results of the mapping calculations for the right APB muscle for Experiment 2 (standard MagStim figure-of-eight coil). The left column shows the results using only the recorded data from the experiment. The right column shows the results using additional artificial "zero-measurements". The tetrahedra in the pictures indicate the stimulation positions. The colour of the tetrahedra encodes the stimulator output needed to obtain a muscle response of 1 mV. The colour of a brain region depicts the value of the statistical mapping algorithm for the point. Mapping colours range from grey and red (unlikely representation of the APB muscle) to blue (very likely representation).

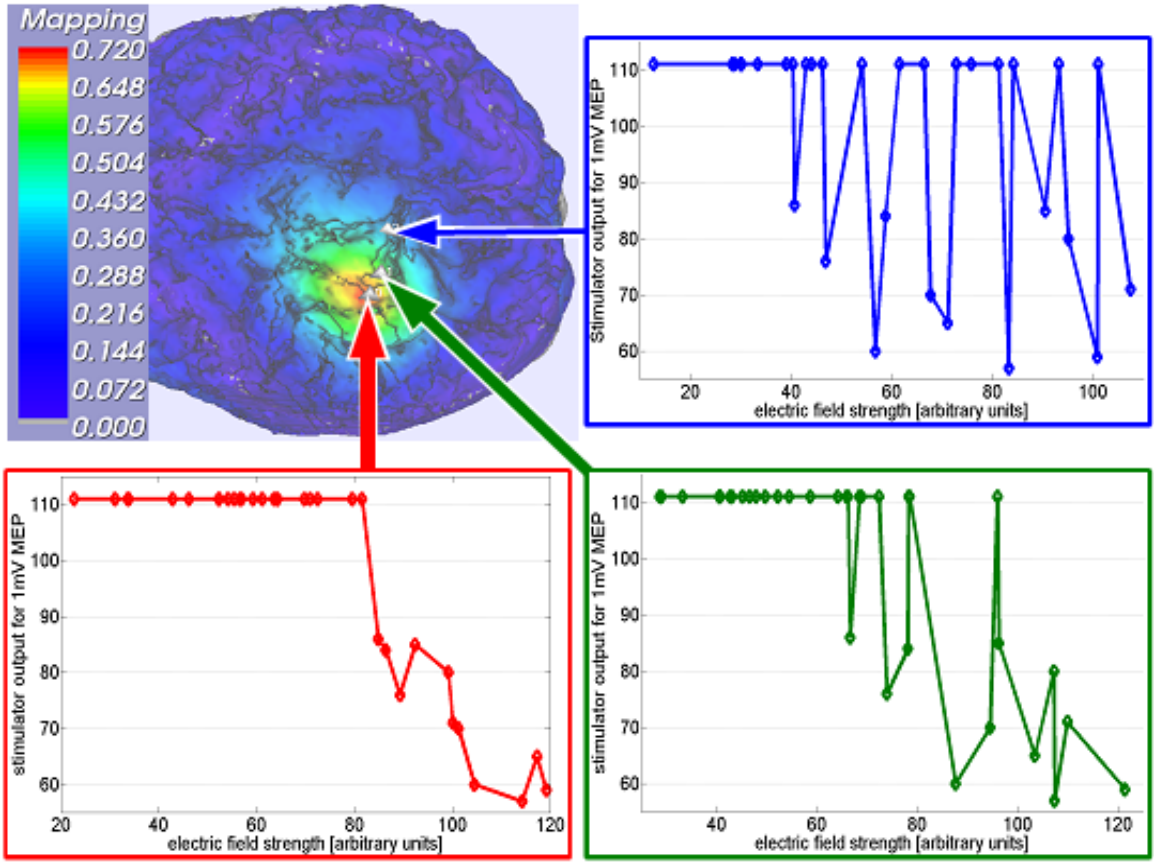

Figure 4.13.: Experiment 2: Calculated electric field strength $X(\mathbf{p})$ (arbitrary units) and respective stimulator output Y (in percent of maximum output) necessary to produce a muscle response of 1 mV peak-to-peak at ADM muscle. Y values of 111 indicate that no sufficient stimulation was possible with stimulator output of 100%. The three graphs show the $(X(\mathbf{p}), Y)$ data pairs for three different brain surface points $\mathbf{p}$, depicted in the upper left picture. The points are chosen such that $\mathbf{p_0}$ (red) is a high mapping value point, $\mathbf{p_1}$ (green) has intermediate mapping value, and $\mathbf{p_2}$ (blue) is a point with low mapping value. The mapping values at the points are $\tau_0 = 0.71$, $\tau_1 = 0.60$, $\tau_2 = 0.37$; $\eta_0 = 0.91$, $\eta_1 = 0.78$, $\eta_2 = 0.32$; $\rho_0 = 0.75$, $\rho_1 = 0.60$, $\rho_2 = 0.21$; $\tilde{I}_0 = 0.76$, $\tilde{I}_1 = 0.59$, $\tilde{I}_2 = 0.49$. The brain in the upper left picture is coloured according to the τ value.

response of 1 mV changes with $\mathbf{p}$. For the mapping hotspot $\mathbf{p_0}$, the stimulator output to elicit an MEP of 1 mV is mainly decreasing with increasing electric field strength at $\mathbf{p_0}$. This gives a justification of our assumption that the electric field strength at the representation point and the stimulator output to elicit an MEP of 1 mV are inversely related, see Equation (4.19). Further, Figure 4.13 exemplifies that even small changes in $\mathbf{p}$, e.g. from $\mathbf{p_0}$ to $\mathbf{p_1}$, lead to big changes in mapping values, because of the associated changes in $E(\mathbf{p})$.

4.5.3.3. Experiment 3

The set-up for the third experiment is the standard one for motor cortex mapping: We used a bend figure-of-eight coil and mapped the MEP responses for a fixed stimulator output.

	τ	η	ρ	$\tilde{I}$	CoG
max @ hand knob	0.91	0.63	0.83	0.59	0.78
unique max	0.88	0.76	0.85	0.05	0.89

Table 4.4.: Algorithm performance for mapping with the Medtronic MC-70 figure-of-eight coil. The row "max @ hand knob" gives the averaged score for each algorithm for having a maximum value at the anatomical hand knob. The row "unique max" gives the averaged score for each algorithm for having a unique maximum point on the brain surface. Scores range between 0 and 1, the latter one indicating a perfect performance. Data are averaged over 48 mappings.

We recorded responses for 20 – 52 coil positions per patient and session and calculated the statistical maps according to Section 4.3. The non-planar shape of the coil prevented that we could measure its electric field, so we used the simulated field in air instead (see Section 4.4.2). We performed 17 stimulation sessions, mapping the ADM, the APB, and the ADD muscle simultaneously. In one of the sessions only the ADM muscle was mapped, in another one only the APB muscle, and in a third one ADM, APB, ADD and the extensor digitorum muscle. In total we recorded data for 48 mappings.

As we have no fMRI data to compare the results to, we evaluate the results of the different algorithms using two simple categories: First, we noted if the algorithm results in a single maximum on the reconstructed brain surface. Second, we checked whether this maximum (or one of the maxima) was on the anterior gyrus in the area of the hand knob. For a clear positive result, we gave a score of 1 for the algorithm's performance, for a clear negative result, we gave a score of 0. If the performance of the algorithm could not be judged that easily, e.g. having a maximum close to but not on the hand knob or having two maxima, but very close together, we gave it the score of 0.5.

Table 4.4 summarises the results for all algorithms over all stimulation sessions. We see that the Rank Coefficient τ statistic gives by far the best results with over 90% correct maximum position. The Correlation Coefficient ρ statistic and the Centre of Gravity algorithm do also perform well with about 80% correct localisation rate. The Correlation Ratio η and Normalised Mutual Information $\tilde{I}$ statistics give worse results with less than two thirds of the times having a maximum value at the hand knob. Furthermore, the $\tilde{I}$ algorithm yields virtually never a unique maximum. Also the η statistic scores worse than the τ, ρ, and CoG algorithms, having a unique maximum in only 76% of the cases compared to 85% to 89%.[10]

For two patients we had the possibility to compare the results of the pre-surgical TMS mapping using the τ algorithm with intraoperative mapping using direct electrical stimulation. The MRI data of the patient's head was used for the TMS examination as well as for the intraoperative navigation. With the help of navigation markers, the coordinates of the maximum stimulation point were determined. Therefore, several anatomical reference points were defined so that the coordinates of stimulated areas could be determined relative to these points. Difference vectors were calculated for each reference point and each muscle. These vectors were used to find the TMS mapping points during operation with the help of the navigation software (BrainLAB, Germany).

[10] The Centre of Gravity point in space is of course unique, but its projection to the cortex might not be, i.e. there are situations where two gyri have about the same distance from it.

The brain was stimulated intraoperatively with a spheric electrode. The difference between the pre- and intraoperative points of maximum stimulation was less than 5 mm. Hence, the TMS mappings were indeed correct. We remark that the reliability of this comparison is limited. Due to factors like brain shift, landmark ambiguity, registration error, and the size of the electrical stimulation device, we do not expect the TMS coordinates to agree with the surgical coordinates within more than 5 to 10 millimetres.

The data of a third patient also supports the correctness of our TMS mapping. The pre-surgical MRI of the patient showed a sharply bounded tumor on the postcentral cortex. Mapping with TMS τ algorithm (pre-surgical: 40 measurements, post-surgical 23 measurements, Figure 4.14) yielded a unique maximum on the motor cortex in all cases (pre- and post-surgical, ADM, APB, ADD). The pre-surgical maps indicated that the tumor area is distinct from the motor area and could thus be resected without paralysing the patient. This was confirmed by investigations during the surgical procedure and finally by the post-surgical checkup.

The TMS maps also show a clear shift in the localisation of the muscles in head coordinates before and after the resection (compare left and right column of Figure 4.14). We think that this is caused by the shift of brain matter as the consequence of the resection of the tumour. Note that the post-surgical maxima are located on the same gyrus as the pre-surgical maxima. Additionally, the direction and size of the shift of the localisations is about the same for all three muscles mapped. This is a further indication that the difference between the pre- and post-surgical localisation is real and not an error of our localisation algorithm.

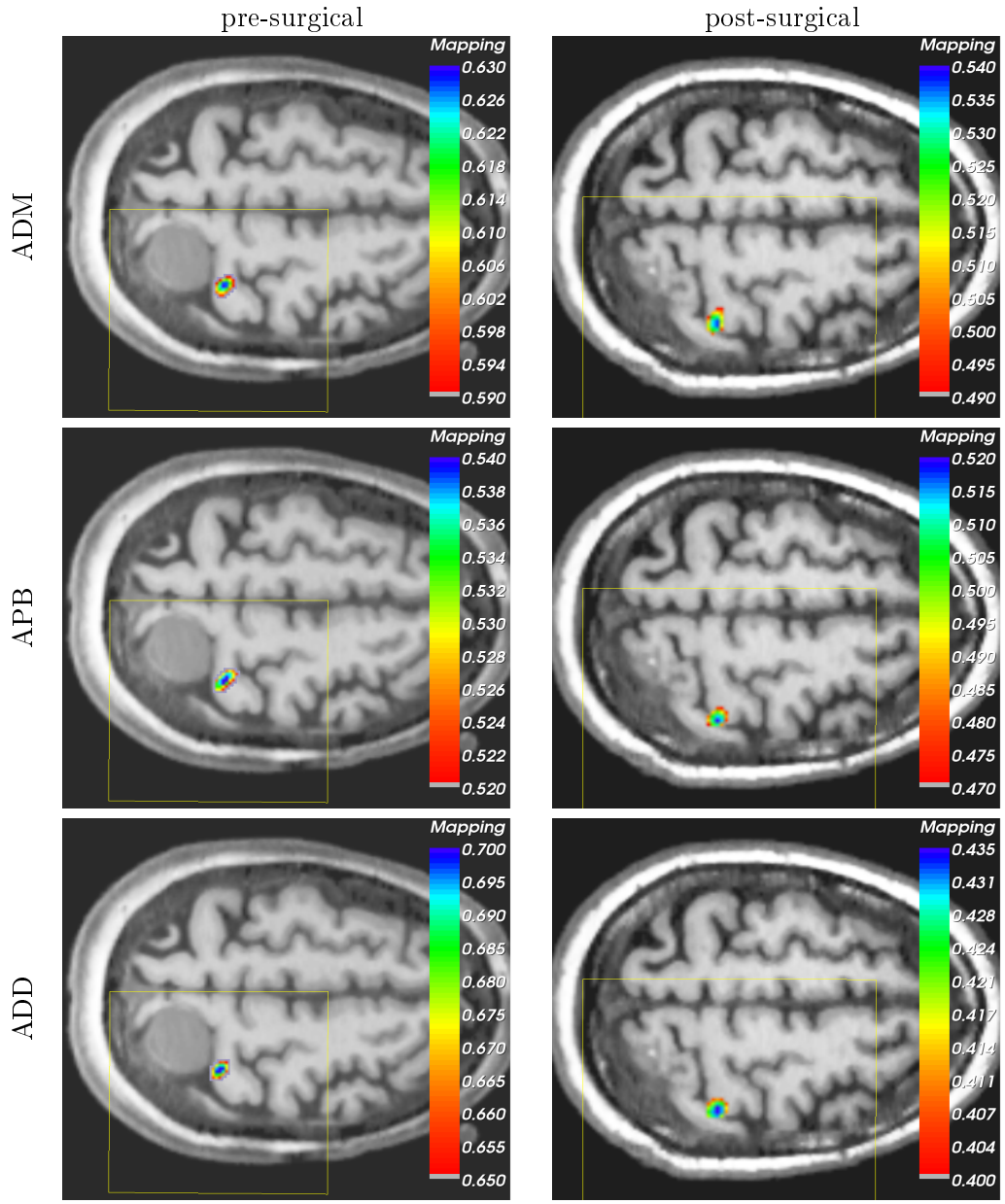

Figure 4.14.: TMS mapping of the ADM, APB, and ADD muscle before and after tumor resection using the τ statistic. The mapping values were calculated within the area of the yellow rectangle. Mapping colours range from transparent and red (unlikely representation of the muscle) to blue (very likely representation). The anatomical image slices are all taken in the same height relative to the head. A big shift in brain tissue occurred due to the resection of the tumor, changing the form of the gyri nearby (lower left part in the images). This brain shift is likely to explain the shift in localisation between the pre- and postoperative mapping.

5. The system in practice – experiences and results

In this chapter we report about the application of the robotised system in a number of different stimulation setups. We emphasise the adaptation of the system to the special needs of each application, the advantages we found over non-robotised stimulation, and special problems we encountered. To present the neurophysiological results of the studies in detail is beyond the scope of this thesis; the findings will be published separately by the medical investigators of the studies.

5.1. Motor cortex mapping

5.1.1. Theory

Our aim is to establish brain mapping, or, more precisely, motor cortex mapping, with TMS as alternative functional imaging tool to functional magnetic resonance imaging (fMRI), positron emission tomography (PET), or single photon emission computed tomography (SPECT). The advantage of TMS is its direct functional base, whereas all other non-invasive functional imaging techniques rather map regions of high metabolic activity. This metabolic dependence can be problematic in patients with brain tumours in the central region, i.e. tumours close to the motor cortex, because the metabolic brain response to a movement task is disguised by the tumour activity. Thus, a major application of motor cortex mapping with TMS is preoperative planning for tumour resections [80].

The protocol for motor cortex mapping consists of positioning the coil at a large number (20 – 50) of different sites, single pulse TMS at the sites, and successive recording of the evoked motor potential (MEP) of a selected muscle, see Figure 5.1. The pose information of the coil, the electrical properties of the coil, and the stimulation responses are then used to calculate the representation site in the brain of the selected muscle.[1]

The stimulation sites for the mapping can be defined in three ways:

1. Single points selected on the virtual cranium – The user marks a point on the virtual head outline as described in Section 3.4.1 and sets coil distance (normally to 0) and coil orientation (normally to 45° for a figure-of-eight coil). By repeating this procedure, the complete mapping plan is created.

[1] Chapter 4 is solely devoted to this topic. Here, we only describe the medical application of our system.

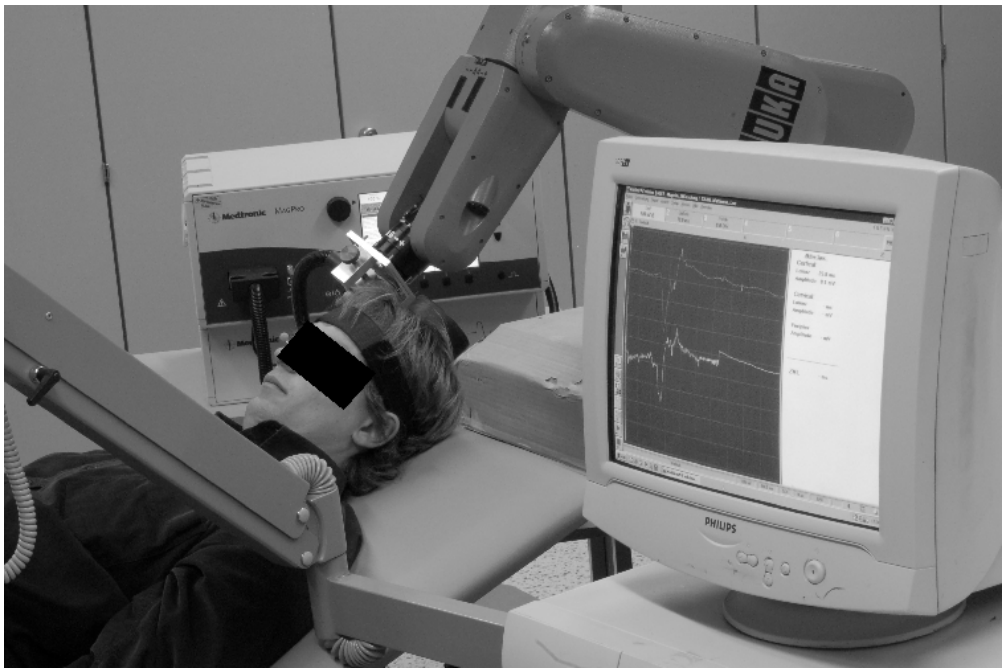

Figure 5.1.: Experimental setup for motor cortex mapping. The head is tracked using a marker attached to the head. Motor evoked potentials (displayed on the computer screen in the foreground) are recorded from the right abductor pollicis brevis muscle (a muscle that moves the thumb, APB) and related to the coil position at the head.

2. Single points selected on the real cranium – A tracked pointing device is held to the target spot for stimulation as described in Section 3.4.1. On a user input, the coordinates of the pointer tip relative to the head are recorded and the corresponding point on the virtual cranium is marked. The user adjusts coil distance and orientation and proceeds as in 1.

3. Automated regular grid creation – The user defines a coil target pose ${}^{\mathrm{I}}p_{\mathrm{C}}$ as in 1 or 2, including coil distance and orientation. Furthermore, she / he defines grid spacing for x- and y-direction as well as the number of columns / rows in x and $y-$ direction. The program then creates a rectangular grid of the user-defined size in the x_C-y_C-plane of the coil at ${}^{\mathrm{I}}p_{\mathrm{C}}$. For each grid point $g_{i,j}$, the closest head outline point $h_{i,j}$ is calculated. This point is then used as the base point for the stimulation pose ${}^{\mathrm{I}}p_{\mathrm{C}}^{i,j}$, i.e. ${}^{\mathrm{I}}p_{\mathrm{C}}^{i,j}$ is calculated as if $g_{i,j}$ was set as coil target by the user in 1 or 2. The distance and orientation of the coil are taken from setting ${}^{\mathrm{I}}p_{\mathrm{C}}$. For an example of a grid created this way see Figure 5.2.

Stimulation sites are visualised as small trihedrons, representing the position and orientation of the coil when stimulating there. MEP recordings are visualised as coloured spheres centred at the site of stimulation that evoked them. The colour hereby corresponds to the recorded value (MEP amplitude or stimulator output), see Figure 5.3. The visualisation provides a good overview over the sites that have been stimulated and the responses obtained. Based on this visualisation, further stimulation sites can be defined.

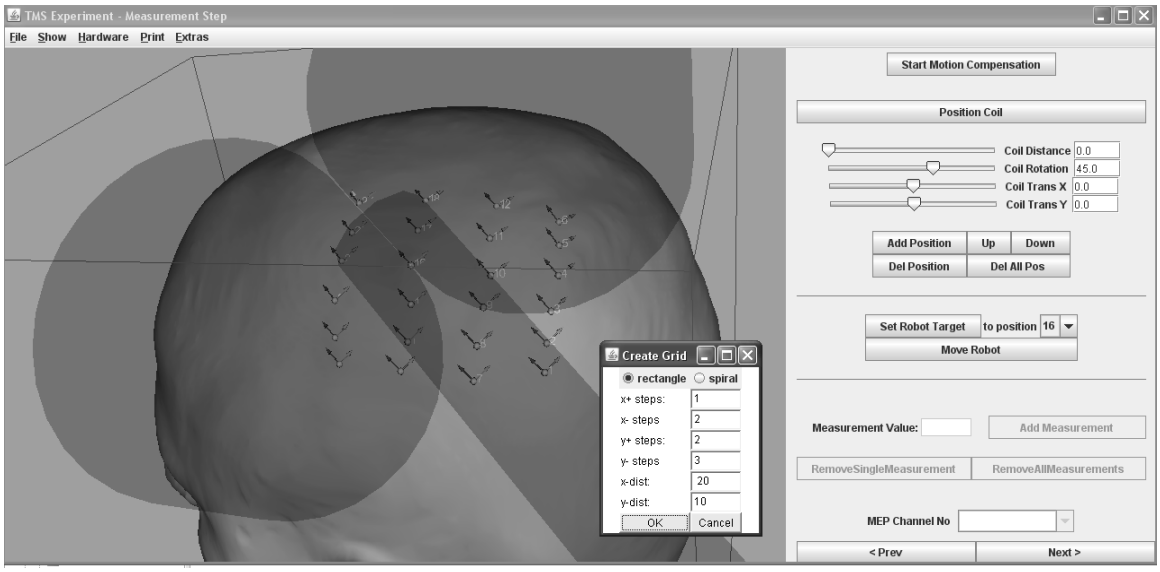

Figure 5.2.: Automated grid creation for motor cortex mapping. The grid is created in the x-y-plane of the coil at a base position and projected to the cortex. Coil distance and orientation are taken from the base position, grid spacing and extent are defined via a separate input window. In the figure, base position is at grid point 15, grid spacing is 20 mm in x- and 10 mm in y-direction. Grid extent is $(1, 2, 2, 3)$ *in* $x+$, $x-$, $y+$, *and* $y-$ *direction. Coil distance is set to 0 mm, coil orientation to* $45°$. *The broad extent of the grid results in slightly irregular vertex distances at the outer edges, caused by the projection of the grid points to the cortex. Note that there exists no rectangular grid on surfaces with non-zero curvature.*

When the stimulation responses for stimulation at all planned sites have been recorded, data are directly exported to another software module calculating the most likely representation point of the muscle mapped. Chapter 4 discusses the mapping algorithm in detail and presents examples of mapping results.

5.1.2. Practical experience

So far we used the robotised TMS system to map 10 subjects. Each session lasted between 90 and 150 minutes and we recorded motor responses from 20 to 52 points. Stimulation points were arranged irregularly with a distance of 5 to 10 mm to each other.

As some of the experiments we performed in an early stage of the system's development, we used mainly Procedure 1 from Section 5.1.1 in an iterative scheme to define the stimulation points. So we defined a stimulation target on the virtual cranium, evaluated the stimulation response, and decided on the next stimulation target according to the responses obtained so far. This procedure worked well as soon as a small number of responses had been obtained. But when defining the the first stimulation point, the method suffered from the indirectness of defining the target points for the patient on a computer screen. The medical personnel trained in TMS could identify potentially good target spots for the coil easily on the real head, but had difficulties in marking these points on the screen because of the lacking 3D view, the missing / distorted features of the head on the screen (no hair, smoothed outline,

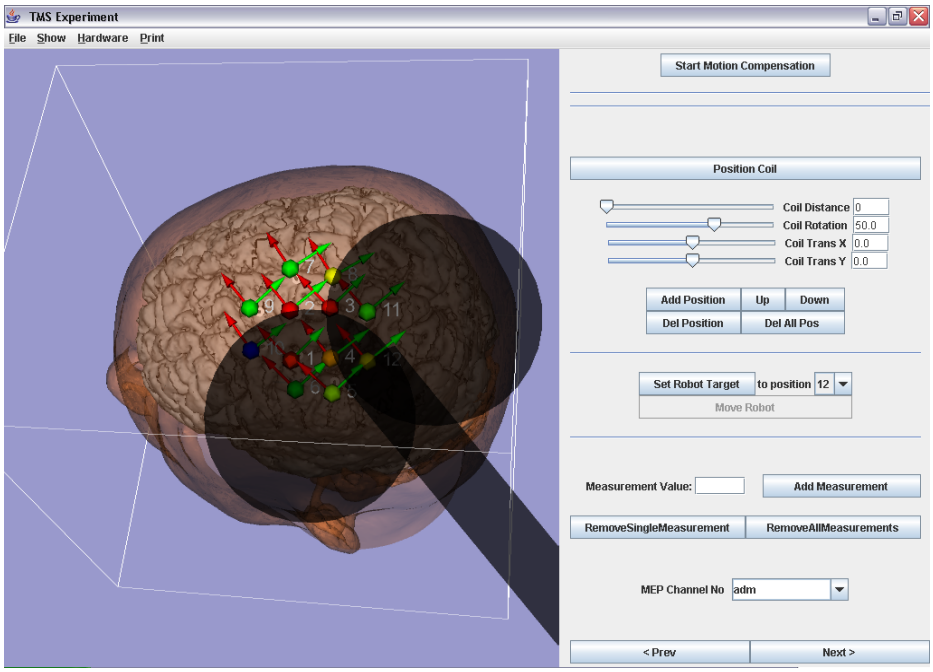

Figure 5.3.: Graphical user interface for the motor cortex mapping step. The stimulation sites are depicted as small trihedrons, showing position and orientation of the coil at the site. Mapping responses are depicted as coloured spheres. In this case we were mapping the right Abductor digiti minimi (ADM, a muscle that moves the little finger). Colours correspond to stimulator output intensity to yield an MEP of 1 mV. They range from red (57% of maximum stimulator output) to blue (artificial 111%, to denote that even with maximum stimulator output no stimulation was possible). For better visualisation the user can change the opacity of the coil, the skin and the brain. All objects, including the trihedrons and the measurement spheres, can also be hidden. The brain was segmented from MRI data using SPM software [6].

segmentation artefacts, etc.), and the lack of tactile input. Therefore, we now provide a method to mark the target spot for the coil directly on the real head, i.e. Method 2 from Section 5.1.1. First trials defining the coil's target directly on the real head confirmed that this is much easier and more intuitive for the experienced "conventional" TMS users than defining a target spot on a computer screen.

In all human motor cortex mapping sessions, we defined new stimulation points in an iterative process, taking the motor responses at previous stimulation sites into account. It does not take more than a few seconds to add a new target point to the plan, so there was no need to create a full grid beforehand using Method 3 from Section 5.1.1 and to forbear from adapting the plan to motor responses obtained so far. But if the system is going to be used routinely in the future, the mapping plan has to be created in an automated way. Further, if we need a regular grid with small spacing, e.g. for research purposes, Method 3 provides it perfectly, as we show in Section 5.4.

The robot system allowed us to stimulate at the planned sites with high accuracy. Accuracy in implementing the plan is of fundamental importance, because motor responses change quickly even for small displacements of the coil. Of similar importance is the ability of the

robot system to place the coil exactly tangential to the head, because the stimulated brain tissue has a distance of 2 to 3 millimetres from the head surface. That implies that a minor tilt of about 10° has the same effects as a coil shift of 5 millimetres and hence leads to changed muscle responses.

For the mapping, the coil needs to be held in place for more than half a minute, because several stimulations per point should be averaged to give more stable results. The motion compensation feature of the robot allowed here for the first time recordings undisturbed by tension resulting from fixation of the head or inaccuracies induced by a change in coil position or orientation.

The last two features – tangential placement and motion compensation – were highly requested, especially by inexperienced TMS users. They report having difficulties obtaining a clear and stable mapping without a robot using only a navigation device. This is probably due to the fact that they are able to position the coil exactly at a spot using the navigation aid, but not to orient it correctly and to keep the orientation stable during the several stimulations at a site. As shown in Chapter 4, motor responses obtained with the robot system allowed precise mapping and gave stable inter-session results, indicating that the system was able to position the coil correctly and to keep it in place during probing of one site.

5.2. Combined TMS-EEG-experiments

In recent years, combined TMS-EEG examinations have become a new, exciting tool in neurophysiological research [64, 67, 76, 124, 177]. For example, Ilmoniemi et al. used TMS combined with high resolution EEG and source localisation techniques to investigate the connectivity of the brain [63]. For an overview of recent studies see [173].

The problem when combining TMS and EEG lies in the artefacts introduced by pressing the coil against the electrodes or movements of the coil with respect to them. Furthermore, EEG equipment is sensitive to human operators standing close to the subject. These circumstances make it difficult to position and hold the coil at its desired position without introducing artefacts or constraining the subject, causing discomfort.

Our robotised system solves all these issues by keeping the coil a few millimetres above the electrodes and avoiding contact using the motion compensation feature. As the recorded EEG data revealed, there were virtually no artefacts produced by the robot itself. For the experiment described in Section 5.2.1 we used the Kuka KR3 robot with brushless direct current motors, so there were little electromagnetic artefacts to expect. But also in the experiment described in Section 5.2.2, where we used the Adept Viper s850 robot with alternating current motors, we saw little artefacts in the EEG traces.

Contrary to the motor cortex mapping application 5.1, navigation in EEG experiments often requires positioning the coil exactly over the electrodes. Its position with respect to the brain is only of secondary interest. Therefore, using a reconstruction of the head outline as described in 3.3 instead of an MRI was unproblematic. The position of the target electrodes was indicated on the virtual head by holding a tracked pointer at their centre.

The pointer coordinates were then transformed to the virtual space using ${}^{\mathrm{I}}T_{\mathrm{T}}$, see Section 3.2.2, and used as the base point for defining the stimulation pose, see Section 5.1.1.

The EEG studies were the only ones where we used a virtual head reconstruction from outline points. One example of the reconstruction can be seen in Figure 3.9. We noticed that even though reconstruction from MRI was much more detailed, reconstruction from outline points was sufficient for robotic coil positioning. The problem we faced was the calculation of the surface normal required for placing the coil tangentially to the head. Due to technical reasons the patients already wore the EEG cap when outline points were acquired, limiting the point sampling range and introducing position errors. Nevertheless, after iterated smoothing the outline was smooth enough to yield reliable normals. The loss in spacial accuracy caused by the smoothing was about 2 – 3 millimetres as our checks with the pointing device (see Sections 3.3 and 3.5) revealed.

The reconstruction algorithm [4] combined with the smoothing algorithm [172] produced a virtual head outline which was slightly smaller than the real head (about 2 to 3 millimetres in diameter). This inaccuracy was not a problem, because the coil had to be kept several millimetres away from the head surface to avoid contact with the EEG electrodes.

5.2.1. Combined TMS-EEG for epilepsy research

The study performed in collaboration with the Department of Clinical Neurophysiology of the University of Göttingen was mainly concerned with the influence of TMS on the brain cortex of epileptic patients [61]. The test protocol that has been used consisted of a single pulse transcranial magnetic stimulation (up to 60 pulses per stimulated site) with a 4 seconds long interstimulus interval. It has been applied for the stimulation of four epileptic patients with a duration of the measuring session (not including the time for the preparation of the electrodes) of 60 minutes. The most direct way to identify the dynamics of the cortical responses (in form of electroencephalographic event related potentials, ERPs) following the TMS pulses is to collocate them temporally and spatially, hence a suitable spatial definition is needed. The way that has been tried during the tests performed consisted in identifying spatial references on the scalp upon the electrodes position. The application of the robot revealed its usefulness under multiple aspects under this conditions.

So far, we have used the combined EEG-TMS robot system on four patients. For one subject, the robot system did not respond fast enough to head movements to avoid all contacts between coil and electrodes. As measurements showed, the robot-tracking feedback loop runs with 30 to 60 Hz (depending on the tracking system used) for a nearly still head (less than 1 mm movement) and no averaging of the tracking data. But due to jitter in tracking recordings, we needed to average between 3 and 6 tracking values, see Section 3.4.4.3. This delayed the response to a movement of the head by about 100 ms. Together with the reduced robot speed and acceleration[2] this caused the robot to react too slowly to small, fast wiggles of the head.

[2] See Section 3.5 (Safety).

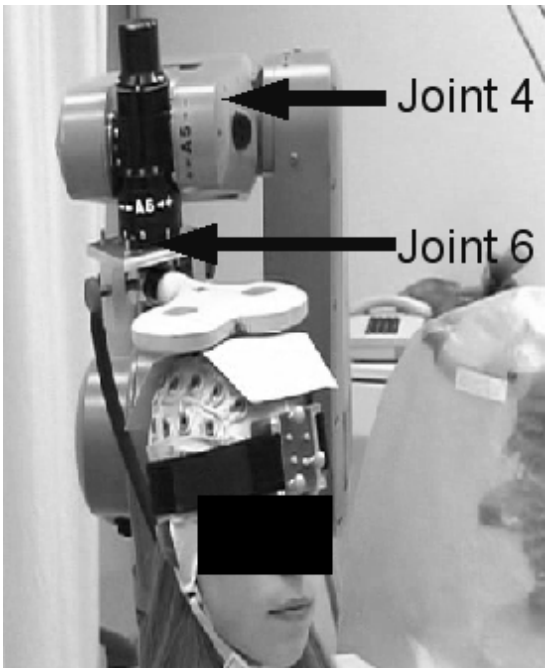

Figure 5.4.: Experimental setup for EEG measurements under TMS. The picture shows the final stage of moving the coil over C_Z. The paper tissue is required to avoid contact between TMS coil and EEG electrodes during small, fast head movements.

We remark that we saw this insufficient performance in an experiment with the Kuka KR3 robot. Optimising the tracking software for a better trade-off between error cancellation by averaging and movement detection and using the Adept robot, we are confident to improve here in the future. For the experiment, we solved the problem of the coil touching the electrodes by placing some paper tissue between coil and electrodes, see Figure 5.4.

5.2.2. Combined TMS-EEG for neuronal signal processing research

A second TMS-EEG study was performed in collaboration with the Clinic for Neurology at the University of Lübeck. Here, we used the robot system for a study on lateralised RSVP (Rapid Serial Visual Presentation) performance [182]. In short, the subject fixates a cross on the centre of the screen and is presented a stream of black letters on the left and on the right of the cross. At a certain point (called T1), a red letter appears in the stream. After continuation of the black letter stream for 100, 200, or 500 ms, a black number is presented (called T2). After the stream ends, the subject is asked to name the black number.

Experiments have shown that the performance of the subjects is significantly better, if the T2 stimulus is presented on the left side of the screen, independently from the presentation side of T1. The question arising is whether only one hemisphere is active during the task and the better performance for left T2 is due to a better performance of the right hemisphere, or if both hemispheres are active during the task and the worse performance for a right T2

Figure 5.5.: Setup of the RSVP experiment. The robot is positioned over electrode position P3 (here) or P4 and kept in place during the experiment using motion compensation. Electrodes at P7 and P8 measure EEG responses in the visual cortex, electrodes on the face measure the eye movements to correct for EOG (electrooculographic) artefacts in the EEG. The subject follows the display of letters on the screen and types on the keyboard the letter which was not black and number appearing afterwards. Head motions are tracked using the headband the subject wears and the Polaris tracking camera on the left.

is due to a inhibitive effect of the right hemisphere on the left one, which is responsible for processing the right T2.

To decide the question, we applied a short train of 5 Hz rTMS pulses at the time of T2 to the left or right brain area responsible for recognising the T2 event. During the first 30 runs of the experiment we stimulated over the P3 area (left hemisphere), during the second 30 runs we stimulated over the P4 area (right hemisphere). The rTMS pulse over these areas is thought to suppress local signal processing. For further analysis, electroencephalographic signals were recorded using electrodes at P7 and P8.

The robot system was employed for the experiment in much the same way as in 5.2.1. We first recorded the head outline using the tracked pointer device and reconstructed the head outline with the power crust algorithm [4]. We marked P3 and P4 as stimulation targets using again the pointer and commanded the robot first to P3. As there were no electrodes placed at P3 and P4, we could lower the coil such that it touched the head gently, see Figure 5.5. Then we started the motion compensation feature and kept it enabled during the first half of the experiment. After 30 runs, we then commanded the robot to P4 and enabled motion compensation until the end of the experiment.

The robot system's performance depended very much on the participant's behaviour. The experiment required the participant to follow some visual input from a computer screen and to respond to it by pressing a key on a computer keyboard on their lap. In some participants,

the change of attention from screen to keyboard was accompanied by a large head movement to look at the keyboard. In those participants the motion compensation was too slow to keep the coil at its place relative to the head. We refrained from increasing robot speed and acceleration, because at the time of the experiment the force sensor, Section 3.5.1, was not yet ready to use.

In participants with less head movement, the robot performance was generally acceptable. In those patients we could show that the response rates to right T2 when stimulating P4 (located over the right hemisphere) where about the same as the response rates for left T2 when stimulating P3 (located over the right hemisphere). On the contrary, the recognition rates for right T2 and P3 stimulation were still worse than left T2 and P4 stimulation. This favours the second explanation from above, i.e. that the right hemisphere is also activated for a right T2 and hinders the recognition work from the left hemisphere.

Unfortunately, due to the drop-out of the participants with strong head movement, we had not enough data for significant results. But a second study, using head fixation and static coil placement instead of the motion compensation, confirmed our findings and will be published shortly.

5.3. Tinnitus and chronic pain

Several studies show a positive influence of low frequency rTMS applied to the primary or secondary auditory cortex on tinnitus [34, 73, 90, 127, 128, 133].

In cooperation with the Clinics for Neurology, Neurosurgery, and Ear, Nose and Throat Medicine at the University of Lübeck we started a pilot study to confirm these findings and to investigate the potential of rTMS tinnitus treatment to predict the outcome of neurosurgical tinnitus treatment. If we find a correlation between rTMS treatment outcome and surgical outcome, some patients could be spared the invasive procedure whereas others with high operative success probability can be especially selected for the procedure.

The target points for rTMS tinnitus treatment are different from the usual targets in so far as there is no immediate response to a TMS pulse (like for the motor cortex) or external marker (like an EEG electrode). The primary and secondary auditory cortex can only be found based on anatomic or functional imaging. We used an fMRI paradigm (1 or 4 kHz pure tone on / off) to visualise the auditory cortex contralateral to the tinnitus. Data was pre-processed (functional overlay) using MRIcro software [143] an loaded as slice data with 1 mm spacing into our TMS program.

The stimulation protocol required first to determine the motor threshold, i.e. the percentage of maximum stimulator output with which a measurable motor response from the hand contralateral to the tinnitus could just be obtained. Therefore, we selected the hand representation area in the anatomic MRI and set the coil target as the nearest cortex point to it. This works as an automated procedure, see Section 3.4.1. We then evaluated the motor response at this point and four points in the neighbourhood of it for a fixed stimulator

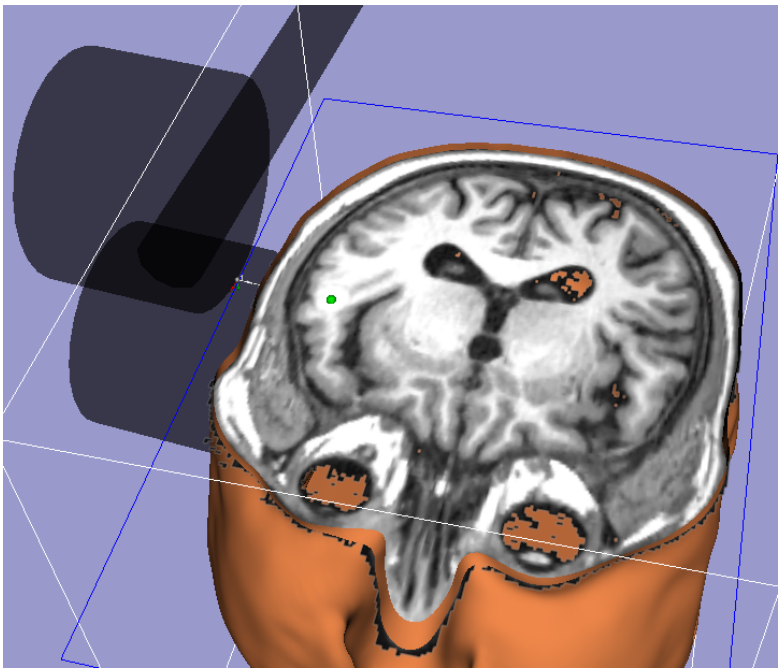

Figure 5.6.: Planning the stimulation at the auditory cortex for tinnitus treatment. The bright area represents the fMRI response area to a 3 kHz tone. The centre of the fMRI hotspot is marked (green sphere) as the stimulation target. The computer calculates the closest head surface point to the target and pre-positions the coil with the user defined distance (here: 10 mm) and orientation (here: 0°).

output.[3] At the hotspot, i.e. the point with the highest motor response, we determined the motor threshold as described above.

We then targeted the fMRI maximum that indicated the primary or secondary auditory cortex using the same method: We marked the fMRI maximum on the functional overlay of the anatomic image and let the computer position the coil at the surface point closest to it, see Figure 5.6. We set the coil orientation to 0°, i.e. the coil handle pointing backwards, and the coil distance such that the coil gently touched the head. Hereby, we used the adaptive coil distance modality described in Section 3.4.4.2: We fist commanded the robot to a position 1 cm above the head surface and gradually lowered the distance until the patient notified us that she / he could feel the coil touching. This procedure was necessary, because sometimes the patient's ear or the headband prohibited a coil distance of 0 mm (i.e. touching the head over the stimulation target). For two patients, we had to keep the coil away from the head surface by 5 – 6 mm, because of the ear being pressed too much or the headband being in the way of the coil. For the other two patients we didn't have that problem, since their head and ears allowed the headband to be put differently and out of the way of the coil.

The patients were stimulated on four to five consecutive days for 30 minutes in each session.

[3] The other four points basically confirmed that the initial point in their middle, taken from the anatomical images, was really the hotspot. Only in one of four subjects, the initial central spot did not give the highest motor response and the hotspot had to be found by stimulating at more points. The reason was that accidentally a false region was assumed to represent the hand area.

We used the motor hotspot from the first day on the next days for determining the motor threshold, assuming that no plasticity effects would lead to a strong shift of the hotspot during a period of five days. Using the robot system and the virtual coordinate system, in which we stored the stimulation points of the first day, we were able to place the coil on the same spot on the head on each of the days, see Section 3.3.3.

The motion compensation during the 30 minutes of rTMS worked mainly without problems. In one case, tracking data were not stable, i.e. the rotation information reported from the Polaris tracking system was sometimes inaccurate. This led to changes in coil position by about 1 cm. This clearly invalidated motion compensation in this case, so that we disabled the feature for the session and instructed the patient to hold the head as still as possible. Unfortunately, the reason for this faulty behaviour of the tracking system could not be fully identified; we suspect tiny scratches on the reflective coating of the reflective marker spheres and unfavourable light conditions (sun light coming through openings in the curtains) as causes. After replacing the reflective spheres and working on the curtains to close properly, the error could not be reproduced.

Apart from motion compensation, using the robotised system had also another advantage over manual TMS for this application. All stimulation positions were stored with respect to the virtual head, reloaded, and re-approached by the robot with a few mouse clicks. Thus, after the short mapping procedure to find M1, the best responding position was re-approached with one mouse click and treatment could start.

When the patients then came back for the next treatment session, we directly loaded the M1 position from file to determine the motor threshold and the stimulation pose for the auditory cortex for the rTMS treatment. Note that this did not require the same positioning of the headband, since all coil coordinates were stored with respect to the virtual head outline. A new registration ensured that the stimulation points on the real head were the same as last time.

In total, we performed the stimulation on six patients suffering from tinnitus so far. Two of the patients reported an improvement in tinnitus score at the end of the treatment week. One other patient reported a change in tinnitus perception, but this did neither improve nor worsen the impairment by the tinnitus. No patient reported a worsening of the tinnitus after the treatment.

Recent literature also reports a reduction of chronic pain after repetitive TMS over special regions of the cortex [86, 131, 132, 139, 141, 171]. In a short case study with four patients we tried to reproduce these findings using the stimulation setting suggested in [86]. In one patient we did indeed see an improvement on the pain scale, but in three patients the stimulation had no effects. The robotic procedure for stimulation was similar to the one for tinnitus (finding the motor hotspot, 20 minutes of rTMS, several treatment sessions) and so were the findings when analysing the robot's performance.

5.4. Non-human primates

The last example for an application of the robotic TMS system comes from basic neurological research. In Chapter 2 we have seen that most basic principles of TMS are well understood. But many details still await clarification. For example, the exact influence of coil geometry and coil position on the motor response is poorly understood. The main open questions hereby are the extent of motor neurons on the brain surface controlling a muscle and the effect of different electric field strengthes at different dendrites of the neurons.

To shed light on these questions, the Institute for Clinical Neurophysiology of the University of Göttingen devised an animal study on a Rhesus Macaque (*Macaca mulatta*). In the experiment, a small figure-of-eight coil (MagStim animal coil) is moved in very small steps (0.5 mm) form posterior to anterior, crossing the motor cortex at the representation of the hand muscles. At each position, a stimulation with 100% resting motor threshold (RMT) is performed and APB muscle responses are recorded.

The experiment required the use of an animal model mainly for the following reasons: Firstly, the head had to be fixed very rigidly to avoid motions, because accuracy in the range of 10 – 100 micrometres cannot be reached with the motion compensation feature due to the limitations of the tracking device. The fixation requires an invasive procedure before the experiment to attach a metal plate on the forehead, which is not acceptable for human subjects. Secondly, the cortex of Rhesus Macaques is much closer to the coil than the cortex of a human (about 6 mm compared to about 20 mm) so that TMS on Rhesus Macaques leads to much clearer responses than in humans.

There was no need for tracking the head, as the experiment did not require motion compensation, but used a fixed head instead. Therefore, we avoided the headband and recorded the landmark points and outline points necessary for registration directly in the robot coordinate system using the tracked pointer device, see Section 3.3.3. During the stimulation we recorded no tracking data, so we could switch off the tracking system altogether.

The experiment was performed in two sessions. In the first session, we did a coarse (3 mm spacing) screening of the left hemisphere with 23% stimulator output to find the motor hotspot and to estimate the RMT. The resulting grid is shown in Figure 5.7.A. In the second session, we let the robot move the coil in 500 µm steps over the hotspot from the first session. At each point, we stimulated 10 times with 22% stimulator output (equal to the estimated RMT) and averaged the motor responses. The results are shown in Figure 5.7.B.

We see that the motor response increases from about 100 mV at the ends of the stimulation line to a maximum of 600 mV at the hotspot. But the increase is not monotonic, it rather has the form of waves with in increasing amplitudes, see Figure 5.8.A. As we set the stimulator output to the motor threshold, one could assume that only the very peak of the electric field has any excitatory effect (see Figure 4.5 for a visualisation of the electric field of a figure-of-eight coil). Further, it is known that the representation of muscle is not concentrated in a single point, but spread out and interwoven with neighbouring muscle representations, [135]. So the peaks in Figure 5.8.A could be produced by the electric field peak aligning with a colony of the APB neurons. Similarly, low values of the MEP at a stimulation site would indicate that there are less APB neurons at the maximum of the electric field.

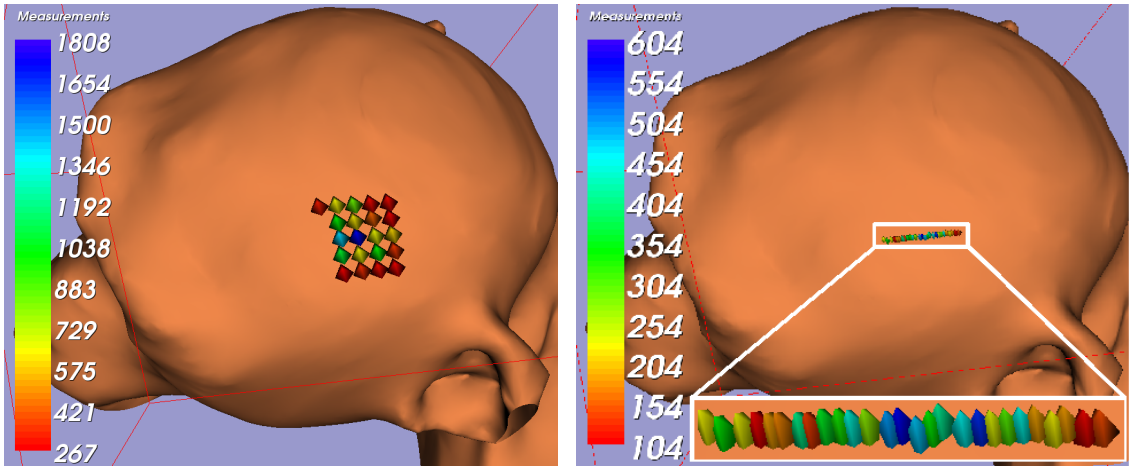

A *B*

Figure 5.7.: Stimulation results for the Rhesus Macaque experiment. A: Grid pattern to find the motor hotspot, stimulator output at 23%. B: Stimulation with 22% stimulator output along a line crossing the central sulcus at the motor hotspot.

But there is also a converse interpretation. Suppose the electric field of the TMS coil has no sharp peak under the centre of the coil, but rather a plateau of high value of several millimetres diameter as Figure 4.5 indicates. Then the MEP response of the APB would indicate how many of these local APB representations are within the plateau area of the field. As the coil is moved towards the hotspot, more APB neurons are recruited, leading to a monotonic increase of the MEP until the hotspot is reached. Clearly, that is not what Figure 5.8.A shows. But recording MEPs is a difficult business, especially if the subject moves its arms from time to time and has no defined muscle tonus at the stimulation.[4] Taking this into account, we smooth the data using a running median filter applied to three neighbouring MEPs, respectively, i.e. the MEP at x_i is the middle value of the MEPs at x_{i-1}, x_i, and x_{i+1}. The result is shown in Figure 5.8.B and complies with the prediction of monotonously increasing MEP response until the hotspot. In this interpretation, the ups and downs of the MEP in Figure 5.8.A have no meaning other than noise in the data.

To resolve the matter, we need to perform additional experiments. These will involve stimulating the same posterior-anterior line in several sessions. If Model 1 (sharp electric field peak) is true, we expect the coordinates of the peaks of the MEPs of the different sessions to agree. If Model 2 is true, the peaks will be distributed randomly with no specific pattern.

Of course, there is the challenge of registering the coordinates of the several sessions. In principle, our system does this by default, see Section 3.3.3. But here we have special requirements on accuracy; we would like the registrations to agree to about 100 µm. Our investigations show that at the moment we do not meet this accuracy requirement for a moving head, see Section 6.1.1.3. But we might be able to meet the accuracy criterion for a fixed head and the accuTrack tracking system, which has a specified precision of 100 µm RMS[7].

[4]For the experiment, only the head of the monkey was restrained whereas the limps could move freely.

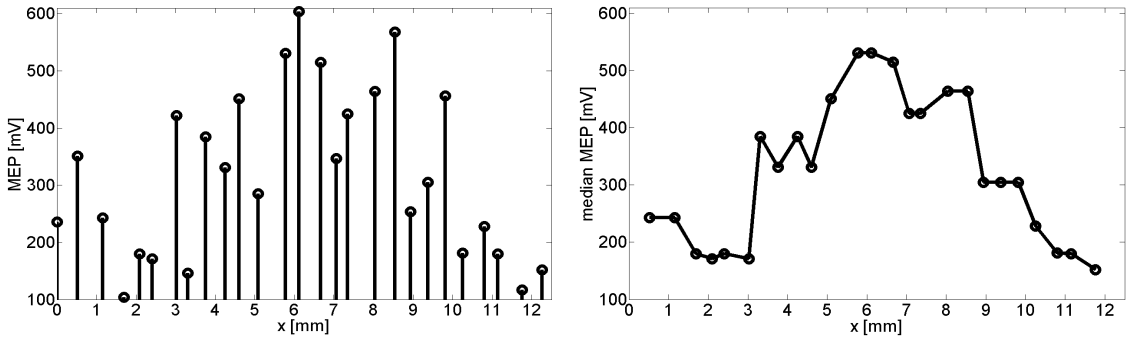

Figure 5.8.: Stimulation results along the posterior-anterior line for the Rhesus Macaque experiment. A: Raw data. B: Running median filter (along x-axis) of size 3 applied to the data of A.

The quality of the registration depends on the accuracy of the sampled landmark points (start value for the ICP) and surface points. We need to investigate the influence of skin motion, hair, and tracking jitter on the sample point recording and subsequent ICP registration to the virtual outline. If the outcome is not satisfactory, we will have to try with higher number of rigid (artificial and natural) landmarks on the ape's head. We would store the position of the landmarks with respect to the virtual head outline in the first session and register the head in subsequent sessions only against these landmarks. This has the advantage of having a closed form solution [58], so that the registration of data between sessions will be quite stable. The disadvantage is that the registration to the virtual head in the consecutive sessions might be worse than in the first session, leading especially to different head normals and thus to different coil orientations in the sessions. Further, it is not clear whether enough well defined and stable landmarks can be found.

6. Discussion

In this thesis, we presented a robotic assistance system for image guided, motion compensated transcranial stimulation and its special application for motor cortex mapping. This chapter discusses the system's performance under laboratory and real world conditions. We first analyse the robot part of the system with respect to accuracy (Section 6.1) and its performance in applications (Section 6.2) before coming to the algorithmic part for the motor cortex mapping application (Section 6.3). Finally, Section 6.4 gives an outlook on the future work to improve the system further.

6.1. Accuracy of the robotic assistance system for TMS

One of the most important questions is the accuracy of the system, because this distinguishes a robotic system from a manual one. We investigate this in two settings: First, the static problem of placing the coil at a defined position, second, the dynamic problem of keeping the coil in place when the target moves.

6.1.1. Static head

6.1.1.1. Component analysis

The following transforms influence the accuracy of the coil positioning by the robot (see also Figure 3.6):

1. ${}^{\mathrm{I}}T_{\mathrm{H}}$ – the transform between the (virtual) image coordinate system and the head coordinate system defined by the head marker. The transform is determined in a two step procedure using landmark and iterative closest point registration, see Section 3.3.3. The error in this step depends on the tracking accuracy, the precision of the head segmentation, the number and distribution of sampled surface points, and the quality of the initialisation with the landmark registration. Furthermore, movements of the head marker relative to the cranium impair the accuracy of ${}^{\mathrm{I}}T_{\mathrm{H}}$.

2. ${}^{\mathrm{H}}T_{\mathrm{T}}$ – the transform between the head marker coordinate system and the tracking system, i.e. the pose of the head marker in tracking coordinates. The accuracy of this step is the accuracy of the tracking system for the head marker geometry.

3. ${}^{\mathrm{T}}T_{\mathrm{R}}$ – the transform between the tracking coordinate system and the robot coordinate system. We register the two coordinate systems recording the position of a marker tool rigidly attached to the robot end effector at several positions and solving an over-determined linear system, see Section 3.2.2. The accuracy of the registration depends on the tracking accuracy, the robot accuracy, and the number and distribution of the recorded marker points.

4. ${}^{\mathrm{R}}T_{\mathrm{E}}$ – the transform between the robot base and the robot end effector, i.e. the positioning accuracy of the robot.

5. ${}^{\mathrm{E}}T_{\mathrm{C}}$ – the transform between the coil and the robot end effector. It is determined by recording the coil coordinate system's origin, a point along its x-axis, and a point in the x-y+-plane with a tracked pointing device. So the error in this step depends on the accuracy with which the pointer is placed on the coil marks, the tracking accuracy, and the robot accuracy.

According to the manufacturer's specifications, the Adept robot has a position repeatability of 30 µm in each direction and uses absolute joint encoders with a resolution of 0.001° [1]. Unfortunately, Adept doesn't specify their calibration accuracy, but assuming that it is of the magnitude of the encoder resolution, we arrive at an error for ${}^{\mathrm{R}}T_{\mathrm{E}}$ of at most 50 µm.

To determine the transform between robot and tracking coordinate system, we usually record data from 20 to 30 positions within a sphere of radius 100 mm and end effector orientation change of 30°. For the combination Adept Viper s850 robot – NDI Polaris tracking system, the RMS error is usually about 0.1 mm and the maximum error is usually about 0.2 – 0.3 mm. Laboratory experiments have shown that these values are not much influenced by the numbers of points recorded or the radius of the sampling sphere. Thus, we take ${}^{\mathrm{T}}T_{\mathrm{R}}$ to be accurate up to 0.2 mm.

As the list shows, tracking accuracy is crucial and influences all transforms but ${}^{\mathrm{R}}T_{\mathrm{E}}$. For the Polaris system and a static marker, measurement distribution has been shown to be approximately gaussian with a standard deviation of 13 µm in x-direction, 10 µm in y-direction, and 40 µm in z-direction [37].[1] Note that these values only represent how much the measurements fluctuate if the marker position is constant. To assess the error over the tracking range of interest, we make use of the error estimates for ${}^{\mathrm{R}}T_{\mathrm{E}}$ and ${}^{\mathrm{T}}T_{\mathrm{R}}$. If we assume the errors of the robot and tracking system to be independent, the 0.2 mm maximum error for ${}^{\mathrm{T}}T_{\mathrm{R}}$ provides an upper limit for the error of the tracking system, i.e. for the transform ${}^{\mathrm{H}}T_{\mathrm{T}}$ and the recordings of the pointer device and the head marker. As the error for ${}^{\mathrm{R}}T_{\mathrm{E}}$ is about one order of magnitude smaller, we can assume this limit to be sharp, i.e. to represent the true error of ${}^{\mathrm{H}}T_{\mathrm{T}}$.

The error in coil registration ${}^{\mathrm{E}}T_{\mathrm{C}}$ depends on the coil used and the coordinates considered. In the current implementation, the coil's coordinate system is directly defined using a tracked pointer to mark a special point, a special line, and a half-plane on the coil's surface. The quality of the registration depends therefore on the ability of the user to point to these features. For example, the standard Medtronic figure-of-eight coil has a slightly curved

[1] The x-vector of the Polaris runs from one camera of the stereo system to the other, the z-vector points along the viewing direction of the camera.

upper surface and no marks on the lower surface (see Figure 5.4), which makes it difficult to mark the required points. By contrast, the Medtronic coils have a flat upper surface with coordinate lines on it, making it easier to select the right points (see Figure 3.7.B). In any case, if the pointer can be placed on a flat surface (bottom surface for MagStim coils, upper surface for Medtronic coils), the registration error along the coil's z-axis (normal to the surface) will be of the magnitude of the tracking system. In contrast, the error in x-y-coordinates will be the error of marking the features correctly, which we estimate to be about 1 mm. The same argument shows that the coil's z-vector is quite accurately defined, whereas there might be some error (depending on the coil's size) in defining the x-vector.

6.1.1.2. Head registration

Of all transforms, the accuracy of the registration between real and virtual head coordinates, ${}^{\mathrm{I}}T_{\mathrm{H}}$, depends most on the experimenter's skills. It has to be ensured that the outline points recorded with the tracked pointer are located on the skin of the subject and distributed as widely over the head as possible. Furthermore, the result of the iterative closest point (ICP) scheme, which computes the final transformation ${}^{\mathrm{I}}T_{\mathrm{H}}$, depends on its initialisation. If the initial matching between the real and virtual landmark is poor, the ICP will get trapped in a local minimum, resulting in a large error of ${}^{\mathrm{I}}T_{\mathrm{H}}$.

We use three benchmarks to evaluate the accuracy of the registration between real and virtual head outline:

1. the mean distance between transformed real surface points and virtual surface,
2. the difference between transforms ${}^{\mathrm{I}}T_{\mathrm{H}}{}^{i}$ for differing samplings i of head surface points and landmark points,
3. the distance between the transformed coordinates of an artificial landmark on the real head and its image in the virtual scene.

Benchmark 1 is the most important one for the safe application of the robot: It gives (roughly) the registration error between the real surface of the head and the virtual surface. If the real and the virtual head outline at the stimulation point disagree, the robot either presses the coil hard against the head (virtual outline inside real outline) or holds the coil with some distance from the head (virtual outline outside real outline). The main factors influencing the result are the quality of head segmentation from 3D-images (CT or MRI) and how good the experimenter was able to keep the pointer in direct contact with the scalp when sampling the outline.

Benchmark 2 evaluates how much the registration depends on the sampling of head surface points. If different samplings lead to much different registration results, special care must be taken to sample enough outline points over a wide range of the head, including especially feature-rich areas like the face. Further, it determines how much the registration depends on the initialisation via the landmark points. It evaluates how much the result changes if the user marks slightly different points as correspondences to the landmarks on the real head and tells how carefully the user should mark the landmark points and their virtual counterparts.

n	outliers	RMS error	mean error	max error
575	15.6	0.44	0.34	1.30
±67	±7.9	±0.05	±0.04	±0.17

Table 6.1.: Benchmark 1 results for 10 registrations of the outline of a plastic phantom head to its reconstructed surface from CT data. The table gives mean ± standard deviation for the following variables: n is the number of sampled surface points, outliers *specifies the number of surface points classified as outliers during the registration,* RMS error *gives the root mean square of the distance of all transformed non-outlier points to the virtual surface,* mean error *gives the average distance of all transformed non-outlier points to the virtual surface,* max error *gives the maximum distance of all transformed non-outlier points to the virtual surface. All error values are given in millimetres.*

Finally, Benchmark 3 specifies the discrepancy between a TMS target defined over the virtual scene, e.g. using an MRI of the subject, and the actual target spot in reality. It is of crucial importance for motor cortex mapping and image based TMS treatment. We have seen in Sections 4.4 and 5.4 that the effects of stimulation change on a millimetre scale. So we need to ensure that the registration as the basis for targeting and mapping procedure is at least accurate to this degree.

Benchmarks 1 and 2 were tested on the plastic phantom head displayed in Figure 3.8. We acquired a CT image of the head with spacing of 0.44 mm × 0.44 mm × 1.0 mm. The 3D image was down-sampled to 1 mm isotropic scaling, loaded into our TMS software and taken as the basis for virtual head outline reconstruction, see Section 3.3.2. The real head outline was sampled 10 times using the Polaris system and referenced to a head marker. The outline consisted of 477 to 652 surface points and four landmarks. The outline points were sampled on the face (about 50% of the points of each run) and on the scalp. As landmarks we took the outer canthi of the eyes, the nasion, and the tip of the nose. For each run, we then marked the corresponding landmark points on the virtual outline and started the registration procedure as described in Section 3.3.3. Table 6.1 summarises the results of the 10 runs for Benchmark 1, Table 6.2 summarises the results of the 10 runs for Benchmark 2.

The values in Table 6.1 demonstrate that our registration approach matches the surfaces of the real head and the reconstructed surface from 3D image data with sufficient accuracy for automated positioning of a TMS coil by a robot. The mean distance of the surfaces of about 0.4 mm allows to command the robot to place the coil with no distance from the head. The small error in distance from the head ensures that the coil is not pressed too much against the head or is too far away from the head.

Table 6.2 shows that the different samplings of the head outline only lead to slight differences in the registration. We see that if the head is registered anew, the transformed coordinates of a target point over the central region of the real head differ by less than a millimetre.

The results for the second benchmark from Table 6.2 also allow an estimate of the inter-session repeatability of the robot aided stimulation. We evaluated the difference between two registrations T_1 and T_2 by the distance between a point $q = (55, 26, -127)$ on the real head, located approximately over the hand area of the right motor cortex, and $q' = (T_2)^{-1} * T_1 * q$. This corresponds to the scenario that a target point q is defined in a first TMS session, stored in virtual coordinates as $T_1 * q$, and re-approached in a second session as $(T_2)^{-1} * T_1 * q$.

	T_x	T_y	T_z	T_α	T_β	T_γ	p_x	p_y	p_z
mean	39.0	178.8	164.6	89.5	63.5	93.5	181.3	101.7	199.0
std	0.36	0.38	0.48	0.62	0.25	0.59	0.46	0.38	0.36

Table 6.2.: Benchmark 2 results for 10 registrations of the outline of a plastic phantom head to its reconstructed surface from CT data. Columns: T_x, T_y, T_z give the x, y, and z value (in millimetres) of the translation vector of the transform matrix describing the registration. T_α, T_β, T_γ give the euler angles (in degrees) of the registration transform. p_x, p_y, p_z give the x, y, and z coordinates (in millimetres) of the transform of a point located approximately over the hand area of the right motor cortex. Rows: mean *gives the average values over the 10 experiments,* std *gives the standard deviation of the values.*

The average distance between q and q' for two different T_1 and T_2 from our experiment was 1.15 mm.

For Benchmark 3, we extended our test framework by adding five CT compatible markers to the plastic phantom head. The markers were placed over the hand areas of the left and right motor cortex (EEG-electrode positions C3 and C4), the central frontal polar region (electrode position Fpz), the central region (electrode position Cz), and the central occipital region (electrode position Oz). Each marker was made from a steel nail of less than a millimetre diameter and 1 cm length. The nails were inserted perpendicular in the phantom, with the nail head aligning with the phantom surface. The markers produced a sharp echo in the CT scan of the phantom without creating too strong metallic artefacts. The nail's head was also easy to mark with the pointer on the real head, giving us corresponding landmark coordinates in both coordinate systems (head marker system H and image coordinate system I) with high spacial resolution.

We used the transforms obtained for Benchmarks 1 and 2 and compared them against the landmark transform for the artificial landmarks. Therefore we took the averaged recordings (10 samples) of the real landmark positions and registered them to the virtual landmark positions from the CT image using Horn's scheme [58]. Assuming a perfect artificial landmark transform, we compute the error of our two-step ICP registrations as

$$\mathrm{d}_i = \|T_{\mathrm{ICP}}^{-1} T_{\mathrm{ALM}} p_i - p_i\|, \tag{6.1}$$

where p_i is the i^{th} artificial landmark, T_{ICP} the transform from the two-step ICP registration and T_{ALM} the artificial landmark transform.

The results for Benchmark 3 are summarised in Table 6.3. The average error in landmark position over 10 trials is 1.1 mm $\pm$ 0.35 mm. We see that the error is nearly independent of the location of the landmark. Thus, targeting structures anywhere on the head on the basis of 3D data with the robotised TMS system will be accurate to about 1 mm.

6.1.1.3. Cumulated analysis

So far, we have analysed the single components influencing the accuracy of the system. Now we inspect the accuracy with which a point, defined on the 3D image data (CT or MRI,

	Fpz	Cz	C3	C4	Oz
mean error	1.13	1.15	1.05	1.27	1.10
std dev	0.35	0.44	0.40	0.34	0.22
max error	1.56	1.94	1.86	1.69	1.55

Table 6.3.: Benchmark 3 results for 10 registrations of the outline of a plastic phantom head to its reconstructed surface from CT data. Each column gives the results for one of the artificial landmarks; the heading specifying the position of the landmark in EEG electrode terms. Rows: mean error *gives the average distance between the artificial landmark and the back projected virtual landmark, see Equation* (6.1)*,* std dev *gives the standard deviation of the error,* max error *gives the maximum error.*

virtual coordinates), is targeted by the robot held coil. Again, we used the phantom head with artificial landmarks and its 3D CT data set described in the last section. The coil we chose for the experiment was the Medtronic MC125 circular coil, because its hole in the centre allowed us to check the alignment of the coil's origin with the target spot. The experiment consisted of commanding the robot to each of the five artificial landmarks using their image representation on the computer, see Section 3.4.1, and measure the distance between the coil's centre and the landmark on the real head.

In total, we performed 5 trials, targeting each of the five artificial landmarks from the previous section. In each trial, we went through the complete system set-up, i.e. we determined all the transforms ${}^{\mathrm{T}}T_{\mathrm{R}}$, ${}^{\mathrm{C}}T_{\mathrm{E}}$, ${}^{\mathrm{I}}T_{\mathrm{H}}$ anew. After the robot completed its trajectory, we marked the position of the coil's origin on the phantom head with a pen. After each trial we measured the distance of each pen mark from its corresponding artificial landmark, namely the hole in the plastic head from the steel nail. We also noted the direction of displacement of the pen mark with respect to the artificial landmark.

The average error over all five landmarks was 2.04 mm with a standard deviation of 0.92 mm. Table 6.4 gives detailed results for each of the five landmarks. We see that the error in targeting central points (C3, Cz, C4) is smaller than the error in targeting frontal (Fpz) or occipital points (Oz), but there seems to be no connection between the distance of the target point from the head marker and the accuracy in positioning the coil.

It is remarkable that there is a strong bias in the direction of the displacement, e.g. the coil's centre position was left of the artificial landmark in all trials. We assume this to be due to an error in marking the artificial landmark as a target in virtual coordinates. Recall that the spacing of the 3D CT data set was 1 mm and that the metal nails (the artificial landmarks) create artefacts of a few millimetres in diameter in the CT. So it is probable that we did not mark the exact point where the nail pinched the phantom head. Indeed, if we calculate the centre of gravity of the coil's centre points for each artificial landmark over the five trials and transform it back to virtual coordinates, it also lies on the nail artefact for all five landmarks.

Therefore, we use a second measure for the static overall performance of the system. We calculated the distance of the coil's centre point for each trial from the centre of gravity over all trials. This corresponds approximately to the scenario when we had chosen the centre of gravity coordinates in virtual coordinates as target representations for the artificial

	Fpz	Cz	C3	C4	Oz
Trial 1	4.0 r	1.5 lf	2.5 l	2.5 r	1.5 l
Trial 2	2.5 rf	1.5 lf	2.5 l	1.0 rf	1.5 l
Trial 3	2.0 r	2.0 lf	2.0 l	1.5 r	3.0 rb
Trial 4	2.0 rf	0.5 r	1.0 l	3.5 rf	2.5 lb
Trial 5	2.0 rf	2.0 lf	1.5 l	0.5 b	4.0 lb
Accuracy	2.5 ± 0.87	1.5 ± 0.61	1.9 ± 0.65	1.8 ± 1.20	2.5 ± 1.06
Repeatability	1.13± 0.54	0.69± 0.62	0.52 ± 0.30	1.29± 0.69	1.83± 0.98

Table 6.4.: Cumulated analysis. Each column gives the results for one of the artificial landmarks; the heading specifying the position of the landmark in EEG electrode terms. Rows: Trial $1-5$ *gives error and direction of displacement (r = right, l = left, f = front, b = back of the head) of the coil's centre when targeting the landmark for each trial.* Accuracy *gives mean and standard deviation of the error when targeting a landmark.* Repeatability *gives mean distance ± standard deviation from the centre of gravity of the coil's centre from trials 1 – 5. All values in millimetres. The accuracy over all five landmarks is 2.04 mm ± 0.92 mm. The repeatability over all five landmarks is 1.09 mm ± 0.77 mm.*

landmarks. It also gives a measure of variability of the targeted points over several sessions (inter-session repeatability). The repeatability over all five trials and five landmarks was 1.09 mm with a standard deviation of 0.77 mm. The repeatability for each single landmark is given in the last row of Table 6.4. We see that apart from Oz, the repeatability error is much smaller than the accuracy error, supporting our argument that we did not mark the exact landmark coordinates on the CT data, introducing a bias error in the accuracy analysis.

6.1.2. Moving head – motion compensation

We evaluate the system's performance in compensating head motions by adjusting the coil's position in two ways:

1. Latency – The time between the start of a movement of the head and the start of the movement of the robot to compensate for the shift in target position.

2. Compensation time – The time between the start of a movement of the head and the moment the coil reaches its target position again. The compensation time depends of course on the speed and extent of the head motion.

Besides the usual set-up with a Polaris tracking system, an Adept Viper s850 robot, and a Medtronic MC125 circular coil, we employed a second robot (also an Adept Viper s850) and an Atracsys accuTrack Compact tracking system to measure the two values. The second robot was used to move the head marker in a controlled manner. The accuTrack system was used to record the movements of the head marker and the coil.[2] We attached one LED on

[2]The two robots are able to record their own positions with timestamps. But to yield reaction time and compensation time, the clocks of the robot controllers must be synchronised up to a millisecond. We avoid this by using a third system – the accuTrack – to measure the movements of both robots. The accuTrack has the further advantage of being external, and thus independent, to our TMS robot system.

the coil and on the head marker, respectively, so to have a tracking speed of 2 kHz available for the accuTrack.

We have shown in Section 3.4.4.2 that no registration of the head is necessary for motion compensation. So we can perform the tests using just the head marker. We position the coil with a distance of about 10 cm from the head marker. In a first experiment, the second robot moves the head marker 10 cm away from the coil along a linear trajectory with maximum speed and acceleration. We measure the latency by determining the start of the movement of the head marker and the coil, respectively, using the accuTrack system. We defined the start time as the first time the accuTrack LED's position changed by more than three times the RMS of its readings in rest (usually between 0.1 and 0.2 mm).

Table 6.5 shows the different latencies of the TMS system in dependence of the TMS robot's speed and acceleration and the number of tracking pose averages used (see Section 3.4.4.3). We see that the latency of the system is about 110 ms for speed and acceleration values of 25% or more of their respective maximum, independently of the number of pose averages for tracking.

For speed and acceleration values of 10% and 3% we measure higher latencies. The reason lies in the internal trajectory planning of the Adept: It calculates a trajectory through the last three commanded points. So if a new position is commanded before the actual position is reached, the robot does not directly move to the new position, but moves through the old position first. In our experiment, we activated motion compensation well before we moved the head marker. As there is always jitter in the head marker measurements, the robot is moving all the time to compensate for these perceived tiny motions. If robot speed and acceleration are low, this still needs some time. Hence, the higher latency measurements for robot speed and acceleration of 10% and, much more pronounced, for robot speed and acceleration of 3% of their maximum value originate in an increased latency on the robot's side.

It is possible to disable the internal trajectory planning of the Adept, which would improve the response time to a head motion. But the only way to do this is to command a stop ("Brake") before each new position. This has the effect of clearing the internal target queue and lets the robot move directly to the new target. The drawback is an unsteady move pattern with many stops and accelerations. In practical tests, this was quite disturbing for the subjects, so we have decided not to use the Brake-command in our implementation and accept a slightly increased latency in response to a head motion.

Table 6.6 shows the compensation times of the TMS system for a displacement of the head marker of 10 cm for different robot speed and acceleration values and number of tracking pose averages. As expected, the compensation time increases with lower robot speeds and accelerations. The compensation rises also with higher tracking average value, but only for low robot speed and acceleration. The reason is that the single change in position of distance d is recognised as n small changes of $\frac{d}{n}$ by the system, n being the tracking pose averaging number. If robot speed and acceleration are high, the robot might implement the perceived change of $\frac{d}{n}$ within one tracking cycle of $\frac{1}{60}$ s. So the robot comes to a near standstill when the next increment of $\frac{d}{n}$ is commanded and has to accelerate to maximum speed again.

	av = 1	av = 3	av = 6	av = 10	av = 30	av = 100
speed = 3	264.4	280.4	164.2	206.5	219.6	128.2
speed = 10	119.4	136.0	152.5	132.5	124.8	143.2
speed = 25	106.8	99.5	106.3	116.5	128.2	117.0
speed = 50	109.7	108.7	117.0	119.4	110.2	110.7
speed = 100	98.0	116.5	104.3	102.9	105.3	108.7

Table 6.5.: System latency in motion compensation for different tracking pose averages (denoted av) and robot speed and acceleration values (denoted speed, values in % of robot maximum speed and acceleration). Latency was measured as time between the start of the head marker movement and the start of the TMS coil movement. Movements were measured with a separate optical tracking system operating at 2000 Hz. All table values in milliseconds.

These additional acceleration and deceleration phases slow down the movement and lead to increasing compensation times with rising tracking pose average numbers.

We see in Table 6.6 that this effect is most pronounced for high robot speed and acceleration values. For safety reason we do not operate our system with such high speeds, see Section 3.5. At our standard setting of speed and acceleration of 10%, we could average about 30 tracking poses without noticeable change in compensation time. Of course, the effects of averaging get stronger with smaller head marker amplitudes d', because a smaller step of $\frac{d'}{n}$ cm can be compensated within one tracking cycle also with lower robot speed. Nevertheless, if we use an averaging value of 3 to 10, as suggested in Section 3.4.4.3, we achieved small latencies in the applications from Chapter 5.

The experiment shows that with the current system set-up we are able to respond to a head motion after about a tenth of a second. The time to restore the original position of the coil with respect to the head depends on the amplitude of the motion and on the robot's speed. The system with its standard settings of speed and acceleration needs about 2 s to compensate a sudden large movement of 10 cm. As indicated in the discussion above, the compensation time depends linearly on the amplitude d of the motion as long as the averaging number n is not too big. Thus, for small head movements of less than a centimetre, the original position relative to the head will be re-established within about 300 ms (100 ms latency + 200 ms compensation time).

6.2. System performance in real-world applications

In the previous section we have analysed the system's performance under laboratory conditions and seen that its accuracy allows for precise targeting, sufficient compensation of target motions, and high inter-session repeatability. In this section, we report on the system's behaviour in the applications from Chapter 5. We highlight three different aspects:

1. Device performance — how the main devices of the system, i.e. the robot and the tracking system, performed,
2. Component performance — issues for the separate components of the treatment, i.e. positioning of the coil, trajectory to a new position, and motion compensation,

	av = 1	av = 3	av = 6	av = 10	av = 30	av = 100
speed = 3	6927.6	6801.1	6657.6	6483.0	7334.2	7859.0
speed = 10	1933.7	2009.1	2000.8	2138.5	2174.9	2827.7
speed = 25	749.8	795.5	812.0	855.8	991.5	1863.6
speed = 50	425.8	384.5	399.1	486.2	669.0	1728.4
speed = 100	154.9	195.3	250.3	339.3	573.7	1701.2

Table 6.6.: Compensation times for a motion of 10 cm for different tracking pose averages (denoted av) and robot speed and acceleration values (denoted speed, values in % of robot maximum speed and acceleration). Compensation time was measured as time between the end of the head marker movement and the end of the TMS coil movement. Movements were measured with a separate optical tracking system operating at 2000 Hz. All table values in milliseconds.

3. System quality attributes — applicability, capability, usability, and comfort.

6.2.1. Device performance

6.2.1.1. Tracking

Although head and instrument tracking appear to be a solved problem when reviewing the literature [38–40, 48, 50, 53, 54, 77–80, 112, 114, 115, 159, 160], we still had some issues with it. For our application we mainly used the Polaris infrared tracking system with passive markers. While the system is very accurate under perfect conditions (0.35 mm RMS error, [116]), which was confirmed in our laboratory experiments, we had big problems operating it when sunlight streamed in from the windows. In this case, markers were often not seen by the system, even though they were clearly within the tracking range. So we had to make sure that as little as possible stray infrared light was present during the experiments.

Furthermore, the accuracy depends crucially on good, homogeneous reflectance of the marker constructing spheres. If one of the spheres is partially occluded or its reflecting cover damaged, its position is incorrectly calculated. This results in errors in the calculation of the marker position and, especially, of the marker orientation. In one of our artificial tests employing the plastic head instead of a real head, the coil was positioned such that it partially occluded one marker sphere. As expected, this resulted in false readings of the head position and a compensation by the robot using motion compensation. This in turn changed the occluding pattern, leading again to another head position reading. Thus, the head appeared constantly moving to the system although it laid perfectly still, resulting in endless motion of the robot.

To avoid the problems related to the Polaris system we tested the MicronTracker2 S60 and H40 video optical tracking systems (0.2 mm– 0.25 mm RMS, [25]), which show more robustness towards light conditions. Another advantage lies in their special marker design. It ensures that the marker pose can be calculated correct even if the marker is partially occluded. Thus, it avoids changes in orientation if parts of the marker are not visible for the camera.

The big disadvantages of the MicronTracker systems compared to the Polaris are the limited tracking range of only 1.20 m and a maximum tracking speed of 30 Hz (S60) / 15 Hz (H40)[3]. This requires the camera to be put very close to the patient and the robot, increasing the danger that the camera is accidentally moved. This would invalidate the robot-tracking-registration ${}^{\mathrm{R}}T_{\mathrm{T}}$ and require a new calibration. Further, the reduced frame rate compared to the Polaris system decreases the quality of motion compensation. Finally, tests with the S60 and H40 system revealed issues with the orientation stability. The jitter in orientation was much higher than for the Polaris system, resulting in false "compensation movements" of the robot, see Section 3.4.4.3. Thus, we mainly used the Polaris system for our applications.

6.2.1.2. Robot

Both robots we have used so far, the Kuka KR3 and the Adept Viper s850 have the same architecture, 6 joints serially linked, with similar link lengths. The workspace of the robots has been large enough to stimulate a wide range of points on the head without changing the head position. For example, we have been able to stimulate the left and right motor cortex in one session (motor cortex mapping, Section 5.1.2 and TMS-EEG experiments, Section 5.2). Only if points at the front and the back of the head are to be be stimulated during one session, e.g. Fpz and Oz, it would be necessary to reposition the head with respect to the robot.

Comparing the two robots, the Adept has bigger joint limits for Joints 4 and 6, allowing for more joint settings implementing a pose. Thus, in general, the trajectories in joint space are shorter for the Adept. This means that the Adept reaches target poses faster and with less arm and coil movement.

Another advantage of the Adept is the more advanced software architecture. The range of commands, and therefore steering possibilities, is much bigger than for the Kuka. Especially the real time capabilities distinguish the two devices. The Adept has seven threads running parallel on its controller, allowing the user to influence a move command during its execution, e.g. enabling a software-controlled stop of a move. Further, Adept uses an internal trajectory module, considering the next three target points when calculating the trajectory. This means that the robot operates much smoother in motion compensation, because it does not stop at a commanded pose and starts a new move to the next target, but moves smoothly through the first target pose towards the second one. Hereby, the user can define the accuracy with which the first target pose is met.

A disadvantage of both robots is the limited range of Joints 4 and 6. This creates situations like the one described in Section 3.2.3 where it is sometimes necessary to move a joint by a large angle $\alpha \gg 90°$ to implement a pose which could otherwise be reached with a small change of $180° - \alpha \ll 90°$ if there were no joint limits. This creates safety problems, because big joint moves can cause big coil movements and bring the coil close to the head. We take care of that with our special trajectory algorithm, see Section 3.4.3, but for the price of prohibiting transitions with large coil movements and restricting the poses which

[3] The recently released H60 system has a tracking range of 2 m operating at 15 Hz. This system was not available for testing for this thesis.

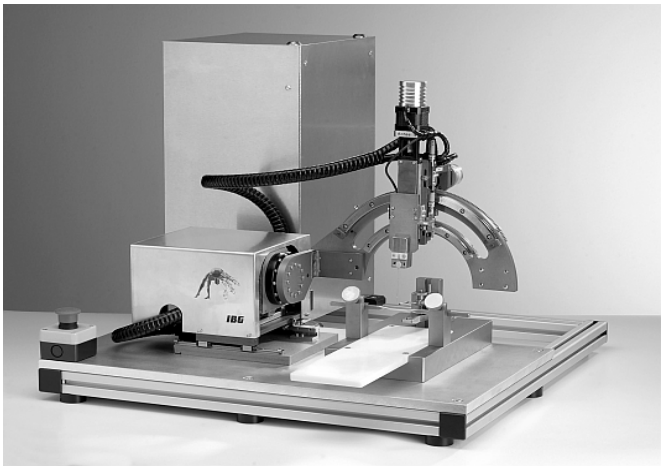

A: The spherical assistant for stereotactic surgery (SASSU) robot, a system for placing electrophysiological recording needles accurately in rodent brains. Picture by Lukas Ramrath, with friendly permission.

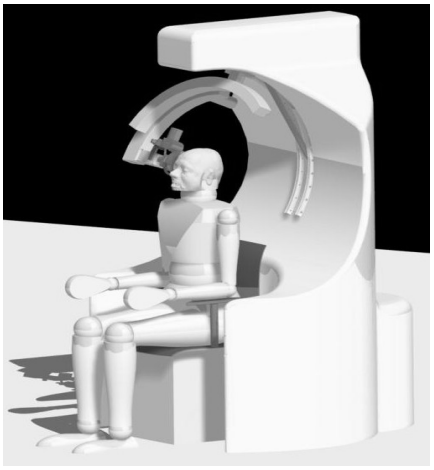

B: Design for a TMS robot proposed by Lebossé et al. . Figure from [84], with friendly permission of the author and the publisher.

Figure 6.1.: Possible alternative robot designs for TMS.

can directly be reached from one position. A solution might be to use robots from other manufacturers like the Kawasaki FS03N which have an unbounded range for Joints 4 and 6. So far we have not been able to test our ideas on it, so we can't judge if there are drawbacks, e.g. in the control of this robot.

Finally, new robot designs like a scaled version of the spherical assistant for stereotactic surgery (SASSU) [134], Figure 6.1.A, or the system proposed by Lebossé et al. [85], Figure 6.1.B, might extend the range of points which can be targeted during a TMS session and ease the transition from one stimulation point to the next. We briefly discuss how our system could be adapted to use such robots in Section 6.4.2.

6.2.2. Component performance

6.2.2.1. Coil positioning

The positioning feature of the system showed satisfying results. In the motor cortex mapping and pain treatment experiments, subjects reported that the coil touched the head surface gently when the distance was set to zero. Problems occurred when the virtual head surface was not sufficiently segmented or reconstructed because of unsuitable MRI data or insufficient sampling of outline points. In those cases the virtual head surface was too rough, leading to false calculations of the surface normal for placing the coil tangentially. This could be resolved partially by increased smoothing of the surface, see 3.3, but for the price of less spacial accuracy. In one case, the experiment therefore had to be suspended to acquire a new sequence of MRI data, featuring the tissue air boundary more clearly.

The recently introduced online coil distance adaptation improved the positioning further. It allowed to place the coil in a safe distance of about 1 cm from the head surface and to reduce this distance until the subject felt the coil on the head. This way, small inaccuracies in the registration ${}^{\mathrm{I}}T_{\mathrm{H}}$ in normal direction to the head can be compensated. It also adapt the positioning to obstacles like EEG electrodes, the headband or the subject's hair, which were not present in the medical image data (MRI, CT).

6.2.2.2. Trajectory

The trajectory algorithm presented in Section 3.4 worked well. The coil was moved sufficiently far away from the head to perform changes in orientation without touching the head. Further, as we explained in Section 3.4.3, our trajectory algorithm tries to minimise coil orientation change during the transition from one trajectory point to the next. If big counter-rotations of Joints 4 and 6 are to be performed, as it is the case when reaching joint limits of Joints 4 or 6, this is done by straighten the fifth joint (i.e. aiming for the hand singularity $\theta_5 = 0°$). This has the effect of the two rotations cancelling each other, see Figure 6.2.

Sometimes it would have been not possible to straightening the fifth joint without touching the patient's head. In those cases no safe trajectory could be found, so a direct move to the target pose was prohibited. Nevertheless, the target pose could still be reached if the robot was commanded first to an intermediate position not on the arc from start to target pose, see Section 3.4.2. Alternatively, the robot was positioned manually so that the coil was close to the target region and the trajectory to the stimulation point did not require big changes in Joint 4 or 6.

6.2.2.3. Motion compensation

The quality of the motion compensation feature depends on the frequency of the tracking system, the accuracy of the tracking values (especially jitter), and the robot speed settings. We found that the 30 – 60 Hz update rates for the Claron MicronTracker S60 and the NDI Polaris tracking systems were sufficient, but that the Kuka robot had difficulties implementing the changes in position with sufficient speed. This was mainly due to a problem in the Kuka internal trajectory planning, which is not designed for real time demands and resulted in a time lag of about 0.5 seconds in responding to motions. The Adept robot with its real time operating system V+ performed much better in first laboratory experiments, see Section 6.1.2, using up to three commanded points in advance to calculate its trajectory. We hope that for the future Kuka will provide state-of-the-art realtime capable controlling software, enabling fast motion compensation also with this robot.

A problem remaining in motion compensation is jitter in head position measurements. Tiny fluctuations in calculated marker positions, caused by the finite angular resolution of the cameras, lead to ever changing position demands for the coil. Hence the robot is constantly moving, even if the head is perfectly still. To reduce the problem, we averaged several

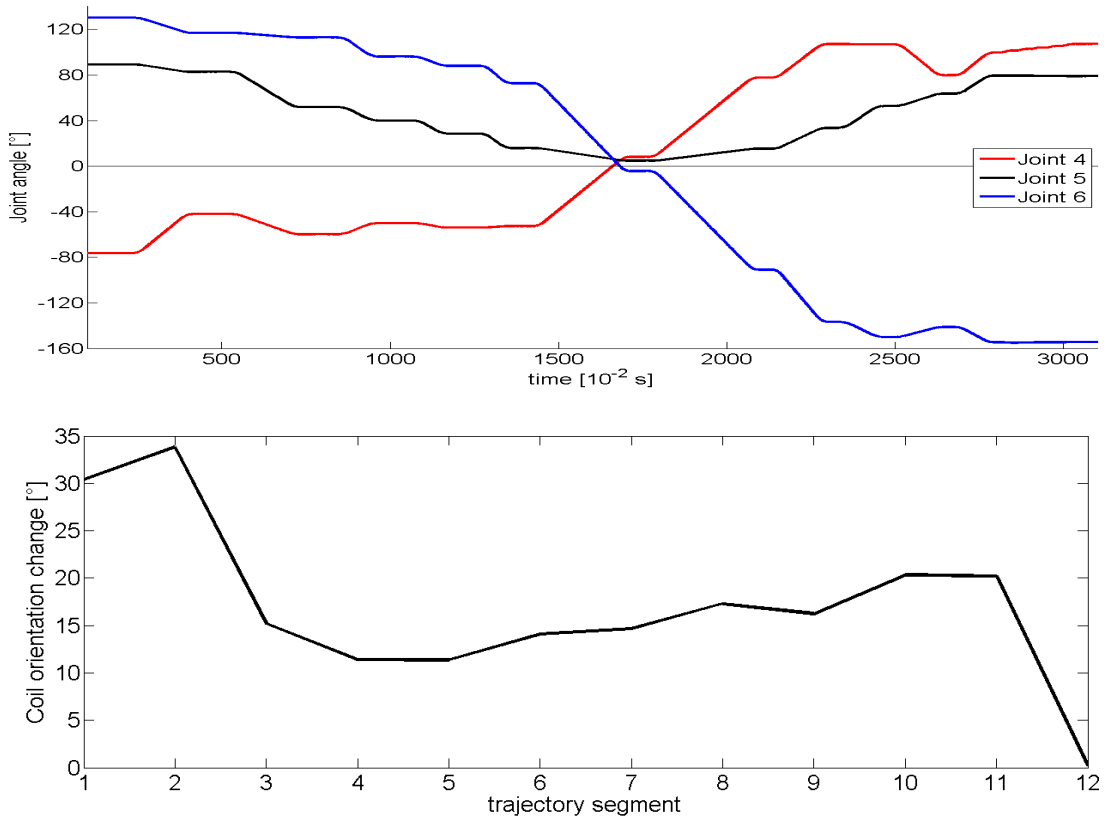

Figure 6.2.: Straightening of Joint 5 allows counter-rotations of Joints 4 and 6. The trajectory is a result of moving the coil from a point on the left side of the head (about electrode position T5) to the right side of the head (about electrode position T6). The relaxation of the pitch angle of the coil along the trajectory allows Joint 5 to straighten such that the necessary big movement of Joint 4 can be counter-balanced by an opposite move of Joint 6 nearly without moving the coil. In fact, the change of 120° *in Joint 4 between seconds 14 to 21 (top picture, red graph) leads only to a coil orientation change of* 15° *to* 20° *(bottom picture). In contrast, the movement of* 40° *of Joint 4 from the first to the second interpolation point led to a coil orientation change of* 34°*, because Joint 5 was bent by about* 80°*.*

measurements of the tracking system, see Section 3.4.4.3. This does not influence the compensation time too much as long as the averaging number is not too big, see Section 6.1.2.

Our practical experiences showed that for the Polaris 3 to 10 positions for averaging were optimal to reduce jitter while still enabling a fast compensation of a change in head position. For the Micron system, we had big issues with the stability of the orientation readings, especially in the direction normal to the marker. Here, a number of about 30 tracking averages was needed to stabilise the readings. This, together with the lower tracking frequency, reduced the quality of the motion compensation way below the Polaris' one.

In rare occurrences, motions of the subjects could not be compensated, because this would have required a turn of Joint 4 to more than 190° (out of working range of the Adept) or a turn of the joint by about 180° (prohibited, see Section 3.4.4.3). Such cases can be avoided when the coil is attached to the robot with Joints 4 and 6 at about 0°.

6.2.3. System quality attributes

In this section we report on the system's performance using the following soft measures:

- Applicability — could the experiments be performed as planned using the system,
- Capability — how diverse is the range of applications for the system and which new applications are possible with it,
- Usability — how difficult and time-consuming was it to use the system,
- Comfort — how did the patients perceive the treatment by a robot.

6.2.3.1. Applicability

The robotic assistance system for TMS was successfully employed for all applications from Chapter 5 with the exception of the TMS-EEG experiment for neuronal signal processing research, Section 5.2.2. In all other applications the objectives of the experiment could be fully reached using the TMS robot.

In the motor cortex mapping experiments, Section 5.1, the positioning accuracy together with the motion compensation quality allowed the recording of very clean MEP data and thus high quality mapping. In the non-human primate mapping experiment, Section 5.4, we could show novel phenomena, because the system was able to move the coil accurately in 500 µm steps over the skull of the animal. In the rTMS experiments, Section 5.3, the system kept the coil sufficiently at its place relative to the head during the 20 to 30 minutes of treatment and we could see a relief of the symptoms of chronic pain and tinnitus for some of the patients.

In the TMS-EEG experiment for neuronal signal processing research, the motion compensation was not fast enough to compensate for the large head motions of the subjects. Their task required to look on a computer screen and then to press some keys on the keyboard. Several subjects moved their head with such a speed that the robot could not follow with its restricted speed and acceleration. As Section 6.1.2 showed, large sudden movements can only be compensated with very high robot speeds. We refrained from relaxing the speed limits of the robot, because we did not want to jeopardise safety for performance. The experiment required to give the stimulus at the time of the maximum head movement, so we often ended up stimulating the wrong spot or having the coil not close enough to the head. Therefore, we could not reproduce the results of a previous experiment with a fixed head.

We conclude that our system is applicable in all situations apart when the stimulus appears at times of large fast head motions. For such applications, we still need to find a way to allow very high robot speeds while ensuring the patient's safety.

6.2.3.2. Capability

Our system for robot aided TMS stimulation can be used for a wide range of applications. The main application areas include precise coil positioning, image guided targeting, motion compensated stimulation, and repeated TMS sessions.

In the area of precise coil positioning on the basis of 3D medical images, our system meets the highest standards, set by the two other TMS robot systems presented in the literature [17, 82]. For both systems, an RMS error of two millimetres in positioning the coil is reported. We have shown in Section 6.1.1 that our system also performs with this accuracy. We note that both systems [17, 82] require a fixed head whereas our solution allows for frameless stimulation.

Conventional image guided TMS systems, which allow for frameless stimulation, are based on a similar navigation [40, 50, 53, 160] and registration [115] technique as our system, but they all require a manual coil positioning. Hence the accuracy of the stimulation depends on the examiner's ability to maneuver the coil to the target spot using the navigational aids and to hold it there as still as possible. Experience shows that the biggest problem in manual coil positioning is to hold the coil in the desired orientation to the head, i.e. tangential to the head and with a certain rotation around its normal axis. The accurate placement of the coil's centre is less difficult.

Our system solves the problem of operating with high orientational accuracy by using a robot. Its high accuracy in joint adjustment, which translates to position and orientation accuracy of the coil placement, makes the stimulation not only more precise than manual coil placement, but also independent of the examiner. Furthermore, the fine joint angle resolution of the robot makes it possible to shift the coil in steps of down to 30 µm for experimental neuronal research. This is clearly impossible to do with a hand-held coil or with conventional mechanical coil holders. Summarising, our robot system is suitable for all applications requiring exact coil positioning on the basis of 3D medical images, e.g. transcranial magnetic stimulation for motor cortex mapping.

The feature of motion compensation sets our system apart from all existing TMS solutions. The robot solution presented in this thesis allows for the first time to avoid fixation of the head without compromising accuracy. This enables its use in a wide range of applications. For example, virtually all rTMS treatment protocols can easily be implemented with our system. They all have in common that a well defined area of the brain should be stimulated over a longer period of time (e.g. 30 minutes for tinnitus).

By following the movements of the patient's head we ensure that the stimulus is always given at the right position. This could, in principle, also be achieved by fixating the head and using conventional image guidance and a static coil holder. But the loss in comfort for the patient is significant and one should keep in mind that if TMS is used for treatment, it is applied to ill people. For example, one would hardly force a patient suffering from chronic pain in a rigid frame in an uncomfortable sitting position.

Another aspect to consider is the change in physiological response to TMS depending on the subject's current situation (lying or sitting, relaxed or tense, sleeping or alert, etc., [71]).

So if TMS responses like motor evoked potentials (MEP) or electroencephalographic signals (EEG) are recorded over a longer period of time, special care must be taken to ensure that such parameters do not change. If a head rest or a thermoplastic mask are used for head fixation for a longer period of time (e.g. an hour), it can easily lead to muscle tensions or pressure pain. Clearly, a system featuring motion compensation avoids this and allows the subject to stay comfortable even for long periods of time.

Finally, our system has been shown useful in applications which require repeated stimulation at a certain spot. This does not only include intra-session repeatability like for repetitive stimulation (rTMS), but also protocols requiring TMS treatment on consecutive days. All stimulation targets are stored in the system and can easily be re-approached in a new session (inter-session repeatability). If rTMS treatment of diseases like tinnitus or depression could be established, inter-session repeatability would make the system applicable for the clinical routine.

6.2.3.3. Usability

Our system with its many components like a robot, a tracking system, a head marker, a pointing device, and a graphical user interface on a computer is clearly more difficult to operate than a TMS stimulator alone. Thus, we need to ensure that it is neither too time consuming nor too difficult to use the robot TMS system.

Regarding the first aspect, the time required to operate the system, there are three different phases to distinguish:

1. Hardware set-up — The installation time of the robot, the tracking system, the computer, and the TMS device, i.e. the time to connect all cables, screw the robot on its frame, mount the camera on its tripod, is about 30 minutes. This has to be done only once, so this rather long time is acceptable. Afterwards, we need to calibrate the camera to the robot, see Section 3.2.2. This has to be done every time the robot or tracking system is moved and we recommend to do it at the start of each day if one can't be absolutely certain that none of the devices has been moved. This procedure takes about 5 minutes. Finally, the TMS coil needs to be attached to the robot end-effector and calibrated to it. Using a quick release fastener to attach the coil, this hardly takes more than a minute.

2. Subject set-up — If the stimulation is to be based on 3D medical image data, we segment the cranium from the data set. This takes about 1 to 3 minutes (depending on the resolution and quality of the images) and can be done before the subject arrives for stimulation. Note that it needs to be done only once for each subject and data set, so if the subject comes in for a second stimulation session, we only need to load the surface mesh representing the cranium from file, which takes a few seconds. After the participant arrives, she / he is fitted with the head marker. We then record 3 to 5 landmark points and a couple of hundred head surface points with the pointing device and register this head representation to the segmented surface from the image data. This procedure takes about 5 to 10 minutes. If there is no 3D image data available,

we sample more surface points and reconstruct the cranial outline from it. This can be done in a similar time.

3. Stimulation — For stimulation we first define a target point by either pointing on it using the pointer device or by marking a point on the virtual head surface or 3D image data on the computer. This takes only a few seconds. The robot then calculates a trajectory and moves to the coil to the target point. Depending on the distance the robot has to move, this can take between 10 seconds and one minute.

If we summarise the time for the complete procedure – from a disassembled system to the first stimulation – we need 45 minutes to an hour. This is clearly much too long for a normal use. But if we consider that many steps need to be performed only once for an existing installation, this time reduces to about 10 minutes. Still, that is much more than the set-up time required for simple non-navigated stimulation by hand, but the system's main application is not for a couple of quick single pulse stimulation, but rather for lengthy rTMS or research procedures, which usually last 30 minutes to 2 hours. So a 10 minutes set-up time is acceptable.

A point worth mentioning is the transit time from one stimulation point to the next. Although 10 seconds are not a long time, they are considerably longer than the time needed to move the coil by hand. Many TMS research and treatment protocols require to determine the motor threshold before the actual application. If done manually, the coil is shifted with short pauses of about 3 seconds over the most likely area of hand representation to evaluate the motor responses. This way, experienced experimenters can determine the motor threshold with about 30 to 100 stimulations within a few minutes. If the robot system is used, this takes about 10 to 20 minutes, because of the extended time required to move from one stimulation point to the next. In our experiments this reduced the user acceptance of the system considerably.

To reduce the mapping time, we plan to reduce the time to move from one stimulation point to the next by allowing direct coil steering by a force-torque-sensor between coil and robot, see Section 3.5.1. Further, we will incorporate our motor cortex mapping algorithm, Chapter 4, into the motor threshold procedure, which will reduce the number of stimulation points necessary for threshold determination. All in all we are optimistic to reduce the time for threshold determination to 3 to 5 minutes in the future, see Section 6.4.

The second criterion in this Section, how difficult it is to operate the system, is harder to measure. We have tried to keep the user interface as simple as possible, using a work-flow scheme to inform the user what to do next (recording head outline points → head registration → target definition and stimulation → motor cortex mapping analysis). The users generally agreed that the computer interface was easy to understand and to use.

The users found it harder to operate with the pointing device to sample head outline points, because care must be taken that the pointer tip is always on the head surface while recording outline data. This was especially tricky in subjects with long, thick hair, because the headband we used to attach the head marker jammed the hair so that it was hard to move the pointer over the skull. Problems appeared also in EEG experiments, because the EEG cap and the cables running from the electrodes to the amplifier restricted the access to the scalp. In such cases it was best to sample more points from the facial area and to use a

"start-stop-communication", i.e. the first experimenter holds the pointer device and tells the second experimenter when to start and to stop the recording while moving the pointer in trajectories parallel to the hair like a comb over the head of the subject. For the future we plan to improve the recording equipment, e.g. by having a button at the pointer device to start and stop the recording remotely.

Another difficult point for the user was to understand why certain targets or trajectories where impossible for the robot. The workspace restrictions of a serial six joint robot are not easy to visualise, especially if an additional tool like a TMS coil is considered. So if the message "Can't reach target point" appeared on the screen, it was sometimes not clear how to position of the subject should be changed to make the target accessible for the robot. Similarly, it was difficult for the users to resolve the situation when the heuristic for the trajectory planning failed, i.e. when the target point was accessible, but our algorithm could not find a safe way to steer the coil there. For such a case two workarounds were established: The first was to command the robot to an intermediate target which was easily accessible for the robot first and from there to the final target. This would split the original (often very long) trajectory in two new trajectories and enable coil paths away from the plane defined by the start point, the target point and the head centre.[4] In rare cases when such an intermediate target could not be found, the "quick 'n dirty solution" of using the hand panel of the robot to steer the coil manually close to the target point remained. This is clearly not a satisfactory way of operating the robot TMS system, so for the future we will work on improved trajectory heuristics which incorporate the workspace restrictions of the robot.

6.2.3.4. Comfort

Naturally, having a robot moving the coil instead of a human operator first caused some discomfort in the patients. We found that we could improve the situation much by using a mirror such that the patient could see the robot moving the coil. After a short while patients trusted the system, so that they could close their eyes without discomfort, as our questioning after the experiments revealed. This was especially important in our epilepsy EEG experiment, Section 5.2.1, in which the EEG recording is very sensitive to eye movement artefacts [88, 97].

Compared to a conventional TMS system for image guided treatment, the main advantage for the subject was that our system did not require head fixation for longer high precision experiments or treatments. Thus, the subjects could shift their position during the session, which sometimes lasted more than two hours. Also, they did not need to concentrate to hold their heads still; a fact of importance in EEG experiments, where such secondary tasks can influence the outcome of the experiment [118, 181, 187].

Finally, the robot's workspace was big enough to allow stimulation in a number of different positions, e.g. sitting upright in front of a monitor (TMS-EEG experiment for neuronal signal processing, Section 5.2.2), comfortably leaned backwards like in an easy chair (brain mapping experiments, Section 5.1 and tinnitus treatment, Section 5.3), or lying on a bed

[4] The detailed description of the trajectory heuristic can be found in Sections 3.4.2 and 3.4.3.

with the head slightly lifted by a pillow (one paralysed patient for chronic pain treatment, Section 5.3). This way, we could ensure a convenient position for each subject in each experiment.

6.3. Motor cortex mapping with TMS

We presented a new approach to motor cortex mapping based on a calculation of a likelihood map, evaluating the functional monotonic correspondence between the electric field strength at points on the cortex and the motor responses. The method allows for the first time mapping with non-focal TMS coils like circular coils or the H-coil. The method was tested on one subject for two hand muscles, two coil types, and two mapping protocols and compared to alternative mapping from fMRI. For six further subjects, the method was used to determine the cortical representation site for up to four hand muscles in the presence of tumors in or neighbouring the central region. For two of the subjects, a comparison with direct electrical stimulation was performed. All results were compared to the centre of gravity algorithm, which represents the state-of-the-art.

The important feature of the mapping algorithm is the combination of physical responses to stimulation (MEP values) and the electric field produced by the TMS coil. This allows for meaningful mapping resolution of the size of the E-field measurement resolution, see Section 4.4. So even if there are only 12 neurological MEP measurements (Experiment 2), spaced with 1 cm distance, the motor cortex mapping resolution is within millimetre range if the coil field is mapped with this accuracy.

The mapping is calculated using a statistic which calculates the likelihood for the cortical representation of the mapped muscle for each point on the brain surface. We have shown that there are statistics which allow a fast (20 seconds) and stable (12 samples) calculation of the likelihood map of the full cortex.

6.3.1. Mapping statistics

We tested four different statistics to evaluate the functional monotonic correspondence between the electric field strength at points on the cortex and the motor responses. The data showed that Kendall's rank coefficient τ yields the best results in the context of our algorithm.

Kendall's rank coefficient τ is a direct measure of monotonicity, using the number of concordant and discordant pairs for its calculation. The mapping results for the τ statistic are generally in good accordance with alternative mapping by fMRI, see the figures in Section 4.5.3. The TMS map maxima from Experiment 1 are within 11 mm, the TMS map maxima from Experiment 2 are within 4 mm of the fMRI hotspots for the representation of the ADM muscle and the APB muscle. All τ maps of Experiments 1 and 2 and 91% of the τ maps of Experiment 3 have their maximum close to an area which is known as the hand knob in anatomy [194]. When comparing ADM and APB localisation we find that the ADM muscle is represented slightly more medial as the APB muscle, complying with the results from

literature [14]. Finally, the τ maps showed a unique maximum in 88% of the test cases in Experiment 3.

The results for the Pearson's Correlation Coefficient statistic ρ are nearly as good as the results for the τ statistic. For mapping with the planar figure-of-eight coil (Experiment 2), the results for ρ are in good agreement with the results for τ. For mapping with the circular coil (Experiment 1), the ρ statistic gave even better results than τ. The ρ maximum for the ADM map is much closer to the fMRI maximum than the τ maximum. But in Experiment 3, only 83% of the ρ maxima were at an anatomically probable location (the hand knob), a considerably lower portion than for the τ statistic. Nevertheless, the performance of the ρ statistic is remarkable, because it tests only for linear correspondence between the electric field strength list and the MEP list whereas physiologically, the dependence of the MEP on the electric field strength is highly non-linear.

Correlation Ratio η was used as a measure of functional correspondence between the two mapping lists. The comparison of the η maps with the τ and ρ maps revealed little difference in localisation in Experiments 1 and 2. The maxima of the methods were only 4 to 6 mm apart, with the high probability areas for the representation mainly overlapping (coloured areas in Figure 4.11). In Experiment 3, the performance was much worse, with only 63% of the η maxima at the hand knob. Further, the η maps often suffered from side maxima; in Experiment 3 24% of the test cases showed such a behaviour. Finally, the maps produced by taking Kendall's τ or Persons's ρ as a measure were a bit smoother.

The normalised mutual information $\tilde{I}$ was included in the tests, because it measures correspondence in the very broad sense of joint entropy. As our results show, this leads to many points on the brain's surface falsely identified as cortical representation for the mapped muscle. A unique $\tilde{I}$ maximum could only be observed in 5% of the test cases in Experiment 3. Surprisingly, the hotspot points with high τ and ρ values often had $\tilde{I}$ values 15% or more below the $\tilde{I}$ maximum. So the τ and ρ hotspots were less likely representation points according to the $\tilde{I}$ statistic. We think the reason for this lies in the very general nature of the mutual information correspondence measure that can lead to high $\tilde{I}$ values also in the absence of a monotonic or functional dependence. In many cases, values at such points can even be bigger than values at the hotspot as Experiment 3 shows (41% of the test cases had no $\tilde{I}$ maximum values at the hand knob).

6.3.2. Mapping quality

The results in Section 4.5.3 show that the mapping is generally of good quality, but that it is not perfect:

1. TMS mapping values of the fMRI hotspots for the circular coil experiment are not the maximum values.

2. The region of high mapping values for the circular coil maps extend posterior into the postcentral gyrus.

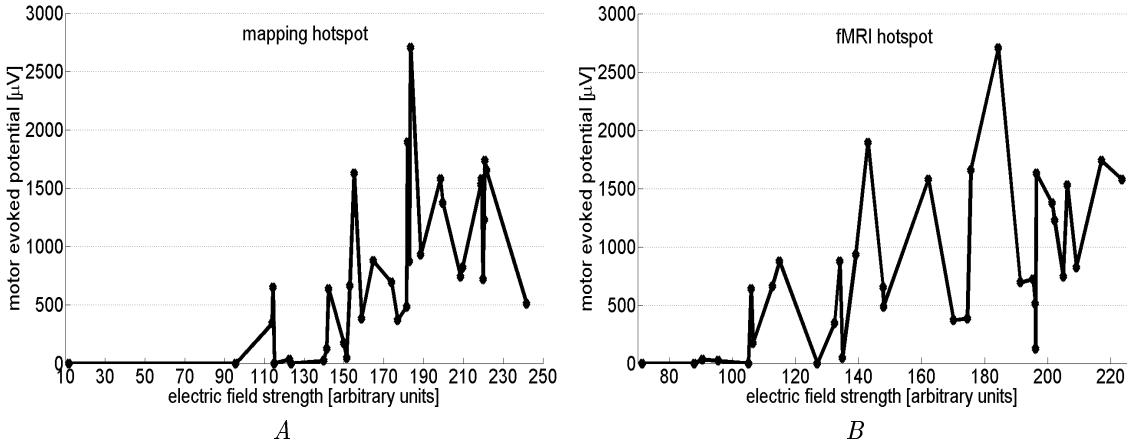

A *B*

Figure 6.3.: Calculated electric field strength $X(\mathbf{p})$ (arbitrary units) and elicited MEP responses Y (peak to peak, in mV*) at the ADM muscle for two different points on the brain surface for mapping with a circular coil. The first point was chosen as the mapping maximum for the τ algorithm (left). The second point was chosen as the fMRI maximum (right). Neither graph shows a clear monotonic relationship between X and Y, exemplifying the limits of our TMS excitation model. Note that the Y-values are the same in both graphs, only the respective X-values differ. Stimulation was performed with a Medtronic MCF-75 circular coil at 34 stimulation sites with a fixed stimulator output, see Experiment 1.*

3. Separate small spots of high mapping value sometimes appear away from the correct localisation. These side maxima were present in about 10% of the cases in Experiment 3.

The following paragraphs discuss possible explanations for the three mapping problems.

For the first problem, our initial assumption that the MEP amplitude Y is a monotonic function of the electric field strength X at the representation point $\mathbf{p}^r$, is not strictly valid. Several reports exist, that also the direction of the field influences the strength of the muscle response [20, 68]. This limits the reliability of our biophysical model of TMS stimulation.

As an example, Figure 6.3 displays the electric field strength values X at two points on the brain surface with their corresponding MEP values Y. The points were chosen as the τ mapping maximum and the fMRI hotspot, respectively. If our excitation model was true without restrictions, we would expect the two points to agree and the relation between X and Y to be monotonic such as for the mapping with the figure-of-eight coil with constant orientation, see Figure 4.1. Figure 6.3 shows that such a monotonic relation is not given for the mapping with the circular coil. Note that mapping with the circular coil implies that the electric field vector at the representation point $\mathbf{p}^r$ changes its orientation by 360° when placing the coil along a circle around $\mathbf{p}^r$. Therefore, our TMS excitation model shows room for improvement.

Fox et al. suggested a direct dependence of the MEP amplitude on the field strength and the angle between the electric field and the brain surface normal at the representation point [44], a finding unconfirmed by other researchers. But it might also be that the quality of the

performed stimulation impaired the mapping. For the circular coil, incorporating postcentral stimulation points should enhance the mapping, because it increases the diversity of the $(X(\mathbf{p}), Y)$ data pairs. Finally, our algorithm does not account for electric field distortions produced by the head. Further research will incorporate field simulations to approximate the true electric field distribution in the head better and allow comparison of the original mapping algorithm presented here and a distortion-corrected one. As explained in Section 4.2, we do not expect big differences, but we are not yet able to quantify this.

Regarding problem two, the extension of the maps to the postcentral gyrus in the case of mapping with the circular coil, we believe that this is mainly due to the restriction to precentral stimulation regions. We hope that after changing the laboratory setup to map patients in a comfortably sitting position we will be able to stimulate points all around the head and thus produce more focal mappings. But it is also possible that the we need to incorporate some E-field directional dependence in our formula, as discussed above.

We remark that the distance between the precentral and the postcentral gyrus is only about 5 mm– 10 mm, as the patient's MRI revealed. Hence our TMS maps seem accurate to about this degree. This performance is especially remarkable given that the stimulation data was not optimal, because the circular coil experiments lacked postcentral stimulation points. Furthermore, we boldly approximated the electric field in the brain by the electric field in air, as explained in Section 4.2. The fact that we got correct mapping results, despite the approximations and the sub-optimal data, demonstrates the robustness of the mapping method.

Problem three seems to be related to the broadness of dependence the statistic measures. For example, monotonicity (τ) or linear dependence (ρ) are relatively narrow types of dependence compared to functional dependence (η) or mutual information ($\tilde{I}$). Therefore, it is not surprising that the problem of side maxima was less pronounced for τ or ρ maps.

In general, there might be points $\mathbf{p}$ on the brain surface exhibiting by chance the kind of dependence between electric field strength $X(\mathbf{p})$ and MEP values Y measured by our statistics. Our experience, however, is that the number and the value of these "false positive" spots decreases with more measurements. This is the reason we included the 15 and 12 artificial measurements, in Experiment 1 and 2, respectively, into the data pairs.

As a test of this "more measurements decrease the number of 'false positives"' – hypothesis, we mapped the APB of a subject, using 46 stimulations with the bend Medtronic figure-of-eight coil according to Protocol 3 (see Section 4.5.1.3). The resulting Rank coefficient τ and Correlation Ratio η values are displayed in Figure 6.4. We see that there is now only one maximum area, namely at the outer side of the hand knob.

6.3.3. Comparison with the state-of-the-art

The state-of-the-art in motor cortex mapping is the calculation of the centre of gravity (CoG) of the stimulation points. The MEPs are hereby taken as the weights for the gravity map. As explained in Section 4.3.5, the CoG is usually not a point on the brain surface, but needs to be projected onto it. As discussed in [119], there are several possible methods for

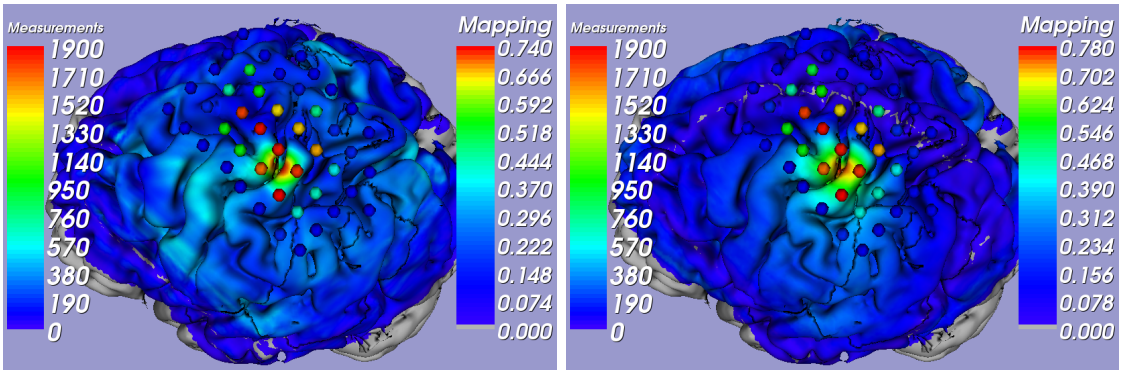

Figure 6.4.: Mapping of the left APB muscle with the figure-of-eight coil. Left: Correlation Ratio η values, right: Kendall's rank coefficient τ values. The spheres indicate the stimulation positions. The colour of the spheres encodes the obtained MEP signal. The colour of a brain region depicts the mapping value and hence likelihood that the mapped muscle is represented there. Colours range from grey and blue (unlikely) to red (very likely).

the projection, leading to ambiguity in the method. Furthermore, the CoG calculation and the projection have no direct physiological meaning associated with them.

Our statistical approach of comparing the electric field values at a point with the muscle responses is more adapted to the problem. Starting from a biophysical model, we associate a direct physiological meaning with our algorithm. Further, as we calculate the mapping values directly for points on the brain surface, we avoid the need to project the result and the ambiguity associated with it. Finally, our algorithm acknowledges the individual electric field shape of every coil design by incorporating the coil-specific electric field into the calculation. Thus, from a theoretical point of view, our algorithm has some advantages compared to the CoG algorithm.

But more importantly, our algorithm has been shown to be more robust than the CoG algorithm. The CoG only works for focal coils like the figure-of-eight coils. For non-focal coils like the circular coil from Experiment 1, the results of the CoG are meaningless. For focal coils, the CoG algorithm requires coil poses to be distributed evenly around the hotspot to give meaningful results. This is immediately clear from the definition, Equation (4.15), because the centre of gravity formula always yields an interpolation point and never an extrapolation. So if data is only sampled on one side from the hotspot, the CoG will also be on this side. In contrast, our algorithm works also in such a case as shown in Experiment 1.

The sensitivity of the CoG method to the choice of stimulation positions is also mirrored in the mapping results from Experiment 3. Only 78% of the CoG maps were centred on the hand knob, compared to 91% for the τ algorithm. In 11% of the test cases in this experiment, the projection of the CoG did not result in a unique point on the brain surface. In those cases, the CoG was calculated to be between two gyri such that the surfaces of them were of similar distance to the CoG. If the stimulation points were chosen carefully around the hotspot, the CoG mapping for figure-of-eight coils generally agreed with the τ maps of our algorithm, see for example Figure 4.11.

6.4. Future work

We conclude the discussion with an outline of improvements to the system we would like to implement in the future.

6.4.1. Trajectory heuristic

The heuristic we use for determining a safe trajectory from the actual position of the coil to the target position has been shown to be valid, but not complete. That means that if the algorithm from Section 3.4.3 finds a trajectory, the coil will not collide with the head during the transition. But sometimes the algorithm fails to find a solution. In the following, we discuss two possible research directions to improve here.

6.4.1.1. Coil-centred approach

The main problem is the restriction of the coil's path to an arc from the start point to the target point around the head's centre. This restriction enables us to compute and solve the shortest graph problem associated with our heuristic in an acceptable time (1 second per calculation, 20 seconds per trajectory). If we relax the coil's path, the computational load rises and thus the time required to calculate the trajectory. We have pointed out in Section 6.2.3.3 that the long transition time for the coil from one stimulation point to the next was subject to criticism by the users, so a further delay would reduce the acceptance of the system.

Thus, an improvement to the trajectory heuristic would rather not require to evaluate more poses of the robot and the coil, but choose the path for the coil centre in a better way. The problem hereby is the unknown orientation of the coil along the path and thus the required pose of the robot end-effector. If we restrict the coil orientation to certain discrete values we can use the algorithm presented in Section 3.4.3 to find a valid trajectory, but for the price of severely reducing the solution space.

6.4.1.2. Robot-centred approach

The coil-centred approach above creates potential trajectory interpolation points which may be outside the workspace of the robot. Therefore, it may fail to find a solution. But if we compare the workspace of the robot with the size of the obstacle (the head of the subject), we find that the obstacle fills only a small part of the workspace. Thus, it might be a good alternative to base the heuristic on the workspace of the robot. The start point of the trajectory is given by the actual position of the robot. The end point is not uniquely given, but must be chosen from one of the eight joint settings corresponding to one of the eight configuration modes of the robot for implementing the target pose. But this is not the main difficulty. The hard problem is to decide the feasibility of a given point in the workspace, i.e. to determine if the robot or the coil intersects the obstacle for a given joint setting.

Again, there are two approaches to the problem. One is to calculate if the outlines (surfaces) of the virtual representations of coil and head or robot and head intersect for each joint setting along the path in workspace. This can be done with software packages like I-COLLIDE [28] or V-COLLIDE [60].[5] The other one is to transform the obstacle into the workspace of the robot and to check if the path in workspace intersects this obstacle. In principle, this would require to calculate the Minkowski sum for all possible coil orientations and to calculate the inverse kinematic for each point of the result. The problem with both approaches is the complexity of the required computations. Clearly, one would need to simplify the problem by discretising it. Hereby, one needs to ensure that the obstacle is always enlarged, i.e. that the simplification does not result in an infeasible pose marked feasible. So any simplification will again result in a reduction of the solution space.

The second problem to be tackled is the question of how to evaluate the quality of a trajectory. Such an objective function will be necessary to avoid large movements of the robot, possibly hitting remote objects not represented in the virtual scene, or time-consuming zig-zag-movements of the coil. Here, functions like the path length of the coil's centre point or the accumulated change in orientation of the coil might be a good start point.

6.4.2. Hardware

6.4.2.1. Force sensor

At the moment, we use the newly introduced force sensor (Section 3.5.1) only for safety purposes. Namely, it stops the robot if a contact with the head is detected. But the device can also be used for some other applications:

Firstly, we can improve accuracy by allowing a gradual lowering of the robot until the coil touches the head lightly. In the following motion compensation module we try to keep the force between coil and head constant, i.e. we move the coil away from the head if the pressure becomes too strong and move it towards the head if the pressure becomes weaker. This way we will eliminate any registration and tracking error in direction normal to the head.

Secondly, the force sensor might allow a new, fast way of positioning the coil. The operator can directly grab the coil and position it using the sensor-robot-loop like a servo steering. The force the user applies to the handle is hereby translated into a direction in which the coil should move. It is possible to constrain the motion to certain surfaces or areas, e.g. only tangential to the head or only within 5 cm distance from the motor cortex. As soon as the coil is released, motion compensation sets in and keeps the coil at its exact position relative to the head. We expect the servo-feature to be especially useful for fast mapping procedures as they are common to find motor threshold, see the discussion in Section 6.2.3.3.

[5] There exist, of course, many more and maybe even better algorithms for collision detection than included in these packages. The ones from the I-Collide and V-Collide collection have been used for testing trajectories of a robotised C-arm device [15, 99] for collision with the patient and the OR table [87].

6.4.2.2. Robot design

The Adept and Kuka robots we use for positioning the coil are multi-purpose-robots, i.e. they are designed to be employed in many different environments for wide range of tasks. The advantage of such robots is the relatively low price and the well-tested device software, as they are manufactured and employed in large quantities. The drawback in our application is that their arm-design with only rotational joints results in a workspace which is only partly suitable for robotic TMS.

On the one hand, the workspace does not include all possible stimulation targets for TMS for a static position of the head. For example, it is impossible to stimulate the central prefrontal cortex, the left and right motor area, and the occipital cortex in one session without moving the patient. This has not been a problem so far, because the head tracking feature allows to reposition the patient during a session. Furthermore, there are few applications and protocols which require the stimulation over a widely distributed area of the head, but with the increasing utilisation of TMS in neuronal research, diagnostics, and therapy this is likely to change.

On the other hand, the workspace of the Adept and Kuka robots is too big for our purposes, as it includes points far away from the patient and points which lie inside the patient's body. This is an inherent safety problem, because we need to take extra care that the robot does not move to such poses and collide with the patient or the lab equipment.

A robot type that is more suited for TMS would have a workspace without these two limitations. Further, it would be adjustable for different positions of the patient, e.g. sitting or lying. Good designs for the problem of workspace seem to be the arc solutions suggested by Ramrath et al. [134] and Lebossé et al. [85], see Figure 6.1.

To date, both systems are not yet ready for the use with TMS. The system of Ramrath must be scaled to be applicable to human heads instead of rodents. This is indeed planned, but for a neurosurgical environment. It is unclear if the enlarged system will be able to meet the speed and acceleration requirements of motion compensated TMS and if it would be able to handle heavy TMS coils for rTMS. The system of Lebossé is to our best knowledge still in the planning stage and has not been shown to meet the accuracy and dynamic requirements of robot TMS. Furthermore, this system seems to be a bit bulky, so that it is not portable and not suited to stimulate subjects in a lying or heavily reclined position.

The limited resources did not allow to design and build a TMS robot ourselves. The Adept and Kuka robots have been the best solution to the static and dynamic requirements of our application so far. For the future, we strive to collaborate closely with the group of Ramrath to make a scaled version of their SASSU robot available for TMS.

6.4.2.3. Tracking

Some new developments in the area of medical tracking devices might help to further improve our TMS robot system. We describe briefly two new systems and their advantages for our application.

High speed tracking The Atracsys company is developing a number of tracking systems with high tracking speed (up to 4000 Hz for the accuTrack systems and 300 Hz for the easyTrack systems). Higher tracking speed could reduce the latency of our system, see Section 6.1.2 and make the motion compensation feature perform better this way. Furthermore, the high tracking frequency allows to check the robot's motions, adding another safety layer to the system. If an abnormal robot speed or trajectory is detected, an emergency stop could be initiated. This only works if the tracking speed is high enough so that critical situations can be detected before a collision. For theoretical calculations about the necessary tracking speed and accuracy see Section 3.5.2.

The disadvantage of all high speed tracking systems so far is the marker design. It seems that such high frequencies are only possible with LED markers. This can be problematic for the TMS application, because the strong magnetic pulse might interfere with the electronics in the marker. It could destroy it or block the transmission, so that tracking is hindered during the stimulation. In EEG applications, electronic devices near the head create artefacts in the recordings, so even if tracking is possible, the experiment might be impaired. Furthermore, most markers require a cable connection to the tracking device, even though some wireless markers with infrared triggering have been introduced recently.

Markerless tracking Claron technologies offers the MicronTracker 2 systems, an alternative technology which is completely passive. Their design with two or three video cameras and checkerboard markers is robust against TMS pulses and changes in light conditions (there must be enough light left to see the markers, but it operates in conditions from dimmed electric bulb light to strong sun light). Furthermore, the markers are very easy to design and to manufacture: They can be printed on a sheet of paper and cut to custom size. Because they can be made of paper, they are of minimal weight and can be glued directly to the skin. So we could use one-time markers for the stimulation, ensuring optimal marker quality and hygienic application in each session. Further, we would need no head band any more to attach the marker to the head. This would be especially useful in EEG applications, where it is always problematic to have anything touching the electrode cap and interfering with the cables. The drawback to time is the relatively low tracking frequency of 30 Hz.

Video tracking devices might also enable completely markerless tracking. Each of the cameras delivers a 2D image of the scene, so in principle the registration of virtual head model and real head can be computed from a pair of stereo images. This way we would avoid the need for an auxiliary marker coordinate system at the head and could omit the registration step, Section 3.3.3.

Pose estimation from stereo images is in itself a large area of research with rapid development, [89, 190–193]. The difficulty lies in the accuracy, robustness, and computation time of the algorithms. To our knowledge, no algorithm has been shown to be able to deliver a tracking accuracy (or rather a registration accuracy) of 1 mm or better with a frequency of 20 Hz or more. So pure markerless tracking is not an option for our system at the moment.

A hybrid approach might improve matters in the future. We could use the marker information of the MicronTracker to initialise the pose for a markerless algorithm. This way a fast and correct convergence of such an algorithm could be ensured; much in the same way as

we use landmark registration to initialise the ICP algorithm for our registration, see Section 3.3.3. Another application would be to use markerless tracking as a way of controlling the marker based tracking. If the poses determined by the two algorithm disagree by more than e.g. twice the accuracy of markerless tracking, a warning could be issued and the robot stopped.

Tracking of the robot With the new tracking systems it is possible to track a large number of markers with an acceptable tracking speed ($\geq 30\,\mathrm{Hz}$). This will allow to track the robot at several links. Tracking the robot base would make the registration between robot and tracking system, Section 3.2.2.1, obsolete, but suffers from the line of sight problem. That means the robot base is often not visible for the tracking system, because the patient or the robot arm is in the way. Therefore, we require at the moment that the positions of robot and tracking system do not change.

If we have (calibrated) markers at links visible to the camera, we can calculate the transform between robot and tracking system, ${}^{\mathrm{R}}T_{\mathrm{T}}$, from the marker poses, the direct kinematics of the robot, and the calibration information of the marker (i.e. where the marker is on the link). This would in theory avoid the need for static robot and camera positions and the initial calibration routine from Section 3.2.2.1. The critical part lies in the movement of the robot and thus the markers. If the robot's joint settings and the marker's tracking data are not recorded at the same time, we introduce an error in the calculation. In the motion compensation application, this would introduce a dangerous closed loop and might lead to uncontrolled movements of the robot.

Therefore, we cannot dispense with the requirement for static robot and camera position. But we can compare the calculated transform from the marker at the link with the initial transform. If they disagree, we must assume a change in the transform and will thus stop the robot. This application is safe, because the errors from one calculation of the transform do not influence the robot's movements and the next calculation of the transform.

We remark that using markers at articulated links for the calculation of the transform between robot and tracking system is only problematic when the robot moves. When the robot is still, we do not have the problem of asynchronous recordings from the robot and the tracking system. So if we have a well calibrated marker at a link, we can use it to determine the transform ${}^{\mathrm{R}}T_{\mathrm{T}}$ without the initial calibration procedure. To calibrate the marker at the robot, the procedure from Section 3.2.2.1 can be used. The only adaptation necessary is to shorten the kinematic chain of the robot to the link the marker is attached to and so to calibrate the marker to the coordinate system of its link.

6.4.3. Motor cortex mapping

Even though our motor cortex mapping algorithm showed good results, there are still improvements and further tests on our list for the future. The following sections discuss our plans to test and extend the mapping model further and to speed up the mapping process.

6.4.3.1. Stimulation model

The excitation model for TMS, i.e. how a TMS pulse activates the brain, from Section 4.2 simplifies the real conditions in the cortex drastically. Firstly, we ignore any distorting influence of the conducting material in the head on the electric field. Secondly, we assume the motor response to a simulation to be expressible as a function of the absolute electric field strength at a single point in the brain. Although both assumptions approximate the reality only coarsely, our mapping algorithm yields good results. Nevertheless, more detailed models might improve the results further.

Electric field distribution in the brain Firstly, we plan to compute the electric field distribution in the head more accurately. Therefore, we need two ingredients: exact knowledge of the coil's electromagnetic properties and good knowledge of the head's electromagnetic properties. The coil's characteristic is easier to obtain, although every single coil is handmade and thus unique. So for an accurate model we need to determine the geometry of the wiring in the coil. We could either accomplish this by recording a CT data set of the coil and segmenting the wires from it. Or we parameterise the wire geometry (e.g. an Archimedean spiral) and determine the parameters by measuring the electric field of the coil with the method described in Section 4.4.1.

It is probably more difficult to obtain a suitable electromagnetic representation of the head. First of all, we need to distinguish the different tissues like skin, bone, cerebrospinal fluid, and grey and white matter. For this task a number of good algorithms exist; we suggest using the ones implemented in the MATLAB SPM library [6]. Further, we need the electromagnetic properties of these tissues. It has been shown that these possess great inter-individual variability [47], but we know of no way to determine the parameters for an individual quickly and non-invasively. So we will have to assume a constant value for each tissue type.

Another question is if we should model directional variances in the conductivity of the tissues. For example, the conductivity of the skull in tangential direction has been shown to be about 10 times higher as in the radial direction and the conductivity along white matter tract fibres is up to 9 times stronger than across the fibres.[6] In principle, the fibre directions in the white matter can be determined using diffusion tensor imaging (DTI), paving the way for a patient-adapted model of anisotropic conductivity.

Finally, we need algorithms to compute the electric field distribution in the brain accurately using the coil's position and characteristic and the head's electromagnetic properties. Numerical computation of electromagnetic propagation is a big field on its own and has been applied to simulate TMS several times already [27, 29, 51, 109, 145, 147, 148, 166, 175, 176]. But to our knowledge, no computation which takes the subject's individual shape of the tissues and the anisotropies into account has been conducted for TMS, although recent publications do use realistic 3D geometric representations of the main tissues of the head and confirm a distortion of the electric field [178, 179]. It will be interesting to quantify the differences in electric field distributions for the different head models (air, sphere models,

[6] See [188] for an overview of tissue anisotropy and it's effect of modelling electromagnetic fields in the head.

isotropic 3D, anisotropic 3D). Only this can tell whether the approach to ignore the head tissue in our algorithm from Section 4.2 is really justified.

Novel excitation models The knowledge about the true electric field distribution in the brain will help us to tackle the next big question: How can we model the effects of TMS more precisely to include the reported directional dependency [20, 106] of the response or the spacial extent of the representation [135]. Such models could distinguish the electric field on the grey matter surface in tangential direction (as suggested by [150]) or in radial direction (as suggested by [44]). Furthermore, the models might extend the well understood excitation of peripheral nerves [93, 158] to the brain, where the complicated entanglement of nerves have hindered a computation of the TMS effects on the scale of single neurons so far.

To test the models we will make extensive use of the motor cortex mapping procedure from Chapter 4. We hope to build a database of stimulation responses for different coils and coil types, including all necessary data like MRI of the patient, fMRI of the patient, stimulation poses, stimulator output, muscle responses, and coil properties. We have already started to compare our mapping results with direct electrical stimulation during navigated neurosurgery, as Krings et al. suggested [77]. Comparison of predicted muscle representation for different TMS excitation models with the results from fMRI and direct electrical stimulation will allow an evaluation of the correctness of the models.

6.4.3.2. Fast mapping

In the discussion of the usability of the robotic TMS system we have pointed to the problem of motor threshold determination at the beginning of many TMS sessions. The procedure takes much longer with the robot system than for manual operation. A solution would be to reduce the number of necessary stimulations by introducing an "intelligent" probing procedure. Instead of a trail and error procedure, in which the coil is shifted rather randomly across the scalp to find the coil position that produces the strongest motor response, we can calculate the most likely hotspot using the algorithm from Chapter 4.

In contrast to Chapter 4, where the algorithm is applied retrospectively to the data of the stimulation, this would require a planning step in which the next stimulation point is suggested. This point should be chosen in such a way that it resolves ambiguity in the calculation of the muscle representation best. We have seen that such ambiguity stems from too little differentiated electric field data available for the brain points. The algorithm should detect such points and suggest a stimulation site with which a higher discrimination is achieved after the next stimulation.

The results from the mapping experiments with the figure-of-eight coil, Section 4.5.3.2, suggest that 12 stimulation points are sufficient for a stable mapping. If the points are chosen not on a grid, but in a more intelligent and adaptive way, we hope that as little as four to six points yield the hotspot. In Figure 6.5 we present an example how the current τ algorithm performs for six stimulation sites. We see that the TMS maximum in the horizontal slice through the motor cortex agrees with the fMRI maximum. But we also see

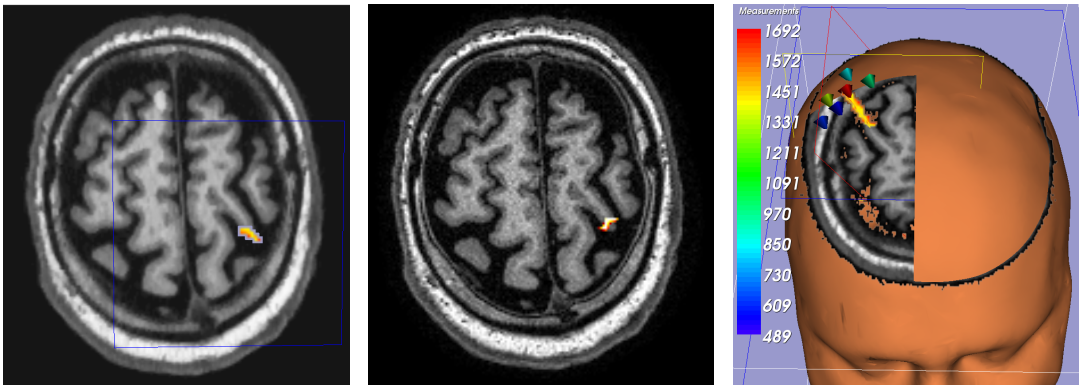

A *B* *C*

Figure 6.5.: Fast mapping result using six stimulation points. A: TMS mapping maximum in a horizontal slice featuring the motor cortex. B: fMRI maximum in the same slice. C: Distribution of the stimulation points (coloured spheres) and the TMS mapping maxima (yellow stripe). The mapping has a sharp resolution in directions parallel to the stimulation plane and virtually no resolution in direction normal to the stimulation plane. Stimulation was performed with the Medtronic MCF-B65 figure-of-eight coil. MEPs were recorded from the right ADM muscle. fMRI images were acquired for a finger tapping task as described in Section 4.5.2.3. TMS mapping was calculated with the τ statistic, see Section 4.5.2.1.

that the TMS maximum has a poor resolution in direction normal to the stimulation sites, Figure 6.5.C. This is where we plan to improve in the future.

Alternatively, it might be feasible to superimpose fMRI images with TMS fast mapping results to localise the cortical representation of a muscle at the common maxima of fMRI and TMS. This might eliminate the uncertainty associated with both techniques: poor normal resolution in fast mapping TMS and accumulation of the BOLD response in veins draining the active cortical area.

A. Discrete CR Versions

The difficulty arising in the application of Correlation Ration for motor cortex mapping is the small number of samples for evaluating η and their continuous range. Normally, in TMS only 20 to 40 samples can be acquired because of time constrains. Furthermore, the sample data is distributed continuously. This requires a new approach to evaluate Correlation Ratio. To our best knowledge, we present in the following the first formula which can reliably cope with a very low number of samples of continuous range. The main idea is to use a non-parametric regression scheme to estimate the conditional expectation $E(Y|X)$. It will be shown that the choice of the Nadaraya-Watson kernel estimator [108, 186] results in a simple algebraic formula for the estimation of η, which can be evaluated in $O(N^2)$, N being the number of samples.

We begin by presenting two common ways from literature. Both methods have their disadvantages. This leads to a new formula combining the strengthes of them and avoiding the weaknesses.

A.1. Binning

If the range of X and Y is finite and discrete, as it is e.g. for digital images, a binning approach to calculate the Correlation Ration value can be used. We define the probability that a random variable X has a certain value r by counting the number of samples with $x_i = r$ and dividing by the total number of samples, N:

$$P(X = r) = \frac{\#\{k|x_k = r\}}{N}. \tag{A.1}$$

This leads to the well known sampling formulae for expectation, variance and conditional expectation. For example, the nominator of (4.11) is given by

$$E(Var[Y|X]) = \frac{1}{N}\sum_{i=1}^{N}\sum_{j=1}^{M}(r_j - E(Y|X = x_i))^2 \frac{\#\{k|x_k = x_i, y_k = r_j\}}{\#\{k|x_k = x_i\}} \tag{A.2}$$

with

$$E(Y|X = x_i) = \sum_{j=1}^{M} r_j \frac{\#\{k|x_k = x_i, y_k = r_j\}}{\#\{k|x_k = x_i\}} \tag{A.3}$$

Here, N denotes the number of samples and $\{r_1, \ldots, r_M\}$ is the set of values of Y. To evaluate (A.2) we need to count the entities $\#\{k|x_k = x_i, y_k = r_j\}$ and $\#\{k|x_k = x_i\}$. That is what we call binning.

The formulae in the last paragraph can be used without problems for discrete random variables X, Y and large sample size N. But if there are only few samples compared to the number of bins, nearly all bins are filled with no or only one element and $\#\{k|x_k = x_i, y_k = r_j\}$ is either zero or one. In the extreme case this leads to $Var[Y|X = x_i] \equiv 0$ and hence to $\eta = 1$ independent of the measurements (x_k, y_k).

It should be noted that if X has ordinal values, one can do a little better by choosing an unbiased evaluation of the variance as Kelley showed in 1935 [69]. Nevertheless, the fundamental problem of having too few values in the bins remains.

If X and Y have continuous values, we need to define artificial bins to use Kelley's formula or the formula presented above. This leads to the problem of how many bins should be defined and how large the single bins should be. Certainly, an equal spacing for the bins seems natural, but also log-size bins could be imagined. Hence, the Correlation Ratio formula does not only depend on the samples, but on the bin number and bin size. Furthermore, binning makes Correlation Ratio discontinuous with respect to the sample values: Small changes in x_i or y_i might put them into a different bin and hence change η. This is especially problematic if the results of the CR evaluation are just the first step in an algorithm, as it is in our case, see Section 4.5.2, or in image registration. Also, the presence of discontinuities makes the use of local optimisers like Powell [130] difficult.

A.2. Parzen windowing

This approach uses the integral formulae (4.12) and (4.13) for the conditional expectation and variance. The idea is to approximate the density p of a random variable X from a sample $\{x_1, \ldots, x_N\}$. Therefore, so called "windowing functions" g_i, which are density functions themselves, are centred at each sample point x_i. The density of X is approximated by summing up all windowing functions:

$$p(x) \approx \frac{1}{N} \sum_{i=1}^{N} g_i(x). \tag{A.4}$$

The same idea can be applied to approximate a joint density. Obviously, the approximation depends on the windowing functions used. There is no general way to set them "right" - a popular choice are Gaussian density functions.

Windowing of the samples defines two new continuous random variables $\tilde{X}$ and $\tilde{Y}$. We define the Correlation Ratio of the samples as the Correlation Ratio of these new random variables:

$$\eta(x_1, \ldots, x_N|y_1, \ldots, y_N) := \eta(\tilde{Y}|\tilde{X}). \tag{A.5}$$

When calculating η numerically, we are left with several integrals which cannot be solved analytically. So we need to approximate the integral values either numerically [130] or by sampling using the law of large numbers [120].

Integrating the densities numerically is a difficult task, especially if the supports of g_i[1] are unbounded. Nevertheless, stable results can be obtained for suitable windowing functions and error bounds can be given. Still, error and speed of the calculation depend heavily on the choice of the windowing function. Hence, windowing is not only performed such that it matches the "true" distribution best, but such that the integrals can be calculated fast and reliable.

If many sample values (x_i, y_i) are present, an approximation of the density using a subsample (x_{i_d}, y_{i_d}) and an evaluation of the integrals using a different subsample (x_{i_s}, y_{i_s}) is a common technique, see [183]. The advantage is a fast evaluation of the Correlation Ratio. The drawback is the dependency on the choice of the subsamples. Furthermore, this method cannot be used if only few samples are available.

A.3. Hybrid method

A solution to the problems associated with A.1 and A.2 is to combine the Parzen windowing method from A.2 with the discrete approach from A.1.

We start the derivation with Equation (4.11). As in Section A.1, we evaluate the denominator using the discrete formula for the variance of Y. For the nominator, we use the well known formulae $Var[Y] = E(Y)^2 - E(Y^2)$ and $E(E(Y|X)) = E(Y)$ to obtain from the total variance theorem (4.10):

$$E(Var[Y|X]) = E(Y^2) - E(E(Y|X)^2). \tag{A.6}$$

The first summand can be calculated using the discrete formula. For the second summand we mix the discrete version for the outer expectation with a windowing approach for the inner conditional expectation $E(Y|X)$. That is were our approach becomes hybrid. We get

$$\begin{aligned} E(E(Y|X)^2) &= \frac{1}{N}\sum_{i=1}^{N} E(Y|X = x_i)^2 \\ &= \frac{1}{N}\sum_{i=1}^{N}\left(\int_{\mathbb{R}} \frac{y p_{XY}(x_i, y)}{p_X(x_i)} dy\right)^2. \end{aligned} \tag{A.7}$$

We approximate the densities p_X and p_{XY} as in A.2:

$$p_{XY}(x, y) := \frac{1}{N}\sum_{i=1}^{N} g_i(x) h_i(y), \tag{A.8}$$

[1] The support is the closure of the set of points x where $g_i(x)$ is not zero

where g_i and h_i are arbitrary density functions centred at x_i and y_i, i.e. $\int x g_i(x)dx = x_i$, $\int y h_i(y)dy = y_i$. Integrating p_{XY} over all $y \in \mathbb{R}$ gives p_X:

$$p_X(x) = \int_{\mathbb{R}} p_{XY}(x,y)dy = \frac{1}{N}\sum_{i=1}^{N} g_i(x) \int_{\mathbb{R}} h_i(y)dy = \frac{1}{N}\sum_{i=1}^{N} g_i(x), \tag{A.9}$$

which is independent of the choice of density functions h_i. Furthermore,

$$\int_{\mathbb{R}} y p_{XY}(x_i,y)dy = \frac{1}{N}\sum_{j=1}^{N} g_j(x_i) \int_{\mathbb{R}} y h_j(y)dy = \frac{1}{N}\sum_{j=1}^{N} g_j(x_i) y_j. \tag{A.10}$$

The important observation is that also here the result does not depend on the h_j's. Inserting (A.9), (A.10) into (A.7) yields

$$E(E(Y|X)^2) = \frac{1}{N}\sum_{i=1}^{N} \left(\frac{\sum_{j=1}^{N} y_j g_j(x_i)}{\sum_{j=1}^{N} g_j(x_i)} \right)^2. \tag{A.11}$$

Note that our approach led naturally to a generalisation of the Nadaraya-Watson kernel estimation for $E(Y|X)$, see [108, 186].

Expression (A.11) can be evaluated without difficulties by a computer as soon as windowing functions g_j are defined. In our implementations, we took them to be Gaussian density functions with mean x_j and standard deviation σ. We set σ to ten times the average distance of an X-sample to its next neighbour, see Section 4.5.3. Note that other windowing functions are also perfectly valid, but the setting presented here was found to perform well for our application.

Formula (A.11) has several advantages compared to the versions found in A.1 and A.2: Firstly, it has no "bins", i.e. it can be used for discrete as well as for continuous sample values. Secondly, the result depends smoothly on the sample values x_i, y_i, if a smooth windowing function is chosen. Thirdly, it can be evaluated fast and stable with any windowing function without further numeric theory. Fourthly, it gives stable results, even if the number of samples is low, see Section 4.5.

We should remark that by following the idea of (A.11) being the mean of the square of the regression function $E(Y|X)$, one could implement a number of different formulae for η by choosing a different regression. For example, Mammen et al. suggest using a combined Nadaraya-Watson and local linear smoother [95]. Their formula has the advantage of preserving linearity in the data, a property not possessed by the Nadaraya-Watson kernel alone. The disadvantage of Mammen's approach is the relatively costly calculation of the regression, disqualifying it for our application, see Section 4.5.

Bibliography

[1] *Adept Viper s850 specification*. Adept Technology, Inc., Livermore, CA, USA. URL `http://www.adept.com/products/pdf/AdeptViper_s850_specs.pdf`.

[2] V. E. Amassian and R. Q. Cracco. Human cerebral cortical responses to contralateral transcranial stimulation. *Neurosurgery*, 20(1):148–155, Jan 1987.

[3] V. E. Amassian, M. Stewart, G. J. Quirk, and J. L. Rosenthal. Physiological basis of motor effects of a transient stimulus to cerebral cortex. *Neurosurgery*, 20(1):74–93, Jan 1987.

[4] Nina Amenta, Sunghee Choi, and Ravi Krishna Kolluri. The power crust, unions of balls, and the medial axis transform. *Computational Geometry*, 19(2-3):127–153, 2001. URL `citeseer.ist.psu.edu/article/amenta01power.html`.

[5] Andrea Antal, Tamas Z Kincses, Michael A Nitsche, Orsolya Bartfai, Iris Demmer, Martin Sommer, and Walter Paulus. Pulse configuration-dependent effects of repetitive transcranial magnetic stimulation on visual perception. *Neuroreport*, 13 (17):2229–2233, Dec 2002. doi: 10.1097/01.wnr.0000044216.09266.64. URL `http://dx.doi.org/10.1097/01.wnr.0000044216.09266.64`.

[6] J. Ashburner and K.J. Friston. Image segmentation. In R.S.J. Frackowiak, K.J. Friston, C. Frith, R. Dolan, K.J. Friston, C.J. Price, S. Zeki, J. Ashburner, and W.D. Penny, editors, *Human Brain Function*, chapter 5. Academic Press, 2nd edition, 2003.

[7] *atracsys accuTrack specification*. Atracsys LLC, Bottens, Switzerland. URL `http://www.atracsys.com/pdfs/accuTrack.pdf`.

[8] A. T. Barker, R. Jalinous, and I. L. Freeston. Non-invasive magnetic stimulation of human motor cortex. *Lancet*, 1(8437):1106–1107, May 1985.

[9] P. J. Basser and B. J. Roth. Stimulation of a myelinated nerve axon by electromagnetic induction. *Med Biol Eng Comput*, 29(3):261–268, May 1991.

[10] P. J. Basser and B. J. Roth. New currents in electrical stimulation of excitable tissues. *Annu Rev Biomed Eng*, 2:377–397, 2000. doi: 10.1146/annurev.bioeng.2.1.377. URL `http://dx.doi.org/10.1146/annurev.bioeng.2.1.377`.

[11] E. P. Bastings, H. D. Gage, J. P. Greenberg, G. Hammond, L. Hernandez, P. Santago, C. A. Hamilton, D. M. Moody, K. D. Singh, P. E. Ricci, T. P. Pons, and D. C. Good. Co-registration of cortical magnetic stimulation and functional magnetic resonance imaging. *Neuroreport*, 9(9):1941–1946, Jun 1998.

[12] R. Benecke, B. U. Meyer, P. Schönle, and B. Conrad. Transcranial magnetic stimulation of the human brain: responses in muscles supplied by cranial nerves. *Exp Brain Res*, 71(3):623–632, 1988.

[13] P.J. Besl and H.D. McKay. A method for registration of 3-d shapes. *Pattern Analysis and Machine Intelligence, IEEE Transactions on*, 14(2):239–256, Feb. 1992. doi: 10.1109/34.121791.

[14] M. Bähr and M. Frotscher. *Duus' Neurologisch-topische Diagnostik*. Georg Thieme Verlag, 8th edition, 2003.

[15] N. Binder, L. Matthäus, R. Burgkart, and A. Schweikard. A robotic C-arm fluoroscope. *Int J Med Robot*, 1(3):108–116, Sep 2005. doi: 10.1002/rcs.34. URL `http://dx.doi.org/10.1002/rcs.34`.

[16] D. E. Bohning, A. Shastri, E. M. Wassermann, U. Ziemann, J. P. Lorberbaum, Z. Nahas, M. P. Lomarev, and M. S. George. BOLD-fMRI response to single-pulse transcranial magnetic stimulation (TMS). *J Magn Reson Imaging*, 11(6):569–574, Jun 2000.

[17] Daryl E Bohning, S. Denslow, P. A. Bohning, J. A. Walker, and M. S. George. A TMS coil positioning/holding system for mr image-guided TMS interleaved with fMRI. *Clin Neurophysiol*, 114(11):2210–2219, Nov 2003.

[18] B. Boroojerdi, H. Foltys, T. Krings, U. Spetzger, A. Thron, and R. Töpper. Localization of the motor hand area using transcranial magnetic stimulation and functional magnetic resonance imaging. *Clin Neurophysiol*, 110(4):699–704, Apr 1999.

[19] Chad A Bossetti, Merrill J Birdno, and Warren M Grill. Analysis of the quasi-static approximation for calculating potentials generated by neural stimulation. *J Neural Eng*, 5(1):44–53, Mar 2008. doi: 10.1088/1741-2560/5/1/005. URL `http://dx.doi.org/10.1088/1741-2560/5/1/005`.

[20] J. P. Brasil-Neto, L. M. McShane, P. Fuhr, M. Hallett, and L. G. Cohen. Topographic mapping of the human motor cortex with magnetic stimulation: factors affecting accuracy and reproducibility. *Electroencephalogr Clin Neurophysiol*, 85(1):9–16, Feb 1992.

[21] T. C. Britton, B. U. Meyer, and R. Benecke. Variability of cortically evoked motor responses in multiple sclerosis. *Electroencephalogr Clin Neurophysiol*, 81(3):186–194, Jun 1991.

[22] A. Brun, C.-F. Westin, S. Haker, and H. Knutsson. A tensor-like representation for averaging, filtering and interpolation of 3-d object orientation data. In *Proc. IEEE International Conference on Image Processing ICIP 2005*, volume 3, pages III–1092–5, 2005. doi: 10.1109/ICIP.2005.1530586.

[23] H.H. Chen and H.H. Chen. A screw motion approach to uniqueness analysis of head-eye geometry. In *Proc. CVPR '91. IEEE Computer Society Conference on Computer Vision and Pattern Recognition*, pages 145–151, 1991. doi: 10.1109/CVPR.1991.139677.

[24] Edward P Chronicle, A. Jane Pearson, and Cheryl Matthews. Development and positioning reliability of a TMS coil holder for headache research. *Headache*, 45(1): 37–41, Jan 2005. doi: 10.1111/j.1526-4610.2005.05008.x. URL `http://dx.doi.org/10.1111/j.1526-4610.2005.05008.x`.

[25] *Micron Tracker 2 specification.* Claron Technology Inc., Toronto, Ontario, Canada. URL `http://www.clarontech.com/mt2_brochure.pdf`.

[26] J. Classen, U. Knorr, K. J. Werhahn, G. Schlaug, E. Kunesch, L. G. Cohen, R. J. Seitz, and R. Benecke. Multimodal output mapping of human central motor representation on different spatial scales. *J Physiol*, 512 (Pt 1):163–179, Oct 1998.

[27] D. Cohen and B. N. Cuffin. Developing a more focal magnetic stimulator. part i: Some basic principles. *J Clin Neurophysiol*, 8(1):102–111, Jan 1991.

[28] J.D. Cohen, M.C. Lin, D. Manocha, and M. Ponamgi. I-COLLIDE: an interactive and exact collision detection system for large-scale environments. *Proceedings of the 1995 symposium on Interactive 3D graphics*, 1995.

[29] K.R. Davey and M. Riehl. Suppressing the surface field during transcranial magnetic stimulation. *Biomedical Engineering, IEEE Transactions on*, 53(2):190–194, Feb. 2006. doi: 10.1109/TBME.2005.862545.

[30] B. Delaunay. Sur la sphere vide. *Bull. Acad. Science USSR VII: Class. Sci. Math.*, pages 793–800, 1934.

[31] M. P. do Carmo. *Differential Geometry of Curves and Surfaces.* Prentice-Hall, 1976. 503 pages.

[32] S. A. Edgley, J. A. Eyre, R. N. Lemon, and S. Miller. Excitation of the corticospinal tract by electromagnetic and electrical stimulation of the scalp in the macaque monkey. *J Physiol*, 425:301–320, Jun 1990.

[33] S. A. Edgley, J. A. Eyre, R. N. Lemon, and S. Miller. Comparison of activation of corticospinal neurons and spinal motor neurons by magnetic and electrical transcranial stimulation in the lumbosacral cord of the anaesthetized monkey. *Brain*, 120 (Pt 5): 839–853, May 1997.

[34] Peter Eichhammer, Berthold Langguth, Jörg Marienhagen, Tobias Kleinjung, and Göran Hajak. Neuronavigated repetitive transcranial magnetic stimulation in patients with tinnitus: a short case series. *Biol Psychiatry*, 54(8):862–865, Oct 2003.

[35] Peter H Ellaway, Maria Catley, Nick J Davey, Annapoorna Kuppuswamy, Paul Strutton, Hans L Frankel, Ali Jamous, and Gordana Savic. Review of physiological motor outcome measures in spinal cord injury using transcranial magnetic stimulation and spinal reflexes. *J Rehabil Res Dev*, 44(1):69–76, 2007.

[36] C. M. Epstein, D. G. Schwartzberg, K. R. Davey, and D. B. Sudderth. Localizing the site of magnetic brain stimulation in humans. *Neurology*, 40(4):666–70, Apr 1990.

[37] F. Ernst, R. Bruder, and A. Schlaefer. Processing of respiratory signals from tracking systems for motion compensated IGRT. *Medical Physics*, 34:2565, 2007.

[38] G. J. Ettinger, M. E. Leventon, W. E. Grimson, R. Kikinis, L. Gugino, W. Cote, L. Sprung, L. Aglio, M. E. Shenton, G. Potts, V. L. Hernandez, and E. Alexander. Experimentation with a transcranial magnetic stimulation system for functional brain mapping. *Med Image Anal*, 2(2):133–142, Jun 1998.

[39] G.J. Ettinger, W.E.L. Grimson, M.E. Leventon, R. Kikinis, V. Gugino, W. Cote, M. Karapelou, L. Aglio, M. Shenton, G. Potts, and E. Alexander. Non-invasive functional brain mapping using registered transcranial magnetic stimulation. In *Mathematical Methods in Biomedical Image Analysis, 1996., Proceedings of the Workshop on*, pages 32–41, 21-22 June 1996. doi: 10.1109/MMBIA.1996.534055.

[40] E. Fernandez, A. Alfaro, J. M. Tormos, R. Climent, M. Martínez, H. Vilanova, V. Walsh, and A. Pascual-Leone. Mapping of the human visual cortex using image-guided transcranial magnetic stimulation. *Brain Res Brain Res Protoc*, 10(2):115–124, Oct 2002.

[41] M. Finke, R. Bruder, L. Matthäus, and A. Schweikard. Spulenpositionierung bei TMS-Behandlungen mit Hilfe von Kraftsensorik. In *CURAC*, 2007.

[42] M. Finke, T. Fadini, S. Kantelhardt, A. Giese, L. Matthäus, and A. Schweikard. Brain-mapping using robotized TMS. *Conf Proc IEEE Eng Med Biol Soc*, 1:3929–3932, 2008.

[43] A. Flöel and S. Knecht. Transkranielle Magnetstimulation in der Therapie von Schlaganfallfolgen. *Klinische Neurophysiologie*, 33(2):100–5, June 2002.

[44] Peter T Fox, Shalini Narayana, Nitin Tandon, Hugo Sandoval, Sarabeth P Fox, Peter Kochunov, and Jack L Lancaster. Column-based model of electric field excitation of cerebral cortex. *Hum Brain Mapp*, 22(1):1–14, May 2004. doi: 10.1002/hbm.20006. URL `http://dx.doi.org/10.1002/hbm.20006`.

[45] Peter T Fox, Shalini Narayana, Nitin Tandon, Sarabeth P Fox, Hugo Sandoval, Peter Kochunov, Charles Capaday, and Jack L Lancaster. Intensity modulation of TMS-induced cortical excitation: primary motor cortex. *Hum Brain Mapp*, 27(6):478–487, Jun 2006. doi: 10.1002/hbm.20192. URL `http://dx.doi.org/10.1002/hbm.20192`.

[46] K. J. Friston, A. P. Holmes, J. B. Poline, P. J. Grasby, S. C. Williams, R. S. Frackowiak, and R. Turner. Analysis of fmri time-series revisited. *Neuroimage*, 2(1):45–53, Mar 1995. doi: 10.1006/nimg.1995.1007. URL `http://dx.doi.org/10.1006/nimg.1995.1007`.

[47] C. Gabriel, S. Gabriel, and E. Corthout. The dielectric properties of biological tissues: I. literature survey. *Phys Med Biol*, 41(11):2231–2249, Nov 1996.

[48] O. Ganslandt, S. Behari, J. Gralla, R. Fahlbusch, and C. Nimsky. Neuronavigation: concept, techniques and applications. *Neurol India*, 50(3):244–255, Sep 2002.

[49] M. S. George, E. M. Wassermann, W. A. Williams, A. Callahan, T. A. Ketter, P. Basser, M. Hallett, and R. M. Post. Daily repetitive transcranial magnetic stimulation (rTMS) improves mood in depression. *Neuroreport*, 6(14):1853–1856, Oct 1995.

[50] L. D. Gugino, J. R. Romero, L. Aglio, D. Titone, M. Ramirez, A. Pascual-Leone, E. Grimson, N. Weisenfeld, R. Kikinis, and M. E. Shenton. Transcranial magnetic stimulation coregistered with MRI: a comparison of a guided versus blind stimulation technique and its effect on evoked compound muscle action potentials. *Clin Neurophysiol*, 112(10):1781–1792, Oct 2001.

[51] L. Heller and D. B. van Hulsteyn. Brain stimulation using electromagnetic sources: theoretical aspects. *Biophys J*, 63(1):129–138, Jul 1992.

[52] U. Herwig and C. Schönfeldt-Lecuona. [the study of central nervous information processing with transcranial magnetic stimulation]. *Fortschr Neurol Psychiatr*, 68(7): 289–300, Jul 2000. German Title: Die Untersuchung zentralnervöser Informationsverarbeitung mit transkranieller Magnetstimulation.

[53] U. Herwig, C. Schönfeldt-Lecuona, A. P. Wunderlich, C. von Tiesenhausen, A. Thielscher, H. Walter, and M. Spitzer. The navigation of transcranial magnetic stimulation. *Psychiatry Res*, 108(2):123–131, Nov 2001.

[54] Uwe Herwig, Klaus Kölbel, Arthur P Wunderlich, Axel Thielscher, Cyrill von Tiesenhausen, Manfred Spitzer, and Carlos Schönfeldt-Lecuona. Spatial congruence of neuronavigated transcranial magnetic stimulation and functional neuroimaging. *Clin Neurophysiol*, 113(4):462–468, Apr 2002.

[55] Uwe Herwig, Peyman Satrapi, and Carlos Schönfeldt-Lecuona. Using the international 10-20 eeg system for positioning of transcranial magnetic stimulation. *Brain Topogr*, 16(2):95–99, 2003.

[56] A. L. Hodgkin and A. F. Huxley. A quantitative description of membrane current and its application to conduction and excitation in nerve. *J Physiol*, 117(4):500–544, Aug 1952.

[57] Hugues Hoppe, Tony DeRose, Tom Duchamp, John McDonald, and Werner Stuetzle. Surface reconstruction from unorganized points. In *SIGGRAPH '92: Proceedings of the 19th annual conference on Computer graphics and interactive techniques*, pages 71–8, New York, NY, USA, 1992. ACM Press.

[58] B.K.P. Horn. Closed-form solution of absolute orientation using unit quaternions. *J. Opt. Soc. Am. A.*, 4(4):629–42, April 1987.

[59] D. A. Houlden, M. L. Schwartz, C. H. Tator, P. Ashby, and W. A. MacKay. Spinal cord-evoked potentials and muscle responses evoked by transcranial magnetic stimulation in 10 awake human subjects. *J Neurosci*, 19(5):1855–1862, Mar 1999.

[60] T.C. Hudson, M.C. Lin, J. Cohen, S. Gottschalk, and D. Manocha. V-COLLIDE: accelerated collision detection for VRML. *Proceedings of the second symposium on Virtual reality modeling language*, 1997.

[61] A. Hufnagel, C.E. Elger, D.K. Boker, D.B. Linke, M. Kurthen, and L. Solymosi. Activation of the epileptic focus during intracarotid amobarbital test. electrocorticographic registration via subdural electrodes. *Electroencephalogr Clin Neurophysiol*, 75 (6):453–63, 1990.

[62] R. J. Ilmoniemi and J. Karhu. Transcranial magnetic stimulation – towards navigated targeting. *Global Health Care*, Issue 3, September 2002. URL `http://www.incm.cnrs-mrs.fr/Seminaires/Ilmoniemi&Karhu2002.pdf`. The World Medical Association.

[63] R. J. Ilmoniemi, J. Virtanen, J. Ruohonen, J. Karhu, H. J. Aronen, R. Näätänen, and T. Katila. Neuronal responses to magnetic stimulation reveal cortical reactivity and connectivity. *Neuroreport*, 8(16):3537–3540, Nov 1997.

[64] John R Ives, Alexander Rotenberg, Roberto Poma, Gregor Thut, and Alvaro Pascual-Leone. Electroencephalographic recording during transcranial magnetic stimulation in humans and animals. *Clin Neurophysiol*, 117(8):1870–1875, Aug 2006. doi: 10.1016/j.clinph.2006.04.010. URL `http://dx.doi.org/10.1016/j.clinph.2006.04.010`.

[65] R. Jalinous. Technical and practical aspects of magnetic nerve stimulation. *J Clin Neurophysiol*, 8(1):10–25, Jan 1991.

[66] H. Joe. Relative entropy measures of multivariate dependence. *J Am Stat Assoc*, 84 (405):157–164, 1989.

[67] S. Kahkonen, J. Wilenius, S. Komssi, and R.J. Ilmoniemi. Distinct differences in cortical reactivity of motor and prefrontal cortices to magnetic stimulation. *Clin Neurophysiol*, 115(3):583–8, 2004.

[68] T. Kammer, S. Beck, A. Thielscher, U. Laubis-Herrmann, and H. Topka. Motor thresholds in humans: a transcranial magnetic stimulation study comparing different pulse waveforms, current directions and stimulator types. *Clin Neurophysiol*, 112(2): 250–58, Feb 2001.

[69] Truman L. Kelley. An unbiased correlation ratio measure. *Proc Natl Acad Sci U S A*, 21(9):554–9, 1935.

[70] Eman M Khedr, Mohamed A Ahmed, Nehal Fathy, and John C Rothwell. Therapeutic trial of repetitive transcranial magnetic stimulation after acute ischemic stroke. *Neurology*, 65(3):466–468, Aug 2005. doi: 10.1212/01.wnl.0000173067.84247.36. URL `http://dx.doi.org/10.1212/01.wnl.0000173067.84247.36`.

[71] L. Kiers, D. Cros, K. H. Chiappa, and J. Fang. Variability of motor potentials evoked by transcranial magnetic stimulation. *Electroencephalogr Clin Neurophysiol*, 89(6): 415–423, Dec 1993.

[72] Dong-Hun Kim, G.E. Georghiou, and C. Won. Improved field localization in transcranial magnetic stimulation of the brain with the utilization of a conductive shield plate in the stimulator. *Biomedical Engineering, IEEE Transactions on*, 53(4):720–725, April 2006. doi: 10.1109/TBME.2006.870244.

[73] T. Kleinjung, T. Steffens, B. Langguth, P. Eichhammer, J. Marienhagen, G. Hajak, and J. Strutz. [treatment of chronic tinnitus with neuronavigated repetitive transcranial magnetic stimulation (rTMS).]. *HNO*, 54(6):439–444, Jun 2006. doi: 10.1007/

s00106-005-1329-8. URL http://dx.doi.org/10.1007/s00106-005-1329-8. German Title: Neuronavigierte repetitive transkranielle Magnetstimulation (rTMS). Ein neuartiges Verfahren zur Behandlung des chronischen Tinnitus.

[74] Masahito Kobayashi and Alvaro Pascual-Leone. Transcranial magnetic stimulation in neurology. *Lancet Neurol*, 2(3):145–156, Mar 2003.

[75] I. Kojadinovic. On the use of mutual information in data analysis: an overview. In *Applied Stochastic Models and Data Analysis (ASMDA)*, Brest (France), May 2005.

[76] Soile Komssi, Seppo Kähkönen, and Risto J Ilmoniemi. The effect of stimulus intensity on brain responses evoked by transcranial magnetic stimulation. *Hum Brain Mapp*, 21(3):154–164, Mar 2004. doi: 10.1002/hbm.10159. URL http://dx.doi.org/10.1002/hbm.10159.

[77] T. Krings, B. R. Buchbinder, W. E. Butler, K. H. Chiappa, H. J. Jiang, B. R. Rosen, and G. R. Cosgrove. Stereotactic transcranial magnetic stimulation: correlation with direct electrical cortical stimulation. *Neurosurgery*, 41(6):1319–25; discussion 1325–6, Dec 1997.

[78] T. Krings, C. Naujokat, and D. G. von Keyserlingk. Representation of cortical motor function as revealed by stereotactic transcranial magnetic stimulation. *Electroencephalogr Clin Neurophysiol*, 109(2):85–93, Apr 1998.

[79] T. Krings, K. H. Chiappa, H. Foltys, M. H. Reinges, G. R. Cosgrove, and A. Thron. Introducing navigated transcranial magnetic stimulation as a refined brain mapping methodology. *Neurosurg Rev*, 24(4):171–179, Dec 2001.

[80] T. Krings, H. Foltys, M. H. Reinges, S. Kemeny, V. Rohde, U. Spetzger, J. M. Gilsbach, and A. Thron. Navigated transcranial magnetic stimulation for presurgical planning–correlation with functional MRI. *Minim Invasive Neurosurg*, 44(4):234–239, Dec 2001. doi: 10.1055/s-2001-19935. URL http://dx.doi.org/10.1055/s-2001-19935.

[81] *Kuka KR3 specification*. KUKA Roboter GmbH, Augsburg, Germany. URL http://www.kuka.com/NR/rdonlyres/926CEC2C-A2C5-4537-A5C5-05A76F6CC09C/0/kr3_de_en_fr.pdf.

[82] Jack L Lancaster, Shalini Narayana, Dennis Wenzel, James Luckemeyer, John Roby, and Peter Fox. Evaluation of an image-guided, robotically positioned transcranial magnetic stimulation system. *Hum Brain Mapp*, 22(4):329–340, Aug 2004. doi: 10.1002/hbm.20041. URL http://dx.doi.org/10.1002/hbm.20041.

[83] V. Di Lazzaro, A. Oliviero, P. Profice, E. Saturno, F. Pilato, A. Insola, P. Mazzone, P. Tonali, and J. C. Rothwell. Comparison of descending volleys evoked by transcranial magnetic and electric stimulation in conscious humans. *Electroencephalogr Clin Neurophysiol*, 109(5):397–401, Oct 1998.

[84] C. Lebossé. Stimulation methods. *International Journal of Computer Assisted Radiology and Surgery*, 1:137–145, 2006.

[85] C. Lebossé, P. Renaud, B. Bayle, M. de Mathelin, O. Piccin, and J. Foucher. A robotic system for automated image-guided transcranial magnetic stimulation. In *Proc. IEEE/NIH Life Science Systems and Applications Workshop LISA 2007*, pages 55–58, 2007. doi: 10.1109/LSSA.2007.4400883.

[86] J-P. Lefaucheur, X. Drouot, I. Menard-Lefaucheur, F. Zerah, B. Bendib, P. Cesaro, Y. Keravel, and J-P. Nguyen. Neurogenic pain relief by repetitive transcranial magnetic cortical stimulation depends on the origin and the site of pain. *J Neurol Neurosurg Psychiatry*, 75(4):612–616, Apr 2004.

[87] Dana Linnepe. Entwicklung einer Simulationsumgebung zur Kollisionserkennung am Beispiel eines robotisierten mobilen C-Bogens. Bachelor thesis, Institute for Robotics and Cognitive Systems, University of Lübeck, Lübeck, Germany, 2006.

[88] O. G. Lins, T. W. Picton, P. Berg, and M. Scherg. Ocular artifacts in EEG and event-related potentials. I: Scalp topography. *Brain Topogr*, 6(1):51–63, 1993.

[89] Z.G. Liu, Y.F. Li, and P. Bao. Stereo-based head pose tracking with motion compensation model. In *Robotics and Biomimetics, 2004. ROBIO 2004. IEEE International Conference on*, pages 700–704, 22-26 Aug. 2004.

[90] Alain Londero, Jean-Pascal Lefaucheur, David Malinvaud, Pierre Brugieres, Philippe Peignard, Jean-Paul Nguyen, Paul Avan, and Pierre Bonfils. [magnetic stimulation of the auditory cortex for disabling tinnitus: preliminary results]. *Presse Med*, 35(2 Pt 1):200–206, Feb 2006.

[91] W.E. Lorensen and H.E. Cline. Marching cubes: A high resolution 3D surface construction algorithm. *Proceedings of the 14th annual conference on Computer graphics and interactive techniques*, pages 163–169, 1987.

[92] M. Lotze, R. J. Kaethner, M. Erb, L. G. Cohen, W. Grodd, and H. Topka. Comparison of representational maps using functional magnetic resonance imaging and transcranial magnetic stimulation. *Clin Neurophysiol*, 114(2):306–312, Feb 2003.

[93] P. J. Maccabee, V. E. Amassian, L. P. Eberle, and R. Q. Cracco. Magnetic coil stimulation of straight and bent amphibian and mammalian peripheral nerve in vitro: locus of excitation. *J Physiol*, 460:201–219, Jan 1993.

[94] J. Malmivuo and R. Plonsey. *Bioelectromagnetism: Principles and Applications of Bioelectric and Biomagnetic Fields*. Oxford University Press, New York, 1995. ISBN 0195058232.

[95] E. Mammen and J.S. Marron. Mass recentred kernel smoothers. *Biometrika*, 84(4): 765–77, 1997.

[96] Volker Martens, Floris Ernst, Thomas Fränkler, Lars Matthäus, Stefan Schlichting, and Achim Schweikard. Ein Client-Server Framework für Trackingsysteme in medizinischen Assistenzsystemen. In *curac.08 Tagungsband*, 7. Jahrestagung, pages 7–10, Leipzig, September 2008. Deutsche Gesellschaft für Computer- und Roboterassistierte Chirurgie.

[97] F. Matsuo, J. F. Peters, and E. L. Reilly. Electrical phenomena associated with movements of the eyelid. *Electroencephalogr Clin Neurophysiol*, 38(5):507–511, May 1975.

[98] L. Matthäus, P. Trillenberg, C. Bodensteiner, A. Giese, and A. Schweikard. Robotized TMS for motion compensated navigated brain stimulation. In *Computer Assisted Radiology and Surgery (CARS), 20th International Congress*, Osaka, Japan, June 28 - July 1 2006.

[99] L. Matthäus, N. Binder, C. Bodensteiner, and A. Schweikard. Closed-form inverse kinematic solution for fluoroscopic C-arms. *Advanced Robotics*, 21(8):869–886, 2007.

[100] L. Matthäus, P. Trillenberg, T. Fadini, M. Finke, and A. Schweikard. Brain mapping with transcranial magnetic stimulation using a refined correlation ratio and Kendall's tau. *Stat Med*, 27(25):5252–5270, Nov 2008. doi: 10.1002/sim.3353. URL `http://dx.doi.org/10.1002/sim.3353`.

[101] L. Matthäus, T. Fadini, P. Trillenberg, A. Giese, D. Rasche, C. Bodensteiner, V. Martens, M. Finke, and A. Schweikard. Robotised transcranial magnetic stimulation. *IEEE T Robot*, submitted.

[102] Lars Matthäus, Alf Giese, Daniel Wertheimer, and Achim Schweikard. Planning and analyzing robotized TMS using virtual reality. *Stud Health Technol Inform*, 119:373–378, 2006.

[103] J.C. Maxwell. A dynamical theory of the electromagnetic field. *Philosophical Transactions of the Royal Society of London*, 155:459–512, 1865.

[104] D. R. McNeal. Analysis of a model for excitation of myelinated nerve. *IEEE Trans Biomed Eng*, 23(4):329–337, Jul 1976.

[105] B. U. Meyer, J. Noth, H. W. Lange, C. Bischoff, J. Machetanz, A. Weindl, S. Röricht, R. Benecke, and B. Conrad. Motor responses evoked by magnetic brain stimulation in huntington's disease. *Electroencephalogr Clin Neurophysiol*, 85(3):197–208, Jun 1992.

[106] K. R. Mills, S. J. Boniface, and M. Schubert. Magnetic brain stimulation with a double coil: the importance of coil orientation. *Electroencephalogr Clin Neurophysiol*, 85(1): 17–21, Feb 1992.

[107] T. Morioka, A. Mizushima, T. Yamamoto, S. Tobimatsu, S. Matsumoto, K. Hasuo, K. Fujii, and M. Fukui. Functional mapping of the sensorimotor cortex: combined use of magnetoencephalography, functional mri, and motor evoked potentials. *Neuroradiology*, 37(7):526–530, Oct 1995.

[108] E.A. Nadaraya. On estimating regression. *Theory Prob. Applic.*, 10:186–90, 1964.

[109] M. Nadeem, T. Thorlin, O.P. Gandhi, and M. Persson. Computation of electric and magnetic stimulation in human head using the 3-D impedance method. *Biomedical Engineering, IEEE Transactions on*, 50(7):900–907, July 2003. doi: 10.1109/TBME.2003.813548.

[110] K. Nakashima, Y. Wang, M. Shimoda, K. Sakuma, and K. Takahashi. Shortened silent period produced by magnetic cortical stimulation in patients with parkinson's disease. *J Neurol Sci*, 130(2):209–214, Jun 1995.

[111] M.H. Nayfeh and M.K. Brussel. *Electricity and Magnetism*. Wiley, New York, 1985.

[112] S. F W Neggers, T. R. Langerak, D. J L G Schutter, R. C W Mandl, N. F. Ramsey, P. J J Lemmens, and A. Postma. A stereotactic method for image-guided transcranial magnetic stimulation validated with fMRI and motor-evoked potentials. *Neuroimage*, 21(4):1805–1817, Apr 2004. doi: 10.1016/j.neuroimage.2003.12.006. URL `http://dx.doi.org/10.1016/j.neuroimage.2003.12.006`.

[113] L. Niehaus, K. von Alt-Stutterheim, S. Röricht, and B. U. Meyer. Abnormal postexcitatory and interhemispheric motor cortex inhibition in writer's cramp. *J Neurol*, 248 (1):51–56, Jan 2001.

[114] Q. Noirhomme, E. Romero, O. Cuisenaire, M. Ferrant, Y. Vandermeeren, E. Olivier, and B. Macq. Registration of transcranial magnetic stimulation, a visualization tool for brain functions. In *Proceedings of DSP 2002 - 14th Intl Conference on Digital Signal Processing*, pages 311–4, Santorini, Greece, July 1-3 2002.

[115] Q. Noirhomme, M. Ferrant, Y. Vandermeeren, E. Olivier, B. Macq, and O. Cuisenaire. Registration and real-time visualization of transcranial magnetic stimulation with 3-D MR images. *Biomedical Engineering, IEEE Transactions on*, 51(11):1994–2005, Nov. 2004. doi: 10.1109/TBME.2004.834266.

[116] *NDI Polaris specification*. Northern Digital Inc., Waterloo, Ontario, Canada. URL `http://www.ndigital.com/medical/polarisfamily-techspecs.php`.

[117] P. Nunez and R. Srinivasan. *Electric Fields of the Brain: The Neurophysics of EEG*. Oxford University Press, 2nd edition, 2006.

[118] C. J. Ochoa and J. Polich. P300 and blink instructions. *Clin Neurophysiol*, 111(1): 93–98, Jan 2000.

[119] Masako Okamoto and Ippeita Dan. Automated cortical projection of head-surface locations for transcranial functional brain mapping. *Neuroimage*, 26(1):18–28, May 2005. doi: 10.1016/j.neuroimage.2005.01.018. URL `http://dx.doi.org/10.1016/j.neuroimage.2005.01.018`.

[120] A. Papoulis and S.U. Pillai. *Probability, Random Variables and Stochastic Processes*, volume 4th. McGraw-Hill, Inc., 2002.

[121] A. Pascual-Leone, J. Valls-Solé, E. M. Wassermann, and M. Hallett. Responses to rapid-rate transcranial magnetic stimulation of the human motor cortex. *Brain*, 117 (Pt 4):847–858, Aug 1994.

[122] A. Pascual-Leone, B. Rubio, F. Pallardó, and M. D. Catalá. Rapid-rate transcranial magnetic stimulation of left dorsolateral prefrontal cortex in drug-resistant depression. *Lancet*, 348(9022):233–237, Jul 1996.

[123] A. Pascual-Leone, N.J. Davey, J. Rothwell, E.M. Wassermann, and B.K. Puri. *Handbook of Transcranial Magnetic Stimulation*. Arnold, 2002.

[124] T. Paus, P. K. Sipila, and A. P. Strafella. Synchronization of neuronal activity in the human primary motor cortex by transcranial magnetic stimulation: an EEG study. *J Neurophysiol*, 86(4):1983–1990, Oct 2001.

[125] K. Pearson. On the general theory of skew correlation and non-linear regression. *Drapers' Company Research Memoirs: Dulau and Co*, 1905.

[126] Angel V Peterchev, Reza Jalinous, and Sarah H Lisanby. A transcranial magnetic stimulator inducing near-rectangular pulses with controllable pulse width (ctms). *IEEE Trans Biomed Eng*, 55(1):257–266, Jan 2008. doi: 10.1109/TBME.2007.900540. URL `http://dx.doi.org/10.1109/TBME.2007.900540`.

[127] Christian Plewnia, Mathias Bartels, and Christian Gerloff. Transient suppression of tinnitus by transcranial magnetic stimulation. *Ann Neurol*, 53(2):263–266, Feb 2003. doi: 10.1002/ana.10468. URL `http://dx.doi.org/10.1002/ana.10468`.

[128] Christian Plewnia, Matthias Reimold, Arif Najib, Gerald Reischl, Stefan K Plontke, and Christian Gerloff. Moderate therapeutic efficacy of pet-navigated repetitive transcranial magnetic stimulation against chronic tinnitus: a randomised, controlled pilot study. *J Neurol Neurosurg Psychiatry*, Aug 2006. doi: 10.1136/jnnp.2006.095612. URL `http://dx.doi.org/10.1136/jnnp.2006.095612`.

[129] R. Plonsey. *Bioelectric Phenomena*. McGraw-Hill Education, 1969.

[130] W.H. Press, S.A. Teukolsky, W.T. Vetterling, and B.P. Flannery. *Numerical Recipes in C++. The Art of Scientific Computing*. Cambridge University Press, Cambridge, UK, 2nd edition, 2002.

[131] S. Pridmore and G. Oberoi. Transcranial magnetic stimulation applications and potential use in chronic pain: studies in waiting. *J Neurol Sci*, 182(1):1–4, Dec 2000.

[132] Saxby Pridmore, Gajinder Oberoi, Marco Marcolin, and Mark George. Transcranial magnetic stimulation and chronic pain: current status. *Australas Psychiatry*, 13(3): 258–265, Sep 2005. doi: 10.1111/j.1440-1665.2005.02197.x. URL `http://dx.doi.org/10.1111/j.1440-1665.2005.02197.x`.

[133] Saxby Pridmore, Tobias Kleinjung, Berthold Langguth, and Peter Eichhammer. Transcranial magnetic stimulation: potential treatment for tinnitus? *Psychiatry Clin Neurosci*, 60(2):133–138, Apr 2006. doi: 10.1111/j.1440-1819.2006.01477.x. URL `http://dx.doi.org/10.1111/j.1440-1819.2006.01477.x`.

[134] L. Ramrath, U.G. Hofmann, and A. Schweikard. Spherical assistant for stereotactic surgery. In *Proc. IEEE/RSJ International Conference on Intelligent Robots and Systems IROS 2007*, pages 859–864, 2007. doi: 10.1109/IROS.2007.4398985.

[135] Jean-Alban Rathelot and Peter L Strick. Muscle representation in the macaque motor cortex: an anatomical perspective. *Proc Natl Acad Sci U S A*, 103(21):8257–8262, May 2006. doi: 10.1073/pnas.0602933103. URL `http://dx.doi.org/10.1073/pnas.0602933103`.

[136] F. Rattay. Analysis of models for external stimulation of axons. *IEEE Trans Biomed Eng*, 33(10):974–977, Oct 1986. doi: 10.1109/TBME.1986.325670. URL `http://dx.doi.org/10.1109/TBME.1986.325670`.

[137] J. P. Reilly. Peripheral nerve stimulation by induced electric currents: exposure to time-varying magnetic fields. *Med Biol Eng Comput*, 27(2):101–110, Mar 1989.

[138] P. Renaud, O. Piccin, C. Lebossé, E. Laroche, M. de Mathelin, B. Bayle, and J. Foucher. Robotic image-guided transcranial magnetic stimulation. In *Computer Assisted Radiology and Surgery (CARS), 20th International Congress*, Osaka, Japan, June 28 - July 1 2006.

[139] D. De Ridder, G. De Mulder, S. Sunaert, and A. Moller. Somatosensory cortex stimulation for deafferentation pain. *Neuromodulation*, 9(2):143–153, 2006. doi: 10.1111/j.1525-1403.2006.00046.x. URL `http://www.blackwell-synergy.com/doi/abs/10.1111/j.1525-1403.2006.00046.x`.

[140] A. Roche, G. Malandain, and N. Ayache. The correlation ratio as a new similarity measure for multimodal image registration. In *Proc. of First Int. Conf. on Medical Image Computing and Computer-Assisted Intervention (MICCAI'98)*, volume 1496 of *Lecture Notes in Computer Science*, pages 1115–24, Cambridge, USA, October 1998. Springer Verlag.

[141] Jens D Rollnik, Stefanie Wüstefeld, Jan Däuper, Matthias Karst, Matthias Fink, Andon Kossev, and Reinhard Dengler. Repetitive transcranial magnetic stimulation for the treatment of chronic pain - a pilot study. *Eur Neurol*, 48(1):6–10, 2002.

[142] Pantaleo Romanelli, Achim Schweikard, Alexander Schlaefer, and John Adler. Computer aided robotic radiosurgery. *Comput Aided Surg*, 11(4):161–174, Jul 2006. doi: 10.1080/10929080600886393. URL `http://dx.doi.org/10.1080/10929080600886393`.

[143] C. Rorden. MRIcro software. www.mricro.com. Version 1.40.

[144] P. M. Rossini, C. Caltagirone, A. Castriota-Scanderbeg, P. Cicinelli, C. Del Gratta, M. Demartin, V. Pizzella, R. Traversa, and G. L. Romani. Hand motor cortical area reorganization in stroke: a study with fmri, meg and tcs maps. *Neuroreport*, 9(9): 2141–2146, Jun 1998.

[145] A. Rotem and E. Moses. Magnetic stimulation of curved nerves. *Biomedical Engineering, IEEE Transactions on*, 53(3):414–420, March 2006. doi: 10.1109/TBME.2005.869770.

[146] B. J. Roth and P. J. Basser. A model of the stimulation of a nerve fiber by electromagnetic induction. *IEEE Trans Biomed Eng*, 37(6):588–597, Jun 1990. doi: 10.1109/10.55662. URL `http://dx.doi.org/10.1109/10.55662`.

[147] B. J. Roth, J. M. Saypol, M. Hallett, and L. G. Cohen. A theoretical calculation of the electric field induced in the cortex during magnetic stimulation. *Electroencephalogr Clin Neurophysiol*, 81(1):47–56, Feb 1991.

[148] Yiftach Roth, Abraham Zangen, and Mark Hallett. A coil design for transcranial magnetic stimulation of deep brain regions. *J Clin Neurophysiol*, 19(4):361–370, Aug 2002.

[149] Yiftach Roth, Alon Amir, Yechiel Levkovitz, and Abraham Zangen. Three-dimensional distribution of the electric field induced in the brain by transcranial magnetic stimulation using figure-8 and deep h-coils. *J Clin Neurophysiol*, 24(1):31–38, Feb 2007. doi: 10.1097/WNP.0b013e31802fa393. URL `http://dx.doi.org/10.1097/WNP.0b013e31802fa393`.

[150] D. Rudiak and E. Marg. Finding the depth of magnetic brain stimulation: a re-evaluation. *Electroencephalogr Clin Neurophysiol*, 93(5):358–371, Oct 1994.

[151] J. Ruohonen, M. Panizza, J. Nilsson, P. Ravazzani, F. Grandori, and G. Tognola. Transverse-field activation mechanism in magnetic stimulation of peripheral nerves. *Electroencephalogr Clin Neurophysiol*, 101(2):167–174, Apr 1996.

[152] J. Ruohonen, P. Ravazzani, J. Nilsson, M. Panizza, F. Grandori, and G. Tognola. A volume-conduction analysis of magnetic stimulation of peripheral nerves. *IEEE Trans Biomed Eng*, 43(7):669–678, Jul 1996. doi: 10.1109/10.503174. URL `http://dx.doi.org/10.1109/10.503174`.

[153] Jarmo Ruohonen. *Transcranial Magnetic Stimulation: Modelling and New Techniques*. Dissertation, Helsinki University of Technology, Laboratory of Biomedical Engineering (BioMag), 1998.

[154] Suzanne Ryan, Leonardo Bonilha, and Stephen R Jackson. Individual variation in the location of the parietal eye fields: a TMS study. *Exp Brain Res*, 173(3):389–394, Aug 2006. doi: 10.1007/s00221-006-0379-9. URL `http://dx.doi.org/10.1007/s00221-006-0379-9`.

[155] F. S. Salinas, J. L. Lancaster, and P. T. Fox. Detailed 3D models of the induced electric field of transcranial magnetic stimulation coils. *Phys Med Biol*, 52(10):2879–2892, May 2007. doi: 10.1088/0031-9155/52/10/016. URL `http://dx.doi.org/10.1088/0031-9155/52/10/016`.

[156] G. Saporta. *Probabilités, analyse des données et statistique*. Editions Technip, Paris, 1990.

[157] A. Schlaefer, J. Fisseler, S. Dieterich, H. Shiomi, K. Cleary, and A. Schweikard. Feasibility of four-dimensional conformal planning for robotic radiosurgery. *Med Phys*, 32 (12):3786–3792, Dec 2005.

[158] V. Schnabel and J. J. Struijk. Magnetic and electrical stimulation of undulating nerve fibres: a simulation study. *Med Biol Eng Comput*, 37(6):704–709, Nov 1999.

[159] C. Schönfeldt-Lecuona, M. Spitzer, and U. Herwig. Positionierungsstrategien für die transkranielle Magnetstimulation. *Nervenheilkunde*, 22:177–81, 2003.

[160] Carlos Schönfeldt-Lecuona, Axel Thielscher, Roland W Freudenmann, Martina Kron, Manfred Spitzer, and Uwe Herwig. Accuracy of stereotaxic positioning of transcranial magnetic stimulation. *Brain Topogr*, 17(4):253–259, 2005.

[161] W.J. Schroeder, L.S. Avila, and W. Hoffman. Visualizing with VTK: a tutorial. *Computer Graphics and Applications, IEEE*, 20(5):20–27, Sept.-Oct. 2000. doi: 10.1109/38.865875.

[162] A. Schweikard, J.R. Adler, and J.-C. Latombe. Motion planning in stereotaxic radiosurgery. *IEEE T Robotic Autom*, 9(6):764–774, 1993. ISSN 1042-296X. doi: 10.1109/70.265920.

[163] A. Schweikard, M. Bodduluri, and J.R. Adler. Planning for camera-guided robotic radiosurgery. *IEEE T Robotic Autom*, 14(6):951–962, 1998. ISSN 1042-296X. doi: 10.1109/70.736778.

[164] A. Schweikard, G. Glosser, M. Bodduluri, M. J. Murphy, and J. R. Adler. Robotic motion compensation for respiratory movement during radiosurgery. *Comput Aided Surg*, 5(4):263–277, 2000. doi: 3.0.CO;2-2. URL `http://dx.doi.org/3.0.CO;2-2`.

[165] Achim Schweikard, Hiroya Shiomi, and John Adler. Respiration tracking in radiosurgery. *Med Phys*, 31(10):2738–2741, Oct 2004.

[166] Sofia Silva, Peter J Basser, and Pedro C Miranda. The activation function of TMS on a finite element model of a cortical sulcus. *Conf Proc IEEE Eng Med Biol Soc*, 2007: 6657–6660, 2007. doi: 10.1109/IEMBS.2007.4353886. URL `http://dx.doi.org/10.1109/IEMBS.2007.4353886`.

[167] K. D. Singh, S. Hamdy, Q. Aziz, and D. G. Thompson. Topographic mapping of trans-cranial magnetic stimulation data on surface rendered mr images of the brain. *Electroencephalogr Clin Neurophysiol*, 105(5):345–351, Oct 1997.

[168] Mark W. Spong, S. Hutchinson, and M. Vidyasagar. *Robot Modeling and Control*. Wiley, 2006.

[169] Klaus H. Strobl, Klaus H. Strobl, and Gerd Hirzinger. Optimal hand-eye calibration. In Gerd Hirzinger, editor, *Proc. IEEE/RSJ International Conference on Intelligent Robots and Systems*, pages 4647–4653, 2006. doi: 10.1109/IROS.2006.282250.

[170] M. A. Stuchly and K. P. Esselle. Factors affecting neural stimulation with magnetic fields. *Bioelectromagnetics*, Suppl 1:191–204, 1992.

[171] Yohei Tamura, Shingo Okabe, Takashi Ohnishi, Daisuke N Saito, Noritoshi Arai, Soichiro Mochio, Kiyoharu Inoue, and Yoshikazu Ugawa. Effects of 1-Hz repetitive transcranial magnetic stimulation on acute pain induced by capsaicin. *Pain*, 107(1-2): 107–115, Jan 2004.

[172] Gabriel Taubin, Tong Zhang, and Gene H. Golub. Optimal surface smoothing as filter design. In *ECCV '96: Proceedings of the 4th European Conference on Computer Vision-Volume I*, pages 283–292, London, UK, 1996. Springer-Verlag. ISBN 3-540-61122-3.

[173] Paul C J Taylor, Vincent Walsh, and Martin Eimer. Combining TMS and EEG to study cognitive function and cortico-cortico interactions. *Behav Brain Res*, 191(2): 141–147, Aug 2008. doi: 10.1016/j.bbr.2008.03.033. URL `http://dx.doi.org/10.1016/j.bbr.2008.03.033`.

[174] Y. Terao, Y. Ugawa, K. Sakai, S. Miyauchi, H. Fukuda, Y. Sasaki, R. Takino, R. Hanajima, T. Furubayashi, B. Pütz, and I. Kanazawa. Localizing the site of magnetic brain stimulation by functional mri. *Exp Brain Res*, 121(2):145–152, Jul 1998.

[175] Axel Thielscher and Thomas Kammer. Linking physics with physiology in TMS: a sphere field model to determine the cortical stimulation site in TMS. *Neuroimage*, 17 (3):1117–1130, Nov 2002.

[176] Axel Thielscher and Thomas Kammer. Electric field properties of two commercial figure-8 coils in TMS: calculation of focality and efficiency. *Clin Neurophysiol*, 115(7): 1697–1708, Jul 2004. doi: 10.1016/j.clinph.2004.02.019. URL `http://dx.doi.org/10.1016/j.clinph.2004.02.019`.

[177] Gregor Thut, John R Ives, Frank Kampmann, Maria A Pastor, and Alvaro Pascual-Leone. A new device and protocol for combining TMS and online recordings of EEG and evoked potentials. *J Neurosci Methods*, 141(2):207–217, Feb 2005. doi: 10.1016/j.jneumeth.2004.06.016. URL `http://dx.doi.org/10.1016/j.jneumeth.2004.06.016`.

[178] Nicola Toschi, Tobias Welt, Maria Guerrisi, and Martin E Keck. Transcranial magnetic stimulation in heterogeneous brain tissue: Clinical impact on focality, reproducibility and true sham stimulation. *J Psychiatr Res*, May 2008. doi: 10.1016/j.jpsychires.2008.04.008. URL `http://dx.doi.org/10.1016/j.jpsychires.2008.04.008`.

[179] Nicola Toschi, Tobias Welt, Maria Guerrisi, and Martin E Keck. A reconstruction of the conductive phenomena elicited by transcranial magnetic stimulation in heterogeneous brain tissue. *Phys Med*, 24(2):80–86, Jun 2008. doi: 10.1016/j.ejmp.2008.01.005. URL `http://dx.doi.org/10.1016/j.ejmp.2008.01.005`.

[180] R.Y. Tsai, R.Y. Tsai, and R.K. Lenz. A new technique for fully autonomous and efficient 3d robotics hand/eye calibration. *IEEE Trans. on Robs. and Aut.*, 5(3):345–358, 1989. ISSN 1042-296X. doi: 10.1109/70.34770.

[181] R. Verleger. The instruction to refrain from blinking affects auditory P3 and N1 amplitudes. *Electroencephalogr Clin Neurophysiol*, 78(3):240–251, Mar 1991.

[182] Rolf Verleger, Andreas Sprenger, Sina Gebauer, Michaela Fritzmannova, Monique Friedrich, Stefanie Kraft, and Piotr Jaśkowski. On why left events are the right ones: Neural mechanisms underlying the left-hemifield advantage in rapid serial visual presentation. *J Cogn Neurosci*, Jun 2008. doi: 10.1162/jocn.2009.21038. URL `http://dx.doi.org/10.1162/jocn.2009.21038`.

[183] P.A. Viola. *Alignment by Maximization of Mutual Information.* PhD-thesis, Massachusetts Institute of Technology, Artificial Intelligence Laboratory, 1995.

[184] Weiping Wang and S.R. Eisenberg. A three-dimensional finite element method for computing magnetically induced currents in tissues. *IEEE T Magn*, 30(6):5015–5023, 1994. ISSN 0018-9464. doi: 10.1109/20.334289.

[185] E. M. Wassermann, B. Wang, T. A. Zeffiro, N. Sadato, A. Pascual-Leone, C. Toro, and M. Hallett. Locating the motor cortex on the mri with transcranial magnetic stimulation and pet. *Neuroimage*, 3(1):1–9, Feb 1996. doi: 10.1006/nimg.1996.0001. URL `http://dx.doi.org/10.1006/nimg.1996.0001`.

[186] G.S. Watson. Smooth regression analysis. *Sankhya*, A 26:101–6, 1964.

[187] T. C. Weerts and P. J. Lang. The effects of eye fixation and stimulus and response location on the contingent negative variation (CNV). *Biol Psychol*, 1(1):1–19, 1973.

[188] C. Wolters. *Influence of Tissue Conductivity Inhomogeneity and Anisotropy on EEG/MEG-Based Source Localization in the Human Brain.* Dissertation, MPI of Cognitive Neuroscience, Leipzig, Germany, 2003.

[189] G. Wunderlich, U. Knorr, H. Herzog, J. C. Kiwit, H. J. Freund, and R. J. Seitz. Precentral glioma location determines the displacement of cortical hand representation. *Neurosurgery*, 42(1):18–26; discussion 26–7, Jan 1998.

[190] P. Wunsch and G. Hirzinger. Registration of CAD-models to images by iterative inverse perspective matching. In IEEE Computer Society, editor, *Proceedings of the 1996 International Conference on Pattern Recognition (ICPR '96)*, pages 78–83, 1996.

[191] M. Xu and T. Akatsuka. Detecting head pose from stereo image sequence for active face recognition. In *Third IEEE International Conference on Automatic Face and Gesture Recognition*, pages 82–7, Nara, Japan, 1998.

[192] Ruigang Yang and Zhengyou Zhang. Model-based head pose tracking with stereovision. In *FGR '02: Proceedings of the Fifth IEEE International Conference on Automatic Face and Gesture Recognition*, pages 242–7, Washington, DC, USA, 2002. IEEE Computer Society.

[193] Youngrock Yoon, G.N. DeSouza, and A.C. Kak. Real-time tracking and pose estimation for industrial objects using geometric features. In *IEEE International Conference on Robotics and Automation (ICRA '03)*, volume 3, pages 3473–8, September 2003.

[194] T. A. Yousry, U. D. Schmid, H. Alkadhi, D. Schmidt, A. Peraud, A. Buettner, and P. Winkler. Localization of the motor hand area to a knob on the precentral gyrus. a new landmark. *Brain*, 120 (Pt 1):141–157, Jan 1997.

[195] Abraham Zangen, Yiftach Roth, Bernhard Voller, and Mark Hallett. Transcranial magnetic stimulation of deep brain regions: evidence for efficacy of the h-coil. *Clin Neurophysiol*, 116(4):775–779, Apr 2005. doi: 10.1016/j.clinph.2004.11.008. URL `http://dx.doi.org/10.1016/j.clinph.2004.11.008`.